Unstable and Stable Mass Transfer in Stellar Binaries: From Common Envelopes to Circumbinary Outflows

Thesis by
Peter John Scherbak

In Partial Fulfillment of the Requirements for the
Degree of
Doctor of Philosophy



CALIFORNIA INSTITUTE OF TECHNOLOGY
Pasadena, California

2026
Defended May 20th, 2026

© 2026

Peter John Scherbak
ORCID: 0000-0003-4221-9097

All rights reserved

ACKNOWLEDGEMENTS

First and foremost, I owe an enormous debt to my advisor, Jim Fuller, whose physical intuition and enthusiasm for the weird corners of stellar physics made this work possible — and whose patience with my occasional detours into "what if we also tried this" was remarkable.

Among my collaborators, I am grateful to Wenbin Lu, whose sheer infectious excitement for astronomy has reminded me why I got into this field in the first place. Kevin Burdge's uncanny talent for finding white dwarfs where none were known to exist handed me the keys to my first two papers. Mansi Kasliwal offered consistently sharp and encouraging guidance, and I always left our conversations with more clarity than I arrived with. Abi Polin was a great mentor in the early stages of my PhD, and I'm grateful for her generosity with her time and expertise. Thank you also to the other members of my thesis committee - Sterl, Tom, and Chuck - for the advice and feedback along the way.

To the Caltech astronomy grad students as a whole — thank you for the commiseration, the camaraderie, and the reminder that suffering through quals is a shared human experience. Nik Prusinski, Evan Haze Núñez, Tony Rodriguez, and Samantha Wu deserve particular mention for their friendliness and generous advice.

Caltech itself deserves acknowledgment as an institution: the opportunities it has afforded me, scientific and social, have been extraordinary. The campus is also genuinely beautiful, which matters more than anyone admits when you're trying to clear your head between debugging sessions. To JoAnn Boyd: thank you for handling everything I didn't know needed handling, and for always being friendly and encouraging.

I also owe a deep thanks to the mentors and faculty in Cornell's astronomy department, who first set me on this path. I would not be here without those early experiences.

My great friend Thomas Watts, possibly the most creative scientist I have ever met, has been a constant source of inspiration and a reminder that the best science often starts with someone saying "okay, hear me out."

And to Katherine, who endured countless late nights filled with the soft glow of a terminal window and the sound of me muttering at a MESA error message: thank

you for your patience, your support, and your willingness to look past the fact I still haven't memorized the constellations or discovered a star.

Finally, to my parents — thank you for everything you have done for me and shown me. To my mom, thank you for the love and support during the ups and down of my PhD.

ABSTRACT

Close binary star systems undergo dramatic mass transfer events that reshape their orbital and physical properties, ultimately producing gravitational wave sources, thermonuclear transients, and other high-energy phenomena. This thesis investigates the physics governing close binary formation and evolution, spanning both stable and unstable mass transfer, the strong tidal interactions that follow, and the transients to which mass transfer can give rise.

The earlier chapters constrain the evolutionary history of close WD binaries. In **Chapter II**, I model a sample of double WD binaries to infer the efficiency of common envelope (CE) ejection, finding a low and nearly constant efficiency can explain their formation. These constraints inform binary population synthesis models, where uncertainties in the CE propagate to many phenomena. In **Chapter III**, I compute the tidal heating of ultrashort-period WD binaries self-consistently within binary evolution models. Although tidal heating enhances surface temperatures at short orbital periods, it is not the dominant luminosity source in observed systems, which are instead consistent with intrinsically young, hot WDs also formed with a low CE efficiency.

In **Chapter IV**, I analyze the host galaxies and delay time distributions of calcium-rich gap transients versus other classes of supernova, using ZTF Census of the Local Universe data. These transients favor massive, quiescent hosts similar to those of 91bg-like supernovae, suggesting long delay times and old progenitor systems. The delay time distributions and inferred offsets from host light are consistent with a compact binary progenitor in which a prior episode of mass transfer has played a key role.

The later chapters investigate stable mass transfer through hydrodynamical simulations. In **Chapter V**, I present three-dimensional simulations of rapid, stable mass transfer and find that gas escaping through the outer Lagrange points forms an equatorially concentrated circumbinary outflow, carrying specific angular momentum close to that of the L2 point. This circumstellar material can efficiently shrink the binary's orbit and can interact with ejecta from a subsequent supernova, producing observable transient signatures. In **Chapter VI**, I extend the simulations of Chapter V, incorporating radiative cooling and simulating a wider range of mass transfer rates. Significant L2 outflows emerge when the mass transfer rate

exceeds $\sim 10^{-3}\, M_\odot\, \mathrm{yr}^{-1}$, generating cooling luminosities of $\sim 10^5\, L_\odot$ and producing potentially observable optical transients from both the accretor's disk and the circumbinary outflow itself.

PUBLISHED CONTENT AND CONTRIBUTIONS

Scherbak, Peter, Wenbin Lu, and Jim Fuller (Mar. 2026). "Radiatively Cooled Binary Mass Transfer: Flow Structure, Luminosities, and L2 Outflows Across Mass Transfer Rates". In: *Publications of the Astronomical Society of the Pacific* 138.3, p. 034206. DOI: 10.1088/1538-3873/ae453c.
P.S. conceptualized the project, ran the hydrodynamical simulations, carried out the analysis, and wrote the manuscript.

Scherbak, Peter, Wenbin Lu, and Jim Fuller (Sept. 2025a). "Rapid Binary Mass Transfer: Circumbinary Outflows and Angular Momentum Losses". In: *The Astrophysical Journal* 990.2, p. 172. DOI: 10.3847/1538-4357/adf067.
P.S. participated in the conception of the project, ran the hydrodynamical simulations, carried out the analysis, and wrote the manuscript.

Scherbak, Peter, Abigail Polin, Mansi Kasliwal, Kishalay De, Peter Behroozi, Dave Cook, and W. V. Jacobson-Galán (Nov. 2025b). "Characterizing the Host Galaxies and Delay Times of Ca-rich Gap Transients versus 91bg-like SNe and Normal Type Ia SNe". In: *Publications of the Astronomical Society of the Pacific* 137.11, p. 114207. DOI: 10.1088/1538-3873/ae1cef.
P.S. participated in the conception of the project, identified the transient sample and the host galaxies, carried out the analysis, and wrote the manuscript.

Scherbak, Peter and Jim Fuller (Feb. 2024). "Ultra–short-period WD Binaries Are Not Undergoing Strong Tidal Heating". In: *The Astrophysical Journal* 962.2, p. 185. DOI: 10.3847/1538-4357/ad1dd6.
P.S. participated in the conception of the project, ran the MESA simulations, carried out the analysis, and wrote the manuscript.

Scherbak, Peter and Jim Fuller (Jan. 2023). "White dwarf binaries suggest a common envelope efficiency $\alpha \sim 1/3$". In: *Monthly Notices of the Royal Astronomical Society* 518.3, pp. 3966–3984. DOI: 10.1093/mnras/stac3313.
P.S. participated in the conception of the project, ran the MESA simulations, carried out the analysis, and wrote the manuscript.

TABLE OF CONTENTS

Acknowledgements . . . iii
Abstract . . . v
Published Content and Contributions . . . vii
Table of Contents . . . vii
List of Illustrations . . . x
List of Tables . . . xiii
Chapter I: Introduction . . . 1
1.1 Basics of Mass Transfer . . . 2
1.2 Is mass transfer stable or unstable? . . . 5
1.3 What leads a system to mass transfer? . . . 8
1.4 Corollaries of Mass Transfer . . . 9
1.5 Outline of thesis . . . 11
Chapter II: White dwarf binaries suggest a common envelope efficiency $\alpha \sim 1/3$ 12
2.1 Introduction . . . 12
2.2 He WD Simulations . . . 15
2.3 CO-core WD simulations . . . 30
2.4 RGB progenitor models . . . 34
2.5 Results . . . 40
2.6 Discussion . . . 49
2.7 Conclusion . . . 55
2.A Effect of progenitor mass on WD models . . . 57
2.B Creation of He WD models . . . 59
2.C Effect of metallicity on He WD models . . . 60
2.D Flashing He WD models: Extra Details . . . 61
2.E Effect of He core boundary definition on envelope binding energy . . . 63
Chapter III: Ultrashort-period WD binaries are not undergoing strong tidal heating . . . 64
3.1 Introduction . . . 64
3.2 Basic tidal physics . . . 66
3.3 Tidal effects in MESA simulations . . . 68
3.4 Tidal heating: simulations and observed systems . . . 77
3.5 Discussion . . . 83
3.6 Conclusion . . . 85
3.A AM transport . . . 87
3.B Calculation of wave breaking . . . 88
3.C Effect of hydrogen envelope mass on tidal heating . . . 89
Chapter IV: Characterizing the host galaxies and delay times of Ca-rich gap transients vs 91bg-like SNe and normal Type Ia SNe . . . 91
4.1 Introduction . . . 91

4.2 Observations: The ZTF-CLU Experiment . . . 93
4.3 Determining properties of host galaxies . . . 94
4.4 Results . . . 98
4.5 Discussion . . . 104
Chapter V: Rapid Binary Mass Transfer: Circumbinary Outflows and Angular Momentum Losses . . . 110
5.1 Introduction . . . 110
5.2 Simulation setup . . . 113
5.3 Analysis . . . 122
5.4 Dependence on simulation parameters . . . 138
5.5 Discussion . . . 140
5.6 Conclusion . . . 145
5.A Gas properties . . . 147
5.B Outflow at different radii . . . 152
5.C Convergence tests . . . 153
Chapter VI: Radiatively-Cooled Binary Mass Transfer: Flow Structure, Luminosities, and L2 Outflows across Mass Transfer Rates . . . 157
6.1 Introduction . . . 157
6.2 Simulation setup . . . 160
6.3 Analysis . . . 168
6.4 Conclusion . . . 185
6.A Ratio of gas to radiation pressure . . . 187
6.B Timescales . . . 188
6.C Adopted opacities . . . 189
Chapter VII: Conclusion and Future Directions . . . 192
7.1 Future discoveries . . . 192
7.2 Future methods and approaches . . . 193
7.3 Future astrophysical modeling . . . 195
7.4 Where will this field be in one or two decades? . . . 196
Bibliography . . . 198

LIST OF ILLUSTRATIONS

Number *Page*

2.1 WD cooling behavior 20
2.2 WD models vs observation 22
2.3 Parameter space of WD cooling behavior 25
2.4 WD models undergoing a H flash 27
2.5 Flashing vs non-flashing models 29
2.6 CO WD models vs observation 33
2.7 Parameter space of He vs CO WD formation 35
2.8 Red giant envelope binding energy 38
2.9 WD binary post-CE periods 41
2.10 Estimated α_{CE} values 44
2.11 Estimated α_{CE} values for multiple priors 45
2.12 Estimated α_{CE} values for CO WD primaries 48
2.13 CO WDs arising from different mass progenitors 59
2.14 Post-CE periods for lower metallicity binaries. 61
2.15 Effect of core/envelope boundary definition on envelope binding energy 62
3.1 WD tidal spin synchronization 69
3.2 Gravity wave excitation 71
3.3 Effectiveness of tidal heating, for a 0.25 $M_{\odot}$ WD 74
3.4 Effectiveness of tidal heating, for a 0.35 $M_{\odot}$ WD 75
3.5 Effectiveness of tidal heating, for a 0.45 $M_{\odot}$ WD 75
3.6 The effect of tidal heating on WD temperature 76
3.7 Tidal heating for a range of WD binary models 77
3.8 Tidal heating models compared to an observed 9 minute binary . . . 79
3.9 Tidal heating models compared to an observed 13 minute binary . . . 80
3.10 Tidal heating models compared to an observed 14 minute binary . . . 80
3.11 Tidal heating models compared to an observed 20 minute binary . . . 81
3.12 Values of $\alpha_{\rm CE}$, including ultrashort period WD binaries 84
3.13 Tidal heating for WDs of various envelope masses 89
4.1 CLU catalog data vs PROSPECTOR modeling 97
4.2 Stellar masses and specific star formation rates of transient host galaxies 99

4.3 Stellar masses and specific star formation rates of Ca-rich gap transient hosts, including literature transients . . . 100
4.4 DTDs for Ca-rich gap transients . . . 102
4.5 DTDs for 91bg-like supernovae . . . 103
4.6 DTDs for Ca-rich gap transients vs 91bg-like supernovae vs Type II vs Type Ia SNe supernovae . . . 103
5.1 Mass transfer simulation initial conditions . . . 115
5.2 Mass transfer morphology . . . 123
5.3 Equatorial snapshots of mass transfer . . . 124
5.4 Gas velocities during mass transfer . . . 125
5.5 Meriodonal snapshots of mass transfer . . . 126
5.6 Gas outflowing angle . . . 128
5.7 Mass transfer rate versus time . . . 130
5.8 Flows through L2 and L3 . . . 131
5.9 Gas outflow properties . . . 134
5.10 Outflow energetics . . . 135
5.11 Gas specific angular momentum versus binary mass ratio . . . 139
5.12 Gas energetics and velocities, versus binary mass ratio . . . 139
5.13 Gas temperature . . . 148
5.14 Disk properties near accretor . . . 152
5.15 Gas specific angular momentum versus radius . . . 153
5.16 Gas specific angular momentum convergence study . . . 154
5.17 Effect of envelope heating and numerical resolution . . . 155
5.18 Effect of softening potential . . . 156
6.1 Equatorial snapshots of density for simulations of varying mass transfer rate . . . 165
6.2 Meridional snapshots of density for simulations of varying mass transfer rate . . . 167
6.3 Mass transfer efficiency vs mass transfer rate . . . 170
6.4 Predicted values of mass transfer efficiency . . . 172
6.5 Gas cooling luminosity for simulations . . . 173
6.6 Gas temperature for simulations . . . 174
6.7 Effective gas temperature near accretor and in outflow . . . 175
6.8 Specific angular momentum of outflowing gas . . . 179
6.9 Energetics and velocity of outflowing gas . . . 179
6.10 Gas pressure versus radiation pressure in simulation domain . . . 187

6.11 Opacity in the simulation domain 190

LIST OF TABLES

Number *Page*

2.1 The sample of post-CE WD binaries 16
2.2 He WD model results 26
2.3 CO WD model results 31
2.4 Effect of progenitor mass on post-CE period 57
3.1 Observed ultrashort period WD binaries 78
4.1 Modeled properties of transient host galaxies 97
5.1 Grid of 3D mass transfer simulations 118
5.2 Simulation conversion to astrophysical binaries 120
5.3 Comparison of specific angular momentum at relevant locations in the binary 131
6.1 Grid of 3D simulations of varying mass transfer rate 163
6.2 Mass transfer efficiency and angular momentum losses for a suite of simulations 182

Chapter 1

INTRODUCTION

The night sky presents stars as solitary objects, but this impression is deceiving. Most stars are members of binary or higher-order multiple systems, and a significant fraction of these are close enough that their evolution is fundamentally altered by the presence of a companion. Among solar-type stars, roughly half reside in binaries, with approximately 15% close enough to interact over their lifetimes (Raghavan et al., 2010; Moe and Di Stefano, 2017). For more massive O-type stars, the binary fraction approaches unity, and the majority are expected to exchange mass with a companion during their lives (Sana et al., 2012). Binary interaction is therefore a mainstream channel through which a large fraction of all stars pass. The interacting stars themselves span the full range of stellar evolution: donors and accretors may be main-sequence stars, evolved giants, white dwarfs, neutron stars, or black holes, giving rise to a diverse zoo of systems.

The consequences of these interactions are far-reaching. Many of the most energetic and observationally interesting phenomena in astrophysics — Type Ia supernovae, gravitational wave sources, cataclysmic variables, X-ray binaries, luminous red novae, and a growing collection of exotic transients — either require or are substantially shaped by mass transfer between binary companions. A white dwarf cannot accumulate enough mass to detonate without a donor; a neutron star cannot be spun up into a millisecond pulsar without accreting from a companion; a luminous red nova cannot occur without the two stars undergoing common envelope evolution. Remove binary mass transfer, and much of the transient sky goes dark.

Despite its importance, mass transfer remains one of the least understood processes in stellar physics. The rate at which mass flows between stars, the fraction that is accreted versus ejected, the angular momentum carried away by outflows, and the efficiency with which the binary's orbit shrinks during unstable mass transfer — all of these remain uncertain at the order-of-magnitude level in many regimes. This uncertainty propagates into predictions for gravitational wave merger rates, delay time distributions of Type Ia supernovae, and the demographics of compact object populations. Progress on these open problems requires better theoretical and numerical models of the transfer process itself, motivated by observational

constraints and samples.

1.1 Basics of Mass Transfer

1.1.1 Roche Geometry and Lagrange Points

The geometry of a binary system is most naturally described in the co-rotating reference frame in which both stars rotate at the binary's orbital angular velocity Ω. The effective gravitational potential, the Roche potential, is the sum of the gravitational potentials of the two stars and the centrifugal potential arising from the rotating frame:

$$\Phi(\mathbf{r}) = -\frac{GM_1}{|\mathbf{r}-\mathbf{r}_1|} - \frac{GM_2}{|\mathbf{r}-\mathbf{r}_2|} - \frac{1}{2}\Omega^2|\mathbf{r}-\mathbf{r}_{\rm com}|^2, \tag{1.1}$$

where M_1 and M_2 are the masses of the two stars, $\mathbf{r}_1$ and $\mathbf{r}_2$ are their positions, and $\mathbf{r}_{\rm com}$ is the position of the center of mass. When mass transfer occurs, we assume here that M_1 is the donor, which loses mass. The Roche potential defines a set of equipotential surfaces that determine how mass can flow in the binary. If one of the stars evolves and expands, it will fill successively larger equipotential surfaces, with its pressure and density constant along the equipotential.

The Roche potential has five equilibrium points, known as the Lagrange points, where the net force on a test particle in the co-rotating frame vanishes. The most important of these is the inner Lagrange point L1, which lies on the line connecting the two stars, closer to the less massive one. Because L1 is an unstable equilibrium point, mass displaced toward either star will tend to flow toward that star, and so L1 is the point through which mass transfer in most interacting binaries proceeds. In addition, the sonic point for a streamline of mass, where the flow transitions from subsonic to supersonic, must occur within the vicinity of L1 (Lubow and Shu, 1975). The area around L1 is therefore sometimes known as the L1 nozzle, or a de Laval-like nozzle (Linial and Sari, 2017; Cehula and Pejcha, 2023; Cehula and Pejcha, 2026). Not included in the Roche potential is the Coriolis force, which nevertheless significantly impacts the flow of the mass transfer stream through L1 (Ryu et al., 2025).

The equipotential surface passing through L1 defines the Roche lobe of each star — a teardrop-shaped volume within which material is gravitationally bound to that star. When a star underfills its Roche lobe, mass transfer does not occur, except if its wind is captured by the companion. But when a star expands, e.g. through nuclear evolution, to fill its Roche lobe, mass begins to flow through L1 toward the

companion, initiating Roche lobe overflow (RLOF). Mass can directly impact the companion, or form an accretion disk around it.

The outer Lagrange points L2 and L3, located beyond each star along the binary axis (with L2 on the side of the less massive star), define potential escape routes for mass from the system. When the mass transfer rate is high enough that the accretion disk around the companion overflows, or when the donor overfills its Roche lobe substantially, material can escape through L2 and L3, forming a circumbinary outflow.

A very good approximation for the volume-equivalent radius of the Roche lobe of the donor star is given by Eggleton (1983b):

$$\frac{R_L}{a} = \frac{0.49q^{2/3}}{0.6q^{2/3} + \ln(1 + q^{1/3})}, \tag{1.2}$$

where a is the orbital separation and $q = M_1/M_2$ is the mass ratio of the donor to the accretor.

1.1.2 Mass Transfer Rate

The most important quantity governing the evolution of a mass-transferring binary is the mass transfer rate: the rate at which mass flows through L1. For stars where the overflow above L1 is small, or when the star's photosphere is underfilling its Roche lobe (as its atmosphere can still extend to L1), the mass transfer rate is described by the formula of Ritter (1988), where the mass transfer is optically thin and isothermal. The resulting mass transfer rate is:

$$\dot{M} = \dot{M}_0 \exp\left(\frac{R_* - R_L}{H_P}\right), \tag{1.3}$$

where R_* is the donor's radius corresponding to its photosphere, R_L is its Roche lobe radius, H_P is the photospheric pressure scale height of the donor, and $\dot{M}_0$ is the mass transfer rate when the donor's photosphere exactly fills its Roche lobe. In terms of other quantities, $\dot{M}_0 = \rho_{\rm phot} v_s A$, where v_s is the isothermal sound speed at L1, A is the cross-sectional area of the flow at L1 and $\rho_{\rm phot}$ is the density at the photosphere. A can be approximately written as $2\pi R_* H_P F(q)$ where $F(q)$ is a function of the mass ratio (Ritter, 1988). Combined with $H_P = \frac{P}{\rho g} = \frac{v_s^2}{g}$, A can also be written as $2\pi R_* \frac{v_s^2}{g} F(q) = 2\pi \frac{v_s^2}{\Omega_*^2} F(q)$, where $\Omega_*^2 = \frac{GM_1}{R_*^3}$.

The exponential dependence on the degree of Roche lobe overflow means that the mass transfer rate is extremely sensitive to the difference $R_* - R_L$. A simple

derivation illustrates why. Hydrostatic equilibrium in the stellar atmosphere gives

$$\frac{dP}{dr} = -\rho g, \tag{1.4}$$

which, combined with the definition of the pressure scale height,

$$H_P = \frac{P}{\rho g}, \tag{1.5}$$

yields an exponential density profile,

$$\rho(r) = \rho_{\rm phot}\ \exp\!\left(-\frac{r - R_*}{H_P}\right), \tag{1.6}$$

The density at the L1 point is then

$$\rho_{\rm L1} = \rho_{\rm phot}\ \exp\!\left(\frac{R_* - R_{\rm L1}}{H_P}\right). \tag{1.7}$$

Since mass transfer through L1 proceeds at roughly the local sound speed through a nozzle of cross-sectional area A, the mass transfer rate scales as

$$\dot{M} \sim \rho_{\rm L1}\, v_s\, A \propto \exp\!\left(\frac{\delta}{H_P}\right), \tag{1.8}$$

where $\delta \equiv R_* - R_{\rm L1}$ is the Roche lobe overfill. When $\delta > 0$ the donor overflows its Roche lobe and the mass transfer rate increases; when $\delta < 0$ the donor is detached and the exponential suppresses the rate to small values.

Strictly speaking, the Ritter (1988) formula assumes the donor is detached ($\delta < 0$), with mass transfer driven by the atmospheric tail extending beyond the photosphere to L1. When $\delta > 0$, the formula loses some physical accuracy, but captures the correct scaling for $\delta \ll H_P$ (Büning and Ritter, 2004; Büning and Ritter, 2006). When the overfill is large, however, the flow through L1 becomes optically thick and the simple exponential scaling breaks down. A better prescription in this regime is derived in Kolb and Ritter (1990) and revisited in Marchant et al. (2021). The transition between the optically thin and optically thick regimes, and the appropriate mass transfer rate in the intermediate regime, remains an area of active research (Cehula and Pejcha, 2023).

Mass transfer affects the binary orbit through conservation of angular momentum: as the component masses change, the orbital separation must too. For conservative mass transfer, where all mass is accreted by the companion, the total mass $M = M_1 + M_2$ is constant and the orbital angular momentum

$$J = \frac{M_1 M_2}{\sqrt{M_1 + M_2}}\sqrt{Ga} \tag{1.9}$$

is conserved. Setting $\dot{J} = 0$ and using $\dot{M}_2 = -\dot{M}_1$ gives (using a logarithmic derivative for the quickest derivation)

$$\frac{\dot{a}}{a} = -2\frac{\dot{M}_1}{M_1}\left(1 - \frac{M_1}{M_2}\right), \tag{1.10}$$

where $\dot{M}_1 < 0$ is the mass loss rate of the donor. Mass transfer is therefore stabilizing (orbital widening, $\dot{a} > 0$) when the donor is less massive than the accretor ($M_1 < M_2$), and destabilizing ($\dot{a} < 0$) in the opposite case.

If mass transfer is not conservative, some mass will leave the binary, carrying with it angular momentum, so angular momentum is no longer conserved. The evolution therefore becomes more complex. Assuming a fraction β of the transferred mass accretes onto M_2, the orbital separation evolves as (see Pols (2011) for a derivation)

$$\frac{\dot{a}}{a} = -\frac{2\dot{M}_1}{M_1}\left(1 - \beta\frac{M_1}{M_2} - (1-\beta)\left(\gamma + \frac{1}{2}\right)\frac{M_1}{M_1 + M_2}\right), \tag{1.11}$$

The last term represents angular momentum lost by outflowing gas (of fraction $1 - \beta$), which is parameterized by γ, the specific angular momentum of outflowing gas in units of the specific AM of the binary, i.e.

$$\frac{\dot{J}}{\dot{M}} = \gamma\frac{J}{M_1 + M_2}, \tag{1.12}$$

where $\dot{J}$ and $\dot{M}$ are the net mass and angular momentum outflow rates. When $\beta = 1$, all mass is accreted by the companion and mass transfer is conservative. Non-conservative MT can occur when the accretor is thermally or rotationally limited (i.e. cannot accept any more mass) (e.g., Lechien et al., 2025) or when a compact object accretor approaches the Eddington limit and drives strong outflows (e.g., Toyouchi et al., 2024).

Equation 1.11 describes the orbital evolution given a mass transfer rate $\dot{M}_1$, but says nothing about how $\dot{M}_1$ itself evolves. Whether mass transfer accelerates or self-regulates depends on the stability of mass transfer.

1.2 Is mass transfer stable or unstable?

The response of the donor and the orbit to mass loss generally determines whether mass transfer is stable or unstable. If the donor shrinks faster than its Roche lobe as mass is lost, the system reaches an equilibrium and mass transfer proceeds stably on a thermal or nuclear timescale. If instead the donor expands relative to its

Roche lobe as mass is lost, the mass transfer rate grows on a dynamical timescale, leading to unstable mass transfer and either a common envelope or direct merger. The boundary between unstable and stable mass transfer, and such boundary's dependence on donor structure and mass ratio, is a central uncertainty in binary evolution.

The responses of the donor and the orbit are characterized by the mass-radius exponents

$$\zeta_* \equiv \left(\frac{d \log R_*}{d \log M_\mathrm{d}}\right), \qquad \zeta_\mathrm{L} \equiv \frac{d \log R_\mathrm{L}}{d \log M_\mathrm{d}}, \tag{1.13}$$

where the exponent ζ_* describes the response of the donor to mass loss (which, for more accurate analysis, can be separated into its immediate adiabatic response and its equilibrium thermal-timescale response) and ζ_L describes how the Roche lobe radius changes as the donor loses mass.

If $\zeta_\mathrm{L} \leq \zeta_*$, the donor shrinks faster than its Roche lobe upon mass loss, and must re-expand to initiate further mass transfer, which then proceeds stably on a nuclear timescale. If instead $\zeta_\mathrm{L} > \zeta_*$, the donor expands relative to its Roche lobe, meaning its overfill fraction and mass transfer rate will increase without bound, becoming unstable and likely leading to a common envelope or stellar merger.

For conservative mass transfer, ζ_L depends only on the mass ratio (Pols, 2011),

$$\zeta_\mathrm{L} \approx 2.13 \frac{M_1}{M_2} - 1.67. \tag{1.14}$$

The value of ζ_* depends critically on the donor's envelope structure. Stars with deep convective envelopes — e.g. red giants — have $\zeta_* \lesssim 0$, expanding in response to mass loss. Stars with radiative envelopes have $\zeta_* \gg 0$ and shrink rapidly upon mass loss. Consequently, mass transfer from donors with convective envelopes has historically been thought to be dynamically unstable when the initial mass ratio $q = M_1/M_2 > 1$, as ζ_L will be greater than 0.46. White dwarfs have $\zeta_* \sim -1/3$, so applying Eq. 1.14, mass transfer is stable between two white dwarfs when $q < 2/3$ (Marsh et al., 2004).

Several important caveats apply to this framework. First, Eq. (1.14) holds only for conservative mass transfer; non-conservative mass loss and angular momentum loss modify ζ_L in ways that depend on the assumed mode of mass ejection (Soberman et al., 1997). Second, the behavior of the donor star is not always as simple as described above, as incorporating non-adiabatic response of donor and more realistic stellar

models than a polytrope has suggested that mass transfer is more stable than thought before (Ge et al., 2010; Temmink et al., 2023). Third, the response of the accretor to the infalling stream — including thermal expansion and possible formation of a contact binary — can lead to unstable mass transfer even when the above donor stability analysis would deem it stable.

Episodes of stable and unstable mass transfer can occur in the evolutionary history of a single binary. For example, low-mass X-ray binaries are undergoing stable mass transfer, but were likely preceded by unstable mass transfer (common envelope evolution) between the massive progenitor of the compact object and the stellar companion (Tauris and Heuvel, 2006). Conversely, high-mass X-ray binaries are descendants of systems that avoided unstable mass transfer within the original binary of two massive stars, but will likely undergo a common envelope event in the future (Tauris and Heuvel, 2006; Heuvel, 2018). It is also a subject of current debate whether stable or unstable mass transfer is the primary channel to form merging binary black holes (for a recent summary, see Dorozsmai and Toonen 2024).

1.2.1 More about unstable mass transfer

Common envelope evolution (CEE) or a direct stellar merger can occur when mass transfer becomes unstable. In CEE, the companion inspirals within the donor's envelope, depositing orbital energy. In contrast, a stellar merger occurs when two stars coalesce without a well-defined envelope, although the distinction between merger and common envelope is not always clear (Schneider et al., 2025).

In CEE, the companion becomes engulfed within the outer layers of the donor, and the two cores spiral inward through a shared, co-rotating envelope (Paczynski, 1976a). CEE is a (uncertain) cornerstone of binary stellar evolution, thought to be responsible for drastically shrinking orbital separations and producing the compact binaries we observe today.

Beyond the structural mass-transfer instabilities discussed in the previous section, tidal instabilities provide an additional pathway to unstable mass transfer. If the spin angular momentum of the system is large compared to the total orbital angular momentum, the orbit becomes unstable to the Darwin instability, leading to orbital shrinkage and subsequent RLOF (Ivanova et al., 2013).

Once initiated, CEE can unfold in distinct phases. Initially, the companion plunges inward on a dynamical timescale, depositing orbital energy into the envelope through frictional drag. If the plunge-in does not lead to a prompt merger, a phase of self-

regulated inspiral lasting for a thermal timescale can occur, as the envelope expands and drops in density. Two outcomes are ultimately possible: either the deposited energy is sufficient to unbind and eject the envelope entirely, leaving a tightened post-CE binary, or the inspiral continues until the two cores merge.

The standard framework for predicting post-CE orbital separations is the α energy prescription (Livio and Soker, 1988), which balances the change in orbital energy against the binding energy of the ejected envelope:

$$\alpha_{\rm CE}\left[\frac{GM_1M_2}{2a_i}-\frac{GM_{1,c}M_2}{2a_f}\right]=E_{\rm bind}, \tag{1.15}$$

where a_i and a_f are the orbital separations before and after the CE event, $M_{1,c}$ is the mass of the donor's core (which becomes the primary of the post-CE binary), $\alpha_{\rm CE}$ is the efficiency with which orbital energy is converted to kinetic energy of the ejecta, and the binding energy $E_{\rm bind}$ is negative. $E_{\rm bind}$ is often parameterized as

$$E_{\rm bind}=-\frac{GM_1M_{1,\rm env}}{\lambda R_*}, \tag{1.16}$$

where $M_{1,\rm env}=M_1-M_{1,c}$ and λ encapsulates the binding energy structure of the donor envelope, including gravitational and internal (and potentially recombination) energy (Dewi and Tauris, 2000; Dewi et al., 2002). An alternative angular-momentum-based prescription, parameterized by γ (Nelemans et al., 2000), has been proposed when the energy approach fails to reproduce observed post-CE configurations. In practice, both $\alpha_{\rm CE}$ and γ remain poorly constrained, contributing to large uncertainties in population synthesis predictions for compact binary formation rates (Ivanova et al., 2013).

In principle, hydrodynamical simulations offer the most direct path to understanding a CEE. Recently, several simulations have succeeded in following the evolution through to near-complete envelope ejection (Law-Smith et al., 2022; Lau et al., 2022; Moreno et al., 2022). Nevertheless, CEE remains one of the most numerically challenging problems in stellar astrophysics: the vast range of lengthscales and timescales in the problems means no current simulation can self-consistently capture both plunge-in and self-regulated phases.

1.3 What leads a system to mass transfer?

Much of the preceding analysis assumes mass transfer is already occurring, but what brings a binary to that point? Binaries start off detached, with both stars underfilling

their Roche lobes, and mass transfer (other than capture of winds) will only begin when the donor fills its Roche lobe, which requires either the donor to expand or the orbit to shrink. The three primary drivers are:

Stellar evolution. A star expands as it evolves off the main sequence, eventually filling its Roche lobe if a companion is present. This is the dominant channel for wide binaries, where angular momentum losses are negligible.

Gravitational wave emission. Compact binaries lose angular momentum to gravitational radiation, driving the orbit to shrink until the donor fills its Roche lobe. This is the dominant driver in short-period systems containing white dwarfs, neutron stars, or black holes.

Magnetic braking. Magnetized stars lose angular momentum through a magnetized stellar wind, but in a tidally locked binary, the stellar spin is coupled to the orbit, so angular momentum is also extracted from the orbit. Magnetic braking is important at intermediate orbital periods where gravitational wave emission is not efficient at shrinking the orbit, and is particularly important for cataclysmic variables (Knigge, 2011) and low-mass X-ray binaries (Verbunt and Zwaan, 1981; Van et al., 2019).

1.4 Corollaries of Mass Transfer

Mass transfer does not occur in isolation. As a binary evolves toward and through Roche lobe overflow, physical processes are triggered that shape both the binary's fate and its observational appearance.

1.4.1 Tidal Interactions

As a binary's orbit shrinks, tidal forces between the two stars grow rapidly. Tides manifest in two forms: the equilibrium tide, a deformation of the stellar surface in response to the companion's gravitational potential, and the dynamical tide, which involves the excitation of internal waves. The primary effect of tides is to dissipate energy, thereby circularizing the orbit and synchronizing each star's rotation with the orbital motion (Zahn, 2008). By the time a donor approaches Roche lobe filling, it is generally assumed to be synchronized (an assumption implicit in the Roche potential framework).

The efficiency of tidal synchronization depends sensitively on the orbital separation. For the equilibrium tide, the synchronization timescale scales as $(a/R)^6$, making tides extremely sensitive to the size of the orbit (Zahn, 2008; Biscoveanu et al., 2023). Tides become dynamically significant at orbital periods below roughly a

few days for binaries containing main sequence or evolved stars (Zahn, 2008), and below a few hours for white dwarf binaries (Fuller and Lai, 2012; Fuller and Lai, 2013). The dominant dissipation mechanism depends on the internal structure of the star: in stars with outer convective envelopes, turbulent viscosity acting on the equilibrium tide is the primary channel (Sun et al., 2026), while in white dwarfs, the companion's tidal potential excites internal gravity waves that dissipate near the surface through radiative damping or nonlinear effects (Fuller and Lai, 2012; Fuller and Lai, 2013).

Tidal interactions are also closely coupled to the mass transfer process itself. In systems with an accretion disk, tidal torques from the companion are thought to return the angular momentum of accreted material to the orbit (Priedhorsky and Verbunt, 1988). When direct impact accretion occurs, there can still be a synchronizing force between accretor and orbit (Marsh et al., 2004). For white dwarf binaries, the synchronizing timescale determines if the mass transfer remains stable or if the binary merges (Marsh et al., 2004). Tidal distortion also affects the observable properties of mass-transferring systems such as cataclysmic variables, influencing their luminosity, effective temperature distribution, and predicted orbital period minimum (Nelson et al., 1985). As mentioned in Sec. 1.2.1, tidal instabilities can drive the binary into an inspiral and initiate unstable mass transfer and a common envelope.

1.4.2 Transients from Mass Transfer

The endpoints of mass-transferring binaries account for a remarkable number of transients. When a white dwarf accretes sufficient material from a companion, the accumulated hydrogen or helium shell can ignite in a thermonuclear runaway, producing a classical nova or, in the most extreme cases, a Type Ia supernova. The double-detonation channel, in which a helium shell detonation triggers a secondary carbon detonation in the white dwarf core, offers a path to thermonuclear explosion even below the Chandrasekhar mass (Kromer et al., 2010). Mass transfer is also responsible for the stripped-envelope supernovae observed as Type Ib and Type Ic events, in which a massive star loses its hydrogen or helium envelope to a companion before exploding as a core-collapse supernova. When the mass transfer has occurred recently before the explosion, the interaction between the supernova ejecta and the previously formed circumstellar material may produce interaction-powered events as Type IIn, Type Ibn and Type Icn supernovae (Hosseinzadeh et al., 2019; Ransome and Villar, 2025; Salmaso et al., 2025). X-ray binaries, where a neutron star or black hole accretes from a companion, are powered entirely by mass transfer,

with the gravitational potential energy of the infalling material converted into X-ray luminosity. Common envelope events, whether leading to short-period binary formation or merger, may produce luminous red novae, which are powered by shocks and recombination energy of the expanding ejected envelope and reprocessed into the infrared by dust that forms in the cooling outflow (Pejcha, 2014; Pejcha et al., 2017; Metzger and Pejcha, 2017; Karambelkar et al., 2023).

1.5 Outline of thesis

The chapters that follow investigate mass transfer across a range of regimes and binary types. Chapters II and III examine the unstable, dynamical common envelope phase that produces the tightest known double WD binaries, and the strong tidal interactions that can arise in its aftermath. Chapter IV investigates the host environments of calcium-rich gap transients and compares them to those of Type Ia and 91bg-like supernovae, which involve an exploding white dwarf in a binary. Chapters V and VI turn to the hydrodynamics of stable but rapid mass transfer for massive star donors, characterizing the circumbinary outflows that form when mass escapes the system through the outer Lagrange points and the luminous transients they may produce. The results developed here are connected by a single underlying theme: the physics of mass transfer between stars determines the fate of the binary and what we observe as the binary transforms.

Chapter 2

WHITE DWARF BINARIES SUGGEST A COMMON ENVELOPE EFFICIENCY $\alpha \sim 1/3$

Scherbak, Peter and Jim Fuller (Jan. 2023). "White dwarf binaries suggest a common envelope efficiency $\alpha \sim 1/3$". In: *Monthly Notices of the Royal Astronomical Society* 518.3, pp. 3966–3984. DOI: 10.1093/mnras/stac3313.

Common envelope (CE) evolution, which is crucial in creating short period binaries and associated astrophysical events, can be constrained by reverse modeling of such binaries' formation histories. Through analysis of a sample of well-constrained white dwarf (WD) binaries with low-mass primaries (7 eclipsing double WDs, 2 non-eclipsing double WDs, 1 WD-brown dwarf), we estimate the CE energy efficiency $\alpha_{\rm CE}$ needed to unbind the hydrogen envelope. We use grids of He- and CO-core WD models to determine the masses and cooling ages that match each primary WD's radius and temperature. Assuming gravitational wave-driven orbital decay, we then calculate the associated ranges in post-CE orbital period. By mapping WD models to a grid of red giant progenitor stars, we determine the total envelope binding energies and possible orbital periods at the point CE evolution is initiated, thereby constraining α_{CE}. Assuming He-core WDs with progenitors of 0.9 - 2.0 $M_\odot$, we find $\alpha_{CE} \sim 0.2 - 0.4$ is consistent with each system we model. Significantly higher values of $\alpha_{\rm CE}$ are required for higher mass progenitors and for CO-core WDs, so these scenarios are deemed unlikely. Our values are mostly consistent with previous studies of post-CE WD binaries, and they suggest a nearly constant and low envelope ejection efficiency for CE events that produce He-core WDs.

2.1 Introduction

White dwarf (WD) binaries are not only the progenitors of many interesting astrophysical events, but they are also incredibly useful astrophysical laboratories. The discovery rate of WD binaries has greatly accelerated over the past decade, primarily due to two surveys: the Extremely Low Mass (ELM) Survey (e.g., Brown et al., 2020) and the Zwicky Transient Facility (ZTF) survey (Bellm et al., 2019a). The ELM Survey has discovered ∼100 WD binaries, but most are non-eclipsing and have poorly constrained companions. The ZTF survey has doubled the number

of eclipsing WD binaries (e.g., Burdge et al., 2020a) whose masses and radii are usually well constrained. Backwards modeling from the observed properties of these binaries can lead to new insights on their formation history, especially their common-envelope (CE) phase of evolution.

The CE is a stage of binary stellar evolution where two stars orbit inside a shared envelope (Paczynski, 1976b). CE evolution is thought to be crucial for the creation of exotic systems such as double WD binaries (DWDs) and merging neutron stars. These and other short-period binaries that contain at least one compact object likely underwent CE evolution in the past (Ivanova et al., 2013). The CE is the most important phase of such a binary's formation history, because it is responsible for the expulsion of the hydrogen (H) envelope and a drastic reduction in separation, transforming a wide binary into a short-period, compact binary.

Despite its importance, the CE is arguably the least understood stage of binary evolution, representing a limitation of binary population synthesis models. For example, changing the parametrization of the CE event can affect the theoretical rates and delay times of black hole mergers, which is important to interpret the gravitational wave events detected by LIGO-VIRGO (e.g., LIGO Scientific Collaboration and Virgo Collaboration et al., 2019). The rate of Type Ia supernova, as well as the nature of their main formation channel, also depends on the parametrization of the CE (Ivanova et al., 2013). Therefore, uncertainty regarding the CE event propagates to different areas of astronomy.

The most common parametrization of the CE event is based on an energy conservation approach, using an α_{CE} parameter that is defined as the fraction of the change in orbital energy (as the inspiral occurs) that goes into the unbinding of the CE (Livio and Soker, 1988). Hydrodynamical simulations of the CE have produced a range of results for α_{CE}, possibly due to a failure of simulations to converge (Iaconi et al., 2017). They also struggle to track the long-term (thermal time-scale) evolution, which may continue to affect the orbit. Therefore, an independent approach to estimate α_{CE}, based on observations rather than pure simulations, is valuable.

The short orbital period of many WD binaries implies that they were created through CE evolution, and they provide a unique opportunity to constrain the physics of the CE. In addition to the system's orbital period, properties such as component masses, radii, and temperatures are often reported for both WDs, using methods such as light curve fitting and radial velocity measurements. These well-constrained systems can yield detailed insights into the histories of WD binaries.

Estimates of α_{CE} have already been reported from discoveries of WD-M dwarf binaries (Zorotovic et al., 2010; De Marco et al., 2011; Davis et al., 2012), but the evolution of those systems is complicated by poorly understood magnetic braking that dominates orbital decay. Many of these systems are young and hence the braking prescription does not strongly affect their inferred post-CE orbital period (Schreiber and Gänsicke, 2003), but it is still necessary to compare to other types of post-CE systems. WD binaries are simpler to model because their orbit only decays through gravitational wave (GW) emission. Hence, they can provide both comparisons to existing values of α_{CE} and also additional constraints. For instance, if α_{CE} values from WD binaries show agreement with α_{CE} values from WD-M dwarf binaries, it would become more justified to extrapolate that value to all binaries formed through CE evolution and make more robust predictions for population synthesis. The growing number of well-constrained WD binaries makes it possible to report α_{CE} for many such systems, not just a few case studies.

Either one or two phases of CE evolution may be responsible for the formation of DWD binaries. In this paper, we concentrate on the most recent phase of CE evolution, assumed to be responsible for the formation of the hotter, primary WD and also likely responsible for the most drastic reduction in separation. We are motivated by Woods et al. (2011), which found that a *stable* first stage of mass transfer can explain observed systems, but that the second stage (what we model) is indeed unstable and involves a CE.

By backwards modeling of the WD primary, we can therefore constrain α_{CE} for the final phase of CE evolution. Specifically, if the system's "birth period" can be determined - its orbital period immediately following CE ejection, when the primary WD is formed - then we can calculate the post-CE orbital energy. Combining that with the possible binding energy of progenitor stars, plus the pre-CE orbital energy, determines the energy budget for the CE. Nelemans et al. (2000) and Nelemans and Tout (2005) used similar techniques for previously discovered WD binaries, but here we additionally model more recently discovered systems from ELM and ZTF.

In Section 2.2 we discuss the creation of a grid of helium (He) WDs in order to estimate cooling ages and birth periods for 10 binaries. In a similar analysis in Section 2.3, we consider the possibility of the primary WD instead being a carbon-oxygen (CO) WD. In Section 2.4, we construct a grid of red giant stars to model the progenitors of the binaries and determine their envelope binding energies. Section 2.5 presents the ranges for birth period and α_{CE} for all systems. In Section 2.6 we

discuss additional uncertainties and compare our results to estimates of α_{CE} in other works. We conclude and summarize in Section 2.7.

2.2 He WD Simulations

2.2.1 Binary Systems

We modeled short-period WD binaries that 1) have primary masses between $\sim 0.3 - 0.45\ M_{\odot}$ and are likely He-core WDs, 2) have a tight constraint on the secondary mass M_2, and 3) are at orbital periods greater than 20 minutes. We did not model binaries at periods lower than 20 minutes because of the associated uncertainties with strong tidal effects that could change the cooling behavior (Fuller and Lai, 2013). Table 2.1 summarizes the systems we model. All except for two (WD 0957-666 and WD 1101+364) are eclipsing. Each of these systems has a primary mass $M_1 \gtrsim 0.3\,M_{\odot}$ and is likely to be formed by a CE event rather than stable mass transfer (Li et al., 2019a).

From a sample of WD binaries discovered with ZTF, we model ZTF J2029+1534, ZTF J0722-1839, ZTF J1749+0924, and ZTF J1901+5309 (Burdge et al., 2020a). Burdge et al. (2020a) determined radii via light curve modeling and surface temperatures via spectroscopy, then combined radius and temperature measurements to determine masses via mass-radius relations.

We also model SDSS J082239.546+304857.19, found by the ELM Survey (Brown et al., 2017). Radii were reported via light curve modeling, temperature and surface gravity (log g) of the primary from spectroscopy, and mass from evolutionary curves fitted to temperature and log g. A later paper updated the radius of the primary and the orbital period of the system (Kosakowski et al., 2020), which we use in our analysis, but did not contain an updated mass estimate of the primary. Most other binaries in the ELM Survey are not eclipsing and do not have well-constrained secondary masses, which would lead to an inherent uncertainty in the orbital evolution of the system. Hermes et al. (2014) estimated M_1 and M_2 for 8 ELM WDs using the observed ellipsoidal variations - however, M_1 for these systems ($M_1 \lesssim 0.2\,M_{\odot}$) is less than that of the other systems we model, and it is unclear whether these low-mass WDs were created through unstable or stable mass transfer.

For the WD binary CSS 41177 (SDSS J100559.10+224932.3), the mass and radius are measured from light curve plus radial velocity modeling, independent of mass-radius relations (Bours et al., 2014). The temperature of the primary is again from spectroscopy, and log g values are also reported (Bours et al., 2015). Similarly,

System	M_1 ($M_\odot$)	M_2 ($M_\odot$)	$T_{\rm eff,1}$ (kK)	$T_{\rm eff,2}$ (kK)	R_1 (10^{-2} $R_\odot$)	log g	q	$P_{\rm b}$ (min)
ZTF J2029[1]	$0.32\pm^{0.04}_{0.04}$	$0.3\pm^{0.04}_{0.04}$	$18.25\pm^{0.25}_{0.25}$	$15.3\pm^{0.3}_{0.3}$	$2.9\pm^{0.2}_{0.3}$	-	-	20.868
ZTF J0722[1]	$0.38\pm^{0.04}_{0.04}$	$0.33\pm^{0.03}_{0.03}$	$19.9\pm^{0.15}_{0.15}$	$16.8\pm^{0.15}_{0.15}$	$2.24\pm^{0.04}_{0.02}$	-	-	23.709
ZTF J1749[1]	$0.40\pm^{0.07}_{0.05}$	$0.28\pm^{0.05}_{0.04}$	$20.4\pm^{0.2}_{0.2}$	$12.0\pm^{0.6}_{0.6}$	$2.2\pm^{0.3}_{0.4}$	-	-	26.434
SDSS J0822[2,3]	$0.304\pm^{0.014}_{0.014}$	$0.524\pm^{0.05}_{0.05}$	$13.92\pm^{0.255}_{0.255}$	-	$3.1\pm^{0.6}_{0.6}$	$^*7.14\pm^{0.05}_{0.05}$	-	40.501
ZTF J1901[1]	$0.36\pm^{0.04}_{0.04}$	$0.36\pm^{0.05}_{0.05}$	$26.0\pm^{0.2}_{0.2}$	$16.5\pm^{2.0}_{2.0}$	$2.9\pm^{0.1}_{0.2}$	-	-	40.602
SDSS J1205[4]	$0.39\pm^{0.02}_{0.02}$	$0.049\pm^{0.006}_{0.006}$	$23.68\pm^{0.43}_{0.43}$	-	$2.2\pm^{0.03}_{0.03}$	$^*7.37\pm^{0.05}_{0.05}$	-	71.230
WD 0957[5,6,7]	0.37	-	$30\pm^{0.5}_{0.5}$	11	-	$^*7.285\pm^{0.082}_{0.082}$	$1.13\pm^{0.02}_{0.02}$	87.83
SDSS J1152[8]	$0.362\pm^{0.014}_{0.014}$	$0.325\pm^{0.013}_{0.013}$	$20.8\pm^{1.06}_{0.96}$(eclipse) $21.2\pm^{1.2}_{1.1}$ (SED)	$10.4\pm^{0.4}_{0.34}$(eclipse) $11.1\pm^{0.95}_{0.77}$(SED)	$2.12\pm^{0.03}_{0.03}$	$7.344\pm^{0.014}_{0.014}$	-	143.806
CSS 41177[9,10]	$0.378\pm^{0.023}_{0.023}$	$0.316\pm^{0.011}_{0.011}$	$22.439\pm^{0.059}_{0.059}$	$10.876\pm^{0.032}_{0.032}$	$2.224\pm^{0.041}_{0.041}$	$7.322\pm^{0.015}_{0.015}$	-	167.062
WD 1101[8,11,12]	0.29	-	$15.5\pm^{0.5}_{0.5}$	12	-	$^*7.38\pm^{0.049}_{0.049}$	$0.87\pm^{0.03}_{0.03}$	208.4

Table 2.1: Measured parameters for all the systems we model, including the masses of the two components, M_1 and M_2, the radii of the components, R_1 and R_2, the effective surface temperature of the components, $T_{\rm eff,1}$ and $T_{\rm eff,2}$, the surface gravity log g, the mass ratio $q \equiv \frac{M_1}{M_2}$ (if measured), and the orbital period, $P_{\rm b}$. An asterisk next to the log g means there is only a single value reported; otherwise, log g_2 is reported as well. M_1 is defined as the primary via observation of the primary eclipse, except for WD 0957 and WD 1101 where it is the brighter WD. As expected, M_1 is hotter than M_2 when companion temperatures are reported. All companions M_2 are believed to be WDs except for SDSS J1205, where the companion is a brown dwarf. Parameters are from Burdge et al. (2020a)[1], Brown et al. (2017)[2], Kosakowski et al. (2020)[3], Parsons et al. (2017)[4], Maxted et al. (2002)[5], Moran et al. (1997)[6], Bragaglia et al. (1995)[7], Parsons et al. (2020)[8], Bours et al. (2014)[9] , Bours et al. (2015)[10], Marsh (1995)[11], Bergeron et al. (1992)[12].

for the WD binary SDSS J115219.99+024814.4, the masses and radii are measured from light curve plus radial velocity modeling (Parsons et al., 2020). Temperatures and log g values are reported both from light curve modeling and from spectroscopy. The original discovery paper (Hallakoun et al., 2016) had different results (including higher temperatures and mass estimates), but Parsons et al. (2020) uses Gaia data to refine the measurements, and we therefore use the more recent values. We also model the eclipsing WD-brown dwarf (BD) binary SDSS J120515.80-024222.6 (Parsons et al., 2017). The masses and radii are again from light curve plus radial velocity modeling, supplemented by temperature and surface gravity measured via spectroscopy.

Finally, we model two non-eclipsing WD binaries, WD 0957-666 (2MASS J09585493-6653102) and WD 1101+364 (SDSS J110432.56+361049.0). A surface gravity value for WD 0957-666 (from the combined spectrum) is given in Bragaglia et al. (1995), and their reported external uncertainty is used for our modeling (see also Moran et al. 1997). A surface gravity value for WD 1101+364 (from the combined spectrum) is reported in Bergeron et al. (1992), and we use the average value of their reported external uncertainty in our analysis. The mass ratio $q \equiv \frac{M_1}{M_2}$ of these double-lined systems is measured for WD 0957-666 in Maxted et al. (2002) and WD 1101+364 in Marsh (1995). Maxted et al. (2002) also performed spectroscopic modeling to estimate the surface temperatures (with uncertainties estimated to be at least 500 K) and masses for both WDs in both systems.

WD 0957-666 and WD 1101+364 are also modeled in Nelemans and Tout (2005), but we do not model the other binaries from that work because they either have an unconstrained companion mass or the mass of the primary is $\gtrsim 0.45\ M_\odot$ and more consistent with a CO WD as opposed to a He WD. In particular, we do not model WD 1704+481 because Maxted et al. (2002) found that the He WD that Nelemans and Tout (2005) assumed to be the primary (the more recently formed WD) likely formed second. Instead, the more massive CO WD in the binary likely formed after the most recent stage of mass transfer.

For all systems, the primaries have a hydrogen atmosphere. Several of the binaries (those with measured values of both $T_{\rm eff,1}$ and $T_{\rm eff,2}$) are double-lined DA binaries. The two without reported $T_{\rm eff,2}$ are single-lined, with hydrogen absorption lines only detected from the primary.

2.2.2 Creation of He WD Models

All models/simulations are performed using the MESA stellar evolutionary code (Paxton et al., 2011; Paxton et al., 2013; Paxton et al., 2015; Paxton et al., 2018; Paxton et al., 2019). We used MESA version 12778, except for cooling WD models that included H flashes and Roche-lobe overflow (RLOF) in Sec. 2.2.5, for which we used version 10398. MESA inlists used in this work are provided in a Zenodo repository (Scherbak and Fuller, 2022).

WD models were created by evolving a star up the red giant branch (RGB) until its He core reached a desired mass, then stripping away most of its envelope to leave the core as a WD, as briefly outlined in Paxton et al. (2018) and also Burdge et al. (2019b). Unless noted, we we define the boundary of the He core to be where $X_{\rm H}$ < 0.01 and $X_{\rm He}$ > 0.1 (default in MESA). As an example, to create a 0.32 $M_\odot$ WD with a 0.318 $M_\odot$ He core, our specific steps are:

1: Create a star via *create_pre_main_sequence_model = true* with some *initial_mass* and *initial_z*. We use Z = 0.02 for our main grid, but we investigate the effect of changing metallicity on WD models in Appendix 2.C. Different progenitor masses can have an impact on the ultimate behavior of the WD models (Appendix 2.A.1), but we found the cooling behavior similar for initial masses of 0.9 - 2.0 $M_\odot$. This covers the most likely CE progenitor mass for He WDs, which is roughly between 1 and 1.3 $M_\odot$ (Li et al., 2019a). For 2 - 3 $M_\odot$ progenitors (a less likely channel), the newly-formed core is less degenerate, and can cool differently. Above about 3 $M_\odot$, we do not expect a RGB star to be able to form a He WD through the CE channel (see Sec. 2.4.1). We therefore used a 1.2 $M_\odot$ progenitor to create the main grid of models.

2: Evolve star on the main sequence and up the RGB until its He core reaches 0.318 $M_\odot$ via *he_core_mass_limit*.

3: Use MESA's method *relax_mass* to strip away most of the star's H-rich envelope, until *new_mass* = 0.32 $M_\odot$. This leaves only a small H envelope atop the He core.

4: Allow the newly-formed WD to adjust to the mass loss. In all cases, the model experiences an increase in surface temperature and radius, with the surface temperature increasing from ≈10,000 K immediately after relax mass, to 40,000 - 100,000 K depending on the WD's mass, before beginning to cool. In most models, this adjustment period is irrelevant (duration <1,000 years). However, if there is excess H on the model, there will be elevated H-burning that can last for $> 10^5$ years

and cause the envelope to temporarily inflate. As we expect the binaries we model to be at small separations, we reject WD models that expand beyond 1 $R_\odot$. For a typical M_1 of 0.4 $M_\odot$, a typical M_2 of 0.3 $M_\odot$, and a maximum post-CE period of about 200 minutes, the orbital separation is $\simeq$1.0 $R_\odot$. Therefore, none of our systems can fit a WD that expands beyond this value. This restricts the upper age of this adjustment phase at 10^6 years, which is small compared to the resulting cooling ages. See Fig. 2.3 for the upper mass of H this sets in our grid. We save the model for continued analysis when it begins to cool, i.e. when $T_{\rm eff}$ begins to decrease, and define this as a cooling age of zero.

2.2.3 Grid of WD models

The model saved in the previous step, simulating a hot and newly formed WD, can now be introduced into a binary simulation. We run a grid of models with WDs of different total masses and different masses of hydrogen. The lowest measured primary mass we model is reported as $0.32\pm^{0.04}_{0.04}$ $M_\odot$ and the highest as $0.4\pm^{0.07}_{0.05}$ $M_\odot$, and the masses in our grid ranged from 0.24 to 0.45 $M_\odot$ in steps of 0.01 $M_\odot$. We found it difficult to create a He WD at 0.46 $M_\odot$ or above, as these models would instead burn He and form CO cores.

We include diffusion and gravitational settling for all models, but only during their cooling phase (after the post-relax mass adjustment above). These processes are important to include for two major reasons:

- Turning on diffusion noticeably increases a WD model's radius as in Althaus and Benvenuto (2000), who demonstrated the effect both through simulations and through an analytic argument involving the effect of the partially-degenerate H envelope.
- Turning on diffusion changes which models undergo H-burning flashes, which drastically changes their subsequent cooling behavior. Because of the importance of the CNO cycle to H flashes (e.g., Istrate et al., 2016), we included the dominant isotopes of carbon, nitrogen and oxygen in addition to H and He, in our list of elements for diffusion.

The most important diffusion parameter to include was *diffusion_use_cgs_solver* = *.true.*, which correctly accounts for degeneracy when performing diffusion (Paxton et al., 2018).

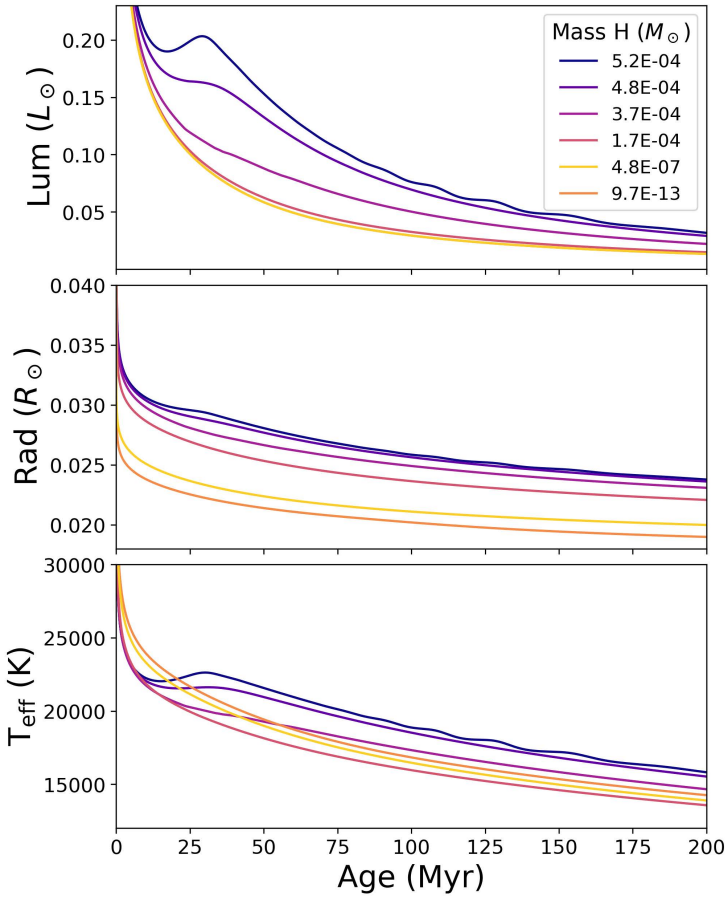


Figure 2.1: The effect of changing the initial hydrogen envelope mass on the cooling behavior of non-flashing WD models with a fixed total mass of 0.35 $M_\odot$. As the H-mass is reduced, the WD's luminosity (top panel), radius (middle panel), and temperature (bottom panel) all decrease faster. The top (dark blue) curve is a model with residual H-burning and narrowly avoids a burning flash. Below $\approx 10^{-7}$ $M_\odot$, further reducing H has a diminishing effect on evolution.

Hydrogen bounds

Overall, there are 3 regimes in WD cooling behavior delineated by the amount of H on a model (See also Fig. 2.3). For large H masses, elevated H-burning occurs and the WD expands beyond 1 $R_\odot$, and such models are not considered in our grid.

For moderate H masses, delayed H-burning flashes can occur (e.g., Istrate et al., 2016). In this regime, unstable H-burning flashes lead to increases in surface temperature and expansions in radius, likely leading to RLOF with the companion. Such simulations are more complicated to run, and are discussed in Sec. 2.2.5. For low H masses, the models steadily cool without ever undergoing a H flash.

Both flashing and non-flashing models models may have an early stage of elevated H-burning post-relax mass, and begin to cool once the mass of H has dropped low enough.

For non-flashing models of a given mass, a varying mass of H leads to a range of cooling behavior (Fig. 2.1). In general, the trend with decreasing H mass is for the model to both contract and cool faster. A model that nearly flashes (upper curve, with $\approx 5.2 \times 10^{-4}\,M_{\odot}$ H) has a brief period of elevated luminosity, temperature and radius. In addition, at high H masses, small changes in H mass (i.e. from $\approx 5.2 \times 10^{-4}\,M_{\odot}$ H to $\approx 4.8 \times 10^{-4}\,M_{\odot}$ H) have a significant affect on cooling behavior. Therefore, it is important to have densely sampled high-H models in our grid. At smaller H masses, the effect of changing H is less pronounced - between the curves representing $\approx 10^{-7}\,M_{\odot}$ H and $\approx 10^{-12}\,M_{\odot}$ H there is only a relatively small decrease in radius and almost no change in temperature and luminosity. Note in the case of Fig. 2.1 we show only a subset of our grid of models of varying H mass.

The lower bound of H mass used in our grid is constrained by the classification of the WD primaries we model as DA WDs, i.e., the presence of H lines in their atmosphere. Therefore, we do not want to completely remove hydrogen from our WD models. We found that when the mass of H was reduced below about $10^{-8}\,M_{\odot}$, H would cease to dominate the model atmosphere. Even with element diffusion/gravitational settling turned on, the fraction of H in the model's outer cells would never rise above about 0.01. Therefore, the lower mass of H included in our grid is $10^{-8}\,M_{\odot}$. We show a model with $\approx 10^{-12}\,M_{\odot}$ H in Fig. 2.1 to demonstrate that, even if such a model was included, it would make little difference in cooling behavior. Including such models *would*, however, slightly change the modeled mass ranges for some of our systems (e.g. a 0.25 $M_{\odot}$ WD is only a good fit for ZTF J2029 when having extremely low H masses of $\approx 10^{-12}\,M_{\odot}$). The modelled lower mass bound would change by 0.01 $M_{\odot}$ in such cases.

2.2.4 Non-flashing models in a Binary: Determining Birth Period

In cases where H-burning flashes do not occur, the only evolution of the binary system is for the WDs to cool and inspiral toward one another due to the emission of GWs. We assume no magnetic braking for the low-mass WDs we model. For all systems (except SDSS J0822, WD 0957-666 and WD 1101+364, see 2.2.4 and 2.2.4), we determine which WD models are good fits by finding the age intervals

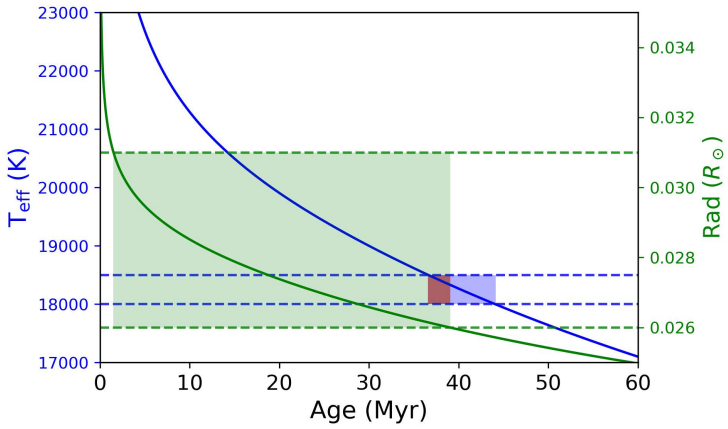


Figure 2.2: In blue (green): temperature (radius) curve of a cooling 0.34 $M_\odot$ WD. Dashed lines show temperature/radius constraints of ZTF J2029's primary. Blue/green shaded regions demonstrate allowed age and temperature/radius ranges independently. Their intersection in red gives the model's age range consistent with both temperature and radius. Repeating this exercise for all primary models (of varying total mass and H mass) traces out the allowed age range.

at which both their radius and temperature match observational constraints for each primary (see Fig. 2.2 for example). The end result for each binary (more accurately, each primary) is a collection of "matching" WD models with an associated mass and cooling age (see Table 2.2). Accounting for any initial phase of elevated H burning would only affect such ages by less than 1 Myr (Sec. 2.2.2), which is generally quite small compared to the possible cooling age range.

Given a matching model with some M_1 and some age, we use the following method to find the associated birth period following the end of the CE. There is an additional intrinsic uncertainty associated with M_2, for which we use the values in the literature (i.e. the values in Table 2.1, going to $\pm 1\sigma$).

- Via Kepler's Third Law, convert the binary's observed period to a separation.
- With $M = M_1 + M_2$, integrate

$$\frac{da}{dt} = \frac{-64G^3 M_1 M_2 M}{5a^3 c^5} \tag{2.1}$$

to find the birth separation of the binary (Peters, 1964). This assumes that gravitational radiation is solely responsible for the inspiral, and is valid for circular orbits, which is a reasonable assumption since systems are expected to leave the CE with an eccentricity $\lesssim 0.1$. (Ivanova et al., 2013)

- Convert the birth separation to the birth period.

With this approach, age (determined by the behavior of the temperature/radius cooling curves of the primary) is the fundamental property of a matching model, and acts as a proxy for the birth period of the binary. For all non-flashing models, we verified that the radius remained well below the Roche lobe so that our assumption of mass transfer not occurring is valid.

In general, the matching model with the maximum age has a relatively high mass and a high mass of H. In contrast, the matching model with the minimum age has a relatively low mass and a low mass of H. As expected, WDs with higher masses tend to cool slower, given their reduced radius. In addition, the presence of a significant H envelope helps prevent cooling. See Fig. 2.5 for an example of the slowest and fastest cooling models for SDSS J0822, also with a comparison to flashing models. The mass range of matching models is in good agreement with the quoted mass of the primaries from the literature (Table 2.2). This is expected since several of the systems had their masses inferred from theoretical mass radius relations.

For two systems (CSS 41177 and SDSS J1152), the reported mass M_1 is from radial velocity and light curve modeling, independent of theoretical cooling models/mass-radius relations. Therefore, we treat M_1 as an independent observational constraint enforced for our range of matching models. This does not significantly change the estimated birth periods for these two systems, but it does ultimately help restrict the range of possible $\alpha_{\rm CE}$ values (which depends on the modelled WD mass).

Apart from CSS 41177 and SDSS J1152, the above analysis fitted models only to observed surface temperature and radius. For four of the systems (CSS 41177, SDSS J1152, SDSS J1205, SDSS J0822), surface gravity data is also reported via spectroscopy. For the first three of these, applying that measurement (using the $\pm 1\sigma$ range in log g) produced no additional constraint because almost all models that matched to temperature and radius were also consistent with log g. So for CSS 41177, SDSS J1152, and SDSS J1205, we do *not* use the surface gravity constraints.

SDSS J0822

However, the surface gravity measurement does affect results for SDSS J0822, because of tension between surface gravity and radius constraints. The WD primary's radius is not well constrained from light curve fitting, with a value of 0.031 ± 0.006 $R_\odot$ (Kosakowski et al., 2021). However, Kosakowski et al. (2021) also performed an

analysis assuming that the mass of the primary was 0.304 ± 0.014 $M_{\odot}$ (which was reported in the discovery paper Brown et al. 2017, using $T_{\rm eff}$ and log g). Assuming this mass and using WD cooling tracks gave a model radius of 0.025 ± 0.001 $R_{\odot}$, just within 1σ of the light curve constraint.

In our analysis, when we fit to $T_{\rm eff}$ and radius constraints alone (the latter from light curve modeling), our modeled mass range extends from 0.22 − 0.32 $M_{\odot}$, mainly because of the high radius errorbars. Only the primary's log g value is reported for this system, but the contribution of the unseen secondary is likely small. If we fit to $T_{\rm eff}$, radius, *and* log g, our modeled mass is reduced to only 0.30 − 0.32 $M_{\odot}$ (overlapping well with the mass estimate from Brown et al. 2017). Discarding the radius and fitting to $T_{\rm eff}$ and log g slightly broadens the range to 0.28 − 0.32 $M_{\odot}$ (therefore the radius constraint is still useful). Therefore, for our results, we fit to $T_{\rm eff}$ and log g (from Brown et al. 2017) and radius (from Kosakowski et al. 2021) to find the range of masses/cooling ages for SDSS J0822.

WD 0957-666 and PG 1101+364

Unlike the systems discussed above, WD 0957-666 and PG 1101+364 have measured log g values but do *not* have measured radii. So for these models, we instead fit our cooling curves to log g and surface temperature to find matching models and the associated cooling age. Maxted et al. (2002) reported surface temperatures for both WDs in each system (Sec. 2.2.1). However, only a combined value of log g is reported (instead of fits to both WD's atmospheres). For WD 0957-666, $T_{\rm eff,1}$ is much larger than $T_{\rm eff,2}$ (30,000 K vs 11,000 K) so the contribution of the secondary likely does not matter greatly. Maxted et al. (2002) estimated a primary mass of 0.37 $M_{\odot}$ by accounting for both WDs and using their luminosity ratio, the same value estimated by Moran et al. (1997) by simply fitting a single star model.

For WD 1101+364, the temperatures of the WDs are closer together (15,500 K vs 12,000 K) and so it is not justified to ignore the secondary. For our upper mass limit, we assume the spectrum is dominated by the primary (lower mass WD), and fit to $T_{\rm eff,\,1}$ and the combined log g, which leads to matching models from 0.34 - 0.40 $M_{\odot}$ (likely too large compared to the true value). For our lower mass limit, we assume the spectrum is dominated by the secondary and fit $T_{\rm eff,\,2}$ and the combined log g to find values for M_2. Then, we use the measured mass ratio q to give the range of primary masses as 0.27 - 0.34 $M_{\odot}$. To determine the cooling age associated with this lower mass range, we fit to $T_{\rm eff,\,1}$ alone - however, any ambiguity in cooling

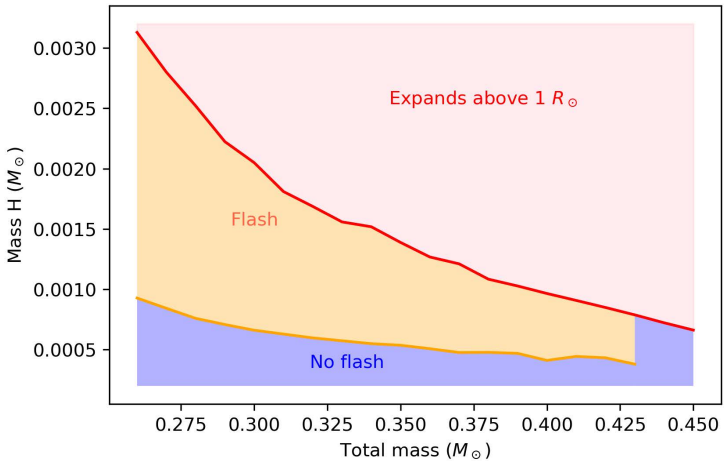


Figure 2.3: WD cooling behavior as a function of WD mass and initial hydrogen mass. Red region: Model has elevated H burning and expands beyond 1 $R_\odot$. The red line is the upper bound of hydrogen included in our main grid. Orange region: model will begin to cool as a proto-WD (Istrate et al., 2016) but then undergo one or more H flashes. Blue region: model will cool without ever experiencing a flash. Above 0.43 $M_\odot$, models do not flash.

age/birth period is less important than the large uncertainty in mass for this system. In summary, we estimate the mass of WD 1101+364's primary to be between 0.27 and 0.4 $M_\odot$.

The other difference for these 2 systems is that the mass ratio q is reported instead of M_2. Therefore, for each WD primary model with mass M_1, we calculate the associated range of M_2 values (going to $\pm 1\sigma$ in q). Then, the cooling ages can be converted to a range of birth periods as before.

2.2.5 Flashing models in a Binary

Basics

A H flash occurs when semi-degenerate H-burning ignites unstably, similar to H-novae in accreting WDs, creating enormous increases in burning luminosity (Althaus et al., 2013). Flashing behavior is made more likely by diffusive mixing (e.g., Istrate et al., 2016). After the onset of the flash, the star expands greatly. If the model was allowed to continue without RLOF, the radius would continue to expand to tens of $R_\odot$ (middle panel of Fig. 2.4). However, in a binary simulation, the model undergoes RLOF and its radius remains fixed at its Roche-lobe value (bottom panel of Fig. 2.4). Our MESA binary simulations included the flashing model as the

System	M_1 ($M_\odot$)	Modeled mass ($M_\odot$)	Cooling age (Myr)	Birth period (min)	Mass of flashing models ($M_\odot$)	Flashing models, birth period
ZTF J2029	$0.32\pm^{0.04}_{0.04}$	0.26-0.35	2.4 - 112.5	23.3 - 70.8	0.26 - 0.34	35 - 66 (31 - 69)
ZTF J0722	$0.38\pm^{0.04}_{0.04}$	0.34-0.4	36.5 - 106.2	47.0 - 74.2	0.39	58 - 64 (56 - 60)
ZTF J1749	$0.40\pm^{0.07}_{0.05}$	0.32-0.45	15.2 - 118.6	36.0 - 78.5	0.37 - 0.43 (0.33 - 0.43)	48 - 71 (44 - 68)
SDSS J0822	$0.304\pm^{0.014}_{0.014}$	0.3-0.32	93.6 - 265.0	75.1 - 113.5	0.31 - 0.32	83 - 104 (79 - 96)
ZTF J1901	$0.36\pm^{0.04}_{0.04}$	0.3-0.39	0.46 - 25.0	40.8 - 54.7	0.31 - 0.39 (0.29 - 0.39)	44 - 63 (44 - 70)
SDSS J1205	$0.39\pm^{0.02}_{0.02}$	0.38-0.43	19.8 - 60.5	72.0 - 74.2	0.42 - 0.43	72 - 73
WD 0957	0.37	0.38 - 0.45	2.0 - 22.2	88.2 - 92.6	0.41 - 0.43 (0.4 - 0.43)	89 - 90 (88 - 90)
SDSS J1152	$0.362\pm^{0.014}_{0.014}$	0.36 - 0.38	31.5 - 54.2	146.0 - 147.8	n/a	n/a
CSS 41177	$0.378\pm^{0.023}_{0.023}$	0.37-0.4	25.5 - 31.5	168.4 - 168.9	n/a	n/a
WD 1101	0.29	0.27 - 0.4	5.8 - 272.0	208.6 - 222.7	0.37 - 0.4	215 - 222 (215 - 221)

Table 2.2: From left to right: System, measured mass range M_1, modeled mass (without flashes), modeled cooling age (without flashes), modeled birth period (without flashes), modeled mass (with flashes), modeled birth period (with flashes). The rightmost columns assume non-mass-transferring flashing models, while numbers in parentheses account for models undergoing mass transfer at an orbital period of 100 minutes and with a companion mass of 0.3 $M_\odot$.

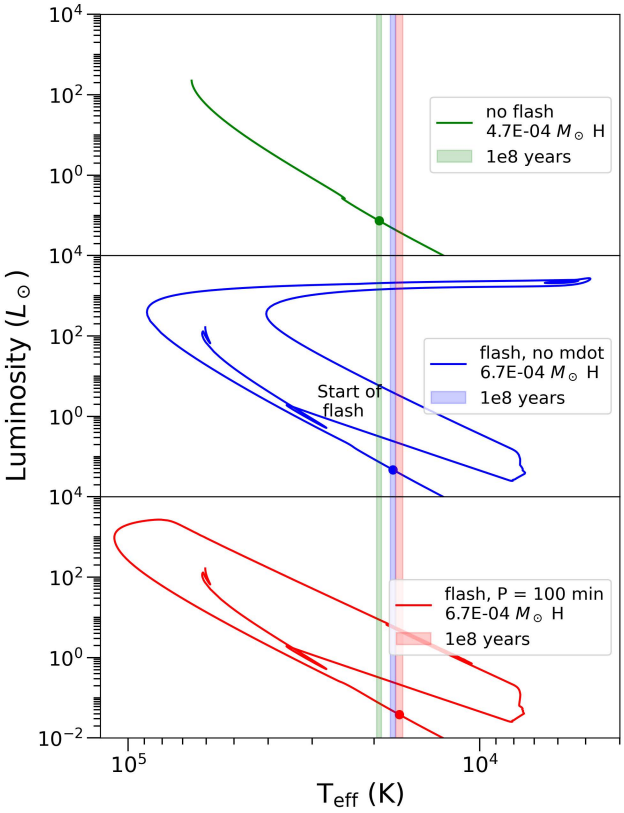


Figure 2.4: HR diagrams for three 0.37 $M_\odot$ models, with different initial masses for H envelopes. Upper: model undergoes leftover, stable H-burning and avoids H flash. Middle: model undergoes H flash, but mass transfer is turned off. Lower: model undergoes H flash, and remains at constant radius once RLOF begins. Coloured bars represent when the model is ≈ 1e8 years old. Therefore, the non-flashing model cools more slowly in the long-term than flashing models.

primary, and a point mass as the secondary. For the bottom panel of Fig. 2.4, the simulation is performed at an orbital period of 100 minutes and with a companion of 0.3 $M_\odot$. See also Appendix 2.D for discussion of the mass transfer prescription and effect of orbital period and companion mass.

Once nuclear burning has subsided, the model's envelope can begin to contract and cool once more. Overall, the flash and subsequent RLOF cause the model to do a loop on a HR diagram, making WD cooling more complicated to model. Fig. 2.3 shows which models do and do not flash (showing results only down to a mass of 0.26 $M_\odot$, which are the masses of models relevant to our systems).

We find that ~75 per cent of the pre-flash H is either lost to mass transfer or burnt to He during a H flash. The mass transfer rate can be very large, approaching 10^{-3}

$M_\odot$/yr at its greatest, and leads to a significant stripping of the H envelope, with total mass loss sometimes above $10^{-3}\ M_\odot$. The speed of our model runs is heavily dependant on what orbital period mass transfer occurs at, as that sets how much material is expected to overflow the Roche-lobe. Therefore, runs at shorter orbital periods are more challenging than runs at longer orbital periods.

For flashing models including mass transfer, we found the effect on the orbit to be small, and the subsequent orbital evolution is nearly identical to that which includes GW-induced inspiral alone. The reason is that even if the entire H envelope is lost (at most $\approx 10^{-3}\ M_\odot$), it will have little effect on the orbital separation, which to order of magnitude changes as $\Delta a/a \sim \Delta M/M$. Such small changes are much smaller than other uncertainties, so we can again safely ignore the effect of mass transfer. For our fiducial simulations, we assumed conservative mass transfer, but changing that prescription led to only small changes in the orbit or the change in the companion mass.

Do flashing models provide upper/lower age bounds?

While we have argued that mass transfer due to a H flash does not greatly affect the system's orbit, mass transfer certainly can affect the cooling of the primary. In no binary did we find the cooling curves pre-flash to be a good fit to constraints, as the radii of pre-flash models were too large.

Post-flash comparison is more difficult. Even though a flashing model temporarily becomes hotter after a flash, it will cool faster in the long term compared to a model that is borderline to flashing, but maintains stable-burning. The stable-burning model retains a high amount of H that inhibits its long-term cooling, whereas the flashing model loses that H in its flash and cools faster. This is demonstrated by the vertical shaded regions in Fig. 2.4, showing the location of the model on the HR diagram at a fixed age. Therefore, non-flashing models are likely to produce longer maximum cooling ages than flashing models.

To test this hypothesis, we ran a full grid of flashing, non-mass-transferring models as well as a grid of flashing models that undergo mass transfer at an orbital period of 100 minutes and a companion of 0.3 $M_\odot$. These grids sampled the flashing region of Fig. 2.3 (i.e. models from 0.26 to 0.43 $M_\odot$, with mass H in the orange flashing region). The results (summarized in Table 2.2) for primary masses and birth periods do not greatly differ between these two flashing grids. Therefore, modeling the mass transfer itself does not greatly affect results. This is because models will burn most of

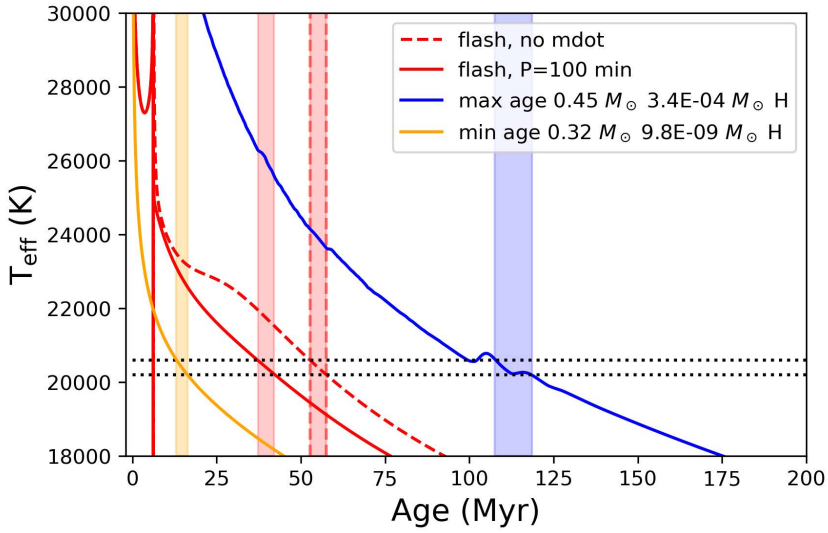


Figure 2.5: For ZTF J1749, we plot four models whose temperature and radius match observational constraints (radius is not shown for simplicity). The dotted lines are the observed temperature range and vertical shaded bands show the ages at which each model matches this temperature. The model with the maximum age (blue curve) is a non-flashing model that is close to flashing and slowly cools. The model with the minimum age (yellow curve) has a thin H envelope and cools quickly. Two flashing models, one with mass transfer that occurs at an orbital period of 100 min (red solid line), and one without any mass transfer (red dashed line) are also shown. Non-flashing models therefore produce the minimum and maximum possible cooling ages.

the H to He even if no H is lost due to RLOF. When comparing individual models, models with mass transfer always cooled faster post-flash. However, the upper bound on birth period is not necessarily lower when comparing the two flashing grids, because different models can be matching in different grids.

For all but two systems, a subset of the flashing models were consistent with observed characteristics, meaning that these WDs could have undergone a flash in the past. However, for the binaries we modeled, we find that their upper and lower age bounds (as well as birth period bounds) are almost always set by non-flashing models. Note that we are *not* comparing models of the same mass - just saying that when compared to the entire grid of non-flashing models, flashing models do not set the bounds.

Fig. 2.5 summarizes the above argument, with all models shown matching observational constraints for ZTF J1749. The upper age bound comes from a non-flashing model with H mass slightly below the threshold required to flash, which cools slowly and with a tell-tale bump in temperature (where it nearly flashes) before it continues

cooling. Flashing models, whether mass transferring or not, give ages below this upper bound. While this is only one system and one set of flashing models, we could construct similar figures in almost all cases.

In one system (ZTF J1901), flashing models *do* give the upper age/birth period bound, but this only occurs when the model matches observations during a very brief period of time right after a flash. This is discussed further in Appendix 2.D.

Another important result is that the grid of flashing models does not change the estimated mass range for the systems (the masses in the flashing column lie within the mass range of the non-flashing models in Table 2.2). This means that flashing models will not significantly increase uncertainties in $\alpha_{\rm CE}$. Again, there is a potential exception for ZTF J1901, where the flashing grid run at a period of 100 minutes introduces a lower mass model, but it is again only a good fit for a brief period of time after the flash.

2.3 CO-core WD simulations

Although the WDs we model have $M_1 \lesssim 0.4\,M_\odot$ and are most likely He-core WDs, it is possible that some are in fact CO-core WDs (sometimes referred to as hybrid WDs), which formed from stars with $M \gtrsim 2M_\odot$ that ignited He-burning at smaller He-core masses than lower mass stars. Hence, we must consider this possibility in our modeling, as it entails significantly different progenitor masses and evolutionary histories.

2.3.1 Creating Grid of Models

In a similar process to the creation of He-core WD models, we create CO-core models through mass stripping of an evolved stellar progenitor. We find that progenitors from about 1 to 4 $M_\odot$ can create CO WDs with masses that are relevant to the binaries we model (Sec. 2.4.1). The progenitor mass can potentially affect the WD cooling behavior - however, we found that such differences are generally small (see Sec. 2.4.3 for further discussion). Therefore, except where noted, we used a 3 $M_\odot$ progenitor to create our grid of CO WD models.

To create a grid of WD models of a given mass (e.g., 0.4 $M_\odot$) our specific steps are:

- Evolve a 3 $M_\odot$ star up the RGB until its He core reaches values close to but beneath 0.4 $M_\odot$ (e.g., 0.39 - 0.3999 $M_\odot$). Significant He-burning may begin before the envelope is stripped.

System	Observed ($M_\odot$)	Matching CO models ($M_\odot$)	Cooling age (Myr)	Birth period (min)
ZTF J2029	$0.32\pm^{0.04}_{0.04}$	0.32	998 - 1074	143 - 160
ZTF J0722	$0.38\pm^{0.04}_{0.04}$	0.33 - 0.38	436 - 707	115 - 143
ZTF J1749	$0.4\pm^{0.07}_{0.05}$	0.33 - 0.45	186 - 1086	84 -161
ZTF J1901	$0.36\pm^{0.04}_{0.04}$	0.33 - 0.37	435 - 1064	114-172
SDSS J1205	$0.39\pm^{0.02}_{0.02}$	0.37 - 0.41	305 - 458	82 - 89
WD 0957	0.37	0.35 - 0.42	243 - 602	124 - 145
SDSS J1152	$0.362\pm^{0.014}_{0.014}$	0.35 - 0.38	414 - 624	169 - 180
CSS 41177	$0.378\pm^{0.023}_{0.023}$	0.35 - 0.4	330 - 496	184 - 196
WD 1101	0.29	0.33 - 0.39	493 - 778	228 - 240

Table 2.3: From left to right: System, observed mass range M_1; mass range, age range, and birth period range of our matching CO WD models. There were no matching CO WD models for the system not shown (SDSS J0822).

- Relax mass to 0.4 $M_\odot$. Helium burning will start, or continue if started before mass stripping. Therefore, the model represents a subdwarf B (sdB) star formed following the CE (e.g., Xiong et al., 2017). The model runs through the sdB phase until it becomes a CO WD.

Different He core masses will leave different masses of initial H on the model. Excess H will burn off during the sdB phase, meaning there is a maximum amount of H possible when the model enters the WD cooling track. For example, a 0.4 $M_\odot$ He star starting with either a 0.39 $M_\odot$ He core or a 0.395 $M_\odot$ He core will wind up with roughly the same mass of H, despite starting with different values. This sets the maximum amount of H used in our grid, which is a few $\times\ 10^{-4}$ $M_\odot$ in the WD mass range of interest. The initial mass of H can affect the duration of the sdB phase, but the effect is small compared to the overall duration. Conversely, CO models with the lowest amount of H correspond to sdB models starting with low H. Similarly to He-core WD models, the exact lower limit does not affect the WD cooling uncertainties and is not important for age estimates.

Our grid of CO WD models has its upper mass bound set by the masses of the primaries we model. Considering WDs 1σ above measured values, that upper limit is 0.47 $M_\odot$ from Table 2.1. The lower limit is set by the transition between a He- and a CO-core WD, which depends on progenitor mass (Sec. 2.4.1), but reaches a low of ≈ 0.32 $M_\odot$ (e.g., Moroni and Straniero, 2009).

2.3.2 sdB + CO WD Behavior

During the sdB phase defined by He-burning, the models stay at an elevated temperature of $T \sim 30,000$ K and radius of $R \sim 0.1$ $R_\odot$. During this phase, the star can exhibit "oscillations" in luminosity, temperature, radius, and nuclear burning power. This is due to He-burning shell flashes, as explained in Iben et al. (1986), Sweigart et al. (2000), and Prada Moroni and Straniero (2009). The sdB phase can last for a few times 10^8 years, meaning that there is a significant time gap between the initial period of mass loss that forms the sdB (in our case, assumed to be CE evolution) and the formation of the CO WD. Once He burning has subsided, the star will cool and contract on to the WD cooling branch, with a CO-core.

Our models' radii during the sdB phase are far too large to match to any of our WD primaries, and they only match during the WD phase. The temperature and radius cooling curves can then be compared to the constraints on the primary, and the cooling age turned into a birth period, in the exact same manner as performed

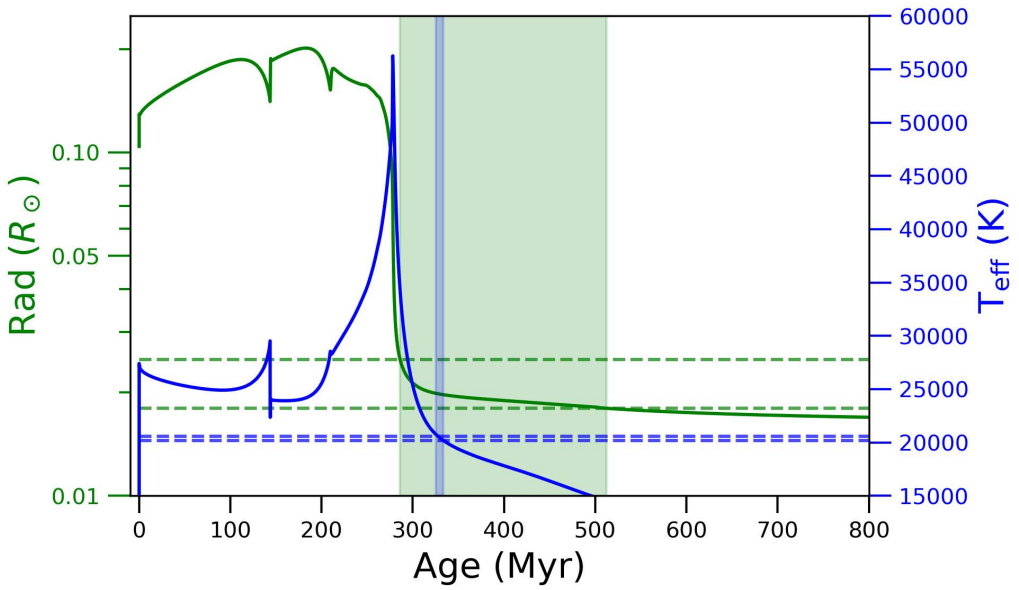


Figure 2.6: Similar to Fig. 2.2, in blue (green) is the temperature (radius) curve of a 0.42 $M_\odot$ sdB star which subsequently cools as a CO WD. Dashed lines show temperature/radius constraints of ZTF J1749's primary. In this case, temperature is the only useful constraint on the model's age. The sdB phase occurs during the first ~300 Myr.

for He WDs in Sec. 2.2.4. Fig. 2.6 shows a typical matching model for one of our binaries, including both the sdB phase and the WD cooling phase. Similarly to Sec. 2.2.4, we instead apply temperature and surface gravity constraints for WD 0957-666 and WD 1101+364.

Table 2.3 presents a summary of the cooling ages/birth periods for each WD primary, assuming it is a CO-core WD formed from a sdB star. The one system not shown in the table (SDSS J0822) had no matching CO-models; unsurprisingly, it had the lowest-mass primary (mean value of 0.3 $M_\odot$), which is unlikely to be a CO WD.

2.3.3 Comparison to He-core Models

Even for models with the same mass and same envelope mass, there are cases where there are good fits for He WD models, but not for CO WD models. Specifically, the radius and temperature cooling curves can be altered based on the model's composition. Most noticeably, the radius of our CO models are always smaller than the radius of a corresponding He model. If the WD cores were purely degenerate, this would be unexpected - however, CO-core models are slightly smaller because of their heavier compositions and not being fully degenerate for the low masses we

include. This is similar to the trend found in Prada Moroni and Straniero (2009), where CO models had lower radii than He models when compared at the same temperature. In addition, Prada Moroni and Straniero (2009) found that CO WD models cooled faster (after the sdB phase) than He WD models.

2.3.4 Effect of mass transfer during sdB phase

Because the sdB star is at an elevated radius, it is possible that it undergoes mass transfer with its companion before ending He burning and contracting into a WD. We modeled conservative mass transfer as in Sec. 2.2.5, focusing on models with the most massive H envelopes during the sdB phase, as these are the most bloated. As expected, mass transfer strips much of the H envelope. However, the cooling behavior after the sdB phase (when mass transfer ends) is similar to models without mass transfer. This is because, even without mass transfer, most of the H envelope is burnt to He. Therefore, the H envelope will wind up being small ($\lesssim$ few $\times$ 1e-4 $M_\odot$) in either case. As long as mass transfer only strips the H envelope, it will likely not affect the parameter space of possible H mass on a cooling CO WD. If mass transfer resulted in mass loss from the He core, then it *would* likely affect the cooling behavior (Bauer and Kupfer, 2021). However, because we model DA WDs, we do not consider this possibility.

We also find that mass transfer of the H envelope does not significantly change the duration of the sdB phase (which is predominantly determined by the burning of He deeper in the star). Therefore, we find that mass transfer does not significantly change $T_{\rm eff}$ or R as a function of age after the sdB phase. In principle, mass transfer affects the orbital period evolution and therefore the inferred birth period. However, the effect is not very large because the amount of transferred mass is relatively small. Therefore, for our results, we run a grid of sdB models/CO WDs that do *not* undergo mass transfer, as the grid's behavior will likely not be significantly altered by mass transfer.

2.4 RGB progenitor models

2.4.1 Possible progenitor masses for CE evolution

For each matching WD model from the previous two sections, we determine the range of possible pre-CE progenitor masses and evolutionary states. Fig. 2.7 summarizes the possible channels to creating WDs through CE evolution. The basic idea is that as a star evolves, its core mass increases and it moves vertically up the chart. It then encounters different regions that determine whether it can

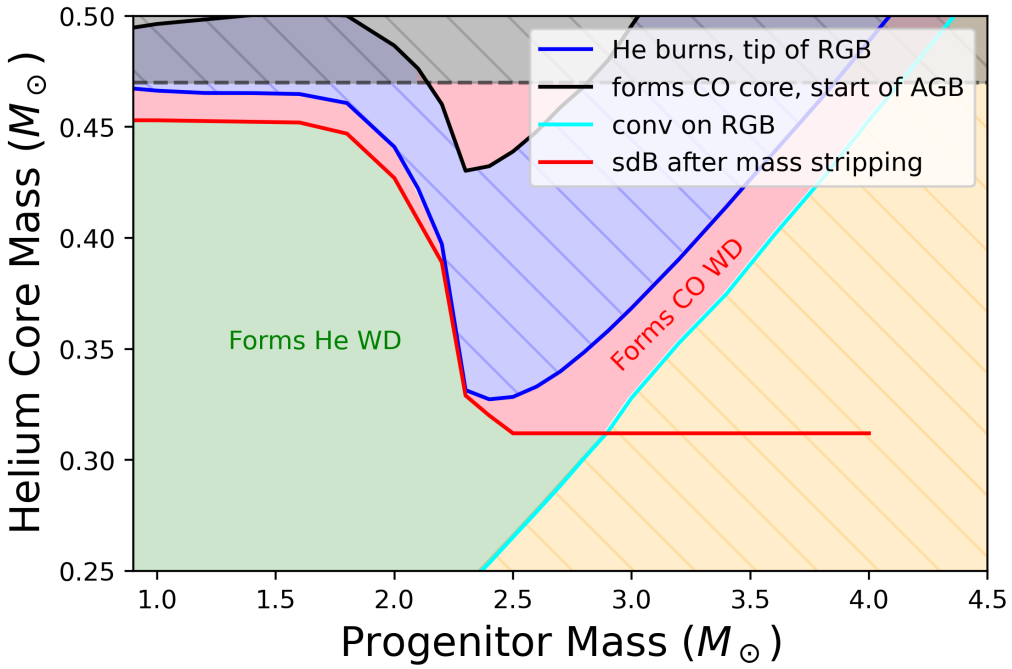


Figure 2.7: A chart showing the range of He/CO core masses that can be formed, as a function of progenitor mass. A given progenitor model moves upward on this diagram as it evolves. The horizontal gray region is above the mass of WDs relevant to our grid. The cyan curve represents the core mass where the model is half-convective by mass or radius - only progenitors above this line will undergo unstable mass transfer, and hence we do not consider WDs from progenitors in the yellow region. The red line is the core mass at which He burning will start following envelope stripping, while the blue line represents the He core mass at the tip of the RGB. The black line represents the formation of a CO core and the start of AGB ascent. In the shaded blue region, the star is smaller than its radius at the tip of the RGB, so a CE event in this region is unlikely. The shaded green region is the possible domain of He WD progenitors, while the shaded pink region is the possible domain of CO WD progenitors.

undergo CE evolution and the resulting composition of the WD. The core mass of the progenitor star is almost exactly equal to the mass of the WD that is formed after the envelope is stripped. We do not consider progenitor masses below 0.9 $M_\odot$ as these stars will not have evolved off the main sequence within a Hubble time. This statement is slightly dependent on metallicity (e.g., Bazan and Mathews, 1990) but very low metallicities are unlikely for the field stars we consider.

Our first criteria for successful CE evolution is that the progenitor star should be predominantly convective in order for unstable mass transfer to occur (Hjellming and Webbink, 1987; Soberman et al., 1997). We find the mass of the He core at the point the star becomes half-convective by mass or radius (whichever comes first, but they occur almost at the same core mass), which is shown by the cyan line in Fig. 2.7. Above this line, the RGB star will be mostly convective and CE evolution allowed; below it, CE evolution is likely not possible. For example, a 2.5 $M_\odot$ star with a 0.25 $M_\odot$ core will not have a thick convective envelope; however, when its core increases to 0.3 $M_\odot$ it will have become mostly convective, and be eligible to undergo CE evolution. A more accurate criterion for CE could be obtained by analyzing whether mass transfer is stable using detailed models (e.g., Pavlovskii et al., 2017). Their results show that mass transfer becomes much more unstable when the star develops a convective envelope after the main sequence. This partially justifies our choice, but a more thorough analysis would need to consider both the evolutionary state and the mass ratio of the system.

CE evolution will occur either on the RGB or AGB as the star is expanding. Between the RGB and AGB, the contracting star will not overflow its Roche-lobe if it has not done so already. We define the tip of the RGB by a spike in He-burning power (or equivalently a decrease in radius). The mass of the He core at the tip of the RGB is plotted in blue in Fig. 2.7 - this curve is similar to one found in Bauer and Kupfer (2021). We define the start of the AGB by the formation of a CO-core. The He core at the start of the AGB is plotted in black. Therefore, the blue shaded region between blue and black lines is another forbidden region for CE evolution when the star is contracting. For example, as a 2.5 $M_\odot$ star's He core evolves from 0.34 to 0.43 $M_\odot$ and it moves through the blue region, it is not likely to undergo CE evolution.

Finally, we consider where mass stripping representing CE evolution will create a He-core WD versus a CO-core WD. The transition between these scenarios is shown by the red line in Fig. 2.7. For a range of progenitor masses, we strip mass as in previous sections, creating a limited set of models. If the He-burning luminosity

is negligible and the model cools similarly to those constructed in Sec. 2.2.2, it becomes a He WD. If He ignites before or after the mass stripping, leading to a sdB phase as in Sec. 2.3.2, it will become a CO WD. Above the red line, any model formed through mass stripping will form a CO WD; below it, a He WD. As a 2.5 $M_\odot$ progenitor moves upward across the red line, it will go from being able to form a He WD to a CO WD when its core mass exceeds $\approx 0.32\,M_\odot$. In a couple of cases, the He-burning power spikes sharply after mass-stripping and leads to numerical difficulties, but for most models we can track the formation of the CO-core as well.

In summary, the region of Fig. 2.7 in which the progenitor will form a He WD through CE evolution is defined as 1) the star is mostly convective, 2) helium has not ignited when the envelope is stripped, and it will not ignite afterwards. This region is shaded green in Fig. 2.7. There is an obvious transition around 2.2 $M_\odot$ where the parameter space to form He WDs drops sharply - this coincides with the boundary of the star's He core being degenerate or not (Nelemans et al., 2000).

The region of Fig. 2.7 that can form a CO WD through CE evolution is defined as 1) the progenitor is mostly convective, 2) the progenitor is in an expansion phase below the tip of the RGB or above the start of the AGB, 3) helium has started burning (or will start burning) when the envelope is stripped. These regions are shaded in pink in Figure 2.7. There is a wide band above 2.3 $M_\odot$, where a CO WD can form with as low a mass as $\sim 0.32\,M_\odot$. There is a smaller region between the red and blue lines from 0.9 to 2 $M_\odot$ - these represent models that undergo CE evolution very close to the tip of the RGB, resulting in the formation of canonical $\simeq 0.47\,M_\odot$ sdB stars (e.g., Xiong et al., 2017). Finally, there is a transitional region from about 2 to 2.3 $M_\odot$.

2.4.2 Determination of $E_{\mathbf{b}ind}$

The CE event involves the unbinding of the donor star's envelope, which requires a source of energy to occur. The binding energy of the envelope in its simplest form is defined to be the gravitational binding energy E_{grav} alone,

$$E_{grav} = \int_{M_{\rm core}}^{M_{\rm tot}} \frac{-Gm(r)dm}{r}\,, \tag{2.2}$$

where $m(r)$ refers to the enclosed mass at some radius r. Unless noted, we define the mass of the He core $M_{\rm core}$ to be where $X_{\rm H} < 0.01$ and $X_{\rm He} > 0.1$ (mass fraction of H drops below 0.01 and mass fraction of He rises above 0.1). We investigate the effect of changing the core boundary definition in Appendix 2.E and find it to

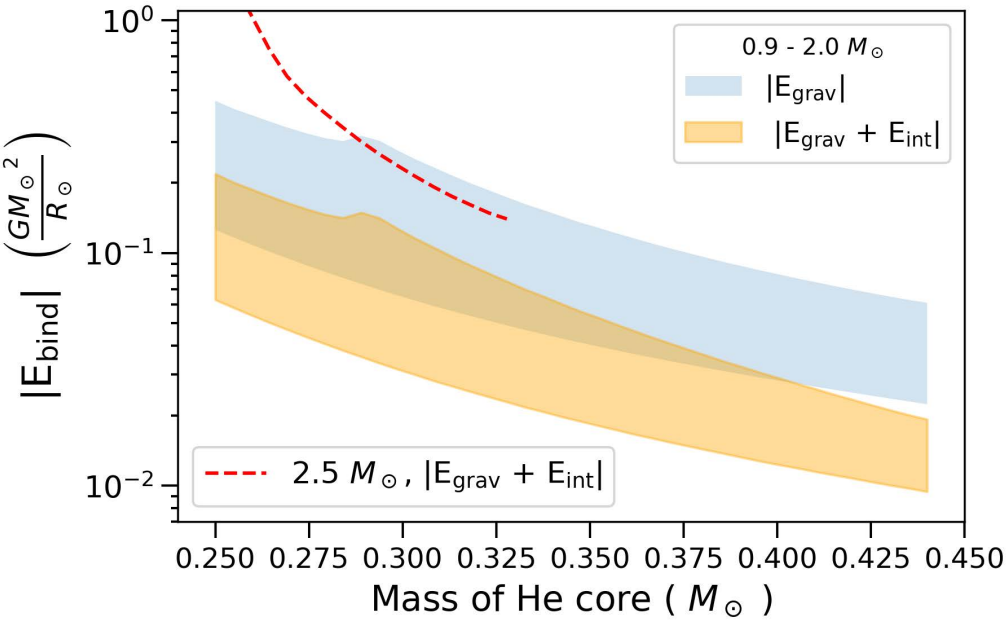


Figure 2.8: Envelope binding energy of RGB stars versus the helium core mass. Since E_{bind} is negative, a higher magnitude represents a more bound envelope. We plot the envelope's gravitational energy (blue shading), and gravitational + internal energies, with internal = thermal + recombination (orange shading). The range of E_{bind} corresponds to the possible range for 0.9 - 2.0 $M_\odot$ RGB stars, with the upper boundary from a 2.0 $M_\odot$ model and the lower from a 0.9 $M_\odot$ model. Also shown is E_{bind} for a 2.5 $M_\odot$ model (red dashed line), shown only up to a core mass of 0.32 $M_\odot$ (the tip of the RGB at that mass).

be small compared to other uncertainties. For all RGB models, we do *not* include mass loss through winds. Including winds may decrease the progenitor mass by up to ~10 per cent (De Marco et al., 2011) at the time of the CE event, but is a small effect relative to other uncertainties.

There are two other sources of energy that can make E_{bind} lower in magnitude, and the envelope easier to eject: the envelope's internal energy E_{int}, and the energy released from recombination of elements within the envelope such as H and He (Han et al., 1994). The internal energy of the envelope E_{int} is simply an integral of the internal energy per unit mass U, over the mass of the envelope:

$$E_{int} = \int_{M_{core}}^{M_{tot}} U dm \,. \tag{2.3}$$

MESA defines internal energy U as a sum of thermal energy and recombination energy (Paxton et al., 2018) and both energy sources are therefore included in our

definition of E_{int}. The total binding energy is

$$E_{bind} = E_{grav} + E_{int} \, . \tag{2.4}$$

With E_{grav} defined as negative, E_{int} is a positive quantity, and therefore makes the total E_{bind} less negative, i.e. the envelope less strongly bound. Here, we assume that *all* the thermal energy contributes to unbinding the envelope, i.e. there is a thermal efficiency of one (Dewi and Tauris, 2000).

The behavior of E_{bind} is shown in Fig. 2.8, and depends both on the total mass of the RGB star and the mass of its core. We focus on RGB masses between 0.9 and 2.0 $M_\odot$ because they correspond to our main grid of He WD models. For a given progenitor mass, the envelope binding energy decreases as the core grows in mass and the RGB star expands. For a given core mass of a star ascending the RGB, the envelope radius is nearly independent of total mass. Hence, the value of E_{bind} is roughly proportional to the total mass squared, spanning a factor of ~4 for $0.9 - 2\,M_\odot$ stars.

2.4.3 Effect of progenitor mass on WD models

The progenitor mass used to actually create our grid of WD models can potentially affect that grid and its cooling behavior. However, we generally find that the effect is small. Therefore, the main uncertainty associated with the mass of the progenitor is through the envelope binding energy (previous section), and *not* the WD cooling.

He WDs

As an example, a 0.3 $M_\odot$ He WD can be formed through a CE from a 0.9 $M_\odot$ to $\approx$ 2.8 $M_\odot$ progenitor RGB star (referring to Fig. 2.7). However, it would be time-consuming and redundant to create a grid of WD models from each possible progenitor mass. As mentioned in Sec. 2.2.2, the cooling behavior of He WDs with a 0.9 - 2.0 $M_\odot$ progenitor are similar and we use a 1.2 $M_\odot$ progenitor model to create these WDs in MESA. However, models created from 2.1 - 2.8 $M_\odot$ progenitors show more significant cooling differences, likely because the core is less degenerate when formed (Nelemans et al. 2000 uses 2.3 $M_\odot$ as the transition to non-degeneracy). See further discussion in Appendix 2.A.1.

CO WDs

As an example, a 0.4 $M_\odot$ CO WD can be formed through a CE from two distinct regions in Fig. 2.7: either the pink region centered around a 3.5 $M_\odot$ progenitor,

or a narrow region between the blue and red lines at $\approx 2.1\ M_\odot$. The latter region represents a sdB star that forms from mass loss very close to the tip of the RGB.

Our main grid of sdB/CO WD models were created in MESA from a 3.0 $M_\odot$ progenitor. We compared models from the 3.0 $M_\odot$ progenitor, to models created from 1.0, 2.0. 3.5, and 4.0 $M_\odot$ progenitors. In general, the main effect is the duration of the sdB phase, not the behavior of the cooling CO WD. In most cases, the change in duration was small compared to the overall duration. The change was more significant when comparing canonical sdB models (creating $\sim 0.47\ M_\odot$ WDs) from the 1.0 $M_\odot$ progenitor. However, such massive CO WDs were not matches to any of our systems (Table 2.3), so they are likely irrelevant. See Appendix 2.A.2 for more details.

2.4.4 Matching WD models to progenitor star

For each matching WD model with mass M_1, we connect that model to the allowed regions of Fig. 2.7 that could have formed it. We do so by assuming that the CE event occurs at the point where the progenitor star's core mass equals the WD's initial core mass. Progenitors of 1.7 $M_\odot$ and below can create any of our He WD models (which go up to 0.45 $M_\odot$ in our grid). Higher mass progenitors can only form lower mass He WD models as shown in Fig. 2.7.

For a given progenitor mass and WD mass, we can therefore calculate $E_{\mathrm{b}ind}$ at the exact point that the progenitor has a core mass equal to the mass of the WD. However, we do not calculate $E_{\mathrm{b}ind}$ as the binding energy of the entire envelope, because our WD models also have a finite H envelope (i.e. not all of the progenitor's H envelope is unbound). We therefore integrate Eqs. 2.2 and 2.3 from M_{wd} to M_{tot}, where M_{wd} is slightly larger than the core mass. This reduces the associated $E_{\mathrm{b}ind}$ for some WD models that have a relatively massive H envelope.

2.5 Results

2.5.1 Birth periods

After finding the range of cooling times consistent with observations, we found the range of possible birth periods for each system that we model. Assuming inspiral due to GW emission only and integrating Eq. 2.1 for possible M_1 and M_2 determines birth period for a given cooling age. The range of possible M_1 is from our matching WD models (i.e. Tables 2.2 and 2.3), which show good agreement with values in the literature. For most systems, the range of M_2 is solely from published literature measurements and uncertainties (i.e., the range in Table 2.1). For WD 0957-666

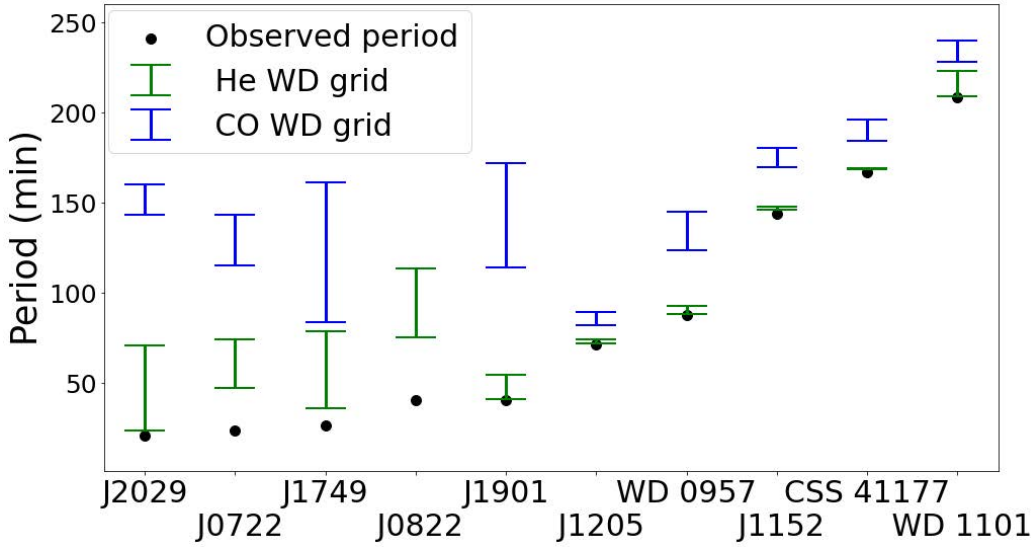


Figure 2.9: The range of possible orbital periods at birth (immediately following the CE) for each of our systems, assuming the primary is a He WD (green points) or a CO WD (blue points). SDSS J0822 has no matching models consistent with a CO WD.

and WD 1101+364, the mass ratio q is instead used to find the range of M_2 values for each M_1. Fig. 2.9 shows the corresponding birth periods for both our main grids: He-core WDs created from a 1.2 $M_\odot$ progenitor and CO-core WDs created from a 3.0 $M_\odot$ progenitor.

Note there are no matching CO models for SDSS J0822 because the primary mass M_1 in this system is relatively low (mean value of 0.3 $M_\odot$) and most CO WDs form at higher masses. In contrast, all the other systems (with higher M_1) have matching CO models. Because of the sdB phase which follows the CE (which can last 100s of Myr), our matching CO models are older than He models and correspondingly give higher estimates for the system's birth period. The maximum birth periods we find correspond to orbital separations on the order of only 1 $R_\odot$ - therefore, the overall assumption of CE evolution taking place is valid, since that separation is much less than the radius of an evolved RGB star.

The possible birth periods sometimes span a wide range due to uncertainties in cooling age, which results from models with a range of masses and hydrogen shell masses being consistent with the observed properties of a primary. In general, the uncertainty in hydrogen mass contributes much of the uncertainty in birth period. For example, for ZTF J2029 the total possible birth period range (considering all primary masses) is 23 - 71 minutes, but 0.32 $M_\odot$ models alone have a wide associated

range (34 - 63 minutes). This latter range is *not* predominantly from uncertainty in M_2 (fixing M_2 only reduces the range by about 3 minutes). Instead, it is mostly due to varying cooling ages for models with different masses of hydrogen.

Several systems have a smaller range of possible birth periods. SDSS J1152 and CSS 41177 have similar age uncertainties to other systems (see Table 2.2), but they were discovered at longer orbital periods. Hence, they cannot have been born at periods much greater than observed, because GW-driven orbital decay is less efficient at long periods. Similarly, the narrow birth period range for SDSS J1205 (the WD-BD binary) arises from the small mass of the BD companion, which decreases the GW orbital decay rate such that the observed period is very close to the birth period. For WD 1101, despite being observed at a long period, the cooling ages can be quite large (due to the system's low $T_{\rm eff}$), so there is a reasonable uncertainty in birth period. Conversely, the cooling ages are small for WD 0957 because of the WD primary's high $T_{\rm eff}$ of 30,000 K, as models of all masses quickly cool below 30,000 K, leading to a small birth period uncertainty.

2.5.2 α_{CE} Constraints

He WD Simulations

The CE efficiency factor, α_{CE}, is defined via an energy parametrization as

$$E_{\rm bind} = \alpha_{\rm CE}\left(-\frac{GM_1M_2}{2a_{\rm f}} + \frac{GM_{\rm i}M_2}{2a_{\rm i}}\right). \tag{2.5}$$

Here, $M_{\rm i}$ is the mass of the progenitor star, and $a_{\rm i}/a_{\rm f}$ are the initial/final orbital separations. The value of α_{CE} represents the fraction of the change in orbital energy that is used to unbind the donor star's envelope (Ivanova et al., 2013). An α_{CE} of unity implies that all the orbital energy released by the inspiral goes into unbinding the hydrogen envelope (full conservation of energy). Values smaller than unity imply that some energy is lost during the CE event (e.g., because it is radiated away) or that the ejected material has positive kinetic energy when it escapes to infinity. Values greater than unity can only be achieved with an extra source of energy, e.g., energy released due to accretion on to the companion during the CE.

Equation 2.5 is a parameterization that relates the initial and final orbital energy to the binding energy of the progenitor star at the "onset" of the CEE. Our method defines this onset to be when Roche lobe overflow first occurs. In principle, there could be a phase of stable mass transfer preceding or following the dynamical CEE

(e.g., Ge et al., 2010). Our inferred value of α_{CE} thus describes the orbital decay resulting from the entire process, but not its individual phases.

For each matching WD model (with mass M_1 and birth separation a_f), we determine the corresponding value of α_{CE} as follows. To link pre- and post-CE states, we map the newly formed WD model to a red giant progenitor model with that same core mass (Section 2.4.4). Then, E_{bind} is computed using equations in Sec. 2.4.2, where the energies are integrated over the ejected envelope. The companion mass M_2 is assumed to remain constant throughout the CE event. It is also assumed constant during any further phases of mass transfer (e.g., a H flash of the primary, or a bloated sdB phase).

The initial semi-major axis a_i is calculated by assuming the donor, which goes on to form the primary WD, is just overflowing its Roche lobe. We use the Roche lobe approximation of (Eggleton, 1983b)

$$\frac{R_i}{a_i} = \frac{0.49 q_i^{2/3}}{0.6 q_i^{2/3} + \ln\left(1 + q_i^{1/3}\right)}, \tag{2.6}$$

where the mass ratio is $q_i \equiv M_i/M_2$, and R_i is the radius of the progenitor star. In practice, the initial orbital energy $GM_iM_2/(2a_i)$ does not matter greatly, since the final orbital energy is much greater in magnitude. For each possible configuration (M_1, M_2, etc.) of each system, we compute the corresponding value of α_{CE} from equation 2.5. We include internal energy (thermal plus recombination) into E_{bind} for our best estimate.

The possible range in α_{CE} for each system, assuming the primary is a He WD, is shown in Fig. 2.10 and Fig. 2.11, for different assumptions involving progenitor mass. Results for our grid of CO models are discussed in Section 2.5.2. The results of Fig. 2.10 correspond to our most general criteria, in which viable He WD-progenitor pairings are made using Fig. 2.7, making the effective upper limit 2.8 $M_\odot$. In addition, progenitors more massive than 2.2 $M_\odot$ cannot form a He WD more massive than about 0.32 $M_\odot$. Therefore, half of the systems we model, with relatively high-mass He WDs, cannot have progenitors more massive than 2.2 $M_\odot$. Note that we use our main grid of WD models, constructed in MESA from a 1.2 $M_\odot$ progenitors, for our calculations (see Appendix 2.A.1 for further discussion).

All systems are consistent with CE efficiencies $\alpha_{CE} < 1$ when considering typical progenitors of ~1-2 $M_\odot$. For several systems, α_{CE} values in Fig. 2.10 can be substantially above unity when considering massive donors. For example, ZTF

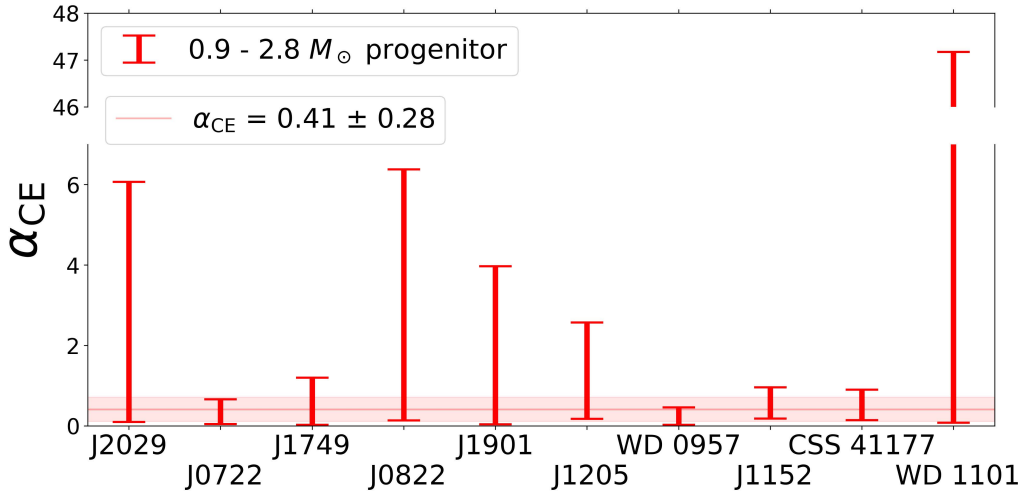


Figure 2.10: Values of α_{CE} using a grid of He WDs and progenitor mass from 0.9 - 2.8 $M_\odot$ (the maximum mass RGB star that can produce a He WD from Fig. 2.7). The horizontal line and shaded region denotes a least squares fit to the ensemble of systems.

J2029 and WD 1101 have extremely high associated α_{CE} values because their low-mass He primaries can be formed from RGB stars up to 2.8 $M_\odot$, leading to high values of E_{bind}. In contrast, systems like WD 0957 and CSS 41177 have higher mass He primaries ($\sim$0.4 $M_\odot$), limiting their progenitors to a maximum of 2.1 $M_\odot$, and hence lower E_{bind} and α_{CE}. If we assume a constant value of α_{CE} applies to all systems, we calculate a value of α_{CE} = 0.41 ± 0.28 using a least squares fit with each system weighted by the inverse of the possible range in α_{CE} (i.e., the maximum - minimum value).

The most likely values of α_{CE} are difficult to determine because they depend on the uncertain progenitor mass distribution, which may have been affected by a previous phase of stable mass transfer. High-mass progenitors are less likely because they require unphysically large values of α_{CE} and are less likely according to the initial mass function. To estimate more realistic ranges α_{CE}, in the top panel of Fig. 2.11, we restrict the progenitor mass to 0.9 - 2.0 $M_\odot$. In this case, possible values of α_{CE} range from $\sim$ 0.1 to $\sim$ 2 for all systems except WD 1101, where α_{CE} reaches a maximum over 5. If we again assume a constant value of α_{CE} applies to all systems, we calculate a value of α_{CE} = 0.33 ± 0.19 using the same method as above.

In the middle panel of Fig. 2.11, we eliminate all values of α_{CE} > 1 as they are not physical under this formalism without an extra source of energy. The resulting best-fit for α_{CE} then becomes α_{CE} = 0.34 ± 0.18. In the bottom panel of Fig.

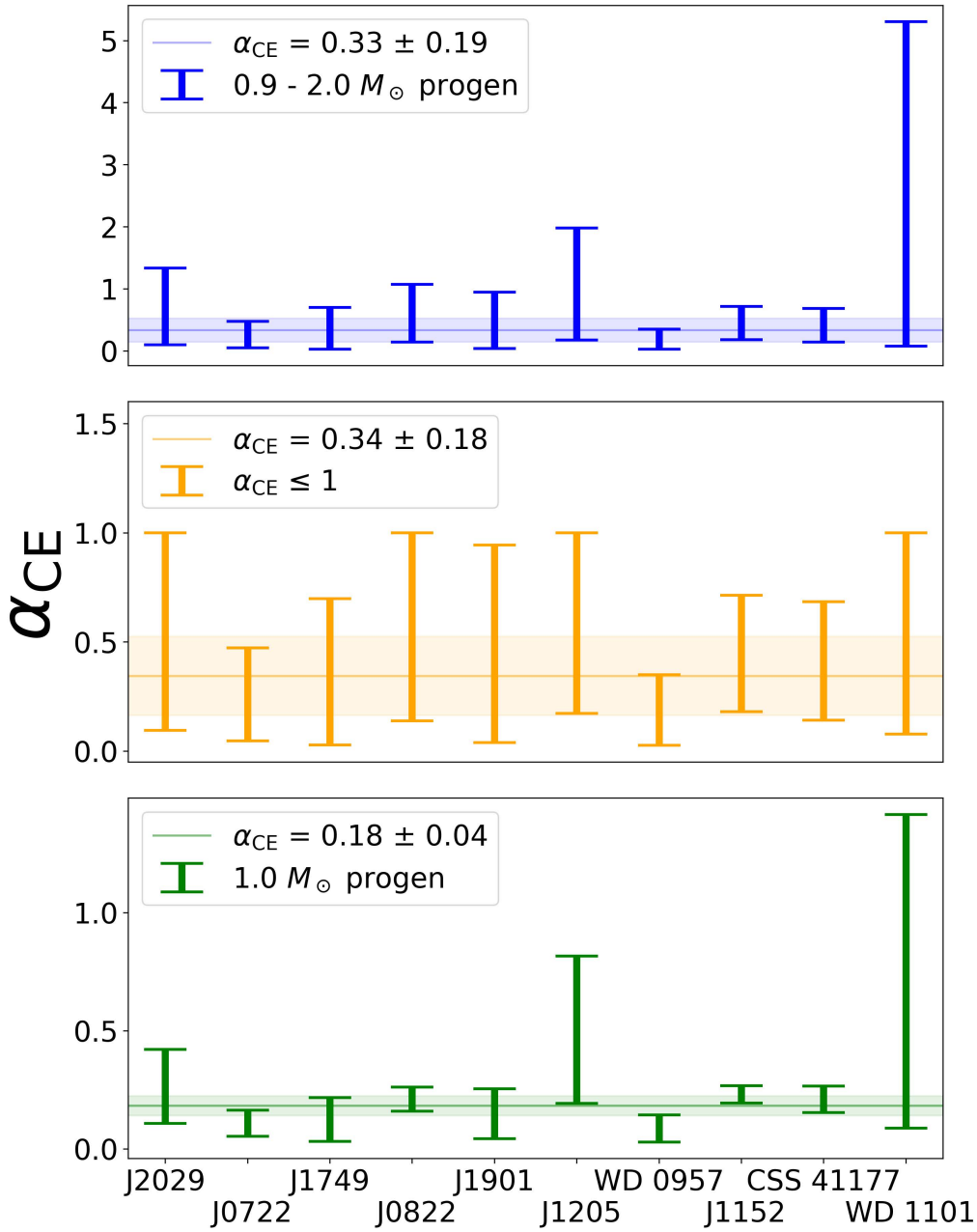


Figure 2.11: Values of α_{CE} for He WDs if progenitors of 0.9 - 2.0 $M_\odot$ are assumed (top), if α_{CE} values above unity are discarded (middle), and if a progenitor of fixed mass 1.0 $M_\odot$ is assumed (bottom). The shaded regions denote least squares fit to each ensemble of systems.

2.11, we instead assume a fixed progenitor mass of $1.0\,M_\odot$ to demonstrate the small ranges in α_{CE} that result. Assuming a $1.0\,M_\odot$ progenitor results in a best-fit $\alpha_{CE} = 0.18 \pm 0.04$, which represents an approximate lower limit to the actual CE efficiency.

In summary, we find that given reasonable assumptions on the progenitor, a universal α_{CE} substantially below unity is favored. This conclusion is strengthened by the fact that several systems can only have low values of α_{CE} due to their high-mass WDs, which require low-mass progenitors with low E_{bind} These several systems therefore have associated α_{CE} values less than unity regardless of our assumptions regarding the progenitor.

Uncertainties in α_{CE}

For most systems, the uncertainty in α_{CE} is a factor of several. Most of the range comes from uncertainty in the progenitor mass, which affects $E_{\rm bind}$ by a factor of ~ 2 - 4 when assuming progenitors of 0.9 - 2.0 $M_\odot$ and by a greater factor if considering progenitors up to 2.8 $M_\odot$ (Figure 2.8). In Fig. 2.11, WD 1101 has the highest associated α_{CE} values because of the combination of a low primary mass (minimum 0.27 $M_\odot$, which results in high envelope binding energies), and a long birth period. The system with the second highest range of α_{CE} values (SDSS J1205) has a BD companion, so the low values for M_2 drive α_{CE} upward.

The second largest uncertainty comes from observational/modeling uncertainties in the primary mass M_1, even though it is usually a secondary uncertainty in regard to birth period. Because lower (higher) values of M_1 require more (less) compact RGB progenitors with higher (lower) binding energies, uncertainty in M_1 translates to a substantial uncertainty in E_{bind} and hence to α_{CE}. Additionally, referencing Table 2.2 and Figure 2.9, there is another factor of $\lesssim 2$ uncertainty from max/min birth periods for these systems (although several have $\lesssim 5$ per cent uncertainty) that arises primarily from the uncertainty in the WD's H shell mass.

The configurations that result in upper/lower values of α_{CE} can be understood by examining equation 2.5. Since the initial orbital energy term is usually small, we can ignore that term and solve for α_{CE}:

$$\alpha_{\rm CE} \sim \frac{2E_{\rm bind}}{GM_1M_2}\left(\frac{G(M_1+M_2)P_{\rm f}^2}{4\pi^2}\right)^{1/3}, \tag{2.7}$$

where $P_{\rm f}$ is the final (birth) period. Maximum values of α_{CE} arise from a high progenitor mass and a low M_1 (creating high $E_{\rm b}{\it ind}$). Although $P_{\rm f}$ tends to *decrease* for lower M_1, that effect is not strong enough to dominate. Minimum values of α_{CE} are associated with models with a low progenitor mass and a relatively high M_1 (creating low $E_{\rm b}{\it ind}$) .

For illustrative purposes, we assume progenitors of 0.9 - 2.0 $M_\odot$ in the following two paragraphs. In the case of ZTF J2029, the maximum value of α_{CE} is associated with a 0.26 $M_\odot$ WD model (the lowest mass consistent with observations), a 2.0 $M_\odot$ progenitor(the highest mass considered in this example), and a birth period of 24 min. The minimum value of α_{CE} is associated with a 0.35 $M_\odot$ WD model, a 0.9 $M_\odot$ progenitor, and a birth period of 55 min. Therefore, the maximum value of α_{CE} counter-intuitively is associated with a model with one of the lowest birth periods, and vice versa.

Similarly, low uncertainties in birth period do not necessarily lead to tight ranges in α_{CE}. ZTF J0722 has a $\sim$ 50 per cent difference between lower/upper values of birth period, whereas CSS 41177 has less than 1 per cent difference. However, the range in possible $E_{\rm bind}$ varies greatly for both (a factor of $\sim$5 for J0722 and a factor of $\sim$3.5 for CSS 41177), leading to high ratios of max/min α_{CE} ($\sim$6 for J0722 and $\sim$4 for CSS 41177). Hence, the benefit of having a well-constrained birth period is largely wiped out by the uncertainty in $E_{\rm bind}$ due to the unknown progenitor mass.

CO WD results

From Fig. 2.7, the progenitors that can form a CO WD through CE evolution can be subdivided into 3 regions, 2 of which we focus on. For 1.8 - 2.2 $M_\odot$ progenitors, CO WDs of mass 0.39 - 0.45 $M_\odot$ can be created. Lower mass progenitors would create CO WDs more massive than 0.45 $M_\odot$, but those are not relevant to our matching CO models (Table 2.3). A 2.3 $M_\odot$ progenitor can only form CO WDs near 0.32 $M_\odot$, and for progenitors more massive than 2.3 $M_\odot$, the mass of viable CO WDs slowly rises. We therefore report α_{CE} values separately for 1.8 - 2.2 $M_\odot$ progenitors and 2.3 - 4.0 $M_\odot$ progenitors. We use the same grid of CO WDs in both cases, although such models were created with a 3.0 $M_\odot$ progenitor (justified in Sec. 2.4.3). Similarly to previous sections, we map the CO WD models to progenitors in the regions of Fig. 2.7 that could have formed them through CE evolution (in this case, the two lower pink regions).

The results for α_{CE} are shown in Fig. 2.12. The α_{CE} values for the progenitors

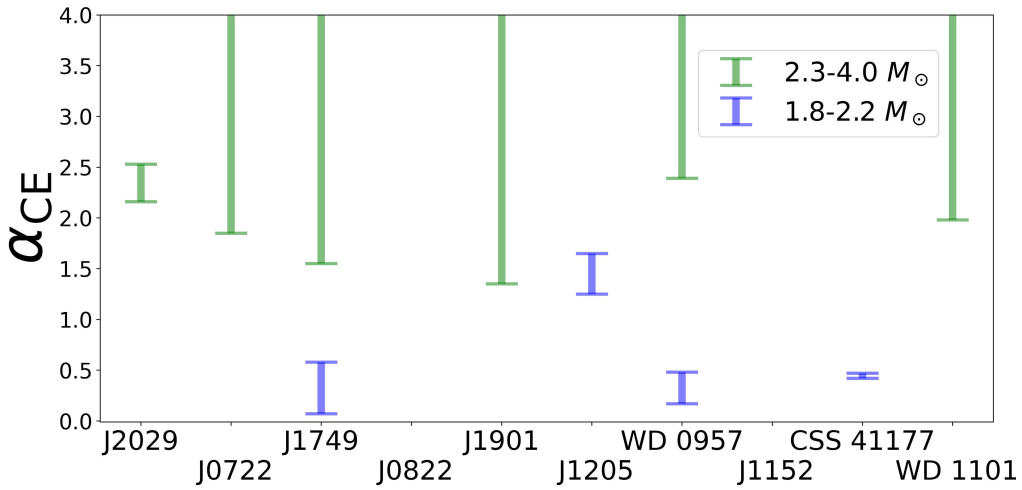


Figure 2.12: α_{CE} ranges assuming CO WDs arising from progenitors of the specified mass ranges. Not shown are green errorbars for J1205 (lower value $\sim$ 10) and J1152 and CSS 41177 (lower values $\sim$ 4). Otherwise, a lack of value indicates such a progenitor cannot create a relevant CO WD.

with $M > 2.3\ M_\odot$ are all greater than 1 and likely represent an unphysical pathway. The lowest values (still greater than 1) come from a 2.3 $M_\odot$ progenitor and CO models near 0.32 $M_\odot$. SDSS J0822 has no matching CO models. SDSS J1152, CSS 41177 and SDSS J1205 have models associated with progenitors of $M > 2.3\ M_\odot$ but the corresponding values of α_{CE} are exceptionally high, with minimum α_{CE} values greater than $\sim$4. The values are so high because these systems have high post-CEE birth periods and associated CO WD masses $\gtrsim$ 0.35 $M_\odot$. From Fig. 2.7, the $M > 2.3\ M_\odot$ progenitors that can form such a CO WD through CE evolution are at masses greater than 3 $M_\odot$, resulting in very high envelope binding energies and high α_{CE}.

The results for 1.8 - 2.2 $M_\odot$ progenitors are more interesting. In the case of 5 systems, no results are shown because this set of progenitors is incapable of forming a CO WD with mass $\lesssim$ 0.39 $M_\odot$ through CE evolution, and these 5 systems only have matching CO WD models with masses below 0.39 $M_\odot$. Again, no result is shown for SDSS J0822 because it has no matching CO WDs of any mass. ZTF J1749, SDSS J1205, WD 0957, and CSS 41177, in contrast, have matching CO WD models with masses $\gtrsim$ 0.39 $M_\odot$. The first three of these can have α_{CE} values less than 1, so a CO WD is possible. For SDSS J1205, the low mass of the BD companion drives α_{CE} higher than 1, so a CO WD is unlikely. Assuming a constant value of α_{CE} applies to all 4 systems and doing a fit in the same manner as in Section

2.5, we find $\alpha_{CE} = 0.46 \pm 0.05$, which lies in the range of our estimate from He WD models.

The CO WD models with 1.8 - 2.2 $M_\odot$ progenitors have α_{CE} values that overlap with the values from our main He WD grid. This may seem surprising, as CO models cool more slowly and entail significantly higher birth periods than He models. However, the behavior of $E_{\rm bind}$ can offset this effect. In the case of ZTF J1749 for example, comparing to the top panel of Fig. 2.11, the maximum value of α_{CE} assuming a He WDis associated with a 0.32 $M_\odot$ WD, 2.0 $M_\odot$ progenitor. The minimum value of α_{CE} assuming a CO WD is associated with a 0.45 $M_\odot$ WD model, 1.9 $M_\odot$ progenitor. Even though the birth period is roughly double for the CO model versus the He model, $E_{\rm bind}$ is reduced by a factor of $\sim$ 10 on account of the *higher* mass WD, which means the progenitor is higher up the RGB.

The large difference between results for 1.8 - 2.2 $M_\odot$ and $M > 2.3\,M_\odot$ progenitors is similarly based on $E_{\rm bind}$. Whereas lower mass progenitors ignite He burning at the tip of the red giant branch, higher mass progenitors ignite He burning closer to the base of the red giant branch when the progenitor is much more compact. This leads to a factor of $\sim$3 change in $E_{\rm bind}$, which results in a gap between the highest values of α_{CE} for the 2.2 $M_\odot$ progenitor and the lowest values of α_{CE} for the 2.3 $M_\odot$ progenitor.

2.6 Discussion

2.6.1 Comparison to previous studies

Nelemans et al. (2000) and Nelemans and Tout (2005) used similar techniques to constrain CE efficiency for several WD binaries. They argued that observed short-period WD binaries require large orbital decay during the second phase of mass transfer, but not the first phase of mass transfer. In other words, they found that an energy formalism based on α_{CE} applied to the first phase of mass transfer could not reproduce observed systems, so they argued for an angular momentum-based CE prescription (the γ-algorithm). We interpret their results as evidence that the first stage of mass transfer is usually stable (though perhaps not conservative), while the second stage of mass transfer is unstable. We have not modeled the first stage of mass transfer, so we defer a more thorough comparison to future work. Based on the modeling presented here, a nearly constant value of α_{CE} in the second phase of mass transfer can reproduce the observed systems.

We can compare our results for WD 0957 and WD 1101 to the work by Nelemans

and Tout (2005), where they present their results in terms of $\alpha_{CE}\lambda$, defined as

$$\alpha_{\rm CE}\lambda\left(-\frac{GM_1M_2}{2a_{\rm f}}+\frac{GM_{\rm i}M_2}{2a_{\rm i}}\right)=\frac{GM_{\rm i}M_{\rm env}}{R}\,, \tag{2.8}$$

where $M_{\rm env}$ is the mass of the star's envelope. In our models, for WD 0957 we find that $\alpha_{CE}\lambda$ ranges from 0.02 to 0.50, whereas for WD 1101 $\alpha_{CE}\lambda$ ranges from to 0.05 to 8.0. We interpret Fig. 5 of Nelemans and Tout (2005) and estimate that the most likely range of $\alpha_{CE}\lambda$ for WD 0957, where many models overlap, is from about 0 to 0.5. This agrees well with our estimate. For WD 1101, their most likely range of $\alpha_{CE}\lambda$ seems to be from about 0.2 to 0.8. If we restrict our WD mass range to 0.27 - 0.31 $M_\odot$, our $\alpha_{CE}\lambda$ values reach a minimum of 0.3, roughly consistent with theirs. However, our possible range of α_{CE} is much larger than Nelemans and Tout (2005) because we consider a wider range of primary masses, corresponding to a wider range of progenitor envelope binding energies and therefore a wider range of α_{CE}.

Zorotovic and Schreiber (2022) performed a similar analysis for several WD-BD binaries, finding that they are consistent with a low CE efficiency (α_{CE} of about 0.2 - 0.4). They exclude recombination energy (but do include thermal energy), meaning their α_{CE} values should be decreased slightly to compare with our values. For SDSS J1205, they found α_{CE} to be between 0.18 and unity using progenitor masses of about 1.1 - 1.9 $M_\odot$. For a similar range of progenitor masses, our value of α_{CE} ranged between 0.19 and 2. However, if we only use masses within 1σ of the quoted values (as Zorotovic and Schreiber 2022 appear to have done), our α_{CE} values reach a minimum of 0.4 instead of 0.19. Therefore our required α_{CE} values appear to be somewhat larger than theirs, but we agree that α_{CE} substantially less than unity can explain WD-BD binaries. SDSS J1205 was also examined by Parsons et al. (2017), who found $\alpha_{CE}\lambda$ for this system ranges from about 0.1 to 0.6 for a progenitor mass ranging from 0.9 to 1.5 $M_\odot$ and a WD mass of 0.43 $M_\odot$ - we find $\alpha_{CE}\lambda$ from about 0.1 to 0.67 for these same parameters. Our values are therefore in good agreement with theirs.

Our primary result for He WDs with 0.9 - 2.0 $M_\odot$ progenitors is that all systems are consistent with a CE efficiency of $\sim$ 0.2 to 0.4. In a study of post-CE binaries composed of a WD and a main sequence star, Zorotovic et al. (2010) determined ranges of α_{CE} for 60 binaries. Note that they refer to recombination energy as internal energy, differing from our terminology. When not including the recombination energy, they find α_{CE} close to 0.5 works best to describe most systems (Zorotovic,

2022). Including some recombination energy would shift α_{CE} to slightly lower values, particularly for progenitors on the AGB. Hence, their results are approximately consistent with our best-fit α_{CE}.

Hernandez et al. (2021) and Hernandez et al. (2022) modeled post-CE binaries and found that α_{CE} between 0.2 to 0.3 can reproduce binaries with a WD and a AFGK-type companion, without the inclusion of recombination energy. However, Hernandez et al. (2021) and Hernandez et al. (2022) also found wider ranges of α_{CE} ($\sim 0.1 - 1$) could be consistent with their systems. Because recombination energy is relatively unimportant for our RGB progenitors, their values of α_{CE} can be compared directly to ours and appear consistent.

Davis et al. (2012) reports α_{CE} values for WD-main sequence binaries. In their models including internal energy, α_{CE} has a large scatter from about 0.02 - 2, but most systems are consistent with our inferred range of 0.2 - 0.4. Similar to Zorotovic et al. (2010), they find higher values of α_{CE} for RGB progenitors versus AGB progenitors. Davis et al. (2012) explain that their α_{CE} values above 1 come from WD-BD binaries. For the single WD-BD binary that we modelled (SDSS J1205), we also find a median value of α_{CE} slightly larger than 1, but the range for that system extends down to $\alpha_{CE} \sim 0.17$. Hence, our results indicate brown dwarfs can only survive the CE when the WD's progenitor is relatively low-mass and high up the RGB. Davis et al. (2012) find that their α_{CE} values *decrease* with increasing progenitor mass and increasing M_2. Because of our smaller sample size, we did not perform a correlation between α_{CE} and the parameters of each system.

For some of the same systems, De Marco et al. (2011) found lower values of α_{CE} than Davis et al. (2012). De Marco et al. (2011) included thermal energy in their estimates of the energy budget. Our inferred range of α_{CE} ($\sim$ 0.2 - 0.4) is consistent with most of their results. They find a trend of *increasing* values of $\alpha_{\mathrm{D}e}$ for increasing progenitor masses. However, they use initial to final mass relations to relate the WD mass to a progenitor mass, which may be problematic. For instance, a 0.55 $M_\odot$ WD could be produced by a 1 $M_\odot$ progenitor high on the AGB, or a 3 $M_\odot$ progenitor soon after core He burning. It is possible their assumption introduces artificial trends into the results. When they modelled binaries that underwent CE evolution on the RGB, they used a progenitor mass of 1.19 ± 0.40 $M_\odot$, based solely on the initial mass function of Kroupa (2001).

Future work should re-investigate whether there really is a trend between α_{CE} and progenitor or companion mass. In our analysis, we find that there may be a trend

where α_{CE} is inversely correlated with the mass of the WD primary, M_1. However, this could be a result of correlations between uncertainties in M_1 and the inferred α_{CE}, because higher values of M_1 correspond to progenitors with smaller binding energies and hence lower inferred values of α_{CE}. More rigorous analysis including the correlations between the measurement and model uncertainties for each system should be the subject of future work.

By analysing WD binaries in the ELM Survey, Brown et al. (2016) found that in order to match the observed number of short-period systems, most of the progenitors of He-CO WD binaries detach from the CE at an orbital period less than 1 hour. Four of the systems (ZTF J2029, J0722, J1749 and J1901) we have modelled were likely born at a period less than an hour, so our results are qualitatively similar to those of Brown et al. (2016). However, the typical WD mass in the ELM Survey of $\sim 0.2\,M_\odot$ is lower than the average mass of systems we analyse. Lower-mass WDs (which have progenitors with higher binding energies) are expected to be born at shorter periods on average, assuming the same α_{CE}, helping to explain the short birth periods they infer. However, we caution that a substantial fraction of low-mass He WDs ($M \lesssim 0.25\,M_\odot$) are likely formed via stable mass transfer rather than through CE evolution (Li et al., 2019a), complicating their analysis.

Han et al. (2002) and Han et al. (2003) examined the formation of short-period sdB binaries through CE evolution, and found α_{CE} of 0.75 to be the most appropriate to replicate the observed period distribution, but with only 75% of thermal energy contributing to envelope binding energy. Therefore, their efficiency factor $\alpha_{\rm H}$ is defined as

$$\alpha_{\rm H}\Delta E_{\rm orb} = E_{\rm grav} + \alpha_{\rm H}E_{\rm int}\,. \tag{2.9}$$

One can show that their efficiency factor can be related to ours by

$$\alpha_{\rm H} = \frac{\alpha_{CE}}{1-\beta+\beta\alpha_{CE}}\,. \tag{2.10}$$

where $\beta = -E_{int}/E_{grav} \approx 0.5$ for stars low on the red giant branch. Hence $\alpha_{\rm H} \sim 0.75$ corresponds to $\alpha_{CE} \sim 0.6$ by our definition, somewhat larger than our preferred value, though they note that α_{CE} could not be accurately constrained.

Recently, Ge et al. (2022) analyzed the CE ejection efficiency short-period binaries containing an sdB star with an M-dwarf or WD companion. A large fraction of their systems are consistent with $\alpha_{CE} \sim 0.2-0.4$, in line with our results. However, some of their systems fall above or below these limits, and it is not clear why.

Sandquist et al. (2000) performed CE simulations for a few different progenitor masses, evolutionary states, and companion masses. Although their simulations only probed the dynamical phase of the CE and could not be run to complete envelope ejection, their estimates of $\alpha_{CE} \sim 0.1 - 0.5$ during the initial phase of the CE are consistent with our empirical estimates. Nandez et al. (2015) used 3D simulations to construct DWD binaries, with low-mass red giant star progenitors from ∼1-1.8 $M_{\odot}$. They incorporated both thermal and recombination energy, and found an α_{unb} of 0.2 - 0.44 (representing energy taken away by unbound material). This is related to the CE efficiency via $\alpha_{CE} = 1 - \alpha_{\mathrm{unb}}$, leading to an α_{CE} of 0.56 - 0.8. The minimum value of this range is slightly above the upper bounds of our fiducial range. Additionally, our maximum values correspond to high-mass progenitors, while their minimum values correspond to low-mass progenitors, so their values of α_{CE} appear to be inconsistent with ours. This tension should be examined in future work.

Simulations by Ohlmann et al. (2015) with a 2 $M_{\odot}$ donor star only ejected 8 per cent of the envelope mass on a dynamical time-scale. They suggest that either processes on a thermal time-scale or the contribution of recombination energy may lead to full unbinding. Similarly, simulations by Ricker and Taam (2012) with a 1.05 $M_{\odot}$ donor star only ejected 26 per cent of the envelope mass, while the rest of the envelope remained bound. Recently, Law-Smith et al. (2022) performed simulations with a 12 $M_{\odot}$ donor star where the envelope was completely ejected. They found $\alpha_{CE} \approx 0.1$ - 2.7 depending on how much material is ejected after the end of their simulations. However, they only included gravitational potential energy in their definition of envelope binding energy, meaning their values should be roughly halved to compare to ours, and therefore appear to be similar to ours.

2.6.2 Constraining the Progenitor mass

The main uncertainty in α_{CE} for each system arises from the uncertain progenitor mass. If this could be constrained some other way, a more precise α_{CE} could be determined. Zorotovic and Schreiber (2022) uses the brown dwarf companions to estimate the total age of the system and therefore constrain the WD progenitor mass. Discovering a double WD binary in a cluster with known turnoff mass could also constrain the initial progenitor masses. Similarly, discovering a WD binary in a widely separated tertiary (Toonen et al., 2016) whose third star could be age-dated could constrain progenitor mass. A complication for both of these scenarios is that the primary (second-formed) WD progenitor may have accreted mass from

its companion during a prior phase of stable mass transfer, increasing the mass of the primary WD progenitor and decreasing its lifetime. Indeed, the population synthesis of Ruiter et al. (2010) predicts that the vast majority of binary He WDs (which represent most of our sample) are formed in this manner.

2.6.3 Other progenitor uncertainties

The effect of metallicity on cooling He WD models is discussed in Appendix 2.C. In the case of SDSS J0822, the discovery paper (Brown et al., 2017) argues that the WD binary is likely located in the Galaxy's halo based on its distance. Therefore, it is possible that it has a significantly lower metallicity than solar. Assuming a tenth of solar metallicity for WD models increases the maximum H envelope mass, thus enlarging the maximum possible cooling age and increasing the maximum birth period for SDSS J0822 by about 35 per cent (while not significantly changing the minimum period).

Metallicity is also important in the progenitor RGB models, where changing metallicity changes the star's radius (and therefore $E_{\rm bind}$) as a function of its He core mass. The difference in $E_{\rm bind}$ (compared to the Z = 0.02 model) ranges from 20 per cent to 40 per cent for Z = 0.0067, and from 40 per cent to 80 per cent for Z = 0.002. These differences would propagate to α_{CE}. However, these uncertainties are still lower than those associated with the mass of the progenitor (where $E_{\rm bind}$ can triple). In the case of SDSS J0822, reducing metallicity for the progenitor star by a factor of ten increases $E_{\rm bind}$ by about 40 per cent. Together, the changes in birth period and $E_{\rm bind}$ lead to values of α_{CE} approximately doubling. Using doubled α_{CE} values for this one system does not substantially affect the least squares fit in Sec. 2.5, but using lower metallicity progenitors to model all systems would substantially increase our best estimate of α_{CE}. However, it seems unlikely that a large fraction of these systems formed from low-metallicity progenitors (but see Thiele et al. 2021).

For a given progenitor mass, parameters such as convective mixing length and convective overshoot can affect the relationships between main sequence mass, core mass, and red giant radius. Decreasing the convective mixing length $\alpha_{\rm MLT}$ has been found to decrease the temperature and increase the radius of a RGB star at the same luminosity (i.e., core mass, Bressan et al. 2012). Our default model has a $\alpha_{\rm MLT}$ of 1.89. When we run a 1.0 $M_{\odot}$ model with $\alpha_{\rm MLT}$ of 1.7, the radius versus core mass increases by up to 9 per cent, while using $\alpha_{\rm MLT}$ = 2.0 decreases the radius versus core mass by up to 5 per cent. Tayar et al. (2017) finds that $\alpha_{\rm MLT}$ ranges from about

1.74 to 2.06 for [Fe/H] ranging from -1 to 1, motivating the range we checked. These changes in radius would affect $E_{\rm bind}$ and α_{CE} by similar factors, but these remain much smaller than the uncertainty due to the unknown progenitor mass.

Convective overshoot on the main sequence (not included in our models) can slightly increase the core mass, causing stars to behave like slightly more massive stars on the RGB. Increasing overshoot would cause the lines in Figure 2.7 to move to the left, slightly decreasing the progenitor masses and binding energies for the same core masses. However, this uncertainty is also dwarfed by the large possible range in progenitor mass.

2.7 Conclusion

For a sample of nine double WD binaries and one WD-BD binary, we model the primary WD's cooling age and thus constrain the system's "birth period" following common envelope (CE) evolution. Each system we analyze has a low-mass primary WD ($M_1 \lesssim 0.45\,M_\odot$) which is likely a He-core WD. By considering all possible red giant progenitor stars for each WD primary, we constrain the range of possible CE ejection efficiencies, α_{CE}. Because of 1) the eclipsing nature of eight of the binaries and resulting low uncertainties for radii, temperatures, and masses, and 2) the lack of magnetic braking (as opposed to WD-M dwarf binaries), the binaries we model are some of the most promising candidates for precisely constraining CE ejection efficiency.

We estimated the cooling age of the WD primary via a grid of WD models. Unlike some prior analyses that use published WD cooling tracks, we perform a comprehensive analysis that accounts for uncertainties such as the WD's hydrogen envelope mass and the possibility of H-burning flashes. Our two separate grids of He- and CO-core WDs incorporated element diffusion and gravitational settling, and assumed solar metallicity. We assumed GW-induced inspiral alone to convert the cooling age to the binary's post-CE birth period. We found that:

- Our models that are consistent with the primary's radius and $T_{\rm eff}$ have masses that generally overlap well with the quoted mass M_1 from discovery papers.
- While hydrogen shell flashes may occur in the WD primary, models with hydrogen flashes and mass transfer do *not* set the upper/lower bounds on birth periods.

- All but one system has a primary that is consistent with a low-mass CO WD as well as a He WD. The birth periods assuming a CO WD are larger than when assuming a He WD, due to the significant duration of the post-CE sdB phase preceding the CO WD's formation.

We created a mapping from our WD models to possible RGB progenitor stars, calculating the envelope binding energy when a viable progenitor has core mass equal to the core mass of the WD. We assumed the binding energy to be the sum of gravitational and internal (thermal plus recombination) energies, and the pre-CE period is calculated from the Roche-lobe overflow criterion. From the ratio of binding energy to the change in orbital energy (as mainly determined by the WD binary's birth period), we calculated α_{CE}. Our results are:

- Assuming He WDs from RGB progenitors between 0.9 and 2.0 $M_{\odot}$ leads to a best-fitting constant α_{CE} in the range $\sim$ 0.2 - 0.4. Therefore, our ten systems are consistent with a value of α_{CE} that is substantially less than unity.

- The main uncertainty in α_{CE} arises from the unknown progenitor star mass, followed by observational uncertainty in the primary WD mass (and hence progenitor core mass and envelope binding energy). Uncertainties stemming from the WD's hydrogen envelope mass, companion mass, metallicity, recombination energy, core boundary definition, modeling uncertainties, and other measurement uncertainties contribute at a lower level.

- Progenitors with $M \gtrsim 2.1\,M_{\odot}$ require larger values of α_{CE} because of the larger progenitor mass and smaller progenitor radius (hence much larger binding energies) when the CE event occurs. However, several systems have associated values of α_{CE} significantly less than unity regardless of our inclusion of massive progenitors because massive progenitors are more limited in the masses of He WDs they can create. Therefore, considering the ensemble of systems, $\alpha_{CE} < 0.5$ is still favored.

- CO WD primaries from RGB progenitors between 1.8 and 2.2 $M_{\odot}$ (creating WDs of $\gtrsim$ 0.4 $M_{\odot}$) are relevant only to 4 systems. In this case, we find a best-fitting $\alpha_{CE} \sim 0.5$. Progenitors of $M \gtrsim 2.3\,M_{\odot}$ (which create CO WDs of $\gtrsim$ 0.32 $M_{\odot}$ and are relevant to nine systems) have associated α_{CE} values larger than unity and are hence unlikely.

System	0.9 $M_\odot$	1.2 $M_\odot$	2.0 $M_\odot$	2.3 $M_\odot$	2.5 $M_\odot$	2.8 $M_\odot$
ZTF J2029	27.9 - 36.7	27.2 - 37.6	31.6 - 41.3	44.9 - 54.2	47.1 - 63.2	51.8 - 59.8
SDSS J0822	75.8 - 83.4	75.1 - 83.8	78.2 - 86.8	85.4 - 94.2	86.7 - 97.0	89.7 - 98.4

Table 2.4: The inferred range of post-CE birth periods (in minutes) for two systems, using progenitors of different initial masses. Top row refers to the initial mass of the progenitor used to create a grid of 0.3 $M_\odot$ He WD models.

Our relatively low α_{CE} values ($\alpha_{CE} \sim 0.2$ - 0.4 for our main grid of He WDs) appear to be consistent with constraints from similar previous modeling of WD-WD, WD-M dwarf, and WD brown dwarf binaries. This motivates further investigation of whether a low α_{CE} is consistent with other types of post-CE binaries, and the corresponding impact on predictions of binary population synthesis. Our work also encourages additional efforts to find and characterize short-period WD binaries, which are extremely useful for constraining α_{CE}. If a universal value of α_{CE} is found to exist, a sample of short-period WD binaries with well constrained masses and temperatures will likely be a major cornerstone in supporting it.

Acknowledgments

We are grateful for support from the NSF through grant AST-2205974. JF is thankful for support through an Innovator Grant from The Rose Hills Foundation, and the Sloan Foundation through grant FG-2018-10515. We thank Sterl Phinney and Kevin Burdge for useful discussions. We thank the anonymous referee for their useful feedback and suggestions.

2.A Effect of progenitor mass on WD models

2.A.1 He models

To characterize the effect of progenitor mass on the behavior of WD models, we created a grid of 0.3 $M_\odot$ He models from several different progenitor masses: 0.9, 1.2, 2.0, 2.3, 2.5 and 2.8 $M_\odot$. We found that models created from higher mass RGB stars tended to cool slower, as expected from considerations that the core is less degenerate at mass stripping and contracts further following the WD's formation, releasing thermal energy. For models from 0.9 - 2.0 $M_\odot$ progenitors, the effect of progenitor mass on the WD cooling and inferred birth period was small compared to overall uncertainties.

However, using models from a 2.2 $M_\odot$ progenitor started to increase the inferred birth period substantially, and using more massive progenitors continued the increase (Table 2.4). We use ZTF J2029 and SDSS J0822 as benchmarks because they are well-matched by 0.3 $M_\odot$ He models. Additionally, the mass of H that formed the boundary between flashing and non-flashing models remained similar for 0.9 - 2.0 $M_\odot$-generated models, but began to change once a progenitor mass of 2.2 $M_\odot$ was reached.

When calculating values of $\alpha_{\rm CE}$, we use the grid of WD models generated from a 1.2 $M_\odot$ progenitor. This is justified because the dominant effect of a massive ($> 2M_\odot$) progenitor will be to increase $E_{\rm bind}$ and therefore increase $\alpha_{\rm CE}$, with the change in WD models/cooling ages a secondary effect. In the case of ZTF J2029, for example, the effect on α_{CE} from different WD cooling models (generated with a 2.0 $M_\odot$ vs 2.3 $M_\odot$ progenitor) will be less than about 30 per cent due to the difference in associated birth period. The change in $E_{\rm bind}$ when comparing a 2.0 $M_\odot$ vs 2.3 $M_\odot$ progenitor is generally much larger and more important. Therefore, we use the same grid of WD models to model the WD primary (i.e. finding the same cooling age/birth period) and to perform the calculation of α_{CE} even when considering high-mass progenitors.

2.A.2 CO models

We compared 0.4/0.45 $M_\odot$ CO WD models made from a 3.0 $M_\odot$ progenitor (in the blue CE-forbidden region of Fig. 2.7) to models made from 3.5/4.0 $M_\odot$ progenitors (in the pink CE-allowed region). The differences occur predominantly in the duration of the sdB phase (which makes sense, given the choice of progenitor determines whether He-burning has already begun before mass stripping). However, the changes are small (a few times 10^7 years) compared to the overall duration of the sdB phase (several times 10^8 years) and do not greatly affect our results. Therefore, even though we do not expect a 3.0 $M_\odot$ progenitor to create a 0.4 or 0.45 $M_\odot$ CO WD through CE evolution (as those are core masses past the tip of the RGB but preceding the AGB), it is reasonable for our purposes to use a 3.0 $M_\odot$ progenitor model.

Similarly, we compared 3.0 $M_\odot$ progenitor models with sdB models formed near the tip of the RGB from 1.0 and 2.0 $M_\odot$ progenitors. It was difficult to run stripped star models that flash *after* mass stripping. While we could create such models, and track the He flash (therefore identifying them as about to become sdB stars), numerical difficulties prevented us from running them through the duration of the sdB. However, as in the MESA test suite and also Bauer and Kupfer (2021), we

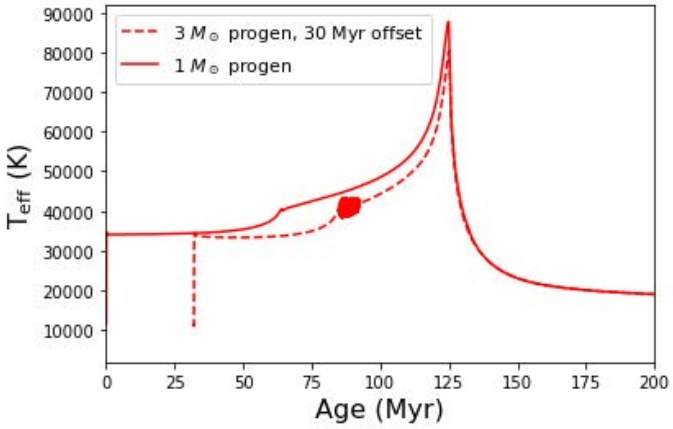


Figure 2.13: Two 0.47 $M_\odot$ CO models, one from a 1 $M_\odot$ progenitor stripped just after He ignition (close to canonical) and one from 3 $M_\odot$ progenitor. The second model shows oscillations due to He-burning flashes (discussed in 2.3.2). The duration of the sdB phase changes (by the offset of 3e7 years), but the WD cooling curves are not significantly affected by the choice of progenitor.

could create and run models that flash just *before* mass stripping.

Therefore, we compared 3.0 $M_\odot$ progenitor, 0.44/0.47 $M_\odot$ WD models (in the blue CE-forbidden region) to 2.0 $M_\odot$ progenitor, $\approx$ 0.44 $M_\odot$ WD models and 1.0 $M_\odot$ progenitor, $\approx$ 0.47 $M_\odot$ WD models (in both cases stripped slightly after the tip of the RGB). Models from a 2.0 $M_\odot$ progenitor were similar to models from a 3.0 $M_\odot$ progenitor. Models from a 1.0 $M_\odot$ progenitor showed a significantly longer sdB phase versus the 3.0 $M_\odot$ progenitor models because the 3.0 $M_\odot$ progenitor models had already burnt much of their He at the time of mass stripping. However, the post-sdB behavior (i.e. the cooling CO WD) showed similar behavior (e.g. Fig. 2.13). Therefore, we would expect 0.47 $M_\odot$ models from two different progenitors to either be both good fits or both bad fits to the observational constraints. Therefore, as no 0.47 $M_\odot$ WD models with a 3.0 $M_\odot$ progenitor were matches to our systems, they would likely not be matches even if created with a 1.0 $M_\odot$ progenitor, and we did not create a full grid of canonical sdB models.

2.B Creation of He WD models

Our He WD models are created through mass stripping of an evolved RGB star. We do not assume *ab initio* the maximum amount of H expected to be found on a cooling WD. In the case of a large amount of H on the model, the model will remain radially extended and its surface temperature will remain elevated (i.e. the model does not cool) until excess H burns. One method is to let the model adjust in

isolation, burning any excess H, then save the model immediately after the surface temperature began to decrease, so that further evolution in the binary starts with the WD primary at the top of its cooling track. The other method is to place the model into a binary as it adjusts, where we find that excess H is lost to mass transfer to the companion on a time-scale of hundreds of years, after which the model begins to cool/contract. Comparing the two methods showed that they result in similar cooling behavior for the model after a time much shorter than the ages we infer, so this initial transient phase is unimportant for our purposes.

For our grid of models, we choose to model them in isolation, saving them for further use when their temperatures begin to decrease. However, we still need a criterion so that the adjustment phase does not extend arbitrarily long for large amounts of H. Therefore, we reject models that expand beyond 1 $R_\odot$ as they will almost certainly undergo mass transfer and lose the excess H to the companion. This limits the adjustment phase to less than 1 Myr and makes it irrelevant to estimating cooling ages. However, it is still important to model this phase to see how much H can survive, which influences the WD cooling behavior.

Creation of models with low masses of H

To create models with a very low mass of H, we take a relatively low-H model as created above in Sec. 2.2.2 (e.g. a 0.3198 $M_\odot$ core, 0.32 $M_\odot$ model) and replace most of its outer H envelope with He, via *replace_element = .true.* and setting the boundaries *replace_element_nzhi* and *replace_element_nzlo* to target the inner regions of the H envelope. This method was used to create models with masses of H below around 10^{-6} $M_\odot$.

2.C Effect of metallicity on He WD models

We have assumed solar metallicity (Z=0.02) in the creation of all WD models. However, a lower metallicity can change WD cooling behavior. At lower metallicity, the threshold of H required to undergo a H flash increases - i.e. there are models that flash at Z=0.02, as opposed to those that maintain stable burning at Z=0.002. Therefore, the main effect of lowering metallicity is to introduce slowly-cooling models with high H, that would have flashed and then cooled more quickly at higher metallicity. This leads to higher possible birth periods for several of the systems that we model (Fig. 2.14). We show only half the systems we model for clarity, because the others have relatively small period uncertainties for either metallicity grid. The

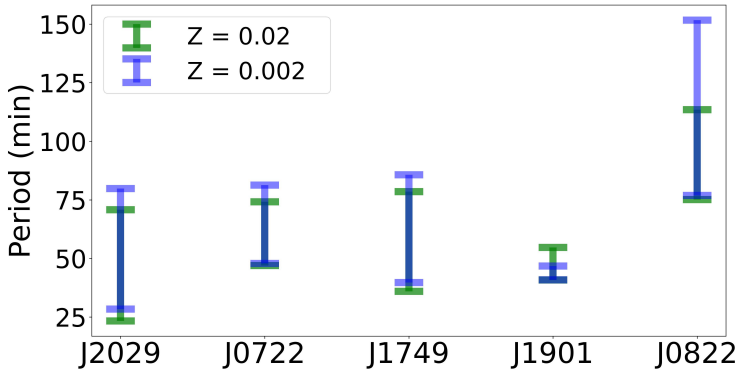


Figure 2.14: A lower metallicity grid results in longer possible birth periods for most of the systems that we model. Not all systems are shown because some have low birth period uncertainties when modeled at either metallicity.

change is largest in the case of SDSS J0822 - models with a large H envelope can take a very long time to cool to its relatively low $T_{\rm eff,1} \simeq 14{,}000$ K. Interestingly, this is the only binary we model where the discovery paper claims it to be located in the galaxy's halo (Brown et al., 2017). Therefore, it is possible that it does indeed have low metallicity, and the upper period quoted for our main grid of solar-metallicity models is an underestimate. The effect of this change, combined with the change in envelope binding energy for progenitor stars of lower metallicity, is discussed in Sec. 2.6.3.

2.D Flashing He WD models: Extra Details

Flashing WDs undergo a large expansion in radius that will likely lead to mass transfer with the companion. When modeled, mass transfer was computed via *mdot_scheme* = *Kolb*. We compared the Kolb and Ritter mass loss schemes for a single model, and found the mass loss and resulting cooling behavior nearly identical, but Ritter requiring more timesteps and computing time. Additionally, we used MESA release 10398 instead of more recent versions, because of its empirical increased computational speed for flashes and mass transfer.

We tested the effect of changing the orbital period and the companion mass on our simulations. Performing a subset of simulations with M_2 of 0.57 $M_\odot$ (the highest feasible M_2 from Table 2.1) made negligible difference with regard to mass loss/post-flash cooling curves. We also ran a subset of models at (more computationally difficult) periods of 60-70 minutes, and found that the amount of H lost or the post-flash cooling behavior was not greatly changed when compared to models at 100

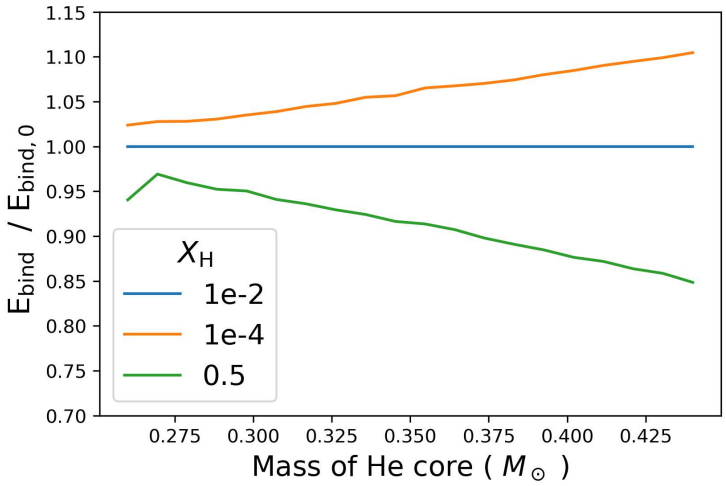


Figure 2.15: Effect of core/envelope boundary definition on envelope binding energy. $X_{\rm H}$ refers to the mass fraction of H below which the He core is defined to begin. $E_{bind,0}$ refers to envelope binding energy with our default definition for core/envelope boundary ($X_{\rm H} = 10^{-2}$).

minute periods. Because the flashing model's envelope wants to expand so greatly beyond the RL (i.e. it would expand to 10s of $R_\odot$ if not modelled in a binary), the exact value of the RL does not matter greatly. As expected, we found that any of these additional models which matched to our systems could be bounded above and below in cooling age/birth period by non-flashing models.

The one exception is ZTF J1901, where flashing models (fitting to observed radius and $T_{\rm eff}$) *do* provide the upper cooling age bound for the system. However, in these cases the upper-bound flashing models only match the observed temperature during the spike in temperature immediately after the flash (such a spike is demonstrated in the nearly vertical red lines in Fig. 2.5). The time-scale for this spike in temperature (which is similar to the time-scale of the large loop in the HR diagram in Fig. 2.4) is less than 10^5 years and these models match the observed temperature for only about 10^4 years. In contrast, the length of time non-flashing models match temperature constraints is closer to 10^6 years for this system. Therefore, it is far less likely that we are observing the system in an immediately post-flash state, as compared to undergoing normal cooling behavior. We reject such flashing models, which show similarly small ages of relevance, for *all* systems we model.

2.E Effect of He core boundary definition on envelope binding energy

An additional uncertainty associated with calculating the binding energy of the H envelope $E_{\rm bind}$ is the exact definition of the envelope/core boundary. For both WD and RGB models, we have used MESA's default definition of the He core to be where the mass fraction of H, $X_{\rm H}$, drops below 0.01. The effect of changing this definition on $E_{\rm bind}$ is shown in Fig. 2.15. To calculate this, we iterate through the saved profiles for a 1.5 $M_\odot$ RGB star, finding when the core reaches a certain mass by a certain definition (e.g. when the core reaches 0.4 $M_\odot$ for $X_{\rm H} = 0.5$). As before, we then integrate down to that mass coordinate to find $E_{\rm bind}$. Using a smaller value of $X_{\rm H}$ decreases the core mass for a given model and therefore increases $E_{\rm bind}$, and vice versa. The change depends on core mass, but can reach up to 20 per cent. However, this uncertainty is small compared to the uncertainty from the unknown total mass of the RGB star.

Chapter 3

ULTRASHORT-PERIOD WD BINARIES ARE NOT UNDERGOING STRONG TIDAL HEATING

Scherbak, Peter and Jim Fuller (Feb. 2024). "Ultra–short-period WD Binaries Are Not Undergoing Strong Tidal Heating". In: *The Astrophysical Journal* 962.2, p. 185. DOI: 10.3847/1538-4357/ad1dd6.

Double white dwarf (WD) binaries are increasingly being discovered at short orbital periods where strong tidal effects and significant tidal heating signatures may occur. We assume the tidal potential of the companion excites outgoing gravity waves within the WD primary, the dissipation of which leads to an increase in the WD's surface temperature. We compute the excitation and dissipation of the waves in cooling WD models in evolving MESA binary simulations. Tidal heating is self-consistently computed and added to the models at every time step. As a binary inspirals to orbital periods less than ∼20 minutes, the WD's behavior changes from cooling to heating, with temperature enhancements that can exceed 10,000 K compared with non-tidally heated models. We compare a grid of tidally heated WD models to observed short-period systems with hot WD primaries. While tidal heating affects their $T_{\rm eff}$, it is likely not the dominant luminosity. Instead these WDs are probably intrinsically young and hot, implying the binaries formed at short orbital periods. The binaries are consistent with undergoing common envelope evolution with a somewhat low efficiency $\alpha_{\rm CE}$. We delineate the parameter space where the traveling wave assumption is most valid, noting that it breaks down for WDs that cool sufficiently, where standing waves may instead be formed.

3.1 Introduction

Double white dwarf (DWD) binaries have increasingly been found at short orbital periods (e.g., Brown et al., 2011; Burdge et al., 2020b), with the tightest detached system at an orbital period of only 6.9 minutes (Burdge et al., 2019a). For these compact systems, tides are expected to be very strong (e.g., Iben et al., 1998), but the effects of tides on the WDs and the resulting observable predictions have remained uncertain.

As DWD binaries inspiral to shorter orbital separations due to the emission of

gravitational waves (GWs), tidal effects will become stronger, and tidal heating could become the dominant source of luminosity (Iben et al., 1998; Burdge et al., 2020c). Measuring tidal heating is one of the principle ways to constrain tidal physics (Piro, 2019). At very short periods, tides may affect the pre-merger conditions of DWD binaries, such as the synchronization of WD rotation with the binary orbit. The degree of synchronization pre-merger is unclear, with some simulations assuming the WDs are tidally locked (e.g., Raskin et al., 2012; Dan et al., 2014), whereas others have assumed the WDs are initially non-rotating (e.g., Yoon et al., 2007; Lorén-Aguilar et al., 2009). When comparing WD merger simulations with these two different initial conditions, Dan et al. (2014) found that the merger timescale and the location of helium detonation were significantly altered. Therefore, the degree of synchronization seems to affect the merger product of two WDs, which is a pathway to Type Ia supernova (e.g., Shen, 2015) and other exotic phenomena.

While tides are expected to contribute to heating of both WDs, quantitative predictions of the heating, and its dependence on WD mass and system orbital period, have not been rigorously performed. Instead, the magnitude of the tidal heating has only been estimated for a few different WD masses and orbital periods (Fuller and Lai, 2013; Yu et al., 2021), and the changing WD structure, heating rate, and location of heat deposition have not been self-consistently modeled. Many recently discovered short-period DWD binaries have measured masses and surface temperatures, meaning that precise predictions of tidal heating can now be directly compared to observations.

In a compact binary, each component feels a tidal force due to its companion's gravitational potential. The equilibrium tidal response, referring to a body's overall deformation in quasistatic equilibrium, is unlikely to be important except when the binary is close to mass-transferring (Fuller and Lai, 2011). Rather, the wave-like or oscillatory tidal response, known as the dynamical tide (Zahn, 1975; Zahn, 1977), is likely dominant. The dynamical tide often involves the excitation of standing-wave gravity modes (Zahn, 2008), or, if there is sufficient dissipation, a train of traveling gravity waves (Goldreich and Nicholson, 1989). In stars on the main sequence, waves are excited at the convective-radiative boundary and their dissipation can drive circularization and synchronization of the binary. Gravity modes are also found in WDs, as demonstrated observationally by pulsating ZZ Ceti stars (Brickhill, 1983). The nature of the tidal excitation, and whether it is in the standing wave or traveling wave regime, will help determine the impact of tides on

a WD's observed properties. Previous works that have focused on standing waves in WDs include Burkart et al. (2013) and Yu et al. (2020).

In a series of papers, Fuller and Lai (2011), Fuller and Lai (2012), Fuller and Lai (2013) applied the theory of dynamical tides to a DWD binary. In particular, Fuller and Lai (2012) and Fuller and Lai (2013) found that, for both CO- and He-core WDs, excited gravity modes are likely to damp in the outer envelope and prevent the formation of standing waves. Fuller and Lai (2013) modeled tidal heating in a WD model, but this analysis was limited to a WD model of fixed mass initialized at fixed temperatures.

In this paper, we investigate tidal effects for WDs of various masses that undergo evolution in a binary and are allowed to realistically cool (if tidal heating is unimportant) or be heated by tides. Only with a grid of models can simulations be compared to known systems to better interpret observations. In addition, Fuller and Lai (2013) assumed that the tidal response is in the strongly dissipated traveling wave regime, and focused on nonlinear wave breaking as the most important dissipative mechanism. Here we model the contributions of both nonlinear wave breaking and radiative damping as dissipative mechanisms, and estimate where the overall traveling wave assumption breaks down.

In this work, we self-consistently implement tidal effects into cooling He-core WD models simulated in the `MESA` stellar evolutionary code (Paxton et al., 2011; Paxton et al., 2013; Paxton et al., 2015; Paxton et al., 2018; Paxton et al., 2019). Sec. 3.2 reviews the physics of the excitation of gravity modes/gravity waves in a DWD binary. Sec. 3.3 describes the implementation of dynamical tides in a DWD binary `MESA` simulation, where the WDs undergo spin-up and heating due to the dissipation of excited gravity waves. Sec. 3.3.2 presents the models where the traveling wave response works best and where it breaks down. Sec. 3.4 presents tidal heating predictions for simulations of differing WD masses and initial orbital periods, and compares these predictions to observed ultrashort-period DWD binaries. We discuss our results in Sec. 3.5 and conclude in Sec. 3.6.

3.2 Basic tidal physics

More detailed analysis of tidally excited oscillations in WDs is found in Fuller and Lai (2012). Here we review the basic quantities needed for our analysis.

Consider a DWD binary with primary mass M_1 and secondary mass M_2 in a circular orbit of separation a and orbital frequency Ω. The following analysis treats the

secondary as a point mass and only models tidal effects in the primary M_1, which has a radius R. The presence of M_2 creates a tidal potential that acts as a forcing term in the fluid equations describing the primary's interior. The tidal potential is predominantly quadrupolar with degree $l = m = 2$. It varies sinusoidally in time with tidal frequency

$$\omega = 2(\Omega - \Omega_s), \tag{3.1}$$

where Ω_s is the spin frequency of the WD.

In the outer region of the WD, the tidal potential can either excite standing g-modes (with a reflective outer boundary condition) or gravity waves (with an outgoing boundary condition). In either case, the restoring force for these oscillations is buoyancy. The Brunt–Väisälä frequency N, or buoyancy frequency, is therefore very important in determining where these modes/waves are excited and where they can propagate.

Because of strong dissipative effects, the wave energy may be depleted before the wave is reflected. Therefore, in this work we assume the response is in the outgoing wave regime (but see Sec. 3.3.2 and Figs. 3.3 - 3.5 for when this assumption breaks down). For a He-core WD, the outgoing wave is excited near the composition gradient at the transition between the WD's He core and H envelope (Fuller and Lai, 2013), where there is a spike in N^2.

In the WKB limit, gravity waves satisfy the dispersion relation

$$k_{r,\mathrm{WKB}}^2 = \frac{\left(L_l^2 - \omega^2\right)\left(N^2 - \omega^2\right)}{a_s^2 \omega^2} \tag{3.2}$$

with the Lamb frequency

$$L_l^2 = \frac{l(l+1)a_s^2}{r^2}, \tag{3.3}$$

where k_r is the radial wavenumber, a_s is the adiabatic sound speed, and r is the internal radius of the WD. We leave l general in our equations although $l = 2$ is always assumed in this paper.

In most of the WD's interior, the gravity waves satisfy $\omega^2 \ll L_l^2$ and $\omega^2 \ll N^2$. However, there are regions near the surfaces of our WD models where ω^2 becomes comparable to L_l^2 (see also Sec. 3.3.2 for how the traveling wave approximation can break down in these cases). If applied to Eq. 3.2, k_r^2 would become very small. We therefore assume a lower limit of k_r^2 as $1/\left(4H^2\right)$, where H is the pressure scale

height. Therefore, our full expression for the radial wave number is

$$k_r^2 = \max\left[\left(L_l^2 - \omega^2\right)\left(N^2 - \omega^2\right)/a_s^2\omega^2, \frac{1}{4H^2}\right]. \tag{3.4}$$

The wave carries both an angular momentum (AM) flux and energy flux toward the surface of the WD. AM and energy will therefore be transferred from the binary orbit to the WD, causing the WD to undergo spin-up and heating.

3.3 Tidal effects in MESA simulations

We create He-core WDs in the `MESA` stellar evolutionary code (Paxton et al., 2011; Paxton et al., 2013; Paxton et al., 2015; Paxton et al., 2018; Paxton et al., 2019). The WD models are created by mass stripping of an evolved red giant branch star when its He core reaches masses of 0.25, 0.30, 0.35, 0.40, and 0.45 $M_\odot$, giving 5 WD masses in our grid. We varied the mass of hydrogen in these WD models from about 10^{-5} to 10^{-3} $M_\odot$, but found that our tidal spin-up and tidal heating results were ultimately not greatly affected, with parameters like WD mass and age mattering much more (see Appendix 3.C for further discussion). However, if the hydrogen envelope was completely stripped, we would not expect a spike in Brunt–Väisälä frequency where the gravity waves are excited and our assumptions would greatly break down. Therefore, our results likely only apply to DA WDs with a hydrogen atmosphere.

We simulate tidal interactions with the WD in a binary `MESA` simulation with a point mass companion. The WD is initialized at a hot surface temperature post-mass stripping, meant to represent a newly-formed WD at the top of its cooling track. We therefore model tidal effects in the younger WD, assuming the companion WD already exists. If tidal heating is not implemented, the WD cools monotonically. The binary system evolves only due to the emission of GWs. The tidal backreaction of tides on the orbit is not implemented, because it is subdominant (Fuller and Lai, 2012; Burdge et al., 2019a). We initialize the binaries at a range of initial orbital periods, which represents the birth period of the DWD binary, i.e. when the younger white dwarf formed. It also corresponds to the post-CE period of the binary, as these DWDs likely went through common envelope evolution (e.g., Nelemans and Tout, 2005).

3.3.1 WD spin-up

We assume that the WD is rigidly rotating and therefore has a constant Ω_s from surface to core (the validity of this assumption is discussed in Appendix 3.A). Fuller

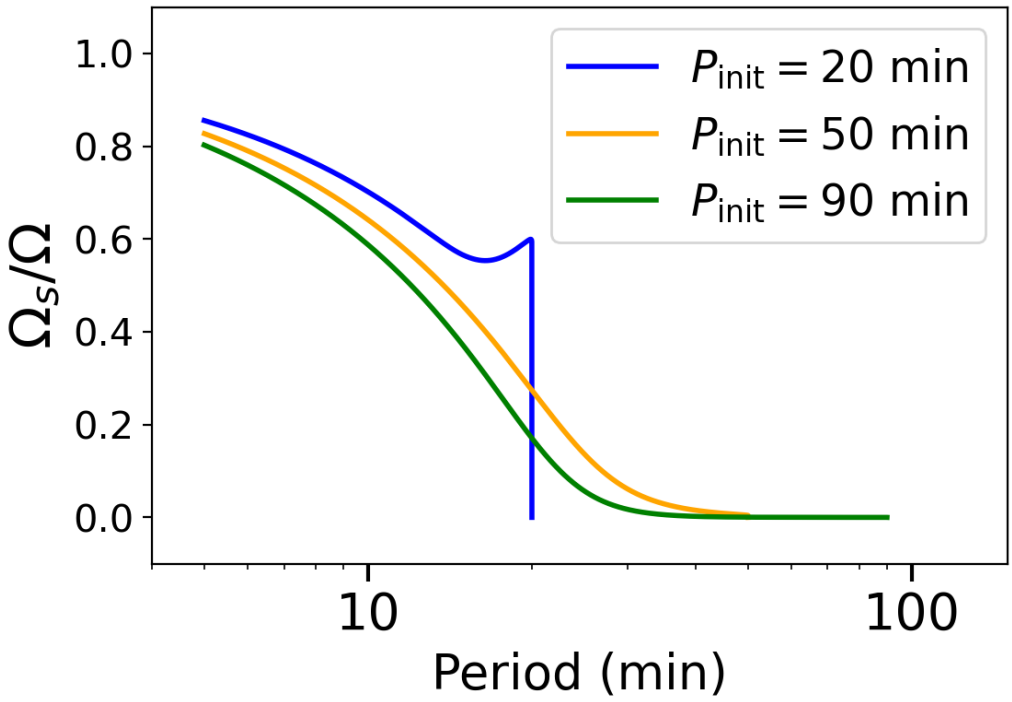


Figure 3.1: Evolution of the spin frequency Ω_s in units of the orbital frequency Ω as a function of the orbital period, due to tidal synchronization. The WDs start with Ω_s = 0. The WD mass is fixed at $0.35 M_\odot$ and WD models start evolution at the same temperature, but in a binary with different initial orbital period. The companion mass is fixed at 0.3 $M_\odot$.

and Lai (2013) finds that the tidal torque $\dot{J}_z$ can be written as

$$\dot{J}_z = T_0 F(\omega). \tag{3.5}$$

Here, $T_0 = GM_2^2 R^5/a^6$ and represents how the magnitude of the tidal forcing scales with the binary system parameters. $F(\omega)$ quantifies the strength of the excited wave and is determined by solving for the waveform of tidally-excited gravity waves at various frequencies. The numerical solver developed in Fuller and Lai (2013) calculates the waveform by solving the equations of stellar oscillation with a tidal forcing term, assuming an outgoing boundary condition for the wave. For our WD models of varying mass, we calibrated $F(\omega)$ by running the solver on `MESA` profiles saved at various ages. We found that $F(\omega)$ approximately scales as

$$F(\omega) = \hat{f}\hat{\omega}^7 \tag{3.6}$$

where $\hat{\omega}$ is ω in units of $\sqrt{GM/R^3}$ and $\hat{f}$ is a function of WD mass and age. This power-law scaling is slightly steeper than that found in Fuller and Lai (2013), where

$F(\omega) = \hat{f}\hat{\omega}^6$. However, the values of $\hat{f}$ are similar, and increase as the WD ages. We implement an interpolation of $\hat{f}$ into `MESA`, interpolating as a function of WD mass and age. As a rough estimate, $\hat{f} \approx \hat{f}_0 t_{\rm age}^{0.4}$ where $t_{\rm age}$ is the age of the WD up to ≈ 1 Gyr and $\hat{f}_0 = 3 \times 10^{-6}$ for a 0.35 $M_\odot$ WD. $\hat{f}_0$ is larger (smaller) by a factor of ≈ 3 for a 0.45 (0.25) $M_\odot$ WD.

Given the tidal torque, the spin-up rate of Ω_s is

$$\dot{\Omega}_s = \frac{\dot{J}_z}{I} = \frac{T_0 \hat{f} \hat{\omega}^7}{I} \tag{3.7}$$

where I is the moment of inertia of the WD. Eqs. 3.1 and 3.7 are coupled and can be numerically solved for Ω_s and ω during the `MESA` simulation. We assume the WD starts with $\Omega_s = 0$ at some orbital frequency Ω, then allow the system to evolve. The WD cools, and the binary inspirals to closer separations/higher orbital frequencies due to the emission of GWs.

The tidal spin-up is shown in Fig. 3.1 for a WD of 0.35 $M_\odot$ starting at orbital periods of 20, 50 and 90 min. The WD's spin becomes synchronized with the orbit at short orbital periods ($\Omega_s/\Omega \rightarrow 1$). By the time the binaries are at periods $\lesssim 30$ min, the binaries starting at 50 and 90 min are in the synchronizing regime where $\dot{\Omega}_s \approx \dot{\Omega}$. The WD starting in a binary at 20 min spins up very rapidly at first because the tidal torque is strong and it is in the short-period regime where synchronization would be expected. However, the young WD's radius also contracts rapidly, leading temporarily to a decreased torque and a dip in the value of Ω_s/Ω, before continuing to approach synchronization at shorter periods.

We find similar behavior for He-core WDs of masses 0.25 to 0.45 $M_\odot$, where the spin becomes increasingly synchronized with the orbit at orbital periods $\lesssim 30$ minutes.

3.3.2 WD heating

With the evolution of spin frequency Ω_s and tidal frequency ω known, the tidal heating can also be estimated. There are two basic steps to the process: **(1)** Calculate the magnitude of the power carried by the outgoing gravity wave, $L_{\rm tide}$. **(2)** Calculate the energy dissipated as heat (therefore lost from the wave) at each mass coordinate m within the WD, between the location of wave excitation and the upper boundary of the wave propagation cavity. The heat is then injected into the WD model via the `MESA` control `s% extra_heat` (with dimension energy/time/mass). The power $L_{\rm tide}$ carried by the wave in the corotating frame of the WD (for the dominant m =

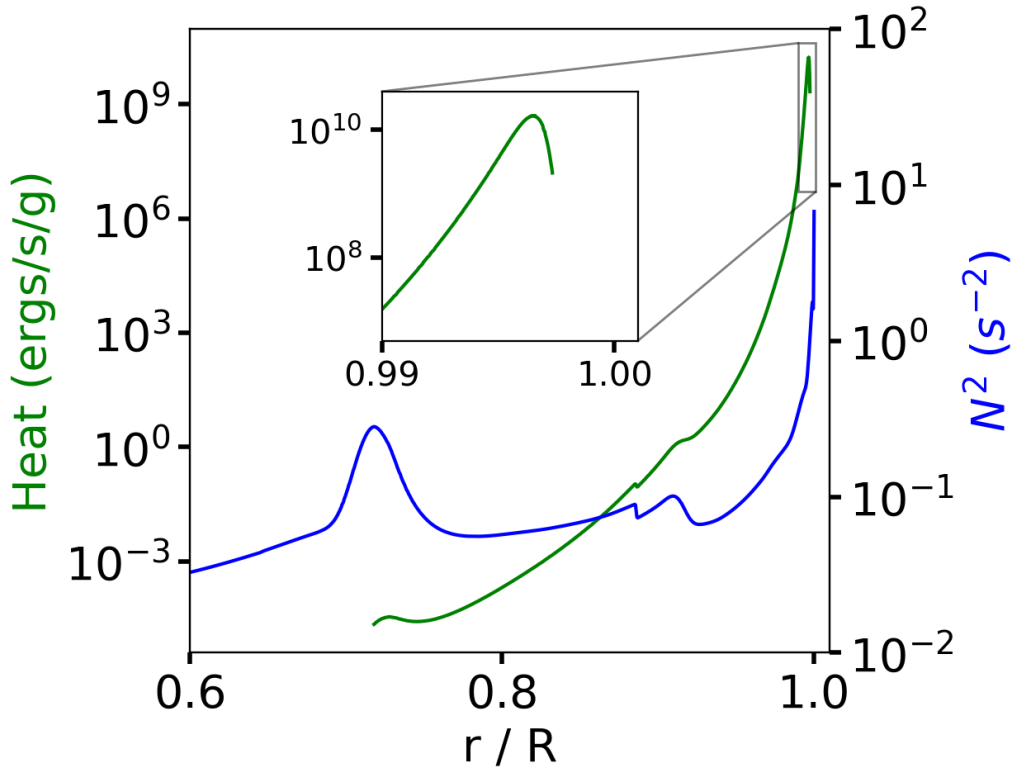


Figure 3.2: Gravity wave excitation in the outer region of a 0.35 $M_\odot$ WD, plotted versus the radius r. The outgoing wave is assumed to originate at the bump in the Brunt–Väisälä frequency squared N^2 (blue curve) corresponding to the core-envelope composition gradient. Heating due to wave dissipation (green curve) only takes place at exterior locations to the composition gradient. This snapshot is shown for an orbital period of 14.3 minutes, and a companion mass of 0.3 $M_\odot$.

2 component of the tidal response) is

$$L_{\rm tide} = \frac{\omega}{2} \dot{J}_z = \frac{\omega}{2} T_0 F(\omega) \simeq \frac{\omega}{2} T_0 \hat{f} \hat{\omega}^7. \tag{3.8}$$

The next step is to calculate the energy dissipated as heat in each cell of the model as the traveling wave propagates outward. In practice, the gravity wave never reaches the surface of the WD because its energy is either dissipated as heat or the wave reaches the end of its propagation cavity, where either $\omega^2 > L_l^2$ or $\omega^2 > N^2$. Moving outward from the excitation location, energy is removed from the wave via two dissipative mechanisms: nonlinear wave breaking and damping due to radiative diffusion. The decrease in $L_{\rm tide}$ over over a cell of mass dm, $dL_{\rm tide}/dm$, is the power per unit mass deposited in a cell, and thus the necessary value for `s% extra_heat`.

If radiative damping alone is included,

$$\frac{dL_{\rm tide}}{dm} = -\frac{L_{\rm tide}}{m_{\rm damp}}\,, \tag{3.9}$$

where $m_{\rm damp}$ is the characteristic mass scale for damping. This is related to the wave damping length scale $h_{\rm damp}$ by

$$m_{\rm damp} = 4\pi\rho r^2 h_{\rm damp} \tag{3.10}$$

and the length scale for thermal diffusion is

$$h_{\rm damp} = v_g / \left(k_r^2 K\right) \tag{3.11}$$

where $v_g \approx \omega/k_r$ is the group velocity of the wave, ρ is the mass density, and K is the thermal diffusivity (e.g., Fuller, 2017). K is given by

$$K = \frac{16\sigma_{\rm SB} T^3}{3\rho^2 \kappa c_p}, \tag{3.12}$$

where $\sigma_{\rm SB}$ is the Stefan–Boltzmann constant, T is internal temperature, κ is the effective opacity (which includes thermal conduction), and c_p is specific heat at constant pressure.

We assume radiative damping always operates. In contrast, nonlinear wave breaking is assumed to only occur when the wave reaches a large enough radial displacement ξ_r such that $|\xi_r||k_r| \geq 1$. See Appendix 3.B for the calculation of ξ_r. We find that wave breaking only occurs in simulations at orbital periods $\lesssim 15$ min, with radiative damping providing all the dissipation at longer periods. Similarly, we define $m_{\rm break}$ as the characteristic mass scale for breaking, related to characteristic length scale $h_{\rm break}$ by

$$m_{\rm break} = 4\pi\rho r^2 h_{\rm break}, \tag{3.13}$$

with $h_{\rm break}$ estimated to be one pressure scale height. Therefore, our full expression for the power deposited per unit mass is

$$\frac{dL_{\rm tide}}{dm} = -\frac{L_{\rm tide}}{m_{\rm damp}} - \frac{L_{\rm tide}}{m_{\rm break}}\Theta(|\xi_r||k_r| - 1) \tag{3.14}$$

where Θ is simply a Heaviside step function such that wave breaking only contributes when $|\xi_r||k_r| \geq 1$.

Figure 3.2 shows a radial profile for the heat deposited in the outer region of a WD model at a short orbital period. The outgoing wave is assumed to originate at the bump in N^2, so heating only exists exterior to this point. For this snapshot, dissipation is only due to radiative damping. The heating per unit mass reaches a maximum close to the surface of the WD, where N^2 is large and the density is low. This behavior is typical for our simulations.

We remove energy from the wave and deposit it as heat by applying Eq. 3.14 until either $L_{\rm tide}$ is zero from losses or the end of the gravity wave propagation cavity is reached. In the first case, the energy injected into the WD $L_{\rm heat}$ is equal to $L_{\rm tide}$. In the second case, $L_{\rm heat}/L_{\rm tide}$ will be less than unity, meaning that not all the wave's energy is deposited inside our model. If this fraction is significantly less than unity, the wave carries a significant amount of energy when it reaches the edge of the propagation cavity and likely reflects. In this case, the assumption that the tidal response is in the traveling wave regime breaks down. Instead, standing wave g-modes of discrete frequencies will likely be excited (Fuller and Lai, 2011; Yu et al., 2021).

Traveling wave regime: validity

We do not model the standing wave regime, but instead estimate for which models our traveling wave assumption breaks down. For 3 different WD masses, Figs. 3.3, 3.4, 3.5 show a colormap of $L_{\rm heat}/L_{\rm tide}$ versus the parameter space of initial period and orbital period. A given simulation has a fixed initial period, but decreases in period, starting on the red line and moving horizontally right to left. A brighter color corresponds to $L_{\rm heat}/L_{\rm tide}$ being closer to unity and the traveling wave assumption justified. When $L_{\rm heat}/L_{\rm tide}$ is close to zero, with a darker shading, our model likely breaks down. As a model moves from right to left on the plot, the simulation may encounter regions where the traveling wave regime is more or less appropriate. The most self-consistent simulations occur for horizontal slices that are completely yellow in color, where all the wave power is always deposited. When $L_{\rm heat}/L_{\rm tide} < 1$, the wave is either encountering the edge of the cavity due to ω^2 rising above L_l^2 (unhatched, "Lamb cavity") or ω^2 rising above N^2 (hatched, "Brunt cavity").

There are several trends evident in Figs. 3.3, 3.4, 3.5. The hatched "Brunt cavity" region occurs for cool WDs in binaries initialized at long orbital periods, because

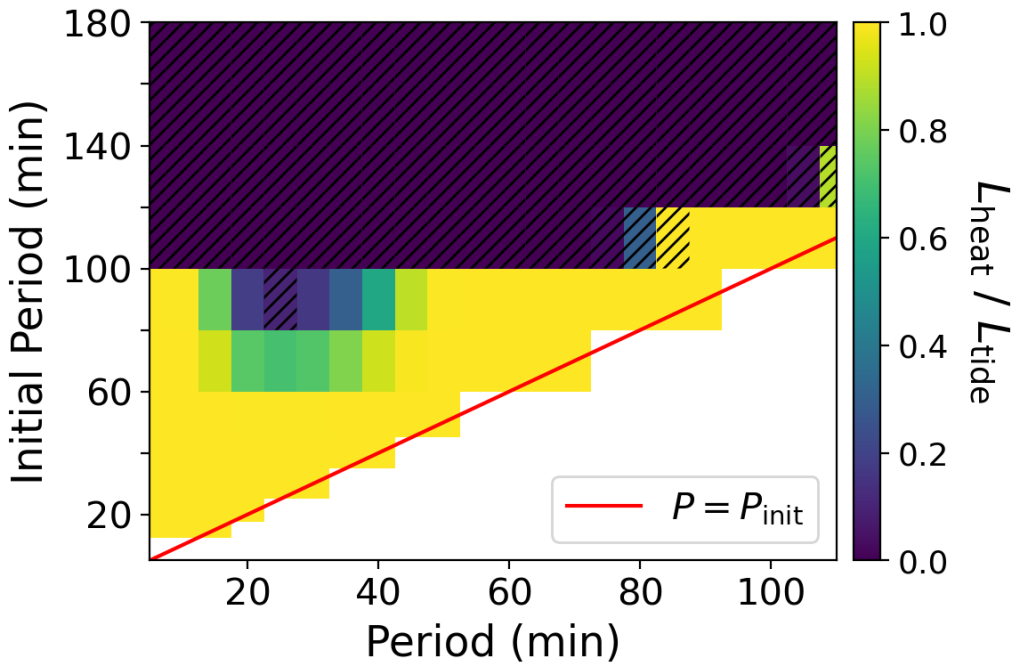


Figure 3.3: The fraction of the wave energy $L_{\rm tide}$ that is deposited as heat $L_{\rm heat}$ (color shading) within evolving WD models of 0.25 $M_\odot$ (with a 0.3 $M_\odot$ companion). A given simulation starts on the red line and moves from right to left horizontally, towards shorter orbital periods as inspiral occurs. If $L_{\rm heat}/L_{\rm tide}$ is less than unity, the wave is encountering the upper edge of the propagation cavity, where the wave frequency either rises above the Lamb frequency (unhatched region) or the Brunt–Väisälä frequency (hatched region). The traveling wave approximation is good in the yellow regions of this diagram.

WDs with $T_{\rm eff} \lesssim 10,000K$ develop a deep surface convective zone with $N^2 < 0$. Less massive He-core WDs cool faster and have slower orbital decay, meaning that the hatched region is pushed to lower initial periods for lower mass WDs.

The darkest unhatched “Lamb cavity" regions tend to occur for orbital periods of ≈15 to 30 min, where the tidal frequency ω is largest, which moves the cavity’s outer boundary inward and also increases the lengthscale for damping (Eq. 3.11). However, at shorter periods, two effects can occur: first, the WD temperature begins to increase due to tidal heating, meaning that radiative damping becomes stronger, which in turn makes more heat dissipate out of the wave before it reaches the cavity’s edge. Second, the increasing power carried by the wave means wave breaking is more likely to occur and dissipate more energy within the cavity. These effects are responsible for the yellow region at short orbital periods, where models are nominally again in a traveling wave regime, despite our traveling wave model

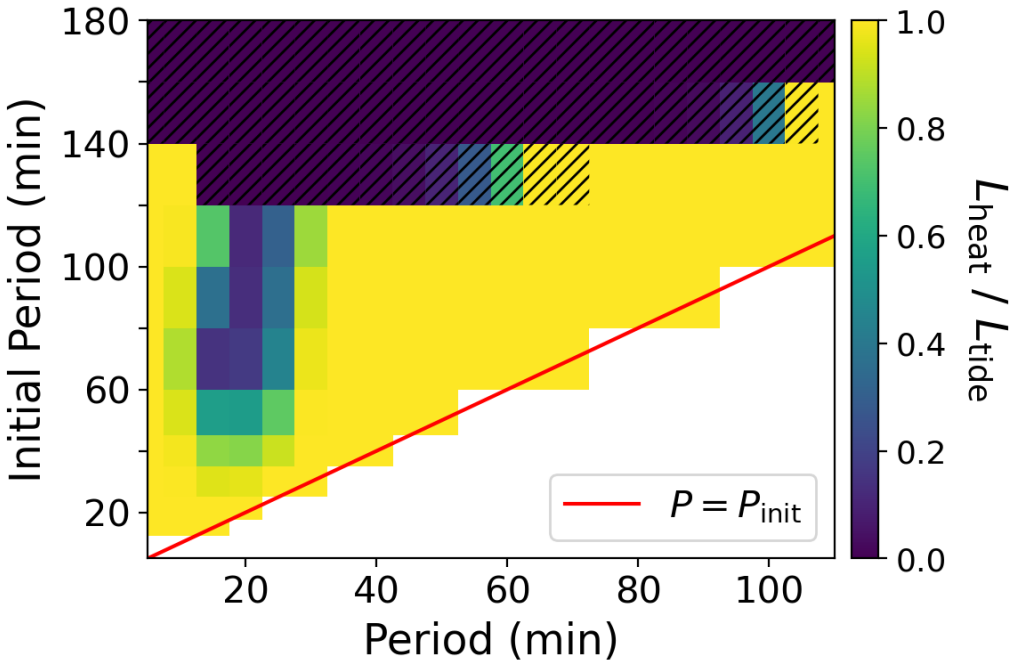


Figure 3.4: Same as Fig. 3.3, but for a 0.35 $M_\odot$ WD model in a binary.

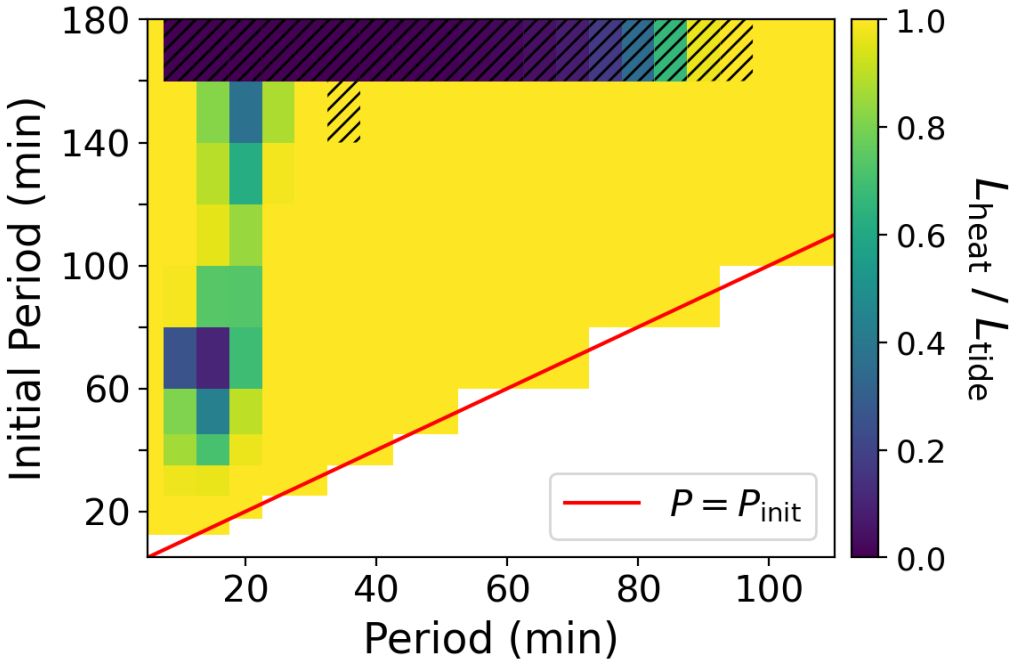


Figure 3.5: Same as Fig. 3.3, but for a 0.45 $M_\odot$ WD model in a binary.

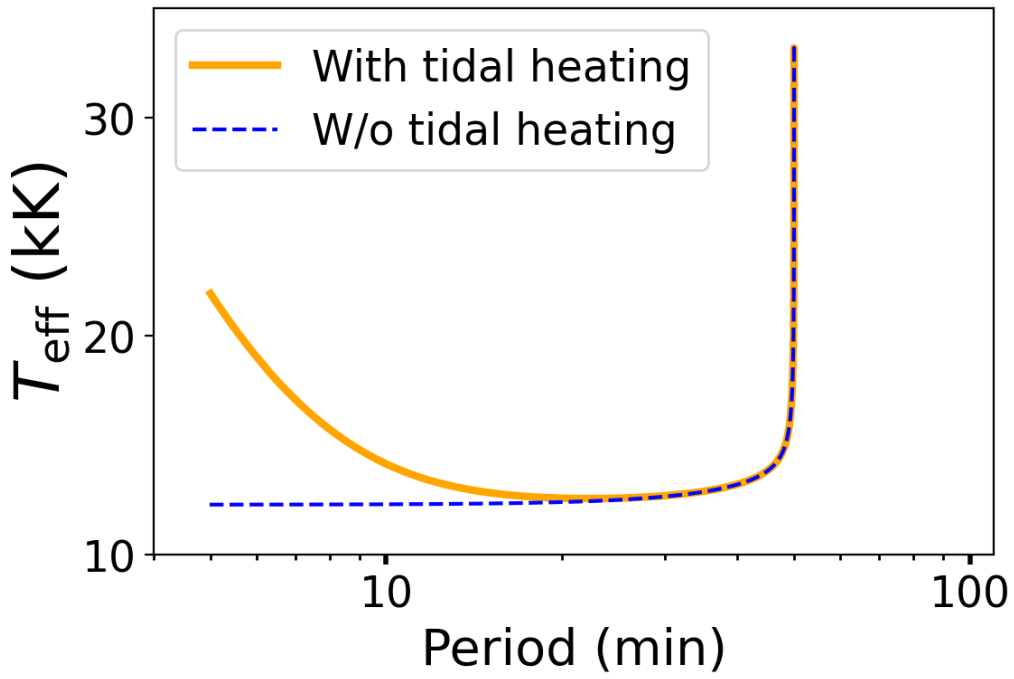


Figure 3.6: The effective temperature for a 0.25 $M_\odot$ WD, with and without tidal heating, as a function of orbital period. The model moves from right to left towards shorter orbital periods as the binary inspirals. The companion mass is fixed at 0.3 $M_\odot$.

potentially failing at earlier periods in their evolution. At a given period, WDs are cooler for a longer initial orbital period, and radiative damping will be weaker, explaining why, in general, colors are darker moving vertically upward within the unhatched “Lamb cavity" region.

In general, we find that there is still a fairly large parameter space where the traveling wave regime is valid. WDs in binaries with shorter initial orbital periods are more likely to be in this regime. Higher mass WDs have a wider range of initial orbital periods where the traveling wave approximation is valid. Previous work has demonstrated that most DWDs are likely born from the common envelope channel at orbital periods shorter than 2 hours (Brown et al., 2016), and many at less than 1 hour (Scherbak and Fuller, 2023). Therefore, the traveling wave regime is likely a good approximation for the evolutionary histories of some systems. In the remainder of this work, we run models by implementing the traveling wave response and only depositing energy within the propagation cavity, but discuss which models are most valid.

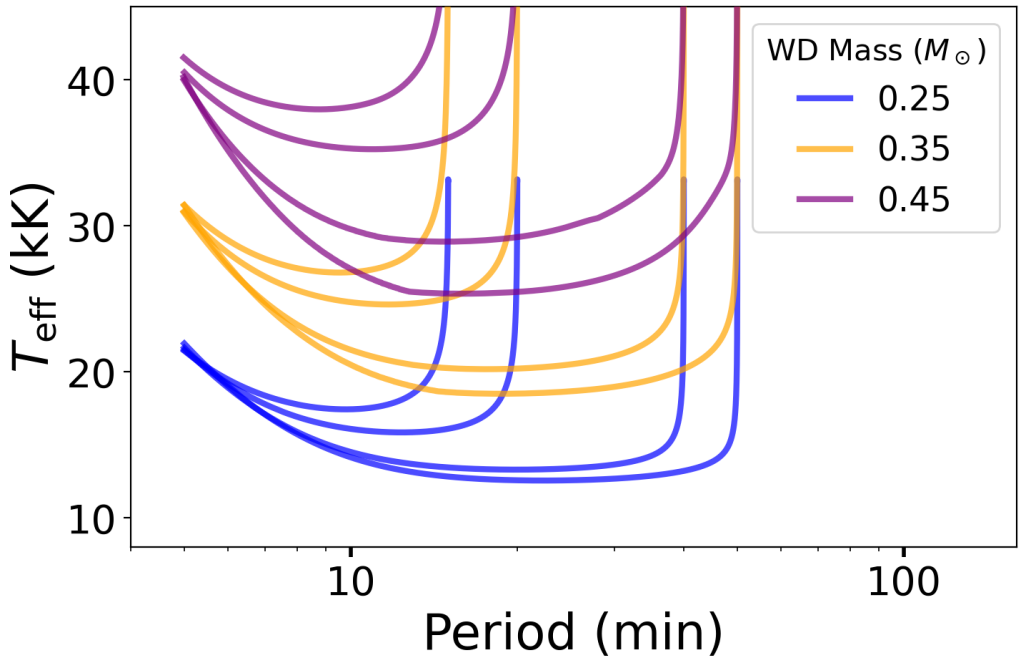


Figure 3.7: The evolution of effective temperature versus orbital period for a grid of WD models undergoing tidal heating. Models of same color are of the same mass. The models begin evolution in a binary at orbital periods of 15, 20, 40, and 50 min. The companion mass is fixed at 0.3 $M_\odot$.

3.4 Tidal heating: simulations and observed systems

Fig. 3.6 demonstrates the effect of tidal heating on a WD's surface temperature as the DWD binary evolves from 50 min to shorter orbital periods. Note from Fig. 3.3 that this simulation (WD mass 0.25 $M_\odot$, initial period 50 min) is likely always in the traveling wave regime. The magnitude of the heating increases with decreasing orbital period because the tidal potential driving the wave is stronger. The temperature of the primary WD is predicted to be much higher at very short periods (a difference of >10,000 K at an orbital period of 5 min) compared to the case where tidal heating is neglected. We find that there is a negligible increase in the radii of our tidally heated models. Significant heating begins at periods $\lesssim$ 15 minutes, corresponding to a gravitational wave inspiral time $\lesssim$ 2 Myr for the component masses. Thus, the heating generally occurs over a short timescale compared to the WD's age. In the following, we present similar results for a grid of WD models.

Fig. 3.7 shows tidal heating for a grid of WDs of different masses initialized in binaries of different initial orbital periods. For simplicity, we show initial orbital

Table 3.1: Properties of the WD binaries we model.

Name	$P_{\rm orb}$ (min)	M_1 ($M_\odot$)	M_2 ($M_\odot$)	$T_{\rm eff,1}$ (K)	$T_{\rm eff,2}$ (K)	$P_{\rm birth}$ (min)
ZTF J1539+5027[1]	6.91	$0.21^{+0.014}_{-0.015}$	$0.61^{+0.017}_{-0.022}$	$< 10,000$	$48,900 \pm 900$	not modeled
ZTF J2243+5242[2]	8.80	$0.323^{+0.065}_{-0.047}$ (LC)	$0.335^{+0.052}_{-0.054}$ (LC)	$26,300^{+1700}_{-900}$ (SED)	$19,200^{+1500}_{-900}$ (SED)	10 - 26
		$0.317^{+0.074}_{-0.074}$ (Spect)	$0.274^{+0.047}_{-0.047}$ (Spect)	$26,520^{+130}_{-130}$ (Spect)	$19,670^{+100}_{-100}$ (Spect)	
SDSS J0651+2844[3,4,7]	12.75	$0.247^{+0.015}_{-0.015}$	$0.49^{+0.02}_{-0.02}$	$16,530 \pm 200$	$8,700 \pm 500$	20 - 30
ZTF J0538+1953[5]	14.44	$0.45^{+0.05}_{-0.05}$	$0.32^{+0.03}_{-0.03}$	$26,450 \pm 725$	$12,800 \pm 200$	36 - 44
SDSS J0935+4411[6,7]	19.80	$0.312^{+0.019}_{-0.019}$	$0.75^{+0.24}_{-0.23}$	$21,660 \pm 380$	n/a	22 – 41

Parameters for all the systems we model, including the orbital period, $P_{\rm orb}$, the masses of the two components, M_1 and M_2, and the effective surface temperature of the components, $T_{\rm eff,1}$ and $T_{\rm eff,2}$. Measured parameters are from Burdge et al. (2019a)[1], Burdge et al. (2020c)[2], Brown et al. (2011)[3], Hermes et al. (2012)[4], Burdge et al. (2020b)[5], Kilic et al. (2014)[6], Brown et al. (2016)[7]. The last column is our estimate of the birth period, the post-common envelope orbital period when the younger WD formed (see text for the analysis).

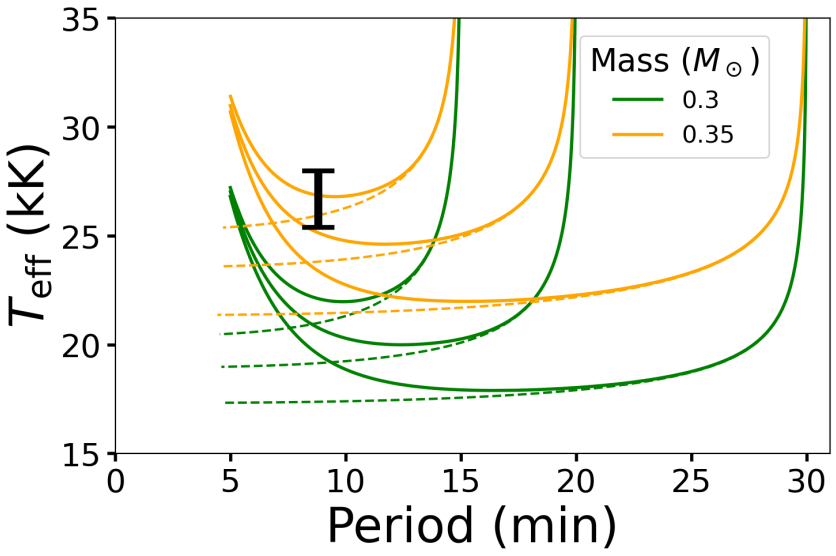


Figure 3.8: Effective temperature versus orbital period for a grid of WD simulations, compared to the observed temperature (black errorbar) of ZTF J2243's hotter component (mass $\approx 0.32 M_\odot$). The models vary in WD mass (differing colors) and initial orbital period of the system, whereas companion mass is fixed at $0.3 M_\odot$. Dashed lines are models with the same parameters, but have tidal heating turned off.

periods of 15 to 50 minutes, although our full grid ranges from 15 to 200 minutes. For the 0.35 and 0.45 $M_\odot$ models initialized at 50 minutes, the traveling wave regime starts to break down (this is the source of the kink for the bottom-most 0.45 $M_\odot$ curve at about 13 minutes, where, from Fig. 3.5, there is a change from a small fraction of $L_{\rm tide}$ being deposited to a larger fraction being deposited). However, the traveling wave regime is likely a good approximation for the other models in this plot.

The power carried by the wave, $L_{\rm tide}$, scales with WD mass approximately as $M_1^{17/6}$ (Fuller and Lai, 2013), so more massive WDs experience greater heating at short periods and have higher temperatures, regardless of their initial orbital period. In addition, more massive WDs have smaller radii and therefore the effect of tidal heating on $T_{\rm eff}$ will be more pronounced.

We also compare our quantitative predictions for $T_{\rm eff}$ to observed ultrashort-period double white dwarf systems. The properties of these systems are summarized in Table 3.1. Note also that these are the 5 detached shortest-period LISA verification binaries systems discussed in Kupfer et al. (2023). In this work, we only simulate tidal heating in the younger, more recently-formed WD, treating the other as a point

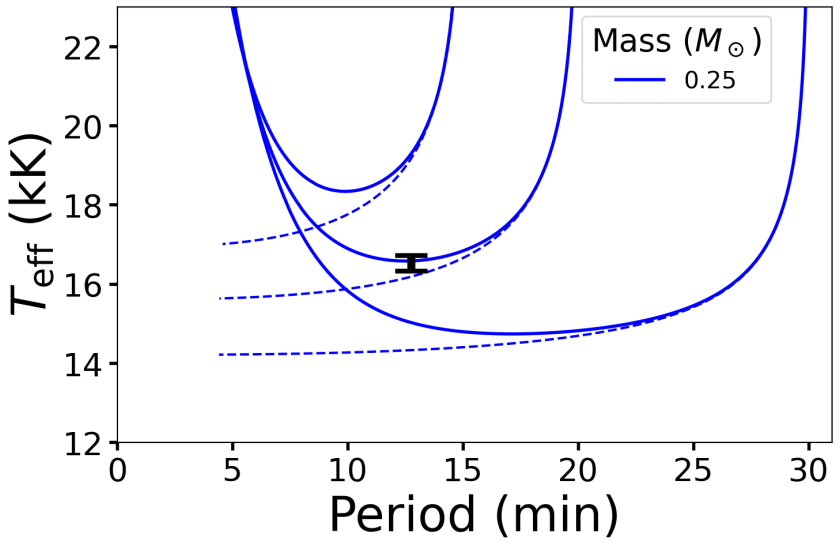


Figure 3.9: Similar to Fig. 3.8, but for SDSS J0651. The mass of the hotter component, which we fit to, is $\approx 0.25 M_\odot$. The companion mass is fixed at $0.5 M_\odot$.

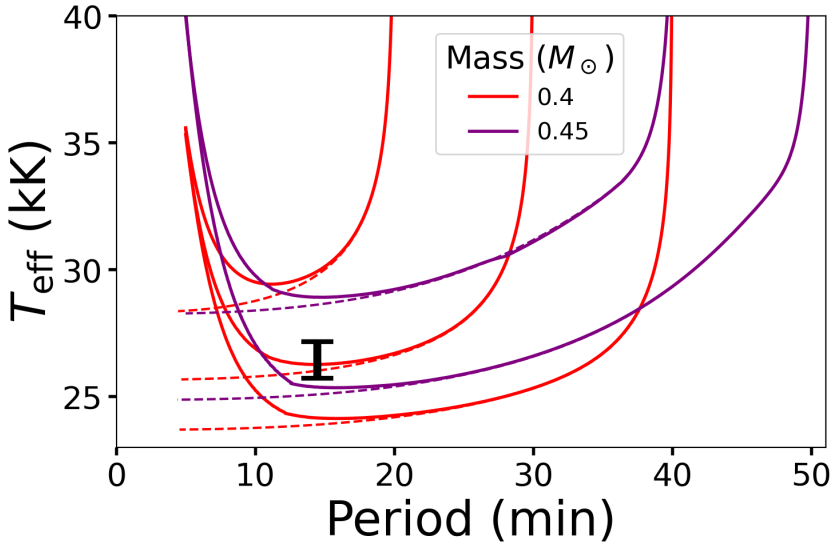


Figure 3.10: Similar to Fig. 3.8, but for ZTF J0538. The mass of the hotter component, which we fit to, is $\approx 0.45 M_\odot$. The companion mass is fixed at $0.3 M_\odot$.

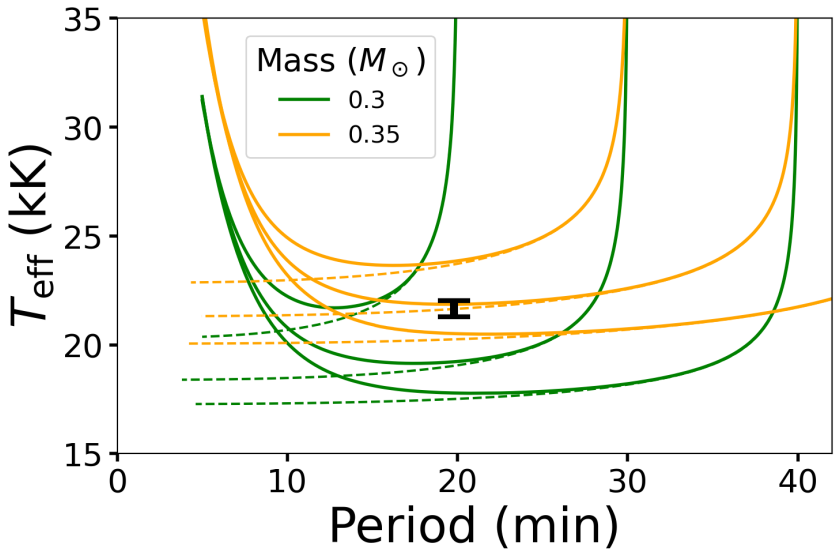


Figure 3.11: Similar to Fig. 3.8, but for SDSS J0935. The mass of the hotter component, which we fit to, is $\approx 0.31 M_\odot$. The companion mass is fixed at $0.75 M_\odot$.

mass. If only one WD has a mass consistent with a He-core WD, we assume that is the younger because its progenitor star likely evolved second (although this may not always be true). If there are two He-core WDs, we assume the hotter one is the younger. In Table 3.1, we define M_1 as the WD we assume is younger and for which we are modeling tidal heating.

Figs. 3.8 - 3.11 show a comparison of our WD models, with and without tidal heating turned on, to the observed $T_{\rm eff}$ of systems in Table 3.1. We do not seek to exactly find the best set of models that match to the observed characteristics, but compare relevant models with and without tidal heating and quantify the difference between them.

In Fig. 3.8, showing the 8.8 minute system ZTF J2243, the models that best match the observed $T_{\rm eff}$ of the WD primary correspond to 0.35 $M_\odot$ WDs. Both simulations with and without tidal heating can match the data - for instance, the two 0.35 $M_\odot$ models starting at a 15 min period are consistent with the error bar. Models starting at 30 min or greater are not hot enough to match the data, even with tidal heating turned on. Therefore, a WD that cools sufficiently is unable to be heated by tides to the observed hot temperature ($\approx$ 26,000 K). Comparing the hottest 2 pairs of 0.35 $M_\odot$ models (the top 2 pairs of orange curves), the increase in luminosity is about 20% with tidal heating implemented. Thus, tidal heating is a relatively small fraction of the WD primary's energy output.

Figs. 3.9 and 3.10 show similar results for the 12.8 minute system SDSS J0651 and 14.4 minute system ZTF J0538. In both cases, the difference between pairs of models with and without tidal heating at the observed orbital period is relatively small, with the change in $T_{\rm eff}$ <1,000 K and the change in luminosity between 5-10%. For J0651, models starting at 20 min match well, but models starting at 15 minutes are too hot and models starting at 30 minutes are too cool. For J0538, models starting at 30 minutes match well, but models starting at 20 minutes are too hot and models starting at 40 minutes are too cool. Accounting for tides, therefore, does not appear to greatly alter the parameter space of initial periods that can replicate these systems.

Finally, Fig. 3.11 shows the 19.8 minute system SDSS J0935, the longest period binary we compare to, and demonstrates that there is little difference between tidally heated and non-tidally heated models at orbital periods near 20 min.

Note that the models in Figs. 3.8-3.11 have short initial periods and are therefore mostly in the traveling wave regime. An exception is the higher-mass, longer initial period (50 min) models in Fig. 3.10, for which our treatment may start to break down. Models born at longer orbital periods than plotted are likely in the standing wave regime, and are unlikely to undergo significantly more heating compared to those in the traveling wave regime. Therefore, since some traveling wave models already fall below the observed $T_{\rm eff}$, the standing wave models are unlikely to further the space of models that can match the observed $T_{\rm eff}$ of these four hot WD primaries.

We do not show a plot for the 7-minute binary ZTF J1539, for which the He-WD component has a $T_{\rm eff}$ of <10,000 K. The history of this system is uncertain, with mass transfer from the He-WD to its companion potentially playing a role (Burdge et al., 2019a). It may have also formed via the stable mass transfer channel rather than the CE channel (Li et al., 2019b; Chen et al., 2022). Our models tend to predict significantly higher $T_{\rm eff}$ than 10,000 K, regardless of initial orbital period, meaning that our traveling-wave models are incompatible with the low observed temperature. However, we note that if a WD were to cool to <10,000 K the tidal response is likely in the standing wave regime, which we do not attempt to model but will involve resonances with g-modes. In our traveling wave models, the tidal power is deposited near the surface of the WD. In the standing wave regime, the tidal heating power could be smaller, and the location of heat deposition could potentially be deeper inside the WD. This could allow for much cooler WDs.

3.5 Discussion

3.5.1 Implications for common envelope efficiency

Our analysis shows that, for the systems in Table 3.1, tides are not transforming a cool WD into a hot one, but instead are only slightly heating already hot WDs. Tidal heating does not significantly alter estimates of the initial orbital period of these ultrashort period DWD binaries. To better understand the formation history of these systems, it is reasonable to use a grid of non-tidally heated models, with varying mass and H envelope mass, to estimate the post-common envelope (CE) periods of these binaries. We performed similar analysis for several DWD systems in Scherbak and Fuller (2023). We follow the same procedure and only briefly outline it here.

We fit a grid of `MESA` models to the observed radii and $T_{\rm eff}$ of the WD primary to estimate the birth period. As this is also the post-CE period, we thereby obtain the post-CE orbital energy $E_{\rm orb,\,f}$. We estimate the pre-CE orbital energy $E_{\rm orb,\,i}$ and the envelope binding energy $E_{\rm bind}$ using a grid of red giant progenitor models whose core mass matches the observed He-WD mass. We then combine these to estimate the common envelope efficiency $\alpha_{\rm CE}$, defined by

$$\alpha_{\rm CE} = \frac{E_{\rm bind}}{E_{\rm orb,\,f} - E_{{\rm orb},i}}. \tag{3.15}$$

Our estimates of the birth period are shown in the rightmost column of Table 3.1. The birth periods are quite short, significantly less than 1 hour, in agreement with the conclusion of Brown et al. (2016) that most low-mass DWD binaries are born at short orbital periods. It also means that the DWD binaries we model are young.

Fig. 3.12 shows the range of $\alpha_{\rm CE}$ for 10 WD binaries modeled in Scherbak and Fuller (2023) and the 4 binaries discussed in Figs. 3.8-3.11. The previously-modeled WD binaries are at longer orbital periods > 20 min. The best-fit range for $\alpha_{\rm CE}$ using these previous 10 systems is from about 0.15 to 0.5 and overlaps well with 3 of the 4 new systems. For the most part, we find that these ultrashort period binaries, which we previously did not model because of the uncertainty of the role of tidal heating, are consistent with a low common envelope efficiency.

An exception is ZTF J0538, which has an even lower associated range of $\alpha_{\rm CE}$ due to its short post-CE orbital period and higher mass WD, which means the progenitor was more evolved up the red giant branch with a lower $E_{\rm bind}$. However, the mass of the WD primary ($0.45^{+0.05}_{-0.05} M_\odot$) is quite large for a He WD, and it could instead correspond to a low-mass CO-core WD. This requires a significantly

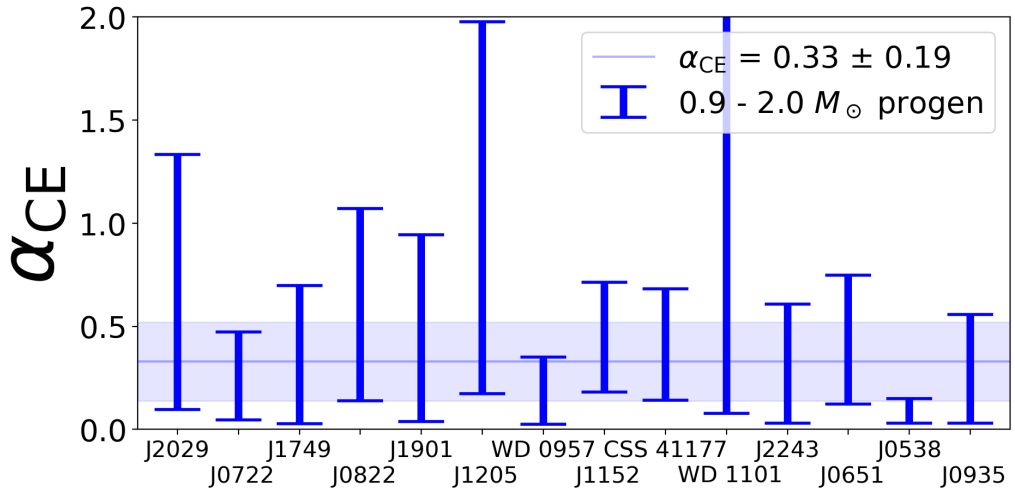


Figure 3.12: Values of α_{CE} using a grid of He WDs to model the WD primary and assuming the progenitor is a red giant star from 0.9 - 2.0 $M_\odot$. The horizontal line and shaded region denotes a least squares fit to the ensemble of systems, excluding the rightmost 4 (the binaries discussed in this work). The other 10 systems used for the fit are longer period WD binaries modeled in Scherbak and Fuller (2023). The inferred values of α_{CE} for the short-period binaries in this work are consistent with expectations, apart from J0538 (see text for explanation).

different evolutionary history, likely involving a He-burning sdB phase following the CE (Han et al., 2003; Xiong et al., 2017). This would entail a much longer evolution time following the CE event, and hence a longer post-CE orbital period than that listed in Table 3.1, and a larger value of α_{CE} than that shown in Figure 3.12.

3.5.2 Application to CO WDs

This work has focused in tidal heating in He-core WDs, where the companion is either a He or CO WD. A discovery of a short-period binary where both WDs have CO cores would motivate modeling of tidal heating in a CO WD as well. The excitation of outgoing gravity waves in a CO WD (Fuller and Lai, 2012) is similar to the He WD case (Fuller and Lai, 2013), although the primary location of the gravity wave excitation is instead at the carbon-helium composition gradient. Therefore, most of our modeling can be directly extended to `MESA` simulations of CO WDs.

The most significant difference would likely be the parametrization of the tidal torque through $F(\omega)$ (Eqs. 3.5 and 3.6), which we could determine by running the numerical waveform solver on CO WD models. In this work, we found smaller values of $F(\omega)$ compared to those in Fuller and Lai (2013), which used older He

WD models. If this trend holds true for CO WDs as well, the results of Fuller and Lai (2012) will be changed somewhat. In particular, the critical period when spin synchronization begins may be shorter, and the magnitude of tidal heating may be higher, than presented in Fuller and Lai (2012). Overall, we expect similar qualitative behavior for CO WD models, with tidal heating becoming significant at periods $\lesssim$ 10-20 min and becoming the dominant source of luminosity pre-merger.

3.5.3 Potential future observations

The discovery of more ultrashort-period double WD binaries would be invaluable to add to our comparison sample. The enhancement in temperature due to tidal heating increases for shorter orbital periods, so systems with orbital periods < 10 min are better for distinguishing tidally heated and non-tidally heated models. Specifically, values of $T_{\rm eff}$ tend to converge for a given WD mass (Fig. 3.7) at the shortest orbital periods pre-mass transfer, which would be a testable prediction. In addition, discovering more systems at similar periods to the 7-minute binary ZTF J1539 would shed light on whether ZTF J1539's cool component is an outlier, perhaps due to its low mass, or if there are additional cool WDs for which the tidal heating may be more complicated than modeled here.

In this work, we have only compared to measured values of $T_{\rm eff}$. Measured spin values would be another way to test our models, which predict spin synchronization as a function of orbital period. In some cases, the projected rotation speed, $v \sin i$, could potentially be measured. For complete synchronization, we expect

$$v \sin i \simeq 200\,{\rm km\,s^{-1}} \left(\frac{R_{\rm WD}}{2\times10^9\,{\rm cm}}\right)\left(\frac{P_{\rm orb}}{10\,{\rm min}}\right)^{-1} \tag{3.16}$$

for an edge-on system. This could possibly be measured from high-resolution spectra resolving the non-LTE line cores of DA WDs, or helium lines of DB or DAB WDs.

3.6 Conclusion

In this paper, we have modeled tidal heating in double WD binary `MESA` simulations, where the dynamical tidal excitation occurs within helium-core WDs and the companion is a point mass. We approximate the tidal response as traveling gravity waves that are damped in the outer layers of the WD. We run a grid of models varying **1**: the mass of the He-core WD M_1 **2**: the mass of the companion M_2 and **3**: the post-common envelope orbital period of the WD binary when the second WD formed.

In our simulations, the binary inspirals to shorter periods due to the emission of gravitational waves. At every time step, we calculate the angular momentum and energy flux carried by the tidally excited waves, which leads to spin-up and heating of the WD. For our grid of WD models, we calibrate the strength of the tidal response using the numerical solver of Fuller and Lai (2013).

The WDs' spins become increasingly synchronized with the orbit at orbital periods $\lesssim 30$ minutes. We model heat deposition in the outer layers of the WD, accounting for damping due to radiative diffusion and nonlinear wave breaking. We self-consistently compute the changing WD structure, heating rate, and heating location. The inner edge of wave propagation is the transition between the He-core and H envelope, and the outer edge is where the wave becomes evanescent. We determine the fraction of the wave's energy which has been deposited before it reaches the cavity's outer edge. If the fraction is low, our traveling wave approximation breaks down and the response will instead likely be a standing wave. Figs. 3.3 - 3.5 demonstrate where the traveling wave response is appropriate. In general, hot and young WDs, corresponding to binaries with short initial orbital periods $\lesssim 2$ hour, are more likely to be in the traveling wave regime. The traveling wave regime extends to longer initial periods for higher mass WDs ($\sim 0.45\ M_\odot$) compared to lower mass WDs ($\sim 0.25\ M_\odot$).

At orbital periods $\gtrsim 20$ min, the WDs follow a cooling track and tidal heating is negligible. However, at shorter orbital periods, the energy flux carried by the tidally excited gravity waves becomes large enough to cause substantial heating. Compared with a non-tidally heated model, the enhancement in $T_{\rm eff}$ can exceed 10,000 K at periods of 5-10 min. When tidal heating dominates, WDs of the same mass tend to converge to similar values of $T_{\rm eff}$, despite differences in their previous cooling history.

We compare our tidal heating models to the five shortest-period double WD systems known, ranging from 8 to 20 min orbital periods. Our tidally heated models that match well to the measurements are likely in the traveling wave regime, but they only cause a mild temperature increase. Both tidally heated and non-tidally heated models are capable of reproducing the measured surface temperatures, but only when starting at a similar range of orbital periods. Therefore, uncertainty in tidal heating does *not* lead to a large uncertainty in the binary's initial period. Since tidal heating is a small fraction of these WDs' luminosities, they are intrinsically hot and young, and they were born at periods $\lesssim 45$ min. The exception to these findings is

ZTF J1539's primary, which is cooler than our tidal heating models would predict, but has caveats involving mass transfer, its formation history, and the role of standing waves at its cool temperature.

Finally, we reconstruct the values of the common envelope (CE) efficiency parameter $\alpha_{\rm CE}$ that can replicate these systems. Since tidal heating does not significantly impact estimates of the initial (post-CE) period of these ultrashort-period binaries, we perform the same analysis as Scherbak and Fuller (2023), which modeled longer period WD binaries. For reasonable assumptions of the progenitor star mass, we find a fairly low value of $\alpha_{\rm CE}$, in the range 0.1 to 0.5, is necessary to form the ultrashort-period systems. These low values of $\alpha_{\rm CE}$ are consistent with those found in Scherbak and Fuller (2023).

Acknowledgments

We are grateful for support from the NSF through grant AST-2205974. JF is thankful for support through an Innovator Grant from The Rose Hills Foundation. We thank the anonymous referee for their useful feedback and suggestions.

Software: MESA (Paxton et al., 2011; Paxton et al., 2013; Paxton et al., 2015; Paxton et al., 2018; Paxton et al., 2019), Python. `MESA` models and files are available in a Zenodo repository (Scherbak and Fuller, 2024).

3.A AM transport

This work has assumed that the WD is rigidly rotating. This requires angular momentum (AM) transport between the location where AM is deposited by the outgoing gravity waves, and the rest of the WD's interior. We have not performed detailed modeling of AM transport in `MESA`. Rather, we have estimated the coupling timescale for AM to be transported by a magnetic dynamo, and compared that to the spin-up timescale of the WD's interior. For coupling from the WD surface at radius R to a location with internal radius r, we define the AM coupling timescale $t_{\rm coup}(r)$ as

$$t_{\rm coup}(r) = \int_r^R dr' \frac{(R - r')}{\nu(r')} \tag{3.17}$$

where ν is the AM diffusivity found in Fuller et al. (2019) which details a modification to the Tayler-Spruit dynamo (Spruit, 2002). It is given by

$$\nu = \alpha^3 r^2 \Omega_s \left(\frac{\Omega_s}{N_{\rm eff}} \right)^2 . \tag{3.18}$$

We use $\alpha \approx 0.25$ (Fuller and Lu, 2022). In calculating ν, we assume that $N_{\rm eff}$ is the full Brunt–Väisälä frequency, as that provides a lower limit on ν and an upper limit on $t_{\rm coup}(r)$. Because our assumption of rigid rotation breaks down for relatively long coupling times, this makes our calculation more conservative.

We define the spin-up timescale $t_{\rm spinup}(r)$ as the timescale to synchronously spin up the layers exterior to r with moment of inertia $I(> r)$. With $\dot{J}_z$ as the full tidal torque as calculated in Eq. 3.5,

$$t_{\rm spinup}(r) = \frac{\Omega I(> r)}{\dot{J}_z}. \tag{3.19}$$

We have found that the coupling timescale is generally less than the spin-up timescale, supporting the assumption of rigid rotation. This assumption is better for lower mass He-core WDs. The assumption of rigid rotation can break down at longer orbital periods $\gtrsim 30$ min, mainly because the spin rate is smaller and hence the AM diffusivity ν is smaller. However, at longer orbital periods, tidal effects are weaker and deviation from rigid rotation will likely not matter, especially for tidal heating. We find at short orbital periods the coupling timescale to be shorter than the spin-up timescale at most internal radii r, and therefore the WD tends to be rigidly rotating when it is rotating closest to synchronization and undergoing the strongest tidal heating.

3.B Calculation of wave breaking

We calculate the radial displacement ξ_r associated with outgoing gravity waves in order to determine when nonlinear wave breaking is likely to occur. Because the power in the wave $L_{\rm tide}$ decreases as the wave moves outwards (Eq. 3.14), $L_{\rm tide}$ is a function of internal radius r. $L_{\rm tide}(r)$ can be related to $\xi_\perp$, the perpendicular displacement, with

$$L_{\rm tide}(r) = 2\sqrt{l(l+1)} \frac{\omega^4 \rho r^3 |\xi_\perp|^2}{N} \tag{3.20}$$

and $\xi_\perp$ and ξ_r are related in the WKB approximation via

$$|\xi_r|/|\xi_\perp| = \sqrt{l(l+1)} \frac{\omega}{N}. \tag{3.21}$$

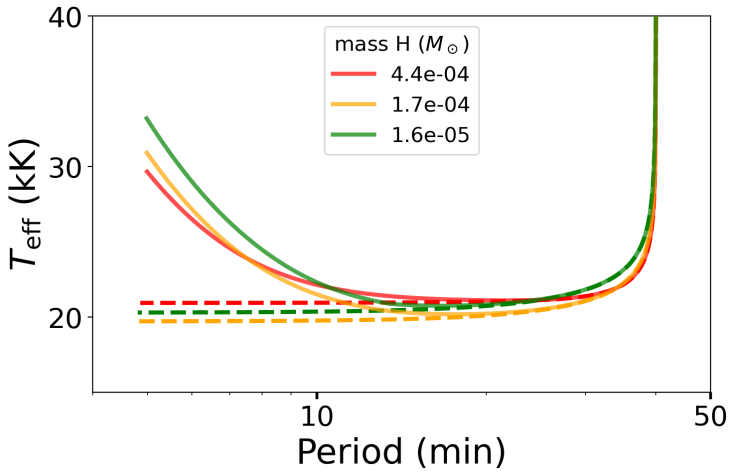


Figure 3.13: The evolution of effective temperature versus orbital period for several WD models undergoing tidal heating, all of total mass 0.35 $M_\odot$ but with a varying hydrogen envelope mass. Dashed lines correspond to the same models, but with tidal heating turned off. The companion mass is fixed at 0.3 $M_\odot$.

These formulae will break down if the wave nears the edge of the propagation cavity where ω^2 becomes comparable to L_l^2 (i.e. if the traveling wave approximation breaks down, Sec. 3.3.2).

3.C Effect of hydrogen envelope mass on tidal heating

He-core WDs can vary in the masses of their H envelopes. We modeled tidal heating for models with a fixed total mass, but varying the mass of the He core and H envelope. Fig. 3.13 demonstrates the evolution of effective temperature for three models of varying H mass, initialized in a binary with the same initial orbital period. Early in the evolution, tidal heating is unimportant but the models exhibit different cooling behavior based on how thick the H envelope is. When tidal heating dominates at short orbital periods, we find that models with a lower mass of H reach higher values of $T_{\rm eff}$, which is a consistent trend over all our WD models. This trend is not necessarily true when tidal heating is turned off and models continue to cool.

The main cause for this behavior is the changing radius of the WD, as models with more H have a larger radius (for the models in Fig. 3.13, the radius changes by a factor of $\approx 10\%$). The radius affects the tidal heating power $L_{\rm tide}$, which scales with the radius R, the moment of inertia I and the tidal torque scaling parameter $\hat{f}$ as (see Eq. 3.6 and Fuller and Lai (2013) for a derivation)

$$L_{\rm tide} \propto \frac{I^{8/7}\hat{f}^{-1/7}}{R^{-31/14}}. \tag{3.22}$$

The values of I and $\hat{f}$ can depend on R, but in our models, a changing radius barely changes I and moderately changes $\hat{f}$, which hardly affects $L_{\rm tide}$. At short periods when tidal heating dominates the luminosity, and neglecting the changes in I and $\hat{f}$,

$$T_{\rm eff}^4 \propto \frac{L_{\rm tide}}{R^2} \propto \frac{R^{-31/14}}{R^2} \propto R^{-59/14}. \tag{3.23}$$

In summary, we find that models with a lower mass of H have smaller radii, and reach higher $T_{\rm eff}$ when tidal heating is strong at very short orbital periods. However, the variance in $T_{\rm eff}$ due to varying H mass is $\lesssim 10\%$ over a wide range of orbital periods. For the systems that we model, the uncertainties in the total WD mass and initial orbital period of the binary lead to greater uncertainties in $T_{\rm eff}$ (see e.g. Fig. 3.7). Thus we do not vary the mass of H in our models for our main analysis. Testing our predictions of the effect of H envelope mass on tidal heating would be difficult, both due to its relatively small influence on $T_{\rm eff}$ and the fact that most WDs do not have measured constraints on their H envelope mass.

Chapter 4

CHARACTERIZING THE HOST GALAXIES AND DELAY TIMES OF CA-RICH GAP TRANSIENTS VS 91BG-LIKE SNE AND NORMAL TYPE IA SNE

Scherbak, Peter, Abigail Polin, Mansi Kasliwal, Kishalay De, Peter Behroozi, Dave Cook, and W. V. Jacobson-Galán (Nov. 2025). "Characterizing the Host Galaxies and Delay Times of Ca-rich Gap Transients versus 91bg-like SNe and Normal Type Ia SNe". In: *Publications of the Astronomical Society of the Pacific* 137.11, p. 114207. DOI: 10.1088/1538-3873/ae1cef.

Calcium-rich gap transients are a faint, fast-evolving class of supernovae that show strong nebular Ca emission lines. Their progenitor systems are uncertain, but they are often associated with old and quiescent host galaxies. In this work, we compare the properties of the hosts of hydrogen-poor Ca-rich gap transients to the hosts of 3 other classes of supernova (SNe): normal Type Ia, 91bg-like, and Type II. We use data from the Zwicky Transient Facility (ZTF) Census of the Local Universe (CLU) experiment to build up our 4 SNe samples and identify the host galaxies. A combination of precomputed host properties from the CLU catalog and those derived from SED fitting are used to characterize each host's stellar mass, star formation rate, and specific star formation rate (sSFR). We find that the hosts of Ca-rich gap transients and 91bg-like SNe occupy a similar parameter space of mass and sSFR, and are more massive and quiescent compared to the hosts of Type Ia and Type II SNe. Additionally, we construct delay time distributions (DTDs) for our 4 samples, finding that Ca-rich gap transients and 91bg-like SNe have the longest peak delay times $\sim 10^4$ Myr, compared to the peak delay times of Type Ia SNe ($\sim 10^3$ Myr) and Type II SNe (~ 10 Myr). The similarity of host environment and DTDs for Ca-rich gap transients and 91bg-like SNe motivates further analysis of the relationship of these two transient classes.

4.1 Introduction

Calcium-rich gap transients are a type of hydrogen-poor supernova (SN) with unique characteristics and unknown progenitors. They are part of a broader class of Ca-rich transients that include hydrogen and that may result from core-collapse supernova (Milisavljevic et al., 2017; Jacobson-Galán et al., 2020b; Das et al., 2023), which

are not the focus of this work. Calcium-rich gap transients are fainter and faster-evolving than Type Ia SNe (SNe Ia) and core-collapse SNe, and are identified by strong [Ca II] emission in their nebular phase (Perets et al., 2010; Milisavljevic et al., 2017; Jacobson-Galán et al., 2020c; Kasliwal et al., 2012; De et al., 2020). They may produce $\sim 0.1 M_{\odot}$ of Ca and thereby may help chemically enrich the universe (Perets et al., 2010). The putative hosts of Ca-rich gap transients are often older and quiescent (Dong et al., 2022) and, curiously, the site of the explosion is commonly located at large offsets from the host (Perets et al., 2010; Foley, 2015; Lunnan et al., 2017; Kasliwal et al., 2012; De et al., 2020). This offset is a real effect, not an observational bias, with the rates of these events between one third to equal that of the volumetric rate of SNe Ia (Frohmaier et al., 2018). Additionally, stellar populations have not been detected at the location of most Ca-rich gap transients, suggesting their progenitors may have traveled a great distance from their parent stellar population (Lyman et al., 2014; Foley, 2015; Lunnan et al., 2017; De et al., 2020) although this is uncertain (Perets and Beniamini, 2021).

Several progenitor models have been put forth to explain Ca-rich gap transients, including helium (He) detonation on a WD (Bildsten et al., 2007; Shen and Bildsten, 2009; Waldman et al., 2011; Dessart and Hillier, 2015), double detonation of a He shell on a WD (Polin et al., 2019; Polin et al., 2021; Touchard-Paxton et al., 2025), a WD disruption/merger (Zenati et al., 2019; Zenati et al., 2023), and the core-collapse of an ultra-stripped massive star (Tauris et al., 2015), but none have been fully validated (Dong et al., 2022). Some Ca-rich gap transients show double-peaked light curves, which may arise from a progenitor star with an extended envelope (Jacobson-Galán et al., 2022; Ertini et al., 2023) or from ^{56}Ni in the outer layers of the ejecta (De et al., 2018).

Similarities between Ca-rich gap transients and 91bg-like SNe may exist. 91bg-like SNe are a subclass of SNe Ia that are fainter and redder than normal SNe Ia, and also show faster decline times than normal SNe Ia (Filippenko et al., 1992; Leibundgut et al., 1993; Turatto et al., 1996). 91bg-like SNe are preferentially found in stellar populations with little recent star formation (characteristic of elliptical or lenticular morphologies (Li et al., 2011; Senzel et al., 2025)), suggesting they explode at much later times (i.e. have longer delay times) than normal SNe Ia (Chakraborty et al., 2024), which are found in stellar populations from the very young to very old (Panther et al., 2019). On average, the hosts of normal SNe Ia tend to be bluer/younger than those of 91bg-like SNe (Barkhudaryan et al., 2019; Hakobyan

et al., 2020; Perrefort et al., 2020; Burgaz et al., 2025). Additionally, Barkhudaryan et al. (2019) found that 91bg-like SNe show no evidence of prompt progenitors. The subluminuous and fast-evolving nature of 91bg-like SNe, their preference for older/quiescent hosts, larger offsets compared to SNe Ia (De et al., 2020), and spectroscopic similarities to some Ca-rich gap transients (Jacobson-Galán et al., 2020a; De et al., 2020) inspire further comparison of these two transient classes.

The usefulness of comparing delay times of normal SNe Ia and 91bg-like SNe motivates construction of delay time distributions (DTDs) of Ca-rich gap transients in comparison to other event types. A DTD shows the transient rate versus time that follows a burst of star formation (Maoz et al., 2012; Freundlich and Maoz, 2021; Heringer et al., 2019). Based on the evolutionary time-scales preceding the transient, different progenitor scenarios for a transient predict different DTDs (Greggio, 2005; Maoz et al., 2012; Heringer et al., 2019). Transients with short (Myr) delay times (e.g. Type II supernova) are linked to massive stars (e.g., Zapartas et al., 2017), whereas those with time delays of Gyrs (e.g. SNe Ia) are linked to less massive stars or less common mechanisms (Behroozi, in prep.). DTDs can be estimated from the fraction of transients that occur in star-forming vs. quiescent galaxies (e.g., Zheng and Ramirez-Ruiz, 2007) because, using ensemble averages, it is possible to constrain star formation histories better than could be done for an individual galaxy (e.g., Pacifici et al., 2016; Behroozi et al., 2019).

We leverage transient discoveries with the Zwicky Transient Facility (ZTF) (Bellm et al., 2019b; Graham et al., 2019) to compare the host galaxies of different transients, especially through the construction of DTDs using host properties plus detections. Section 4.2 describes the survey and the 4 samples we model: Ca-rich gap transients, 91bg-like SNe, normal SNe Ia and Type II SNe. Section 4.3 details the characterization of the host galaxies through both SED modeling with PROSPECTOR (Leja et al., 2017; Johnson et al., 2021), and also with data from the CLU catalog. In Section 4.4, we compare the properties of the host galaxies of the different transient classes, and present DTDs constructed from the masses and star-forming statuses of the hosts. We discuss our results and conclude in Section 4.5.

4.2 Observations: The ZTF-CLU Experiment

The Zwicky Transient Facility (ZTF) is a optical time-domain survey that uses the Palomar 48 inch Schmidt telescope and surveys the Northern Hemisphere sky in three bands (Bellm et al., 2019b; Graham et al., 2019). The ZTF-CLU (Census of

the Local Universe) experiment (De et al., 2020) is designed to classify transients coincident with galaxies in the CLU catalog (Cook et al., 2019). The spatial cross-match radius between transient and galaxy is set to $3 \times D_{25}$ (the isophotal major axis containing 25 of the galaxy's total light) or 280″ when D_{25} is not available (corresponding to 270 kpc at a distance of 200 Mpc) (De et al., 2020). The CLU catalog extends to 200 Mpc and consists of previously-identified galaxies as well as galaxies found with an emission-line (Hα) survey by the Palomar 48 inch telescope (Cook et al., 2019). As of 2023, the CLU catalog contains $\sim$ 270,000 galaxies in total. The CLU catalog includes estimates of a galaxy's stellar mass and SFR, with the latter computed via FUV fluxes.

This work mainly uses a sample of eight hydrogen-poor Ca-rich gap transients identified in the ZTF-CLU experiment from 2018 June 1 to 2019 September 30 (De et al., 2020) (our Gold sample). De et al. (2020) finds that the average Ca-rich gap transient is detectable out to 150 Mpc for a flux limit in *r* band of 20.0 mag (the target limiting magnitude of the ZTF-CLU experiment). We also identify nineteen Ca-rich transients detected earlier (mostly before 2018, by other surveys) and modeled in Dong et al. (2022), which we designate as our Silver Sample (Section 4.3.2). However, only a fraction of these nineteen can be conclusively identified as Ca-rich *gap* transients due to a lack of photometry near peak light which is required for the identification. Additionally, some of the events in the Dong et al. (2022) sample show hydrogen, which represents a different class of Ca-rich transient. We therefore cross match the selection of Dong et al. (2022) with known Ca-rich gap transients compiled in De et al. (2020), which used the same cuts in generating our Gold sample, when comparing the host properties.

We identified other classes of transients through the Fritz data platform[1]. Over the same period as the Ca-rich gap transients were detected, ZTF detected about 290 normal SNe Ia, 270 Type II SNe, and 30 91bg-like SNe as part of the ZTF-CLU experiment. Together these comprise 4 samples of transients, for which we analyze the host galaxies.

4.3 Determining properties of host galaxies

We identify the host galaxies for all transients by querying the CLU catalog, and estimate each host's star formation rate (SFR) and stellar mass M_* through two main methods. All quoted values are median values. For the sample of Ca-rich gap

[1] `https://fritz-marshal.org/`

transients and the sample of 91bg-like SNe, we perform host galaxy modeling in PROSPECTOR, which infers stellar population properties based on photometric data (Leja et al., 2017; Johnson et al., 2021). For all 4 samples we obtain M_* and SFR directly from the CLU catalog, where the quoted SFRs were calculated primarily via the galaxy's FUV flux (from the GALEX mission (Martin et al., 2005; Bianchi et al., 2014)) and additionally are dust-corrected using the W4 flux (Wright et al., 2010), making the derived values more accurate.

In all cases, we calculate the host's specific star formation rate (sSFR) as the ratio of SFR to M_*. We adopt the criteria that sSFR $> 10^{-11}$ yr^{-1} implies a star-forming galaxy, whereas sSFR $< 10^{-11}$ yr^{-1} implies a quiescent galaxy (Fontana et al., 2009).

4.3.1 PROSPECTOR ANALYSIS

For our most rigorous analysis, we characterize the host galaxies using the Python tool PROSPECTOR, which infers stellar population properties based on photometric data (Leja et al., 2017; Johnson et al., 2021) and uses FLEXIBLE STELLAR POPULATIONS (Conroy et al., 2009; Conroy and Gunn, 2010a) and PYTHON-FSPS (Foreman-Mackey et al., 2014).

Where available, we use photometry from the following surveys in our fitting. We use optical data from the Sloan Digital Sky Survey Data Release 17 in u, g, r, i, z bands (Abdurro'uf et al., 2022). We retrieve data (W1, W2, W3, W4 bands) from the AllWISE catalog in the NASA/IPAC INFRARED SCIENCE ARCHIVE (IRSA) (Wright et al., 2010; Mainzer et al., 2011). WISE magnitudes are converted into the AB system using Wright et al. (2010). We use elliptical aperture photometry measurements when available, as these do a better job of capturing extended source brightness (Cutri et al., 2013). We retrieve data (J, H, K bands) from the 2MASS All-Sky Extended Source Catalog (Skrutskie et al., 2006) in IRSA and also convert to the AB system. Finally, we use data (NUV, FUV bands) from GALEX (Martin et al., 2005), accessed through the GALEX GR6/7 Data Release[2] in Mikulski Archive for Space Telescopes (MAST). We use standard SDSS, WISE, 2MASS and GALEX transmission curves from SEDPY (Johnson, 2019).

We retrieve redshifts from the NASA/IPAC Extragalactic Database (NED)[3], and correct SDSS magnitudes for galactic dust extinction using NED (Schlafly and Finkbeiner, 2011). We adopt 10% uncertainties on all spectral fluxes ("maggies" in

[2] `http://galex.stsci.edu/gr6/`

[3] The NASA/IPAC Extragalactic Database (NED) is funded by the National Aeronautics and Space Administration and operated by the California Institute of Technology.

PROSPECTOR) as most fluxes have small observational uncertainties, but systematic uncertainties can exist (Conroy et al., 2009; Conroy, 2013).

We adopt many of the same priors as Dong et al. (2022), who modeled the host galaxies of nineteen Ca-rich transients detected from 2000 - 2019. We use a Chabrier initial mass function (IMF) (Chabrier, 2003), and a Milky Way Extinction law parametrized by Cardelli et al. (1989). We include a model of dust emission from Draine and Li (2007) which describes the PAH thermal emission features, but we keep the dust model's parameters fixed. We also include a nebular continuum in our model and impose a 2:1 ratio on the amount of dust attenuation between the young and old stellar populations (Calzetti et al., 2000). We do not assume a stellar mass - stellar metallicity relationship.

Instead of a parametric delayed-τ model for star formation history (SFH), we use PROSPECTOR's CONTINUITY_SFH_MODEL, which is less biased and produces better error estimates (Leja et al., 2019). We fit to four parameters in this model: metallicity (Z), dust extinction (A_V), total mass formed, and SFR ratios between adjacent temporal bins. Following Dong et al. (2022), we use eight temporal bins, as the fitting should not use less than four bins (Leja et al., 2019). The first two bins are fixed to 0 – 30 Myr and 30 – 100 Myr, while the last bin is calculated as the age of the universe at the galaxy's redshift, using the cosmology calculator of Wright (2006). We ran PROSPECTOR using the DYNESTY sampler (Speagle, 2020).

We convert the total mass formed to stellar mass (M_*) using a fair sample of the posterior. We transform the total mass and SFR ratios into SFR values, and then calculate the host's specific star formation rate (sSFR) by dividing the SFR in the most recent age bin by the surviving stellar mass.

4.3.2 Host properties: PROSPECTOR vs CLU catalog

For the eight Ca-rich gap transients in our Gold sample, the results of the PROSPECTOR fitting for M_*, SFR, and sSFR are shown in Table 4.1. Based on the criterion discussed above, we find that all eight hosts are quiescent. Three hosts lack a detection in one of the four surveys for which we use photometry - however, these three all had at least nine photometry points, which Dong et al. (2022) found to be the minimum required for a confident analysis using the CONTINUITY_SFH_MODEL model.

The CLU catalog contains M_* estimates for all eight hosts, and SFR estimates (from FUV fluxes) for five of the eight. We find a significant discrepancy between the M_*

Transient name	Host name	log ($M_*/M_\odot$)	SFR ($M_\odot$/yr)	log(sSFR) (yr^{-1})	Host morphology
ZTF 18aayhylv/SN 2018ckd	NGC 5463	$11.25\pm^{0.03}_{0.09}$	0.0038	$-13.78\pm^{0.46}_{0.81}$ (q)	S0
ZTF 18abmxelh/SN 2018lqo	CGCG 224-043	$10.86\pm^{0.02}_{0.03}$	0.012	$-12.69\pm^{0.07}_{0.08}$ (q)	E
ZTF 18abttsrb/SN 2018lqu	WISEA J155413.91+133102.4	$9.93\pm^{0.02}_{0.02}$	1.3e-5	$-15.25\pm^{1.61}_{4.37}$ (q)	E
ZTF 18acbwazl/SN 2018gwo	NGC 4128	$10.67\pm^{0.04}_{0.06}$	0.0050	$-13.00\pm^{0.14}_{0.34}$ (q)	S0
ZTF 18acsodbf/SN 2018kjy	NGC 2256	$11.40\pm^{0.02}_{0.02}$	0.0057	$-13.61\pm^{0.16}_{0.25}$ (q)	E
ZTF 19aaznwze/SN 2019hty	WISEA J125534.50+321221.5	$10.40\pm^{0.01}_{0.02}$	0.009	$-12.37\pm^{0.09}_{0.11}$ (q)	E
ZTF 19abrdxbh/SN 2019ofm	IC 4514	$10.70\pm^{0.08}_{0.09}$	0.097	$-11.71\pm^{0.47}_{1.02}$ (q)	spiral
ZTF 19abwtqsk/SN 2019pxu	WISEA J051011.32-004702.5	$10.55\pm^{0.09}_{0.08}$	0.015	$-12.60\pm^{0.87}_{1.93}$ (q)	spiral

Table 4.1: Properties of the host galaxies of eight Ca-rich gap transients (our Gold sample) modeled in PROSPECTOR. Values are generated from the posterior distributions using the CONTINUITY_SFH_MODEL (fitting for total mass, SFR ratios, A_V, and Z). Total mass is transformed into surviving stellar mass M_*. SFR ratios are used to generate the SFR bins. The sSFR is calculated using the most recent SFR bin and M_*, and (q) refers to quiescent (the median sSFR below $< 10^{-11}$ yr^{-1}). Morphologies are from De et al. (2020).

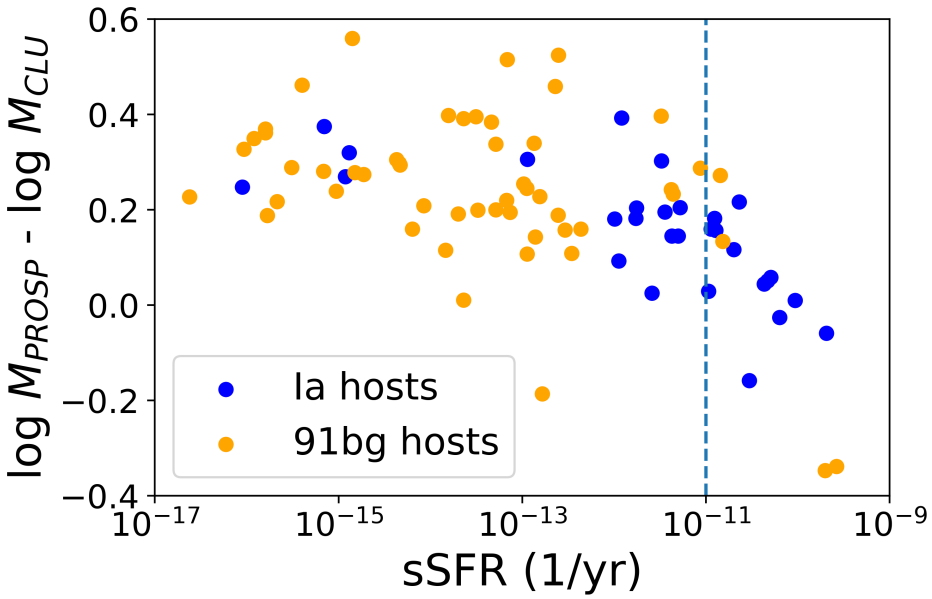


Figure 4.1: The discrepancy between stellar mass as found in PROSPECTOR and the CLU catalog, plotted versus sSFR as found in PROSPECTOR, for 91bg-like SNe and SNe Ia . Additional 91bg-like SNe detected later than 2020 and not in our main sample, but which we modeled in PROSPECTOR, are also included. There appears to be a trend where the discrepancy decreases for star-forming galaxies with sSFR $> 10^{-11}$ yr^{-1} (the boundary marked by the vertical dashed line).

from PROSPECTOR modeling and M_* from the CLU catalog, the difference ranging from 0.2 - 0.8 dex. The difference may be because early-type galaxies have a different

mass to light (M/L) ratio (Leroy et al., 2019), as galaxies with low sSFRs as modeled in PROSPECTOR tend to show higher discrepancies. We also find discrepancies for the SFR, with the CLU catalog suggesting higher values, especially for galaxies that have a low sSFR as modeled in PROSPECTOR. This is likely due to the fact that some elliptical galaxies have higher than expected dust content, which is translated into an artificially high estimate for the SFR (Davis et al., 2014; Simonian and Martini, 2017). However, when we compute the sSFR with CLU catalog data, we find that the five hosts with SFR data were still classified as quiescent.

We perform similar analysis for the sample of 91bg-like SNe hosts. With the PROSPECTOR analysis, 90% of the 91bg-like SNe hosts are quiescent whereas using data from the CLU catalog, 60% of the 91bg-like SNe hosts are quiescent. As with the Ca-rich gap transient hosts, PROSPECTOR appears to consistently underestimate the SFR compared to the CLU catalog's value.

Using the CLU catalog data, 12% of SNe Ia hosts are deemed quiescent, and $< 2\%$ of the Type II SNe hosts are quiescent. Using detections in the Bright Transient Survey, Irani et al. (2022) found that $< 1\%$ of Type II SNe hosts are quiescent, which appears consistent with our results. We did not perform PROSPECTOR analysis for the entirety of the SNe Ia and the Type II SNe hosts because of the large sample size involved (> 500 sources in total), but when a subset of SNe Ia hosts were modeled in PROSPECTOR, we again find a discrepancy where PROSPECTOR analysis favored larger M_* and lower sSFRs. The mass discrepancy decreases for star-forming hosts with a higher sSFR (Fig. 4.1), where we have included additional 91bg-like SNe detected later than 2020 to better demonstrate the trend. We again interpret the discrepancies as the M/L ratio depending on the star formation activity of the galaxy, where low sSFRs should actually be associated with higher M/L ratios. Therefore, the CLU catalog may be undervaluing masses for many of the quiescent hosts we model compared to more sophisticated analysis in PROSPECTOR.

4.4 Results

Fig. 4.2 shows the parameter space of host sSFR and M_* for our transient samples, including Ca-rich gap transients from our Gold sample. Points correspond to the median sSFR and median M_*, with errorbars not shown for convenience. The top plot is generated from SFR and M_* estimates using the CLU catalog for all 4 samples, whereas the bottom plot differs in using SFR and M_* from PROSPECTOR modeling for the Ca-rich gap transient and 91bg-like SNe hosts only (see Sec 4.3.2).

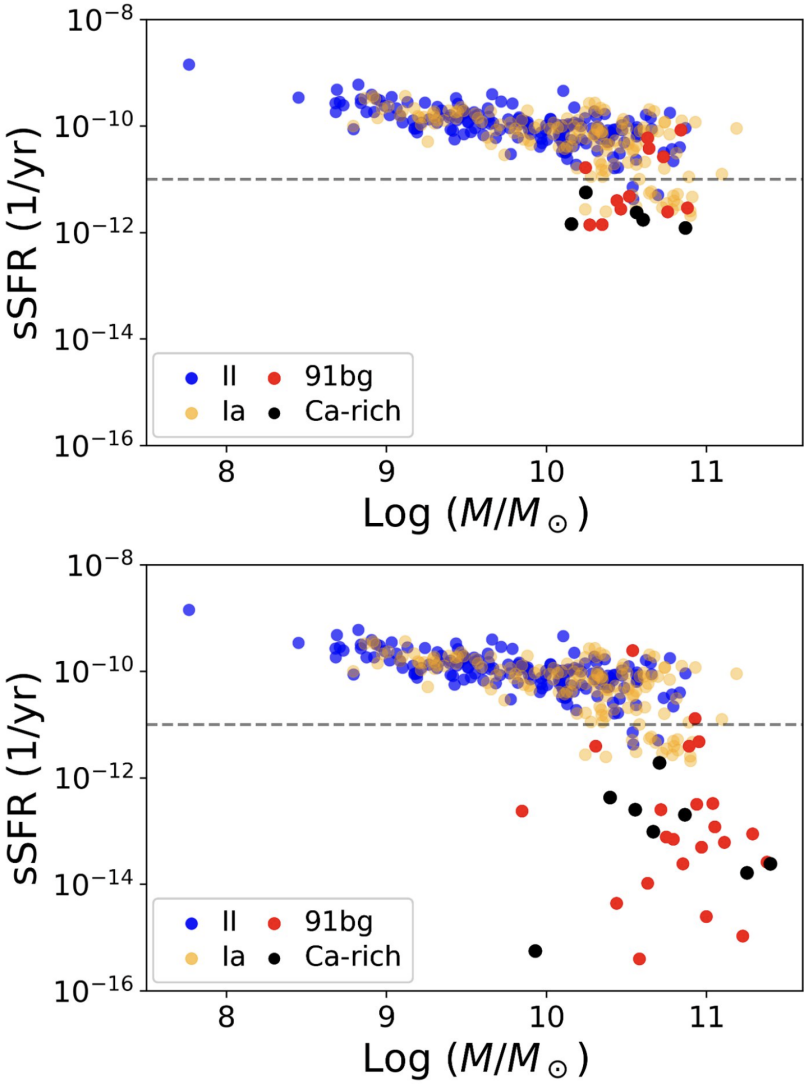


Figure 4.2: The stellar masses and specific star formation rates (sSFR) of the galaxy hosts of 4 classes of transients (Ca-rich gap transients, 91bg-like SNe, normal SNe Ia, Type II SNe). The horizontal line designates the fiducial boundary between star-forming and quiescent galaxies. **Top**: Masses and SFRs are retrieved directly from the CLU catalog for all hosts. **Bottom**: For the hosts of Type II SNe and SNe Ia, same as top panel. For the hosts of Ca-rich gap transients and 91bg-like SNe, masses and SFRs are estimated using PROSPECTOR modeling.

Although PROSPECTOR analysis is likely more sophisticated than using values from the CLU catalog, the large sample size for SNe Ia and Type II SNe hosts means that we did not perform a direct comparison with PROSPECTOR modeling.

We find a significant overlap in the parameter space of Ca-rich gap transient and 91bg-like SNe hosts, where they prefer higher mass, quiescent hosts. However, the

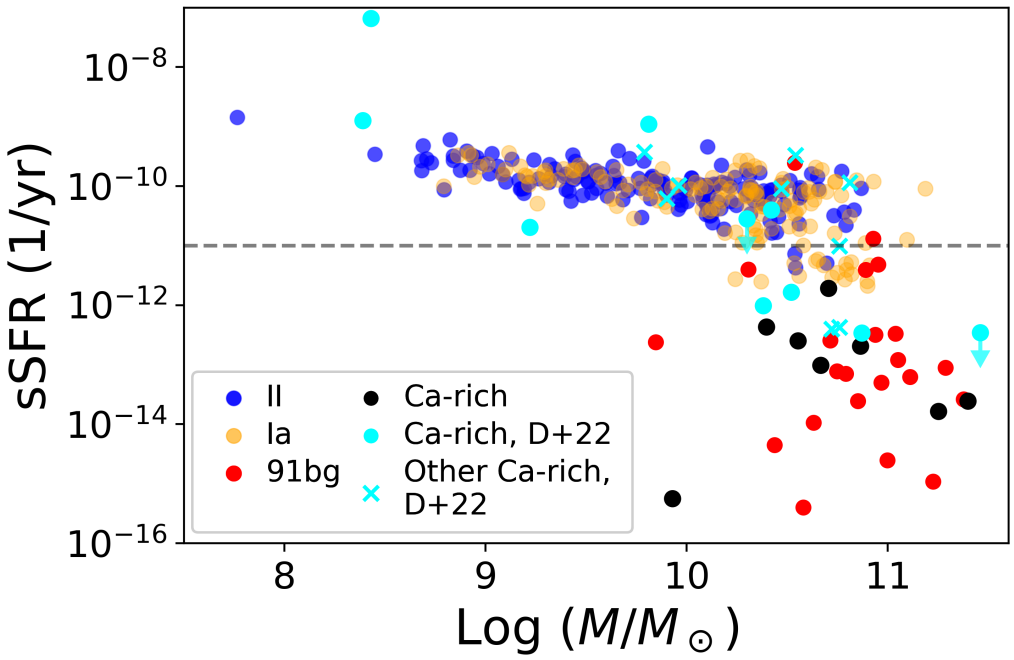


Figure 4.3: Similar to the bottom panel of Fig. 4.2, but with the addition of the Silver Sample, Ca-rich transient hosts identified in Dong et al. (2022) that were modeled in PROSPECTOR. Those from (Dong et al., 2022) labeled as "Other Ca-rich" have strong calcium emission, but are not identified as Ca-rich gap transients. The two points with downward arrows indicate upper limits.

exact region of overlap differs between the top and bottom plot in that PROSPECTOR modeling prefers more quiescent hosts. In comparison, the hosts of SNe Ia and Type II SNe occupy a range of masses that extends to low mass galaxies, and they tend to be star-forming. Almost none of the Type II SNe hosts are quiescent and a minority of SNe Ia hosts are quiescent, in agreement with Irani et al. (2022). The hosts of 91bg-like SNe being more massive and less star-forming compared to hosts of SNe Ia also agrees well with the literature (Panther et al., 2019; Barkhudaryan et al., 2019; Burgaz et al., 2025; Dimitriadis et al., 2025; Senzel et al., 2025).

Fig. 4.3 includes the addition of our Silver Sample, nineteen Ca-rich transient hosts modeled in Dong et al. (2022) (see Sec. 4.2). However, only 10 of these can be conclusively identified as Ca-rich gap transients using the same criteria as De et al. (2020) (low luminosity, hydrogen-poor events that showed strong [Ca II] emission in the nebular phase). Others either have a lack of photometry near peak light to identify them as Ca-rich gap transients, or have photometric properties that differ from Ca-rich gap transients. We therefore differentiate between these

two subclasses, labeling the Ca-rich transients that are not gap transients as “other Ca-rich" in Fig. 4.3.

In their PROSPECTOR analysis, Dong et al. (2022) modeled all nineteen hosts with a parametric delayed-τ model, but only modeled nine with the CONTINUITY_SFH_MODEL model, which requires more photometric points for accuracy. In the latter case, only two of the nine are Ca-rich gap transients. In Fig. 4.3, we therefore plot the results of Dong et al. (2022) when using the parametric delayed-τ model, although the CONTINUITY_SFH_MODEL may be more accurate. Some of their host properties overlap well with ours, corresponding to quiescent, massive galaxies. However, several Ca-rich gap transients hosts from Dong et al. (2022) are much less massive and are more star-forming than those of our sample. Part of the discrepancy is that parametric models tend to underestimate stellar masses, as Dong et al. (2022) found in their comparison of their models. In addition, Dong et al. (2022) found that six of the nine hosts had higher SFRs when using the parametric models. Together, these two effects might push the hosts of the other Ca-rich gap transients somewhat closer to our sample, which uses the CONTINUITY_SFH_MODEL model for analysis. See also Sec. 4.5 for caveats related to the host identification of some of the Dong et al. (2022) sample.

We then use the properties of the hosts to construct DTDs with PYROMETER (Behroozi, in prep.), which forward-models expected transient rates by convolving a given delay time distribution with star formation histories from the UNIVERSEMACHINE empirical model (Behroozi et al., 2019). The UNIVERSEMACHINE infers star formation histories as a function of stellar mass and star-forming status by forward-modeling the star formation rate as a function of host dark matter halo mass and accretion rate, constrained primarily by observed galaxy number densities and spatial clustering. Relevant for this paper, the star formation histories derived in this way are more accurate for early star formation (e.g., more than 2 Gyr ago) than traditional SED-fitting approaches, because they are constrained to match the actual number density of high-redshift galaxies, whereas traditional SED-fitting methods are limited by the color similarity of old stellar populations. Comparisons with advanced SED-fitting approaches (e.g., Pacifici et al., 2016) suggest very similar reconstructions between the UNIVERSEMACHINE and SED-fitting methods over the range of 100 Myr — 2 Gyr.

To compare with observations, PYROMETER calculates expected event rates as above for a bin in redshift, galaxy stellar mass, and star-forming status, and uses Poisson

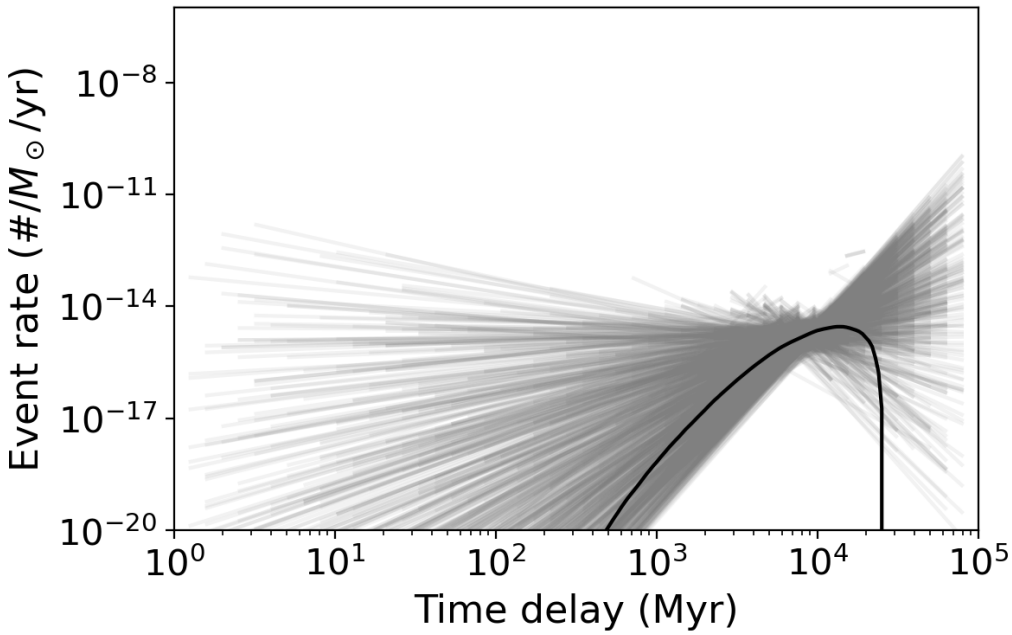


Figure 4.4: Posterior delay time distributions (DTDs) for Ca-rich gap transients, based on the stellar masses and star-forming/quiescent status of their host galaxies. Host properties are determined in PROSPECTOR. The DTDs are assumed to be a power law, and the light gray lines show individual DTDs. The black line is the median event rate from the DTD posterior.

statistics to compute a likelihood function for the observations given a chosen model. It then uses a Markov Chain Monte Carlo method with a combination of adaptive Metropolis (Haario et al., 2001; Goodman and Weare, 2010) steps to compute the posterior for the delay time distributions that best match the observations. We have found that 150,000 burn-in steps and 150,000 sampling steps were always enough to achieve convergence in the posterior distributions for the observations in this paper.

We assume the DTD is a power law with some index from some minimum delay time $t_{\rm min}$ to a maximum delay time $t_{\rm max}$. To normalize the transient event rate, the sky area and duration of the survey is necessary. We use as inputs the stellar mass and star-forming quiescent/status of hosts, as found in Section 4.3, which is a boolean input to PYROMETER. The sky area of ZTF is estimated to be ~26470 degrees (3π of the sky) for all samples (Masci et al., 2018) and we use the survey duration discussed in Sec. 4.2. The area and duration provide a scaling for the DTD event rates, which is approximate, whereas the relative value of event rate between SN types is precise. For the 91bg-like SNe, SNe Ia and Type II SNe samples, we assume a lower redshift bound of 0, and for upper redshift the equivalent to the ZTF-CLU

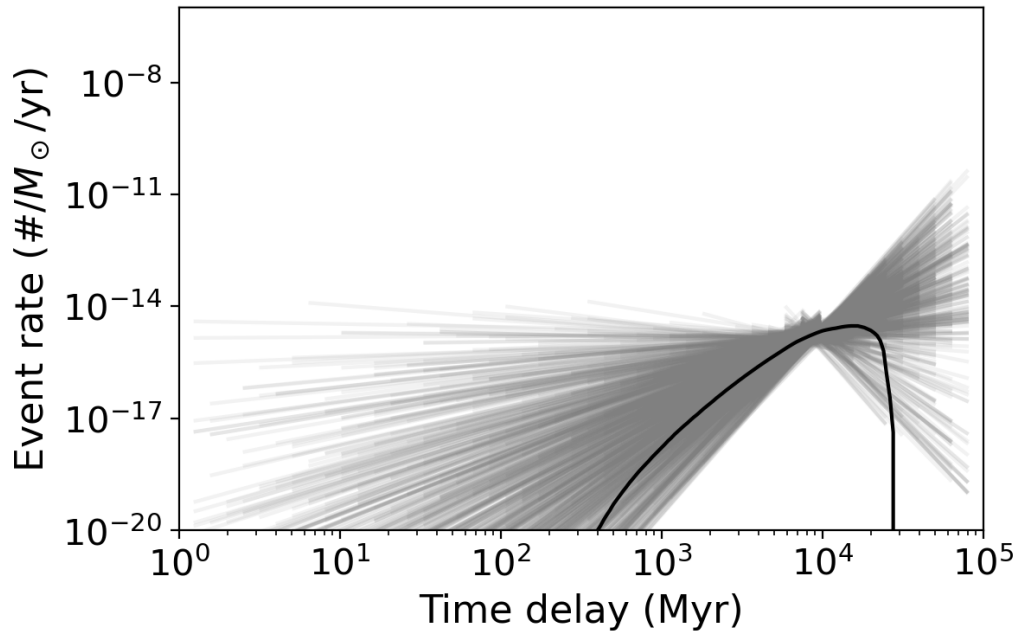


Figure 4.5: Similar to Fig. 4.4, but based on the host galaxies of 91bg-like SNe. Host properties are determined in PROSPECTOR.

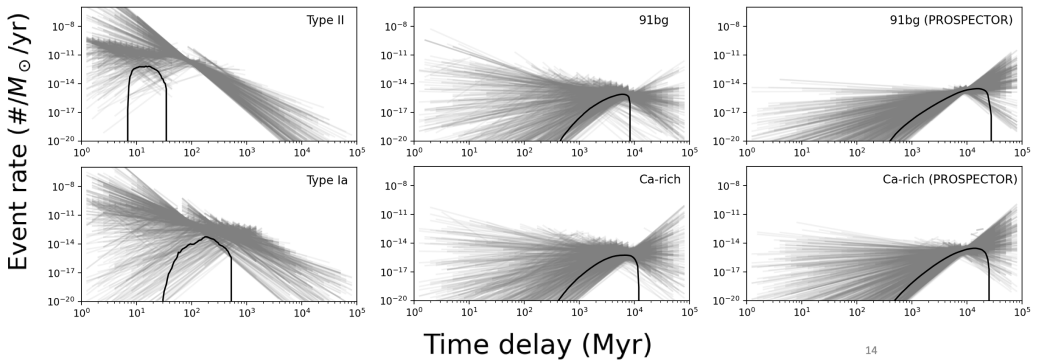


Figure 4.6: Similar to Fig. 4.4, but based on the host galaxies of 4 classes of transients. The left 4 panels have host properties retrieved directly from the CLU catalog, whereas the right 2 panels have host properties from modeling in PROSPECTOR.

experiment's 200 Mpc extent ($z \sim 0.049$). At 200 Mpc, the CLU limiting magnitude of $r \approx 20$ mag (De et al., 2020) corresponds to detections of absolute magnitude $M \lesssim -16.5$. For Ca-rich gap transients we use the equivalent redshift to 150 Mpc ($z \sim 0.034$), which De et al. (2020) found to be the effective radius of detection. Using instead the upper redshift of the other samples for the Ca-rich gap transient sample produced no significant effect on the final DTDs. Finally, we estimate the

minimum host galaxy stellar mass detectable to be about 10^8 $M_\odot$ for both quenched and star-forming galaxies (Cook et al., 2019). Lowering the minimum bound to 10^7 $M_\odot$ produced negligible results on the final DTDs for our samples.

Fig. 4.4 and Fig. 4.5 show posterior distributions of DTDs for Ca-rich gap transients (Gold sample) and 91bg-like SNe generated using host parameters as modeled in PROSPECTOR. Fig. 4.6 shows a comparison for the 4 samples, with DTDs for Ca-rich gap transients and 91bg-like SNe generated both from PROSPECTOR and CLU catalog estimates. In both cases, 91bg-like SNe and Ca-rich gap transients are associated with significantly longer delay times than SNe Ia and Type II SNe, with the median event rate (black line) peaking at longer delay times. Each gray line is an individual DTD demonstrating that power laws of various slopes and various minimum/maximum delay times are consistent with the data. However, the power laws tend to cluster about the median rate. DTDs that have a value of zero at a given time (i.e. a time outside the range $t_{\rm min}$ to $t_{\rm max}$) are not shown. In the case of Type II SNe, the median event rate appears to fall below most of the individual DTDs. This is because the DTDs with zero values at some times bring the median value below the non-zero DTDs.

4.5 Discussion

This work has characterized the delay times of Ca-rich gap transients using a systematic sample from De et al. (2020). Compared to previous samples of Ca-rich transients, our sample includes only those that are faint/fast and do not include hydrogen. Our results for the delay times of the other three classes of SNe (Sec. 4.4) agree with previous work, where 91bg-like SNe, a subset of SNe Ia, have been found to have longer delay times than normal SNe Ia (Barkhudaryan et al., 2019; Panther et al., 2019) and Type II SNe having short delay times (e.g., Zapartas et al., 2017). This paper is the first to calculate DTDs for Ca-rich gap transients, and future work should attempt to connect the DTDs of Ca-rich gap transients to their potential formation histories, as has been done with SNe Ia delay times to distinguish between the single degenerate and double degenerate formation scenario (Maoz et al., 2012).

Comparing the stellar mass-sSFR parameter space of galaxies containing transients is a useful tool (Figs. 4.2 and 4.3), and we encourage similar analysis for more transient classes. Indeed, such a comparison may be more useful than constructing DTDs because PYROMETER only takes a binary input parameter (star forming or quiescent) to estimate DTDs, whereas Figs. 4.2 and 4.3 show the full range of

sSFR. Similar to the results of Dong et al. (2022), we find that a large fraction of Ca-rich gap transient hosts are quiescent. However, we find that all hosts in our sample are quiescent, whereas Dong et al. (2022) found that only approximately half were quiescent (although our PROSPECTOR results use a different, potentially more accurate model that requires more host photometry data). We note that our large fraction of quiescent hosts is not surprising given the majority are classified as ellipticals (Table 4.1). We did not construct DTDs using the Ca-rich transient sample of Dong et al. (2022) because, in addition to about half of their sample not being confirmed as Ca-rich gap transients, the transients they modeled were not detected as part of a systematic survey and the completeness of the sample is unclear.

There are additional caveats, related to the identification of host galaxy, related to some of the hosts of Ca-rich gap transients from Dong et al. (2022) that show the highest sSFR in Fig. 4.3. PTF09dav (Kasliwal et al., 2012) had a fiducial host offset of 40 kpc, and was closer to several faint sources that may be dwarf galaxies (De et al., 2020). PTF11kmb (Lunnan et al., 2017) was located 150 kpc from the most likely host galaxy, and was additionally found in a galaxy group. In contrast, the hosts of our Gold sample had smaller offsets of $\approx 10 - 30$ kpc, and there was less ambiguity as to the host (De et al., 2020). Therefore, two of the Dong et al. (2022) points (cyan coloring) with highest sSFR in Fig. 4.3 could be wrong if the fiducial host is actually incorrect. iPTF16hgs, which had a peculiar double-peaked light curve, also has one of the most star-forming hosts. However, SN 2018lqo in our Gold sample was also double-peaked (De et al., 2020) and has a quiescent host, so there is no obvious relation between this subclass and host properties.

We have so far treated our Gold sample of Ca-rich gap transients as monolithic. However, De et al. (2020) found that among the eight detections, there are three related spectroscopic subclasses: red Ca-Ib/c objects, with SNe Ib/c-like features and a red color at peak light; green Ca-Ib/c objects, similar to previous but with a green color at peak light; and Ca-Ia objects, with SNe Ia-like features. We compare the host properties of these three subclasses to determine if there is any trend, with the limitation of very small numbers in each of these subclasses. We find, in our PROSPECTOR analysis, that the host of the single Ca-Ia object in our Gold sample has the largest sSFR of all the hosts in the Gold sample, although it is still deemed quiescent. In addition, De et al. (2020) identified two Ca-Ia objects in the literature, whose hosts were modeled in Dong et al. (2022) and were determined to be star-

forming galaxies (one of which had the highest sSFR among all the hosts in Dong et al. (2022)). We therefore tentatively suggest that Ca-Ia objects are associated with galaxies that are more star-forming, compared to the other two subclasses.

Otherwise, we do not see any trend among the subclasses, but this should be investigated further. In particular, De et al. (2020) hypothesizes that Ca-Ia objects are the result of He detonation on higher mass CO WDs, compared to the CO WDs in green or red Ca-Ib/c objects. This prediction should be propagated to predictions of delay times and host properties for these subclasses to compare with observed host properties, but an increase in sample size and spectropscopic followup for identification is needed.

This paper has investigated the global host environments of Ca-rich gap transients, specifically focusing on the mass and star formation rate of their entire host galaxies. However, the curiously large offsets of these transients from their hosts suggest that the local host properties could also play a significant role (as has been investigated for SNe Ia by Nugent et al. (2024)). The host environment is particularly important if the progenitor systems formed in such remote locations. Deep imaging of the local stellar population at the transient site would enable analysis of the immediate environment, providing insight into possible progenitor origins.

The analysis of the hosts of Ca-rich gap transients and 91bg-like SNe demonstrates a plausible link between these two classes of transients. The similarity of host environment and delay times is not a conclusive link between these two classes, but it is a necessary ingredient to motivate further analysis of the similarities. Since 91bg-like SNe are a peculiar subclass of SNe Ia, where the progenitor is an exploding white dwarf in a binary, this lends support to the hypothesis that Ca-rich gap transients also involve a WD in a binary system. In particular, it has been suggested that 91bg-like SNe result from the merger of a CO WD and a He WD (Pakmor et al., 2010; Crocker et al., 2017; Barkhudaryan et al., 2019; Panther et al., 2019). Therefore, this merger channel should be investigated in the context of Ca-rich gap transients through detailed hydrodynamical simulations, as has been done in Morán-Fraile et al. (2024), and comparison to yields and light curves, as in Jacobson-Galán et al. (2021).

Acknowledgments

We thank Wren Suess for advice on using PROSPECTOR and Joshua Speagle for useful discussion concerning the DYNESTY sampling tool used by PROSPECTOR. We thank

the anonymous referee for their feedback and suggestions.This research benefited from interactions enabled by the Gordon and Betty Moore Foundation through grant GBMF5076.

W.J.-G. is supported by NASA through Hubble Fellowship grant HSTHF2-51558.001-A awarded by the Space Telescope Science Institute, which is operated for NASA by the Association of Universities for Research in Astronomy, Inc., under contract NAS5-26555.

Based on observations obtained with the Samuel Oschin 48-inch Telescope at the Palomar Observatory as part of the Zwicky Transient Facility project. ZTF is supported by the National Science Foundation under Grant No. AST-1440341 and a collaboration including Caltech, IPAC, the Weizmann Institute for Science, the Oskar Klein Center at Stockholm University, the University of Maryland, the University of Washington, Deutsches Elektronen-Synchrotron and Humboldt University, Los Alamos National Laboratories, the TANGO Consortium of Taiwan, the University of Wisconsin at Milwaukee, and Lawrence Berkeley National Laboratories. Operations are conducted by COO, IPAC, and UW. For publications using products from Phase-II of the survey (taken on or after December 1, 2020), please include this text: Based on observations obtained with the Samuel Oschin Telescope 48-inch and the 60-inch Telescope at the Palomar Observatory as part of the Zwicky Transient Facility project. ZTF is supported by the National Science Foundation under Grants No. AST-1440341 and AST-2034437 and a collaboration including current partners Caltech, IPAC, the Weizmann Institute for Science, the Oskar Klein Center at Stockholm University, the University of Maryland, Deutsches Elektronen-Synchrotron and Humboldt University, the TANGO Consortium of Taiwan, the University of Wisconsin at Milwaukee, Trinity College Dublin, Lawrence Livermore National Laboratories, IN2P3, University of Warwick, Ruhr University Bochum, Northwestern University and former partners the University of Washington, Los Alamos National Laboratories, and Lawrence Berkeley National Laboratories. Operations are conducted by COO, IPAC, and UW.

This publication makes use of data products from the Wide-field Infrared Survey Explorer, which is a joint project of the University of California, Los Angeles, and the Jet Propulsion Laboratory/California Institute of Technology, funded by the National Aeronautics and Space Administration.

This publication also makes use of data products from NEOWISE, which is a project of the Jet Propulsion Laboratory/California Institute of Technology, funded by the

Planetary Science Division of the National Aeronautics and Space Administration.

This publication makes use of data products from the Two Micron All Sky Survey, which is a joint project of the University of Massachusetts and the Infrared Processing and Analysis Center/California Institute of Technology, funded by the National Aeronautics and Space Administration and the National Science Foundation.

Funding for the Sloan Digital Sky Survey IV has been provided by the Alfred P. Sloan Foundation, the U.S. Department of Energy Office of Science, and the Participating Institutions.

SDSS-IV acknowledges support and resources from the Center for High Performance Computing at the University of Utah. The SDSS website is www.sdss.org.

SDSS-IV is managed by the Astrophysical Research Consortium for the Participating Institutions of the SDSS Collaboration including the Brazilian Participation Group, the Carnegie Institution for Science, Carnegie Mellon University, Center for Astrophysics | Harvard & Smithsonian, the Chilean Participation Group, the French Participation Group, Instituto de Astrofísica de Canarias, The Johns Hopkins University, Kavli Institute for the Physics and Mathematics of the Universe (IPMU) / University of Tokyo, the Korean Participation Group, Lawrence Berkeley National Laboratory, Leibniz Institut für Astrophysik Potsdam (AIP), Max-Planck-Institut für Astronomie (MPIA Heidelberg), Max-Planck-Institut für Astrophysik (MPA Garching), Max-Planck-Institut für Extraterrestrische Physik (MPE), National Astronomical Observatories of China, New Mexico State University, New York University, University of Notre Dame, Observatário Nacional / MCTI, The Ohio State University, Pennsylvania State University, Shanghai Astronomical Observatory, United Kingdom Participation Group, Universidad Nacional Autónoma de México, University of Arizona, University of Colorado Boulder, University of Oxford, University of Portsmouth, University of Utah, University of Virginia, University of Washington, University of Wisconsin, Vanderbilt University, and Yale University.

This research has made use of the NASA/IPAC Extragalactic Database (NED), which is funded by the National Aeronautics and Space Administration and operated by the California Institute of Technology.

Facilities: Samuel Oschin 48-inch Telescope, part of the Zwicky Transient Facility project; NASA/IPAC Extragalactic Database (NED)

Software: Astropy (Astropy Collaboration et al., 2013; Astropy Collaboration et

al., 2018; Astropy Collaboration et al., 2022), astroquery (Ginsburg et al., 2019), DYNESTY (Speagle, 2020; Koposov et al., 2024; Skilling, 2004; Skilling, 2006), PROSPECTOR (Johnson et al., 2021), PYROMETER (Behroozi, in prep.), Python-fsps (Conroy et al., 2009; Conroy and Gunn, 2010b; Conroy and Gunn, 2010a), sedpy (Johnson, 2019), NumPy (Harris et al., 2020), matplotlib (Hunter, 2007)

Chapter 5

RAPID BINARY MASS TRANSFER: CIRCUMBINARY OUTFLOWS AND ANGULAR MOMENTUM LOSSES

Scherbak, Peter, Wenbin Lu, and Jim Fuller (Sept. 2025). "Rapid Binary Mass Transfer: Circumbinary Outflows and Angular Momentum Losses". In: *The Astrophysical Journal* 990.2, p. 172. DOI: 10.3847/1538-4357/adf067.

High rates of stable mass transfer likely occur for some binary star systems, but the resulting flow of mass and angular momentum (AM) is unclear. We perform hydrodynamical simulations of a polytropic donor star and a point mass secondary to determine the mass, AM, and velocity of gas that leaves the system, and the dependence on binary parameters such as mass ratio. The simulations use an adiabatic equation of state and do not include radiative cooling or irradiation of the outflow. Mass transfer is initiated by injecting heat into the stellar envelope, causing it to gradually inflate and overflow its Roche lobe. The transferred mass flows into an accretion disk, but soon begins to escape through the outer Lagrange point (L2), with a lesser amount escaping through the L3 point. This creates an equatorially concentrated circumbinary outflow with an opening angle of 10 to 30 degrees with a wind-like density profile $\rho \propto r^{-2}$. We find that the ratios of the specific AM of the outflowing gas over that of the L2 point are approximately $\{0.95, 0.9, 0.8, 0.65\}$ for mass ratios $q = \{0.25, 0.5, 1, 2\}$ (accretor/donor). The asymptotic radial velocity of the outflowing gas, in units of the binary orbital velocity, is approximately 0.1 to 0.2 for the same mass ratios, except for $q = 0.25$ where it might be higher. This outflow, if ultimately unbound from the binary, may be a source of circumstellar material that interacts with ejecta from a subsequent supernova or stellar merger.

5.1 Introduction

Mass transfer (MT) occurring between a donor star and a secondary star is common in binary star systems, especially for binaries containing massive stars (Sana et al., 2012). Episodes of MT precede the formation of isolated compact binaries (Postnov and Yungelson, 2014), including gravitational wave sources currently being discovered by LIGO (LIGO Scientific Collaboration et al., 2023) and sources that will be discovered by LISA (Korol et al., 2022). In addition, a large portion of

core-collapse supernovae occur in binaries that underwent MT in the past (Schneider et al., 2021).

There are multiple uncertainties regarding MT that make predicting the fate of a mass-transferring system difficult. The criteria for MT stability, and whether a common envelope phase occurs (Paczynski, 1976a; Ivanova et al., 2013), remains unclear. The rate of MT can be estimated based on prescriptions applied to 1D stellar evolution models (e.g., Kolb and Ritter, 1990), but recent works appear to disagree with existing prescriptions (Cehula and Pejcha, 2023; Ivanova et al., 2024). Another uncertainty is whether MT is conservative (Huang, 1963; Mink et al., 2007), i.e., what fraction of the material is accreted by the secondary.

When non-conservative MT occurs, a major uncertainty is the angular momentum carried away by the escaping material. Non-conservative MT has been predicted to increase the fraction of binaries undergoing unstable MT and merging (Willcox et al., 2023). Many works assume that the specific angular momentum (angular momentum per unit mass lost) is equal to that of the orbit of the accreting star. However, if mass escapes by flowing through the outer Lagrange point, L2, then its specific angular momentum may be comparable to that of the L2 point (e.g., Huang, 1963; MacLeod et al., 2018b), which is substantially larger than the specific angular momentum of the accretor. In the case of a massive binary with two stellar components, mass loss near L2 has been predicted as a likely outcome (Podsiadlowski et al., 1992) and the specific angular momentum of the outflow has been noted as an important uncertainty (Wellstein et al., 2001). Gallegos-Garcia et al. (2024) (see also Lu et al., 2023) show that, when the accretor is much more massive than the donor, the specific angular momentum lost through winds launched from the outer accretion disk can also be much larger than that of the accretor's orbit.

Several recent works have found that stable MT is an important channel to forming binary black holes (BBHs) (Pavlovskii et al., 2017; Klencki et al., 2021; Gallegos-Garcia et al., 2021; Son et al., 2022; Marchant et al., 2021; Picco et al., 2024). Of these, Marchant et al. (2021) and Picco et al. (2024) noted that L2 mass loss may precede BBH formation and that the amount of specific angular momentum lost is an outstanding uncertainty that impacts the predicted BBH population.

Recently, Lu et al. (2023) found that, for high rates of MT ($\gtrsim 10^{-4} M_{\odot}$/yr), gas in the accretion disk cools inefficiently and is energetic enough such that it is likely to escape through L2 and form a circumbinary outflow. There are several classes of binaries that may achieve the high MT rates for which the assumptions of Lu

et al. (2023) are valid, including: (1) Binaries where the donor star crosses the Hertzprung gap on a short timescale (Hjellming and Webbink, 1987; Marchant et al., 2021; Klencki et al., 2022; Temmink et al., 2023; Dorozsmai and Toonen, 2024); (2) He stars with a neutron star companion, that can initiate high rates of MT following core-He burning, known as case BB MT (Dewi et al., 2002; Tauris et al., 2015; Tauris et al., 2017); (3) A pre-supernova star in a binary, that expands a short time before the explosion due to late stages of nuclear burning or wave heating (Quataert and Shiode, 2012; Mcley and Soker, 2014; Fuller, 2017; Wu and Fuller, 2020; Wu and Fuller, 2022). Observationally, L2 mass loss is likely occurring in binaries such as SS433 (Blundell et al., 2001; Cherepashchuk et al., 2018) and W Serpentis (Shepard et al., 2024).

If the donor star is a supernova progenitor, L2 mass loss resulting in a circumbinary outflow is a source of circumstellar material (CSM), which the supernova ejecta later interacts with. There exists a variety of observational evidence that a large fraction of core-collapse supernovae interact with CSM that occurred from pre-supernova mass loss, like narrow line emission (e.g., Taddia et al., 2013) or faster rise times and more luminous emission at early times (e.g., Clark et al., 2020), but the mechanisms behind CSM formation remain unclear. It is important to quantify the speed and geometry of the circumbinary outflow to predict its observable effects on supernovae interacting with dense CSM.

In this paper, we extend the work of Lu et al. (2023) by performing hydrodynamical models of stable MT, to ascertain whether circumbinary outflows can form near L2. We also aim to determine their morphology, and to compute the angular momentum and the velocity of the ejected material. We use the PLUTO hydrodynamic code (Mignone et al., 2007; Mignone et al., 2012) to examine MT between a donor star and a secondary, as well as any outflows from the accretion disk that result. The simulation domain includes a donor star, a point-mass accretor star, and an extended region about both stars.

There have been previous simulations that have involved outflows through L2, but with differences to our setup. Pejcha et al. (2016b) and Pejcha et al. (2016a) performed smoothed particle hydrodynamic (SPH) simulations of L2 mass-loss, and confirmed the prediction of Shu et al. (1979) regarding the binary mass ratios where material is bound or unbound. Hubová and Pejcha (2019) then broadened the initial conditions of their SPH simulationss to include material with position offsets or velocity offsets from L2, finding a wider range of outcomes.

Previous simulations of mass transfer that have involved mass loss through L2 and sometimes L3 include Nandez et al. (2014), Chen et al. (2017), MacLeod et al. (2018b), MacLeod et al. (2018a), Kadam et al. (2018), Reichardt et al. (2019), MacLeod and Loeb (2020b), MacLeod and Loeb (2020a), and Toyouchi et al. (2024). Several works investigating eccentric binaries and episodic MT also noted the occurrence of L2 mass loss (Regös et al., 2005; Church et al., 2009; Lajoie and Sills, 2010b), as did work focused on wind RLOF (Mohamed and Podsiadlowski, 2012). In contrast to these works, we focus on the approximately steady-state behavior of stable MT where we track the outflow of gas from the binary.

This paper is organized as follows. In Sec. 5.2 we discuss the numerical setup of our simulation, including the structure of the donor star and the heat added to the donor's envelope to initiate MT. Sec. 5.3 describes our analysis methods for characterizing the MT rates, the morphology of the outflow, the angular momentum carried by the gas, and the velocity/energies of outflowing gas. Sec. 5.4 presents our results for the effects of changing binary mass ratio and envelope heating rate on the outflow's angular momentum and velocity. We compare our results to prior simulations and discuss the implications of our results in Sec. 5.5, with a focus on the orbital evolution of the binary and the production of CSM, and we conclude in Sec. 5.6.

5.2 Simulation setup

5.2.1 Grid setup and boundary conditions

We perform Newtonian hydrodynamic simulations using the PLUTO code (Mignone et al., 2007; Mignone et al., 2012), considering MT between a donor star with core mass M_1 and an accretor with mass M_2, separated by a distance a in a circular orbit. Our dimensionless simulations have units such that

$$G = M_{\rm tot} = M_1 + M_2 = a = 1,$$

i.e., the orbital separation is 1 and the orbital period is 2π in these units. The mass ratio is defined as

$$q = \frac{M_2}{M_1} = \frac{\text{accretor mass}}{\text{donor mass}}.$$

See Sec. 5.2.5 for discussion of scaling our system to physical units for astrophysical binaries.

We adopt third-order Runge Kutta time-stepping (Gottlieb and Shu, 1998) and parabolic spatial integration (Mignone, 2014). The Riemann solver is set to be `hllc` (Toro et al., 1994). More details can be found in the PLUTO documentation.

The simulations are performed in 3D spherical coordinates (r, θ, ϕ) in a coordinate frame that is centered on the donor star and co-rotating with the binary's orbit. The radial grid extends logarithmically between the inner and outer boundaries

$$r_{\rm in} \simeq 0.2, \;\; r_{\rm out} = 5,$$

with the number of grid points chosen such that $\delta r/r \approx 0.01$, leading to about 300 radial grid points. The inner boundary varies slightly (from $r = 0.18$ to 0.24) with changing q, such that the total envelope mass is maintained at approximately 0.05 in code units. The inner radial boundary condition is reflective and the outer radial boundary condition is outflow, with the additional constraint that the radial velocity $v_r \geq 0$ at the outer boundary. The ϕ grid extends from 0 to 2π with 600 uniformly-spaced grid points, with resolution chosen such that $\delta\phi \approx \delta r/r$.

The θ grid extends from 0 to $\pi/2$ with a reflective boundary at $\pi/2$, such that we only simulate the top hemisphere of the binary, as the system is mirror symmetric with respect to the equatorial plane. At $\theta = 0$, we adopt PLUTO's "polaraxis" condition, which accounts for the singularity at the pole. We choose 1 point from $\theta = 0$ to 0.2, 10 points from $\theta = 0.2$ to 0.5, and 100 points from $\theta = 0.5$ to $\pi/2$, choosing lower resolution near the pole to avoid short timesteps, but making the resolution in the majority of the grid such that $\delta\theta \approx \delta r/r$.

We define Cartesian coordinates x, y, and z such that $\hat{x}$ points from the donor star to the companion/accretor, $\hat{x}$ and $\hat{y}$ are in the plane of the orbit, and $\hat{z}$ therefore points along the orbital axis of the binary ($\theta = 0$).

5.2.2 Equations solved

The equations that are solved in PLUTO are the continuity equations of mass, momentum, and energy as follows:

$$\frac{\partial}{\partial t}\rho + \nabla \cdot (\rho\vec{v}) = 0 \tag{5.1a}$$

$$\frac{\partial}{\partial t}(\rho\vec{v}) + \nabla \cdot (\rho\vec{v}\vec{v} + P\boldsymbol{I}) = -\rho\nabla\Phi + 2\rho\left(\vec{v} \times \vec{\Omega}\right) \tag{5.1b}$$

$$\frac{\partial}{\partial t}(E_t + \rho\Phi) + \nabla \cdot \left[(E_t + P + \rho\Phi)\,\vec{v}\right] = 0 \tag{5.1c}$$

where ρ is the mass density, P is the pressure, $\vec{v}$ the velocity in the corotating frame, $E_t = \frac{1}{2}\rho|\vec{v}|^2 + \rho u_{\rm int}$ is the kinetic+internal energy density, $u_{\rm int}$ is the specific

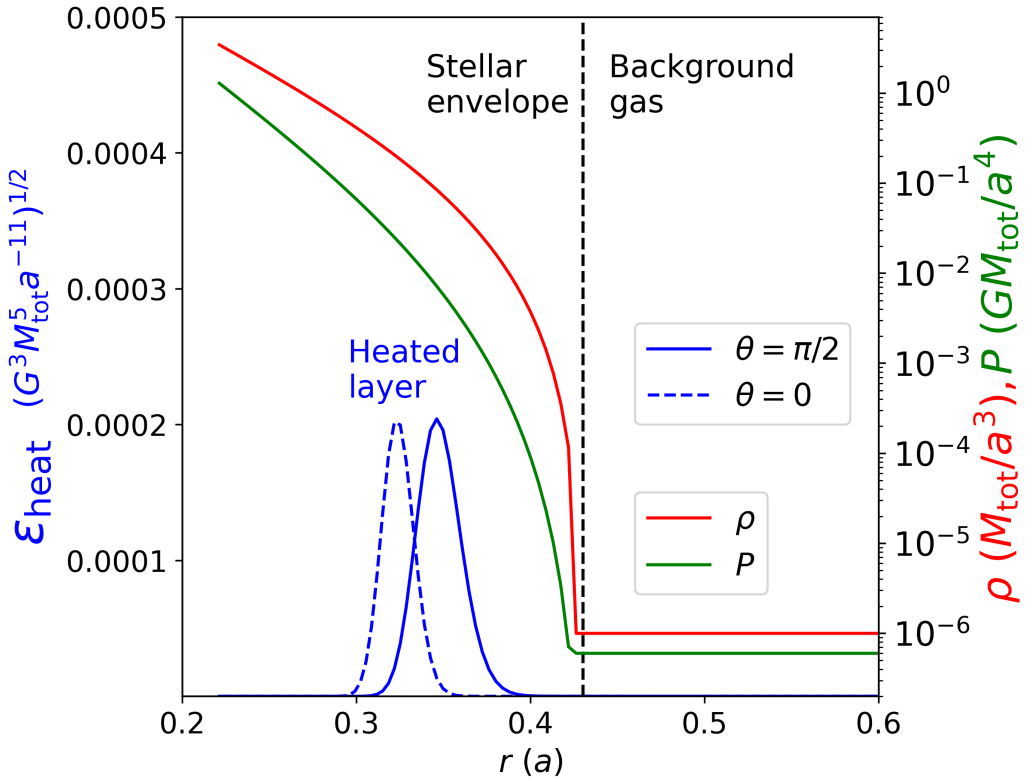


Figure 5.1: Initial conditions and heating for the $q = 0.5$, intermediate heat simulation, q_0.5_mid_heat. Left axis: The steady state heating profile, power per unit volume, for a line along the pole ($\theta \approx 0$, $\phi = 0$) and a line towards the companion star ($\theta = \pi/2$, $\phi = 0$). Right axis: The initial pressure and density, in code units, along a line towards the companion star ($\theta = \pi/2$, $\phi = 0$), with the vertical dashed line indicating the surface of the star.

internal energy, and $\boldsymbol{I}$ is the identity matrix. Φ is the time-independent gravitational potential, which is discussed further below. $\vec{\Omega} = \Omega\hat{z}$ is the orbital angular frequency (and $\Omega = 1$ in our code units), and $2\left(\vec{v} \times \vec{\Omega}\right)$ represents the acceleration due to the Coriolis force (which does no work and hence does not enter the energy equation). P and $u_{\rm int}$ are related by the equation of state (EOS), and we adopt PLUTO's "ideal" EOS

$$P = (\gamma - 1)\,\rho u_{\rm int} \tag{5.2}$$

where γ is the adiabatic index. This reduces to a polytropic EOS (Eq. 5.4) if no dissipative terms are included. We use $\gamma = 1.4$ for our fiducial simulations. In our test simulations, we find that changing γ does not greatly affect our results, and

so we believe that a more realistic equation of state would not strongly affect our overall conclusions.

PLUTO's `ENTROPY_SWITCH = SELECTIVE` condition is used, so that the entropy continuity equation (describing the conservation of entropy without dissipative terms) is used to update zones unless in the vicinity of a shock wave, which we found to help eliminate numerical issues in the accretion disk. We also adopt PLUTO's `SHOCK_FLATTENING = MULTID` condition, which reverts to the more diffusive `HLL` Riemann solver upon strong shock detection. This provides additional dissipation near strong shocks and greatly reduces numerical artifacts in our simulations.

5.2.3 Initial conditions

The majority of the gas is initialized in an envelope atop the core (i.e., above the inner boundary), while a small amount of gas constitutes a low-density ambient background outside the envelope. The core, with mass M_1, is treated as a point mass, and the envelope's self gravity is neglected. With the value of the inner radial grid (above), the mass in the envelope is much less than the mass in the core, justifying this assumption. The envelope is assumed to follow a polytropic EOS and is initialized in hydrostatic equilibrium, such that the initial ρ and P are given by

$$\rho = \left(\frac{\gamma - 1}{K\gamma} \left(\Phi_0 - \Phi \right) \right)^{\frac{1}{\gamma - 1}} \tag{5.3}$$

and

$$P = K\rho^{\gamma} \tag{5.4}$$

where K is the entropy constant, Φ is the external potential acting on the gas, and Φ_0 is the potential evaluated at the surface of the star.

The potential Φ is fixed to the Roche potential,

$$\Phi(\vec{r}) = -\frac{M_1}{|\vec{r}|} - \frac{M_2}{\left(|\vec{r} - a\hat{x}|^2 + \epsilon^2 \right)^{1/2}} - \frac{(x - \mu a)^2 + y^2}{2} \tag{5.5}$$

where $\vec{r}$ is the coordinate vector, $\mu = M_2/M_{\rm tot}$, ϵ is a Plummer softening length, and our choice of units entails the angular orbital frequency is $\Omega = 1$ and the orbital

separation is $a = 1$. We adopt $\epsilon = 0.05$ for our fiducial simulations, but vary the value in Appendix 5.C.2. The secondary M_2 is a point mass which could represent a stellar companion or a compact object. Its mass remains constant over the course of the simulation.

Throughout the course of the simulation, the center of mass (COM) is fixed and is determined by M_1 and M_2 but not the mass in the gas. The binary orbit separation a is also held constant in order to focus on steady-state stable MT. In our analysis, we use the Roche lobe calculator of Leahy and Leahy (2015) to determine the location of the Lagrange points for different mass ratios.

Note that when implementing the potential Φ, we are using a co-rotating frame, and PLUTO therefore internally includes the centrifugal force. However, because our origin is not at the COM, we must "manually" supply the μax portion of the centrifugal term (right term of Eq. 5.5). Therefore, $\Phi_{\rm setup}$, given in the `BodyForcePotential` section of PLUTO, is actually

$$\Phi_{\rm setup} = -\frac{M_1}{|\vec{r}|} - \frac{M_2}{\left(|\vec{r} - a\hat{x}|^2 + \epsilon^2\right)^{1/2}} + \mu ax. \tag{5.6}$$

The star is initialized underfilling its Roche lobe (RL), and the ambient material outside the envelope is initialized with a spatially uniform pressure and density, $P = 6 \times 10^{-7}$ and $\rho = 10^{-6}$. We also set a density floor during the simulations, enforcing a minimum density of $\rho = 10^{-9}$. The right-hand axis of Fig. 5.1 plots the initial density and pressure along the line connecting the stars at $\theta = \pi/2$, $\phi = 0$. The density and pressure increase deeper into the envelope of the donor star, and drop dramatically near the surface, plateauing to the initial values of the background material. The mass in the background material is much less than the mass in the envelope.

From Fig. 5.1, the polytropic density profile drops sharply near the surface and cannot be easily resolved. However, we do not believe resolving the initial surface scale height to be necessary for our simulations, as long as the width of the steady-state L1 MT stream is resolved. Simulations that seek to understand the onset and stability of MT may need a more realistic stellar structure and higher resolution near the surface, but that is beyond the scope of this work.

Initially, we assume perfect co-rotation with the orbit and all gas velocities are set to zero. We do not include cooling or viscosity in our simulations. Therefore, any

Simulation	q	x_0	K	$t_{\rm kh}$	$L_{\rm heat}$
q_0.5_low_heat	0.5	0.43	0.228	960	2.0e-6
q_0.5_mid_heat	″	″	″	525	3.6e-6
q_0.5_high_heat	″	″	″	200	9.5e-6
q_025	0.25	0.48	0.261	525	4.0e-6
q_1	1	0.38	0.187	525	3.2e-6
q_2	2	0.32	0.142	525	2.5e-6
q_0.5_low_res	0.5	0.43	0.228	523	3.6e-6

Table 5.1: Grid of 3D simulations, labeled by mass ratio and the amount of heat added to the envelope. The free parameters are: accretor/donor mass ratio q, maximum stellar surface radius x_0 (along the +x-axis), entropy constant K, and heating luminosity $L_{\rm heat}$. $t_{\rm kh}$ is the KH timescale for the heated layer. For all simulations, we adopt polytropic index $\gamma = 1.4$ and mass exterior to the center of the heated layer $M_{\rm ext} \approx 1.0 \times 10^{-3}$. The q_0.5_low_res simulation is nearly identical to q_0.5_mid_heat, but has a lower spatial resolution (see text).

accretion luminosity from M_2 is neglected. Our simulations may therefore be most applicable when the accretor is a star rather than a compact object. We also do not include radiative transfer or radiative forces on the gas, which may significantly accelerate the gas (Sec. 5.3.4) in some cases.

5.2.4 Injected heat

If no heat is added to the envelope, a star that initially underfills its RL remains in hydrostatic equilibrium and continues to underfill its RL, and no MT occurs. To instigate MT, we inject heat within the interior of the envelope, causing it to slowly expand. We set the power injected per unit volume, $\epsilon_{\rm heat}$, to be a Gaussian function of the Roche potential that is ramped up in time to a steady state value, such that

$$\epsilon_{\rm heat} \propto \exp\left(\frac{-\left(\Phi - \Phi_h\right)^2}{2\Delta\Phi^2}\right) \times \frac{1}{2}\left(\tanh\left(\frac{t - t_0}{\Delta t}\right) + 1\right). \tag{5.7}$$

Here, Φ_h is the potential at the center of the heated shell, and $\Delta\Phi$ is the width of the shell.

We assume the width of the heating to be the density scale height

$$\Delta\Phi = \left| \frac{\rho}{d\rho/d\Phi} \right| \text{ at } \Phi = \Phi_h, \tag{5.8}$$

which, given our initial density, implies

$$\Delta\Phi = (\Phi_0 - \Phi_h)\,(\gamma - 1)\ . \tag{5.9}$$

The heating rate reaches half its maximum steady-state value at t_0, and Δt controls how fast the heat is ramped up. We fix $t_0 = 15$ and $\Delta t = 5$ in all our simulations they are longer than the dynamical timescale of the initial star but shorter than the Kelvin-Helmholtz timescale of the heated envelope (see Eq. 5.12 later), so our results do not depend on t_0 and Δt. No heat is injected at equipotentials outside the stellar surface.

The normalization of the heating rate per unit volume in Eq. (5.7) is set by the total heat power added to the envelope

$$L_{\rm heat} = \int dV \epsilon_{\rm heat}. \tag{5.10}$$

The left axis of Fig. 5.1 shows the spatial heating profile for two latitudes θ, once the heating has been ramped up to its maximum value. The heating profile at $\theta = 0$ peaks at smaller radius than the profile at $\theta = \pi/2$, because the star is less extended at the pole than at the equator and heat is added as a function of equipotential.

For comparison between simulations, it is also useful to calculate the exterior mass to the peak of the heating profile, $M_{\rm ext}$, and the Kelvin-Helmholtz (KH) timescale, $t_{\rm kh}$, for the envelope to expand. We define these as

$$M_{\rm ext} = M(\Phi > \Phi_h), \tag{5.11}$$

and

$$t_{\rm kh} = \frac{M_1 M_{\rm ext}}{R_h L_{\rm heat}}, \tag{5.12}$$

where R_h is the approximate radius corresponding to Φ_h, which is roughly circular inside the donor star. We note from Table 5.2 that the timescale over which the envelope expands may be shorter than the thermal or nuclear timescale for a real star to expand and initiate MT. However, the main goal is to simulate high MT rates, and the MT rates in Table 5.2 are only slightly larger than those expected to occur in massive star binaries (e.g., Marchant et al., 2021; Wu and Fuller, 2022; Klencki et al., 2025), which can easily exceed $10^{-3}\ M_\odot/\text{yr}$.

Quantity	Code	Binary Example			
		A	B	C	D
M_1	2/3	10 $M_\odot$	10 $M_\odot$	10 $M_\odot$	2.8 $M_\odot$
M_2	1/3	5 $M_\odot$	5 $M_\odot$	5 $M_\odot$	1.4 $M_\odot$
a	1	0.1 au	0.22 au	1.04 au	0.03 au
$R_{\rm L1}$	0.442	9.5 $R_\odot$	21.3 $R_\odot$	98.8 $R_\odot$	3.1 $R_\odot$
$P_{\rm orb}$	2π	3 days	10 days	100 days	1 day
$L_{\rm heat}$	3.6e-6	3.5e39 erg/s	4.7e38 erg/s	1.0e37 erg/s	2.5e39 erg/s
$t_{\rm kh}$	525	250 days	830 days	8330 days	85 days
$\dot{M}$	0.6e-5	6.9e-2 $M_\odot$/yr	2.1e-2 $M_\odot$/yr	2.1e-3 $M_\odot$/yr	5.6e-2 $M_\odot$/yr
$\overline{v}'_{r,\rm inertial}$	0.15	55 km/s	37 km/s	17 km/s	51 km/s

Table 5.2: Conversion between code units to physical units for 4 example binaries. The numbers in code units are parameters and approximate results for the $q = 0.5$, intermediate heat simulation, q_0.5_mid_heat. M_1 and M_2 are the stellar masses, a the orbital separation, $R_{\rm L1}$ the volume-averaged Roche radius of the donor, $P_{\rm orb}$ the orbital period, $L_{\rm heat}$ the luminosity added to the donor's envelope, and $t_{\rm kh}$ the expansion timescale of the envelope (Eq. 5.12). $\dot{M}$ is the approximate MT rate (discussed in Sec. 5.3.2) and $\overline{v}'_{r,\rm inertial}$ is the characteristic radial velocity of an outflow (discussed in Sec. 5.3.4). The example binaries have their M_1 and a chosen as values appropriate for astrophysical binaries, and all other quantities are then calculated from code units using M_1, a, and G, the gravitational constant (see Eq. 5.13 for an example).

5.2.5 Varied parameters

The initial structure of the polytropic envelope is controlled by 6 parameters: a, M_1, M_2, K, γ, and Φ_0. These parameters are not independent and can be reduced by one degree of freedom - in this case, we calculate K based on the other parameters. Additionally, by working in units where $M_1 + M_2 = 1$ and $a = 1$, we further reduce the number of parameters by 2, leaving only 3 free parameters. We use the oche_tidal_equilibrium code[1] (Lu, 2025) to calculate the hydrostatic profile of a star in a tidal potential. Specifically, we calculate the value of K for a given $q = M_2/M_1$, γ, and Φ_0. Instead of the surface potential Φ_0, we use the surface position x_0 of the star along the +x-axis toward the companion, which is interchangeable with Φ_0.

[1] `https://github.com/wenbinlu/Roche_tidal_equilibrium`

In our simulations, we fix the polytropic index $\gamma = 1.4$ and $x_0/R_{L1} \approx 0.75$ (i.e. not changing the fraction the star fills its RL), and hence the initial conditions in different cases are only controlled by the mass ratio q. From test simulations performed in 2D polar coordinates, we found changes in the surface position x_0 not to affect our results. We also tested changing γ in 2D simulations, with values of 4/3, 1.4, and 5/3, and found the effects to be subdominant compared to the effect of changing q. Therefore, we consider four mass ratios of $q = 0.25$, 0.5, 1, and 2 as our initial conditions for the 3D simulations.

The dynamical evolution of the system is controlled by 2 more parameters: the heating luminosity $L_{\rm heat}$ and central position of heat deposition Φ_h (and the thickness of the heated layer $\Delta\Phi$ is a derived parameter given by Eq. 5.9). For a given q, we determine Φ_h by taking a *fixed* exterior mass to the Φ_h layer $M_{\rm ext} \approx 10^{-3}$ in code units (Eq. 5.11), which determines the depth of the heating inside the envelope, because our 2D test simulations showed it to have no impact, as long as the envelope mass exterior to the heating profile is well resolved and the heating is not too close to the inner radial boundary. Therefore, across different simulations, we only vary the amount of heating injected into the star $L_{\rm heat}$, which controls the mass transfer rate.

Table 5.1 summarizes the varied properties in the grid of simulations that we perform. The top 3 rows correspond to simulations with fixed $q = 0.5$ and differing magnitudes of heat added ("high", "mid", "low"). The following 3 rows correspond to different mass ratios q, but keeping heating approximately fixed to "mid" heating values, such that $t_{\rm kh}$ is kept at 525. Finally, we include a low spatial resolution version of one of the simulations, the results of which are discussed in Appendix 5.C. This low resolution simulation has $\delta r/r = 0.015$ instead of 0.01 (Sec. 5.2.1), and correspondingly lower resolution in θ and ϕ coordinates based on using approximately cubic cells.

In the plots that follow, we in general use the default case of intermediate heating, q=0.5 simulation, q_0.5_mid_heat, when showing simulation snapshots.

Because we work in dimensionless code units, we scale our simulations to physical units in example binaries in Table 5.2. As an example, to convert from velocity in code units $v_{\rm code}$ to a physical value v, we use

$$v = v_{\rm code} \times \sqrt{\frac{G(M_1 + M_2)}{a}}\,. \tag{5.13}$$

We see that the typical MT rates in the simulations are larger than normally encountered in stellar evolution, and they do correspond to the regime of Lu et al. (2023) in which the gas cools inefficiently and our assumption of no cooling is reasonable. Although we are agnostic to the mechanism driving the expansion of the donor star, the heating rates are consistent with those expected for wave heating (e.g., Wu and Fuller, 2020), within the considerable uncertainties.

5.3 Analysis

5.3.1 Flow Morphology

We run the simulations until significant mass transfer has occurred and a quasi-steady state has been reached, where calculated quantities such as the MT rate (Sec. 5.3.2) are approximately constant. For the simulation q_0.5_mid_heat, Fig. 5.2 plots two density slices at a late simulation time ($t = 600$), when the simulation has reached a quasi-steady state. One slice lies in the equatorial plane (top panel) and the other is a meriodional slice (bottom panel) corresponding to the x-z plane, which is orthogonal to the orbital plane and includes the companion star M_2. The density is plotted out to the maximum radius, $r_{\rm out} = 5$. The core of the donor corresponds to the central white-colored region below the inner boundary, which is not part of the computational domain.

The equatorial slice demonstrates the accretion disk around the companion and tails of material outflowing approximately from L2 and L3 points, which then merge to create a broad spiral outflow. The meriodonal slice shows how gas in the accretion disk and outflow is concentrated near the equator, with the density falling off toward the pole. The gas morphology is discussed further in Figs. 5.3 – 5.5.

Near the start of the simulation, the heat added to the donor's envelope causes it to slowly expand on a thermal time $t_{\rm kh}$ given by Eq. 5.12 (much longer than its dynamical time) such that it remains close to hydrostatic equilibrium. The outer regions of the donor's envelope expand, but the inner layers below the heated region remain almost unchanged in terms of mass, density and pressure. Once the star's surface reaches its RL equipotential, mass begins to flow through the inner Lagrange point, L1, toward the companion. Fig. 5.3 demonstrates the progression of the MT by plotting the mass density in the equatorial plane. Note that $t = 2\pi$ represents one orbit of the binary, and the star's dynamical time (for this mass ratio) is $t_{\rm dyn} \approx 0.35$.

By $t = 100$, the star's outer layers have puffed up and a thin stream of gas flows through L1 and feeds a small accretion disk centered at the companion. At $t = 200$,

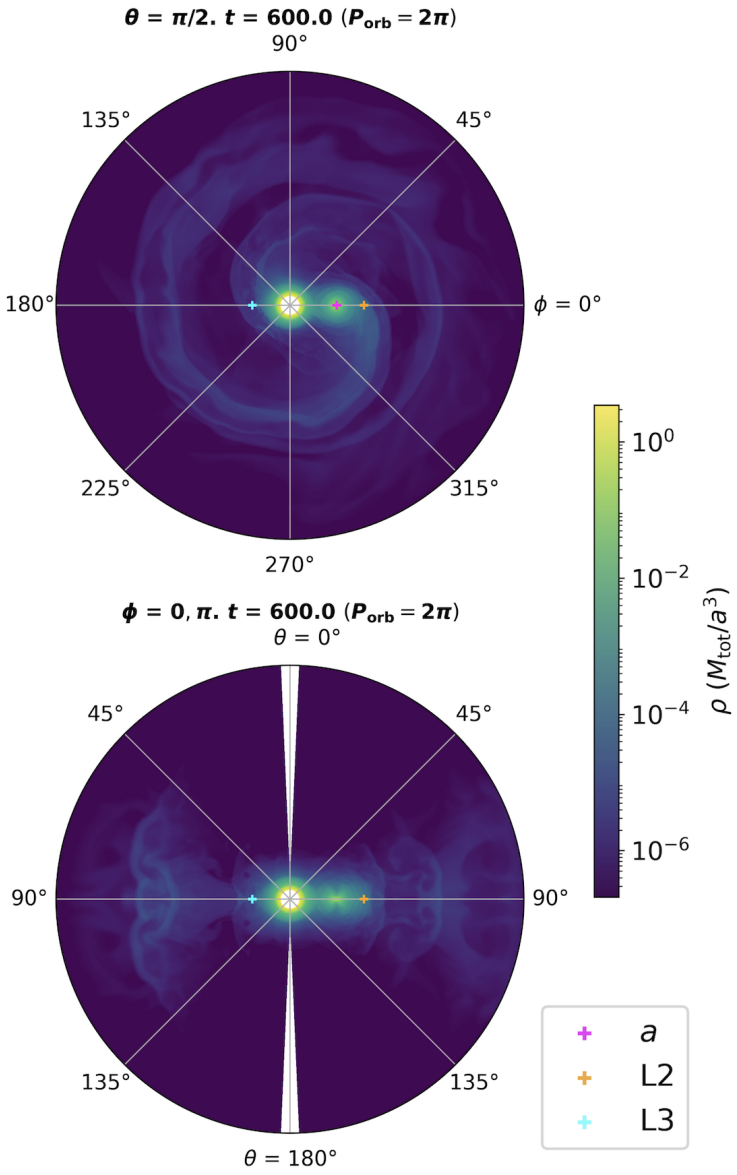


Figure 5.2: Equatorial (top) and meriodional (bottom) slices of the mass density in the intermediate heating, q=0.5 simulation, q_0.5_mid_heat. The domain's full radial extent, out to $r = 5$, is plotted. For the meriodonal slice, we plot the plane that lies between the donor and accretor ($\phi \approx 0$ and $\phi \approx \pi$) and we only simulate $\theta < \pi/2$, so the bottom half of each image is mirrored from the top. The white triangle near $\theta = 0$ is due to low grid resolution at the pole. The legend labels the orbital separation and outer Lagrange points (a is not labeled in the bottom panel for clarity).

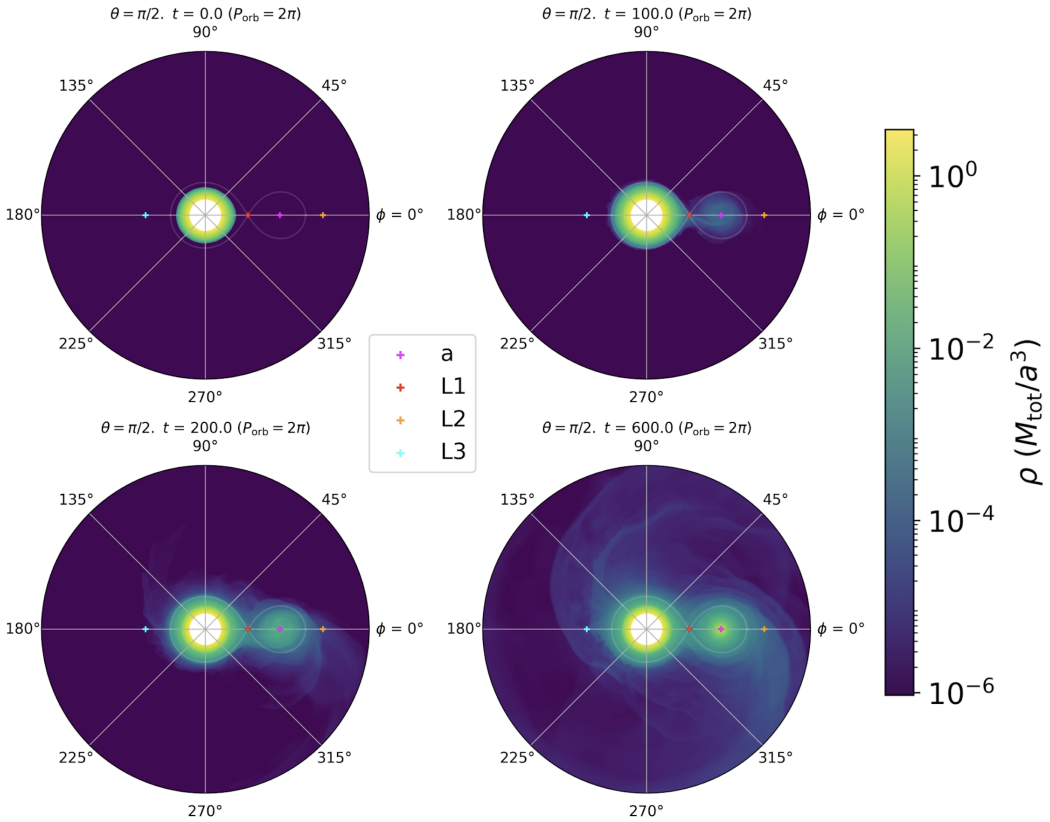


Figure 5.3: Similar to the equatorial slice of Fig. 5.2, but zoomed in, with a maximum $r = 2.2$, and showing the simulation at different timesteps. The white contours show the Roche lobes of the binary. The orbital separation and 3 Lagrange points are labeled in the legend.

the accretion disk around the companion has grown substantially. A circumbinary outflow can be seen, as some gas escapes the disk via a stream in the vicinity of L2. Another stream is located on the left side of the donor, in the vicinity of L3. By $t = 600$, the amount of gas outflowing in these streams has increased greatly. The streams from L2 and L3 are expected from prior work (Shu et al., 1979; Pejcha et al., 2016a). Qualitatively, Figs. 5.2 and 5.3 demonstrate that gas in the disk is able to outflow through outer Lagrange points and escape from the binary.

Note that Figs. 5.2 and 5.3 are in a co-rotating frame, so the outflowing streams lag behind the binary, forming a spiral pattern as gas moves outward and loses angular velocity (Shu et al., 1979). Spiral internal shocks develop within these streams, as can be seen both in the density and velocity profiles in the circumbinary outflow.

In Fig. 5.4, we overplot velocity vectors in the equatorial plane, at one of the same snapshots as Fig. 5.3. The two panels are the same snapshot, with the upper panel

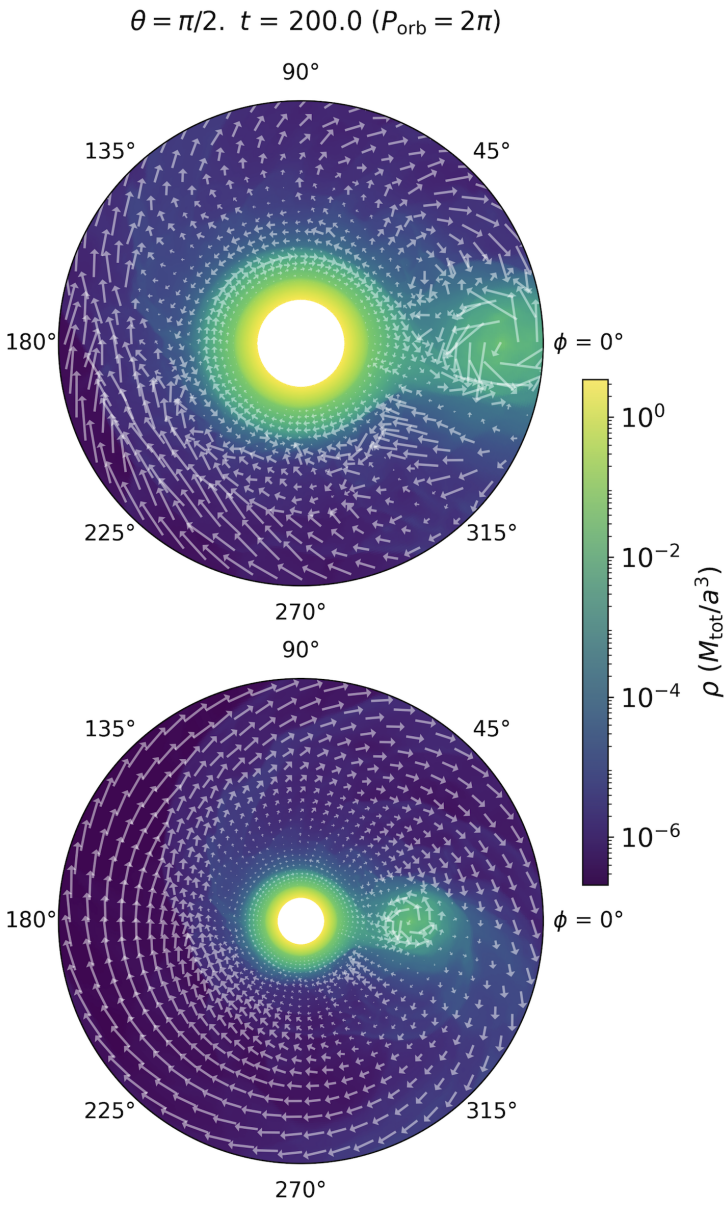


Figure 5.4: Similar to Fig. 5.3, but overplotting the direction of fluid velocities, projected onto the equatorial plane (white arrows). The panels are the same snapshot, but with the bottom panel zoomed out to show larger extent. Velocities are not plotted at very cell, but chosen to illustrate the general behavior.

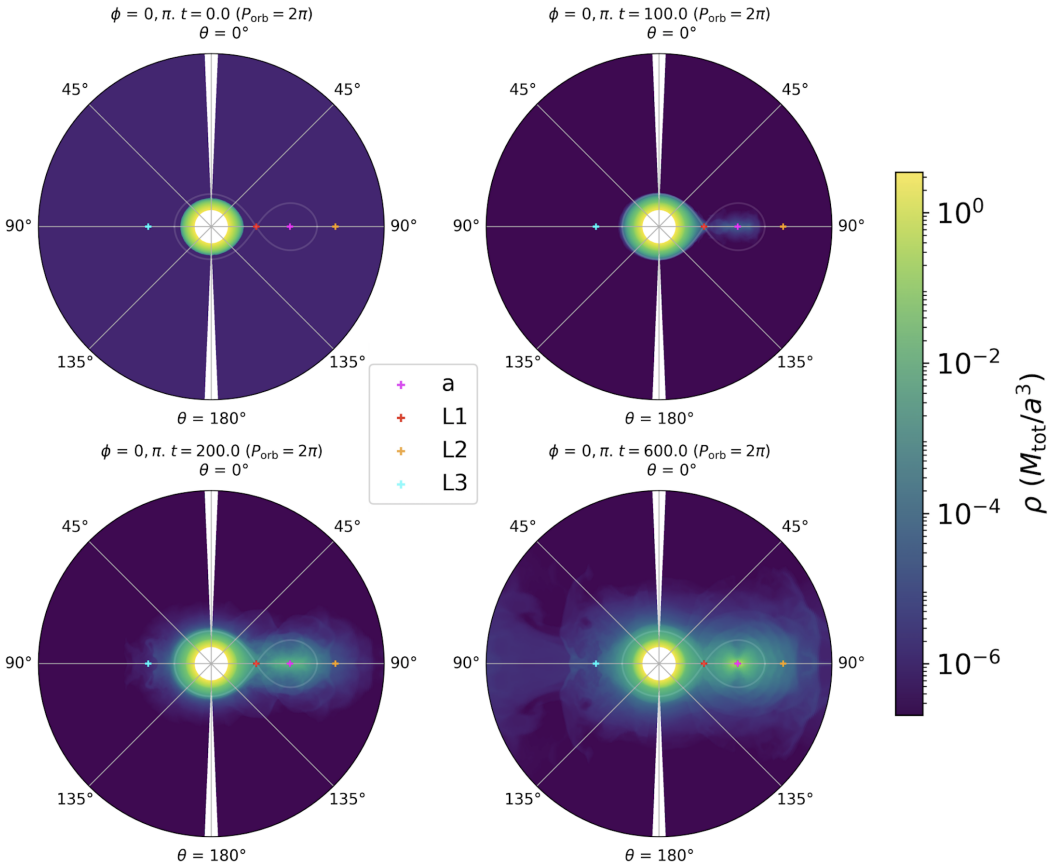


Figure 5.5: Similar to the meriodional slice of Fig. 5.2, but zoomed in, with a maximum $r = 2.2$, and showing the simulation at different timesteps. The white contours show the Roche lobes of the binary. The 3 Lagrange points are labeled in the legend.

more zoomed in. The fluid flows from the donor star toward the secondary, then circulates the secondary in the accretion disk. Beyond the orbit, the velocity vectors trace the outflowing spiral pattern.

Inside the donor star, the outer layers develop a retrograde flow, opposite to the direction of co-rotation. There appears to be two effects contributing to this. The first is the expansion of the donor star, as this retrograde pattern begins to develop while the star expands but before significant MT occurs. This can be understood through conservation of angular momentum in the (inertial) lab frame — as the outer layers expand, their rotation frequency drops and hence they lag behind co-rotation. The second effect is the MT itself, as the flow velocities grow larger as MT occurs. In general, the fluid velocities in the donor star are less than the fluid velocities near L1. Future work should more carefully examine the fluid flows within mass

transferring donor stars, as the asynchronous rotation of the layers near the RL may significantly modify the MT transfer rate, as compared to the analytic prediction based on the often adopted corotating hydrostatic configuration.

Fig. 5.5 shows the same simulation and same snapshots, but now for the meriodional plane. The formation of the accretion disk around the companion can be seen edge-on. Although the mass loss tends to be equatorially concentrated, the outflow forms a thick torus due to shock heating and the lack of cooling in our simulations (see also MacLeod et al., 2018a).

In the top panel of Fig. 5.6, we plot the density drop-off as a function of polar angle for simulations of varying q. The densities are normalized by their value at $\theta = \pi/2$, and averaged over radii, from $r = 2$ to the outer radial boundary at $r_{\rm out} = 5$. The densities are also averaged over ϕ and time. In all cases, ρ tends to decrease away from the equator with a roughly exponential profile. With increasing mass ratio (relatively heavier accretor), ρ drops less steeply away from the equator, with $q = 0.25$ showing the most equatorially concentrated outflow, and $q = 2$ showing the least equatorially concentrated outflow. Some curves show slight upticks near $\theta = 0$, but because of the low resolution near the pole, this behavior may not be reliable.

In Appendix 5.A.3, we estimate the average opening angle of outflowing gas $\theta_{\rm outflow,av}$, which corresponds to one density scale height (one e-folding from the equatorial value) and quantifies how equatorially concentrated the outflow is. The bottom panel of Fig. 5.6 shows $\theta_{\rm outflow,av}$ plotted versus time for simulations of varying q. The steady-state value of $\theta_{\rm outflow,av}$ increases with increasing q, from $\approx 10^{\rm o}$ for $q = 0.25$ to $\approx 30^{\rm o}$ for $q = 2$. The physical reason for this trend of q is unclear. This opening angle may change if cooling is included, which would likely reduce the thickness of our disk and potentially change the geometry of the outflow. Therefore, the angles we calculate are likely more accurate at higher MT rates (see Table. 5.2).

Further properties of the gas related to temperature, optical depth, and the photon diffusion time are discussed in Appendix 5.A and 5.A.1. Because we find large optical depths and long photon diffusion times in all of the simulations when they are scaled to high MT rates, our adiabatic assumption and inefficient gas cooling is justified. The possible observational signature of the MT we simulate is discussed in Appendix 5.A.2. Properties of the accretion disk around M_2 are discussed in Appendix 5.A.4.

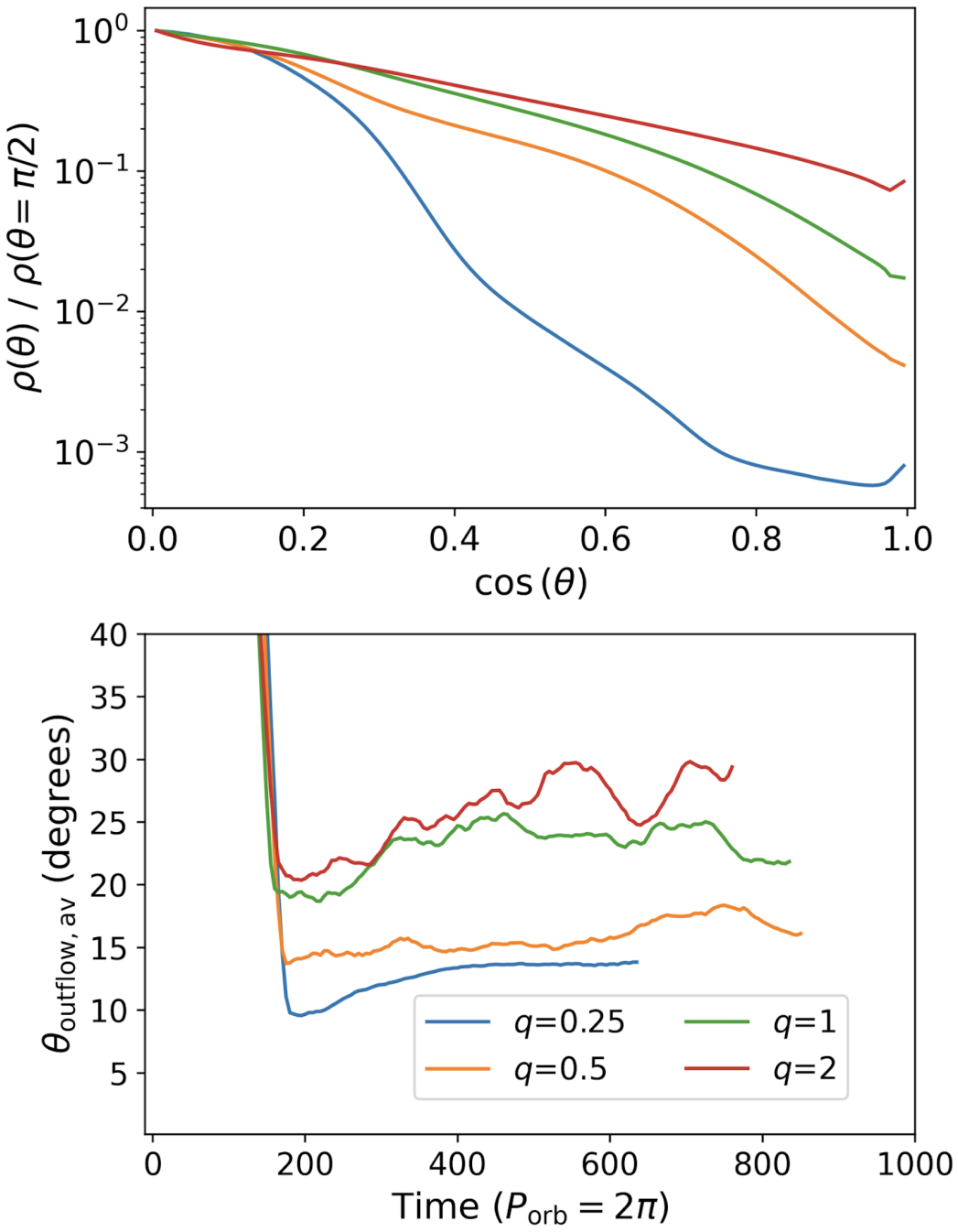


Figure 5.6: Top: The average outflow density (normalized by its value at the equator) as a function of angle from the equatorial plane, for simulations of varying q (simulations q_025, q_0.5_mid_heat, q_1, q_2). The x-axis corresponds to θ extending from $\pi/2$ to 0 (equator to pole). Bottom: The opening angle of the outflowing gas $\theta_{\text{outflow},av}$, plotted versus simulation time, for the same simulations. $\theta_{\text{outflow},av}$ corresponds to one density scale height, such that the density has dropped by a factor of $1/e$ compared to its value in the equatorial plane. Each curve is time-smoothed using a rolling average.

5.3.2 Mass transfer rates

We calculate the mass loss rate of the donor by finding the rate of change of mass within a sphere of radius x_0, where x_0 is the maximum radius of the initial stellar surface, i.e.,

$$\dot{M}_{\rm donor} = \frac{d}{dt} \int_{r=r_{\rm in}}^{r=x_0} \rho \, dV \,, \tag{5.14}$$

where $r_{\rm in}$ is the radius of the inner boundary. An alternative way to calculate the MT rate is via a surface flux integral, i.e. $\dot{M}_{\rm donor,alt} = \int \rho \vec{v} \cdot \vec{dA}$. This yields similar (but not identical) results. Similarly, the mass loss rate from the entire computational domain is

$$\dot{M}_{\rm total} = \frac{d}{dt} \int_{r=r_{\rm in}}^{r=r_{\rm out}} \rho dV, \tag{5.15}$$

where the radial portion of the integral is performed from the inner boundary with radius $r_{\rm in}$ to the outer boundary with radius $r_{\rm out}$.

Fig. 5.7 plots $\dot{M}_{\rm donor}$ and $\dot{M}_{\rm total}$ over time for the simulation q_0.5_mid_heat. The heating inside the star has been ramped up to its maximum value by $t = 30$, but the MT rate does not stabilize until about $t = 200$, comparable to the thermal time $t_{\rm kh}$ of the donor (Table 5.1). The rate at which mass leaves the domain also lags behind, stabilizing around $t = 400$, because it takes time for the circumbinary outflow to form and travel to the outer boundary. After $t = 400$, the mass loss rates are about equal, and the simulation enters a quasi-steady state where the mass loss rate is nearly constant. Additionally, the mass in the disk is about constant, i.e. the disk is being replenished from the donor star at about the same rate as which mass is lost from the system.

As seen in Fig. 5.3, streams of outflowing gas originate in the vicinity of both L2 and L3. We estimate the mass outflow rate in each of these streams by integrating the mass flux over two surfaces of constant radius but limited in angles. With $r_{\rm L2}/r_{\rm L3}$ as the radial coordinate of L2/L3, one extends around L2 with a radius of $1.1\times r_{\rm L2}$, from $\phi = -\pi/2$ to $\pi/4$, and the other wraps around L3 from $\phi = \pi/2$ to $5\pi/4$ with a radius of $1.1\times r_{\rm L3}$. Both surfaces extend from $\theta = 1$ to $\pi/2$. While the exact boundaries of these surfaces are a bit arbitrary, they appear to capture the majority of the mass flow in these 2 streams. Note that for our $q = 2$ simulation, L2 lies on

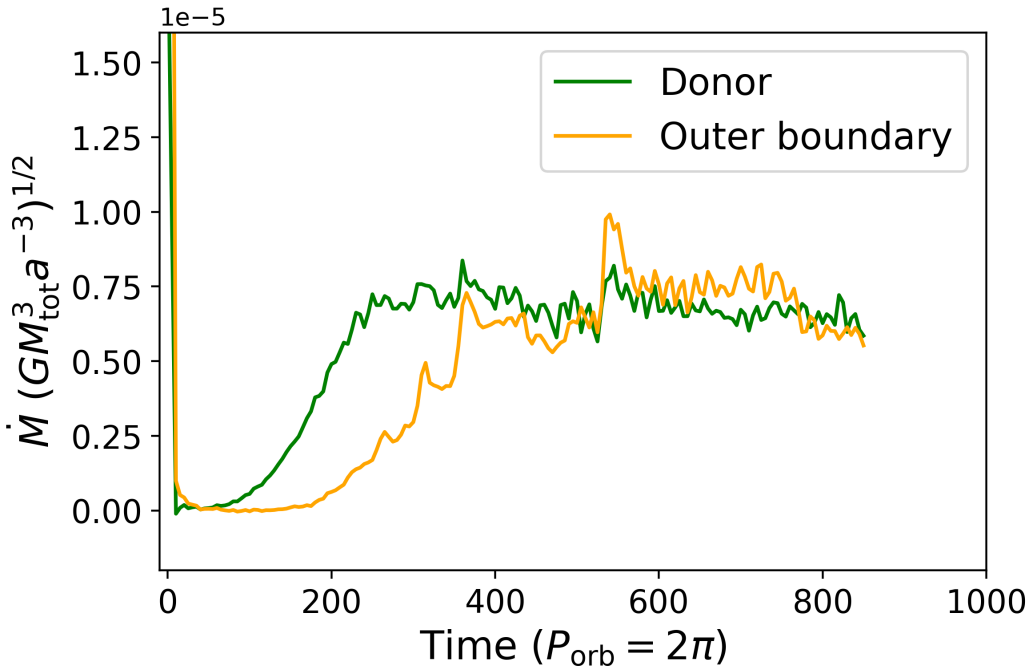


Figure 5.7: The mass loss rate of the donor star (Eq. 5.14) and the mass loss rate of the entire simulation domain (Eq. 5.15), plotted versus time for the q=0.5, intermediate heat simulation, q_0.5_mid_heat. A quasi-steady state is reached by $t \simeq 400$.

the side of the donor and L3 on the side of the accretor, i.e. reversed relative to the points plotted in Fig. 5.3.

Fig. 5.8 plots the ratio of the mass flux near L2 to the mass flux near L3, for simulations of varing q. The ratio reaches roughly steady-state values by $t = 400 - 500$, which is similar to when the mass transfer rates reach a quasi-steady state (Fig. 5.7). There is a trend where the ratio substantially decreases with increasing q from $q = 0.25$ to $q = 1$. The ratios for $q = 1$ and $q = 2$ are approximately equal, with a value between unity and two. Overall, we see that the majority of outflowing gas leaves near the L2 point, even when L2 is on the side of the donor star (and farther away from the accretion disk) in the case of $q = 2$.

5.3.3 Angular momentum fluxes

We compute the specific angular momentum (AM) carried away by the outflowing gas. The specific AM (along $\hat{z}$) of the L1, L2, and L3 points are given by $h_{\rm L1} = \Omega(r_{\rm L1} - r_{\rm com})^2$, $h_{\rm L2} = \Omega(r_{\rm L2} - r_{\rm com})^2$, and $h_{\rm L3} = \Omega(r_{\rm L3} - r_{\rm com})^2$, where $r_{\rm L1}$, $r_{\rm L2}$, $r_{\rm L3}$ and $r_{\rm com}$ are the radial coordinates of L1, L2, L3 and the COM, respectively.

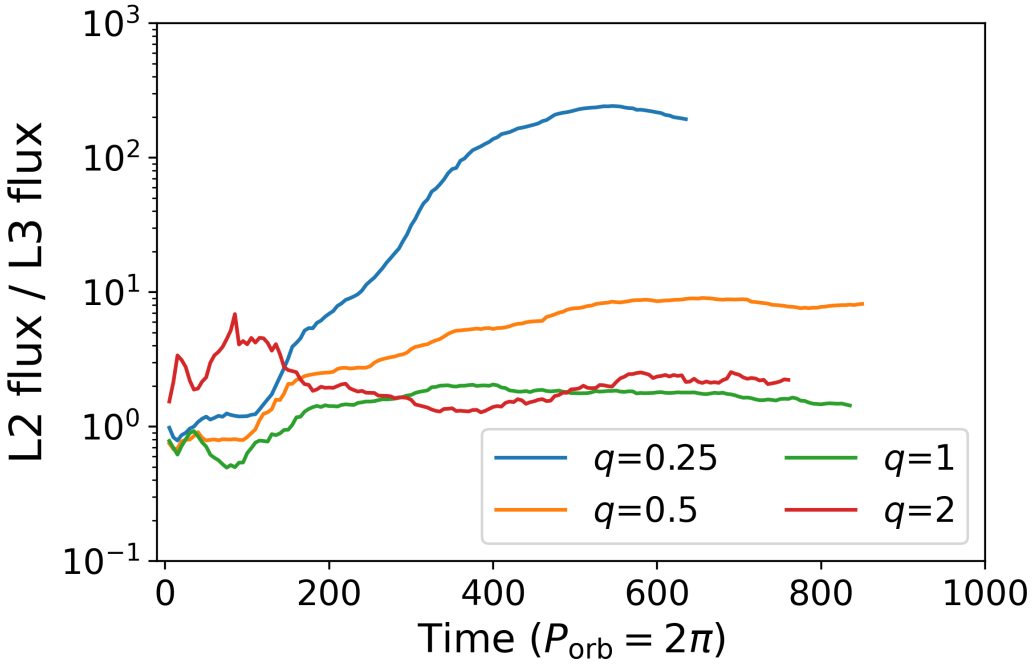


Figure 5.8: The ratio between the mass outflow rates in the stream originating near L2 and in the stream originating near L3. Curves are plotted for varying mass ratio for the same simulations as Fig. 5.6. See text for a description of the surface areas over which the mass flux is integrated for this calculation. Each curve is time-smoothed using a rolling average.

q	$h_{\rm L1}$	$h_{\rm L2}$	$h_{\rm L3}$	h_{M_1}	h_{M_2}
0.25	0.19	1.62	1.17	0.04	0.64
0.5	0.06	1.56	1.29	0.11	0.44
1.0	0.0	1.44	1.44	0.25	0.25
2.0	0.06	1.56	1.29	0.44	0.11

Table 5.3: For different co-rotating locations in the binary, the z-component of the specific AM, h, is calculated for the values of q considered in this work. h is given in units of $\sqrt{GM_{\rm tot}a}$. See text for the relevant equation to calculate h for each point.

The specific AM of M_1 and M_2 (also along $\hat{z}$) are given by $h_{M_1} = \Omega r_{\rm com}^2$ and $h_{M_2} = \Omega(a - r_{\rm com})^2$. Note again that, for the $q = 2$ simulation, L2 is on the side of the donor star, and L3 on the side of the accretor. The h values for the different q considered in this work are summarized in Table 5.3.

The specific AM $\vec{h}$ of an arbitrary fluid element, with coordinate $\vec{r}$ and velocity $\vec{v}$ in the simulation frame, is given by

$$\vec{h} = (\vec{r} - \vec{r}_{\rm com}) \times (\vec{v} - \vec{v}_{\rm com})_{\rm nr} \tag{5.16}$$

$$= (\vec{r} - \vec{r}_{\rm com}) \times \left(\vec{v} + \vec{\Omega} \times (\vec{r} - \vec{r}_{\rm com})\right) \tag{5.17}$$

where $\vec{r}_{\rm com}$ and $\vec{v}_{\rm com}$ are the coordinate and velocity of the binary's COM (in the co-rotating frame). The subscript "nr" refers to evaluation in a non-rotating frame. Therefore, the term $\vec{\Omega} \times (\vec{r} - \vec{r}_{\rm com})$ provides the velocity transformation from the co-rotating frame, where the simulations are performed, to a non-rotating frame. We are interested predominantly in the $\hat{z}$ component of the AM, as the orbital axis of the binary is along $\hat{z}$. The rate of AM outflow $\dot{L}_z$ over a surface with area element $\vec{dA}$ is given by

$$\dot{L}_z = \int_A h_z \rho \vec{v} \cdot \vec{dA} \, . \tag{5.18}$$

Similarly, the rate of mass flow through the same surface can be written as

$$\dot{M} = \int_A \rho \vec{v} \cdot \vec{dA} \tag{5.19}$$

and the average specific AM $h_{\rm loss}$ of the outflowing material through this surface is the ratio of these two integrals, i.e.

$$h_{\rm loss} = \frac{\dot{L}_z}{\dot{M}}. \tag{5.20}$$

Note that Eq. 5.19 uses an area integral over the flux to evaluate the mass flow rate, instead of a time derivative of a volume integral (see discussion following Eq. 5.14).This form is chosen to match the form of Eq. 5.18, and the value $h_{\rm loss}$ is more stable over time when evaluating both integrals as surface integrals.

We find that the value of $h_{\rm loss}$ asymptotes with increasing radius, reaching a nearly constant value similar to that of the L2 point (see Appendix 5.B and Fig. 5.15). The values of $h_{\rm loss}$ for simulations of varying q are discussed further in Sec. 5.4.1.

5.3.4 Speed and energy of outflowing material

We also compute the velocity and energy of the outflowing gas. Velocities relative to the center of mass are

$$\vec{v}_{\rm inertial} = \vec{v} + \vec{\Omega} \times (\vec{r} - \vec{r}_{\rm com}).$$

The radial component $v_{r,\rm inertial}$ is calculated as

$$v_{r,\rm inertial} = \vec{v}_{\rm inertial} \cdot \frac{\vec{r} - \vec{r}_{\rm com}}{|\vec{r} - \vec{r}_{\rm com}|}\,. \tag{5.21}$$

We define the mass-weighted angle-averaged velocity $\overline{v}_{r,\rm inertial}$ as

$$\overline{v}_{r,\rm inertial} = \frac{\int \rho v_{r,\rm inertial} dA}{\int \rho dA}. \tag{5.22}$$

where the integral is performed over a sphere at a constant $|\vec{r} - \vec{r}_{\rm com}|$. Doing the integral instead over constant r does not change the following results greatly, which is unsurprising given that the COM is located close to the origin, relative to the outer regions of the simulation domain.

The total inertial frame energy per unit mass, $E_{\rm tot}$, is calculated as

$$E_{\rm tot} = \frac{|\vec{v}_{\rm inertial}|^2}{2} + u_{\rm int} + \Phi_{\rm grav}, \quad \Phi_{\rm grav} = -\frac{M_1}{|\vec{r}|} - \frac{M_2}{|\vec{r} - a\hat{x}|}, \tag{5.23}$$

where the internal energy is $u_{\rm int} = \frac{P}{(\gamma-1)\rho}$ and the last term corresponds to the combined gravitational potential of the stars. Similarly, the mass-weighted angle-averaged energy is

$$\overline{E_{\rm tot}} = \frac{\int \rho E_{\rm tot} dA}{\int \rho dA}, \tag{5.24}$$

where again the integral is performed over constant $|\vec{r} - \vec{r}_{\rm com}|$. The Bernoulli parameter B is given by

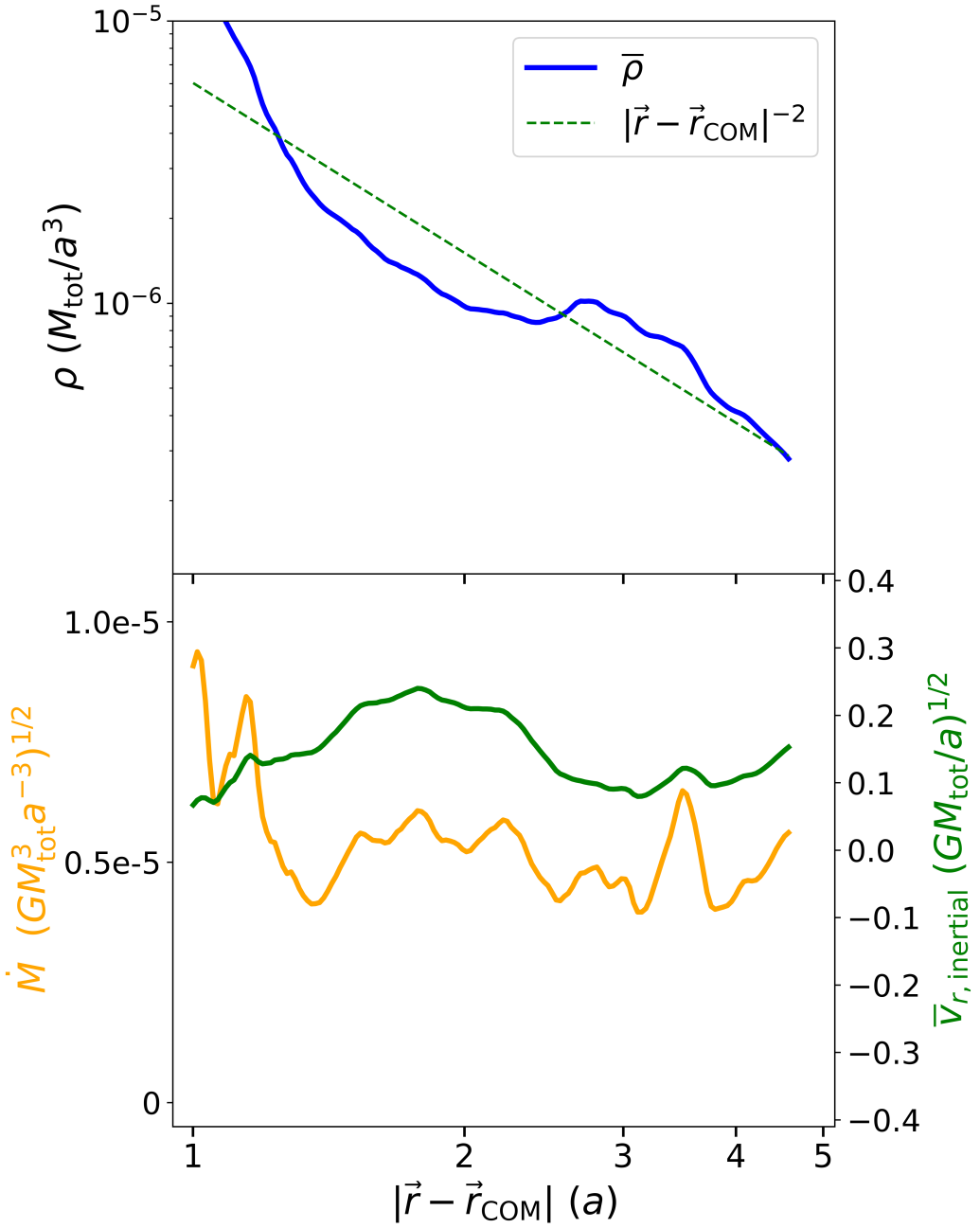


Figure 5.9: Properties of outflowing gas as a function of its distance from the binary COM for the $q = 0.5$, intermediate heat simulation, q_0.5_mid_heat. Top: the angle-averaged density $\bar{\rho}$, in units of $M_{\rm tot}/a^3$, with a $|\vec{r} - \vec{r}_{\rm com}|^{-2}$ power-law fit shown to guide the eye. Bottom: the mass-weighted angle-averaged radial velocity $\overline{v}_{r,\rm inertial}$, and the mass outflow rate, evaluated at surfaces of constant $|\vec{r} - \vec{r}_{\rm com}|$.

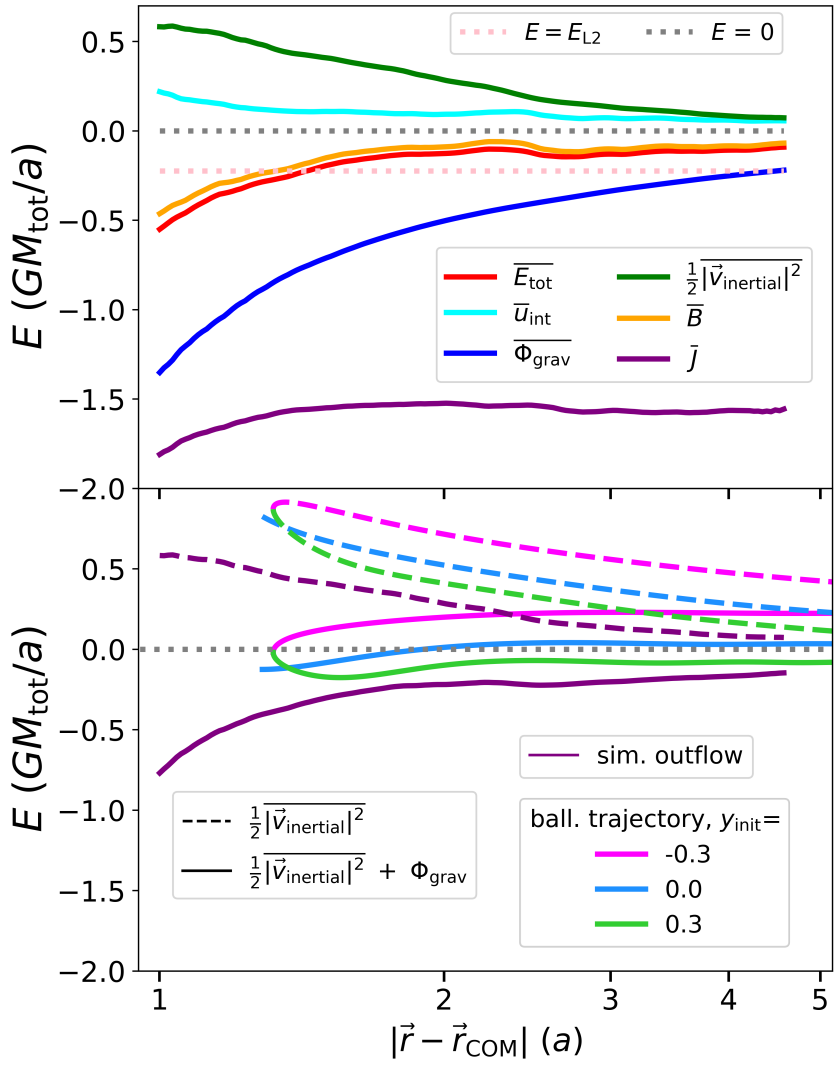


Figure 5.10: Top: The specific total energy $\overline{E_{tot}}$ and each of its component energies (kinetic, internal, and gravitational potential), as seen in Eq. 5.23, as well as the Bernoulli parameter $\bar{B}$ (Eq. 5.25) and Jacobi constant $\bar{J}$ (Eq. 5.26). All quantities are mass-weighted and angle-averaged. Dotted lines show where the specific energy equals 0 and E_{L2}, the kinetic + gravitational energy of the L2 point. Bottom: A comparison of simulation outflow properties to ballistic trajectories. Purple lines correspond to our simulation outflow. Other colors correspond to ballistic trajectories initialized from rest near L2, but with varying y-coordinates from -0.3 to 0.3 (in units of a). The kinetic (dashed lines) and kinetic plus gravitational energy (solid lines) are shown for both the outflow and the ballistic trajectories.

$$B = E_{\rm tot} + \frac{P}{\rho}. \tag{5.25}$$

and the Jacobi constant J is given as the sum of the Roche potential and the kinetic energy in the co-rotating frame

$$J = \frac{1}{2}v^2 + \Phi. \tag{5.26}$$

It is possible to show that the Jacobi constant is also given by $J = |\vec{v}_{\rm inertial}|^2/2 + \Phi_{\rm grav} - \Omega h_z$, where h_z is the z-component of the specific AM. This implies that, as fluid elements gain AM from the binary's torque, they can gain orbital energy as they move out to larger radii. We calculate the corresponding mass-weighted angle-averaged values $\bar{B}$ and $\bar{J}$ similar to $\overline{E_{\rm tot}}$.

Fig. 5.9 shows the density, speed, and energetics of the outflow as a function of distance from the COM, for a typical simulation snapshot. The top panel shows that the angle-averaged density, $\bar{\rho}$, approximately follows a $|\vec{r} - \vec{r}_{\rm com}|^{-2}$ dependence, as expected for a constant mass loss rate and outflow velocity. However, unlike a spherically symmetric wind, the outflow density is concentrated near the equatorial plane. In addition, the kinetic energy of the outflow is dominated by the azimuthal velocity, as expected for a disk-like outflow.

The bottom panel shows the angle-averaged radial velocity $\overline{v}_{r,\rm inertial}$ and the mass outflow rate $\int dA\, \rho v_{r,\rm inertial}$, where the integral is performed over surfaces of constant $|\vec{r} - \vec{r}_{\rm com}|$. We find that $\overline{v}_{r,\rm inertial}$ varies somewhat with radius between $\overline{v}_{r,\rm inertial}/v_{\rm orb} \sim 0.1 - 0.2$, where $v_{\rm orb} = \sqrt{GM_{\rm tot}/a}$ is the system's orbital velocity. The mass outflow rate is approximately steady with radius.

The top panel of Fig. 5.10 shows the total specific energy and the component energies, each of which is mass-weighted and angle-averaged. Near the outer boundary, the total specific energy $\overline{E_{\rm tot}}$ and Bernoulli parameter $\overline{B}$ slowly increases as the fluid elements climb up the gravitational potential ($\Phi_{\rm grav}$ in Eq. 5.23 becoming less negative). Although the outflow is not exactly ballistic, the Jacobi parameter $\overline{J}$ is approximately constant.

The final fate of the material is unclear. The averaged internal energy $\overline{u_{\rm int}}$ and kinetic energy $\frac{1}{2}\overline{|\vec{v}_{\rm inertial}|^2}$ appear to asymptote with radius. If this continues at larger radii, the total energy would continue to increase and the material would become unbound. Physically, this could entail either continued energy input by torques from the binary

or work done by pressure gradient forces (the Bernoulli parameter B does not stay constant for a non-steady flow). However, the tidal torquing far from the binary is minimal - for the simulation snapshot shown in Fig. 5.9, the increase in average specific AM from $|\vec{r} - \vec{r}_{\rm com}| = 3$ to $|\vec{r} - \vec{r}_{\rm com}| \approx 5$ is less than 3% (see also Fig. 5.15).

In the bottom panel of Fig. 5.10, we compare the outflow energetics to that of ballistic trajectories launched near L2.. We initialize test particles at a slightly greater x-coordinate than L2, and at y-coordinates (in units of a) of {-0.3, 0, and 0.3} and integrate the equations of motion using a fourth-order Runge-Kutta solver. The trajectories wrap around the binary in a spiral, with trajectories launched at positive y (initially leading the binary's rotation) ultimately becoming more bound compared to those launched at negative y (initially trailing the rotation). This agrees well with the findings of MacLeod et al. (2018a) and Hubová and Pejcha (2019).

The ballistic trajectories have larger kinetic and total energies than that of our outflow. The difference appears to arise from the launching of the outflow. Near the L2 point, the azimuthal velocities in our simulation are only 70-90% the co-rotation velocity. The outflow thus begins with lower energy than the ballistic trajectories, and this energy deficit remains approximately constant within our simulation domain. This behavior remains true for simulations of varying q.

Note that $u_{\rm int}$ is not included for the energetics of the outflow in the bottom panel of Fig. 5.10. However, the top panel of Fig. 5.10 demonstrates that the addition of $u_{\rm int}$ is not sufficient to unbind the outflow. This does not mean that pressure forces are unimportant. For example, ballistic trajectories initialized near L2 at slightly less than the co-rotational velocity tend to fall in toward the accretor instead of moving outwards. $u_{\rm int}$ is larger than $0.5v_r^2$ near L2, suggesting that pressure forces in particular help launch the outflow near the L2 point, which would not be accounted for in ballistic trajectories. See also Appendix 5.A.4, which discusses how the accretion disk is significantly supported by pressure in addition to rotation.

If the outflow does remain bound, it may form a circumbinary disk that evolves on a viscous time and continues to extract AM from the binary. Tuna and Metzger (2023) modeled the long-term evolution of such disks, finding they could persist for more than 10^4 yr, and could have a major impact on the appearance of a subsequent supernova explosion (see also (Ercolino et al., 2025)).

Future work, perhaps with an outer boundary further from the donor, should focus on the behavior of the material far from the binary. However, the effects of radiative

cooling due to photon diffusion would become important at large radii (see §5.A.2 for a brief discussion), so radiative hydrodynamic simulations with realistic opacities are required to fully understand the fate of the circumbinary outflow found in this work.

5.4 Dependence on simulation parameters

5.4.1 Effects of binary mass ratio

It is important to understand how the angular momentum and velocity of the outflow depend on the binary parameters such as the mass ratio, q. See Sec. 5.3.3 for our calculation of AM fluxes and $h_{\rm loss}$. Fig. 5.11 plots $h_{\rm loss}/h_{\rm L2}$ for simulations of different q. Here, we only plot $h_{\rm loss}$ averaged over the outermost COM-centered sphere, $|\vec{r} - \vec{r}_{\rm com}| = r_{\rm max} \approx 4.65$, because $h_{\rm loss}$ asymptotes with distance from the COM (Fig. 5.15). A steady-state is reached at $t \gtrsim 300$, as the curves flatten, while at early times little MT has occurred. There appears to be a trend that increasing q leads to decreasing $h_{\rm loss}/h_{\rm L2}$, i.e. the material less efficiently extracts AM from the binary. However, the specific AM loss $h_{\rm loss}$ is still substantially larger than the specific AM of the accretor $h_{\rm M_2}$, as shown by the dotted lines of Fig. 5.11 (see also Table 5.3).

The fact that $h_{\rm loss} < h_{\rm L2}$ implies that material has lower AM than if it was co-rotating at L2 initially (MacLeod et al., 2018b). Additionally, although most of the outflowing gas originates in a flow from the disk near L2, some also outflows near L3, which is on the opposite side of the donor star for $q \leq 1$ (Fig. 5.8) and on the side of the accretor for $q = 2$. This is one reason why the escaping gas has somewhat smaller specific AM than $h_{\rm L2}$.

Fig. 5.12 compares the radial velocity and energetics of outflows for simulations of differing q. See Sec. 5.3.4 for our calculation of gas velocities and energies in the inertial frame. The left panel describes how the material near the outer boundary of the simulation domain is bound or unbound, as shown by the mass-averaged Bernoulli parameter $\overline{B}$ over the outermost COM-centered sphere. For all values of q, material near the outer radial boundary has negative total energy and Bernoulli parameter, and is thus not yet unbound. However, our simulations do not provide a decisive answer on whether the outflow is unbound (see the discussion in 5.3.4 for uncertainties).

We calculate a mass-averaged radial velocity $\overline{v}'_{r,\rm inertial}$ in the outer regions of the grid as

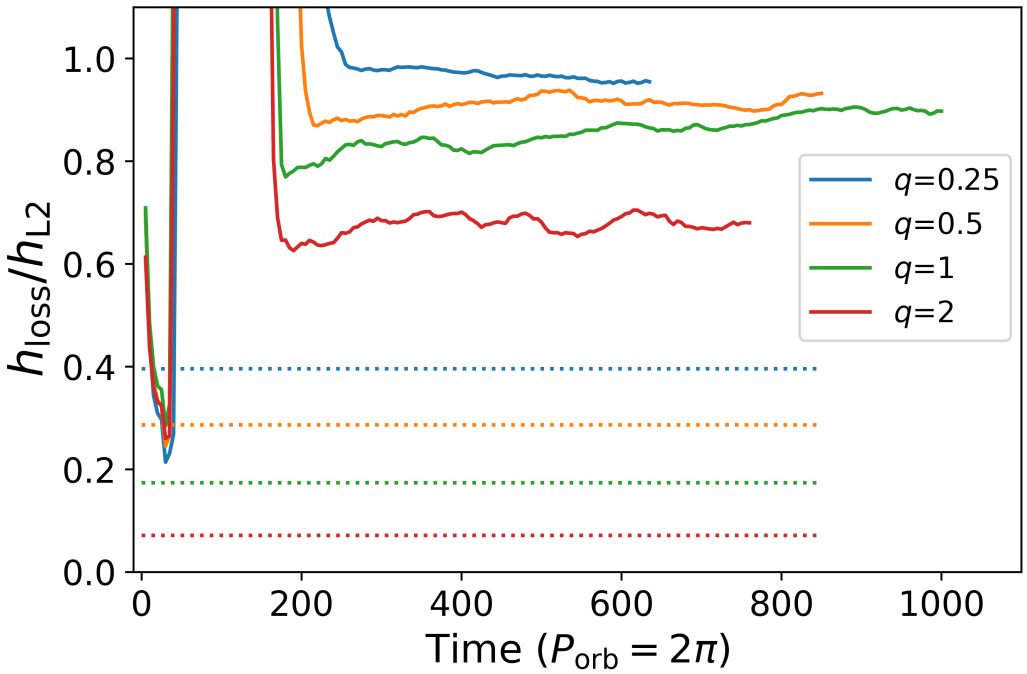


Figure 5.11: The specific AM carried by outflowing gas at $|\vec{r} - \vec{r}_{\rm com}| = r_{\rm max}$, for simulations of varying q and intermediate heating (solid lines corresponding to simulations q_025, q_05_mid_heat, q_1, q_2). For each value of q, the dotted lines show $h_{M_2}/h_{\rm L2}$, which is constant in time.

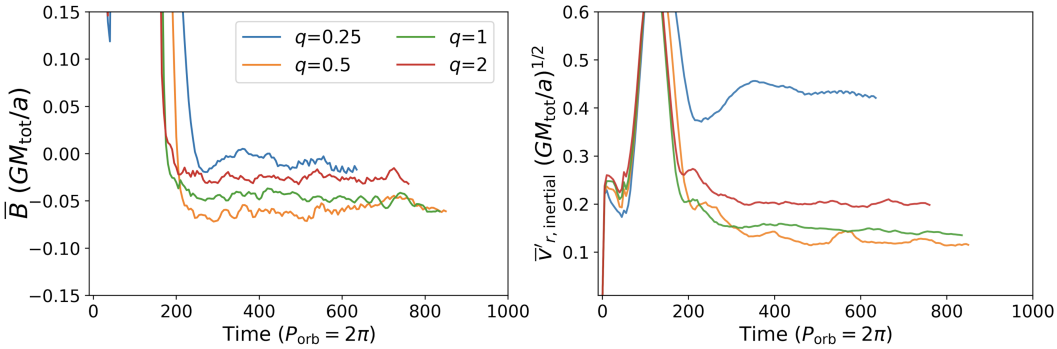


Figure 5.12: Properties related to the energy and velocity of outflowing gas, plotted for the same simulations as in Fig. 5.11. Curves are time-smoothed using a rolling average. Left: The Bernoulii parameter $\overline{B}$, in units of $GM_{\rm tot}/a$, averaged over the outermost COM-centered sphere, $|\vec{r} - \vec{r}_{\rm com}| = r_{\rm max} \approx 4.65$. Right: The volume-averaged radial velocity of the outflow, $\overline{v}'_{r,\rm inertial}$ (Eq. 5.27), in units of $v_{\rm orb} = \sqrt{GM_{\rm tot}/a}$.

$$\overline{v}'_{r,\rm inertial} = \frac{\int_{r=3}^{r=r_{\rm out}} \rho v_{r,\rm inertial} dV}{\int_{r=3}^{r=r_{\rm out}} \rho dV}. \tag{5.27}$$

Note that $\overline{v}'_{r,\mathrm{inertial}}$ involves an integral over angle and radius, whereas $\overline{v}_{r,\mathrm{inertial}}$ of Eq. 5.22 is just integrated over angle. The inner boundary of the integral is chosen to be $r = 3$ to capture the nature of the outflow far away from the two stars. The right panel of Fig. 5.12 plots $\overline{v}'_{r,\mathrm{inertial}}$ for simulations of varying q. For $q = 0.5, 1$ and 2, there is a trend where increasing q leads to slightly higher velocities. However, the highest velocities correspond to the $q = 0.25$ simulation. There is a similar trend for $\overline{B}$, where the $q = 0.25$ simulation shows the highest Bernoulli parameter.

The high velocities of the $q = 0.25$ simulation may be problematic, because for a lower accretor mass, the accretor's Roche lobe will be smaller and may be under-resolved in our simulations. Fig. 5.17 shows that a low-resolution $q = 0.5$ simulation also leads to higher characteristic velocities, suggesting our $q = 0.25$ simulation may need higher resolution in order for the outflow velocity to converge. Furthermore, the stream of material passing through L1 may have a comparable thickness as that of the accretion disk, meaning the flow of mass is not as well defined.

However, there are differences in the morphology of the outflow, comparing $q = 0.25$ simulations to those of higher q, that are seen in both 3D and 2D polar test simulations. The $q = 0.25$ outflows are heavily-dominated by a spiral arm originating at L2, and there is not significant collision with a mass outflow originating at L3. Because these differences are seen in 2D as well, where the MT stream appears to be more resolved, it remains plausible that low q may indeed lead to physical differences in the outflow. We defer further analysis of MT in low q systems to future work, which may require a higher spatial resolution.

5.4.2 Effect of other parameters

In 2D test simulations, we did not see a large effect of changing the adiabatic index γ on our results. In Appendix 5.C, we investigate the the dependence of our results on the envelope heating rate and perform resolution convergence testing.

5.5 Discussion

5.5.1 Comparison to previous work

Our work can be compared to several other investigations of binary MT. MacLeod et al. (2018b), MacLeod et al. (2018a), MacLeod and Loeb (2020b), and MacLeod and Loeb (2020a) (hereafter, the "M+ papers") investigated pre-common envelope MT and stellar coalescence, and thus were focused on unstable MT. In our paper, we focus on the steady state properties of stable MT, and we do not model the coalescence phase.

Despite these differences in focus, there are similarities between our work and the M+ papers. MacLeod et al. (2018b) show mass loss from the binary in spiral flows originating near L2 and L3, and the flow morphology discussed in MacLeod et al. (2018a) is similar to ours, including the toroidal structure of the outflow. MacLeod et al. (2018a) estimate that the outflowing material is concentrated within 30 degrees of the equator, similar to our results (Fig. 5.6). MacLeod et al. (2018a) finds that the outflow leaves L2 more tightly bound than co-rotation would imply, agreeing with our results (Sec. 5.3.4).

For a given value of q, MacLeod et al. (2018a) found that the specific energy and specific AM of the gas asymptotes as a function of radius from the COM. We find similar behavior in regard to specific AM (Fig. 5.15), but our total specific energy is still increasing at our outer radius (Fig. 5.9). This may be a consequence of our simulations having a smaller outer boundary radius. MacLeod and Loeb (2020b) found that with increasing q, the specific AM of outflowing gas is closer to that of L2. They also found a strong dependence of specific AM on the the structural index of the donor star Γ_s (in our simulations, γ). In contrast, we find the opposite trend with q (Fig. 5.11) and a weak dependence on γ. However, MacLeod and Loeb (2020b) notes that the dependence of specific AM on Γ_s is due to the star's response to mass loss and whether the secondary plunges in or remains skimming the star's surface. Because we do not probe this coalescence phase, these differences may be due to modeling stable vs unstable MT. Nonetheless, both works find the specific AM of the gas to be between that of the accretor and L2.

MacLeod and Loeb (2020a) found that larger q leads to higher radial velocities, which agrees with our results for $q = 0.5$ to $q = 2$, but our highest velocities occur for a low q of 0.25 (Fig. 5.12). However, there are potential caveats to our $q = 0.25$ result (see Sec. 5.4.1). MacLeod and Loeb (2020a) also discusses the effect of changing the gas adiabatic index, $\gamma_{\rm ad}$ (in our simulations, γ). They found that the gas AM is insensitive to $\gamma_{\rm ad}$, but that the gas radial velocity in the vicinity of the accretor and L2 changes. In our 2D simulations with changing γ, we find small effects on both gas AM and radial velocity. It is unclear if there is a discrepancy, as we are calculating velocities farther away from the accretor and MacLeod and Loeb (2020a) refers to velocities near the accretor. If there is a discrepancy, its cause is uncertain, but may be a 2D vs 3D effect, or an effect of the softening potential as discussed in MacLeod and Loeb (2020a).

Another work that found mass loss from L2 and L3 was Chen et al. (2017), which

simulated MT from a pulsating AGB star to a companion. In their simulations where an accretion disk formed, the accretion disk filled its Roche lobe and material flowed out through L2 and sometimes L3, but they did not investigate the angular momentum or the velocity of this outflow.

Kadam et al. (2018) performed simulations including the core-envelope structure of both binary components. In the case of their unstable MT simulation, they found mass flow through L2. In their stable MT simulations, the mass accretes directly onto a companion star. The gas never has a chance to form an accretion disk, likely explaining the lack of L2 mass loss in their simulations. Overall, they focused more on the stability of MT and the merger process, rather than the nature of outflowing material.

Nazarenko et al. (2005) performed simulations of mass transfer in Algol-type binaries, finding mass loss through L2 and L3. By including radiative cooling, they obtained more realistic temperatures than this work (see Appendix 5.A).

Nandez et al. (2014) found L2 mass loss preceding a merger of a giant star and a companion, when dynamical timescale MT occurred. Reichardt et al. (2019) saw L2 and L3 mass loss in a simulation preceding a common-envelope, which formed a bound disk that later interacted with common envelope ejecta. In contrast to these works, we focus on steady-state stable MT, not mergers.

Several works have investigated MT in eccentric binaries, where MT occurs episodically near periastron. Regös et al. (2005) found that mass escapes through the L2 point for high eccentricities, when the potential of L2 approaches that of L1. Similarly, in the SPH sims of Church et al. (2009), most of the transferred particles escaped through L2, which has a similar potential to L1 for their binary parameters. Lajoie and Sills (2010b) noted mass loss through L2 and sometimes L3, depending on the component masses (see also (Lajoie and Sills, 2010a)).

We note that both Church et al. (2009) and Lajoie and Sills (2010b) were able to simulate low MT rates in their eccentric binaries (down to $10^{-10} M_{\odot}$/yr in the case of (Church et al., 2009)), whereas the assumptions of our work demand much higher MT rates. However, neither of these works appear to have included radiative cooling. In contrast, Booth et al. (2016) performed sophisticated modeling of cooling in their simulations of symbiotic novae while also modeling a low MT rate ($10^{-7} M_{\odot}$/yr). They investigated the interaction of novae with circumstellar material, which differs from our focus on steady-state stable MT. Mohamed and Podsiadlowski (2012) also

simulated low MT rates with cooling in wind RLOF and found that some of the wind leaves through L2 to form a spiral arm. Future work can improve upon ours by including radiative cooling in order to realistically simulate lower MT rates, which are more common than those considered in this work.

Works that predict mass loss through L2, but without modeling MT from a donor star, include Shu et al. (1979), Pejcha et al. (2016b), Pejcha et al. (2016a), and Hubová and Pejcha (2019). While Pejcha et al. (2016a) predicted unbound outflows, Hubová and Pejcha (2019) showed that the energetics of the outflow can depend on initial conditions in the vicinity of L2, such as the positional offset from L2 and initial velocities of the gas.Our work does does not prescribe the initial condition of the outflow near L2, as we instead drive MT from the donor star toward the accretor. Despite this improvement, there remain uncertainties in our work as to whether the material is ultimately bound or unbound (Sec. 5.3.4).

Recently, Ryu et al. (2025) also simulated steady-state mass transfer, but their simulations focused on flows through the L1 or L2 point and did not include the accretor or circumbinary flows. Their simulations are more useful for understanding the donor response to mass transfer and the width/shape of the L1 stream, while our simulations are more useful for understanding circumbinary outflows and angular momentum loss.

5.5.2 Implications for binary AM loss

For non-conservative MT, the AM carried by outflowing gas is extremely important for predicting the orbital evolution (Huang, 1963; Willcox et al., 2023). Many prior works, including some binary population synthesis codes, have assumed that gas carries a specific AM h corresponding to that of the accretor. Our finding that h is closer to that of the L2 point means that more angular momentum will be extracted from the binary, likely leading to more dramatic orbital decay during phases of stable mass transfer. We note that our results only apply to high rates of MT ($\dot{M} \gtrsim 10^{-4} M_\odot/\mathrm{yr}$, see (Lu et al., 2023)), and future work should carefully define where our results apply.

Stable MT has become a leading candidate for the creation of isolated binary black holes (BBHs) (e.g., Pavlovskii et al., 2017; Klencki et al., 2021; Gallegos-Garcia et al., 2021; Son et al., 2022; Marchant et al., 2021). Stable MT plus efficient AM loss through L2 alters predicted BBH population properties (e.g. orbital periods, mass ratios, and merger rates) versus stable MT without L2 mass loss (Picco et al.,

2024), and may either increase or decrease BBH merger rates compared to stable MT without L2 mass loss. This will also change the BBH merger delay time distribution and the BBH spins due to tidal spin-up (e.g., Qin et al., 2018; Bavera et al., 2020; Bavera et al., 2021; Ma and Fuller, 2023; Olejak et al., 2024).

We do not evolve the binary's orbital separation due to AM losses, so our simulations at face value cannot be used to determine the stability of mass transfer. Rather, our goal is to understand the quasi-steady state during the evolution of binaries in which mass transfer does remain stable. Future work should self-consistently evolve a binary with AM losses appropriate to mass flow through L2, to better understand its role in stable and unstable MT.

5.5.3 Implications for circumstellar material

When mass transfer is occurring at the end of a massive star's life, the circumbinary outflow seen in this work results in circumstellar material that will interact with the supernova ejecta. Metzger and Pejcha (2017) have investigated a related scenario involving the interaction of stellar merger ejecta with circumbinary material ejected before the merger. Future work should build upon Metzger and Pejcha (2017) by investigating the interaction of supernova ejecta with circumbinary material, with properties informed by our 3D simulations. Predicting supernova lightcurves and spectra to compare to observations could then determine what fraction of interacting supernova arise from this scenario.

To perform this analysis, we would need to estimate the radial extent and density of the CSM when the supernova occurs. We have already shown that the outflow density approximately follows a r^{-2} dependence (Fig. 5.9). We can estimate the CSM radius R given a time $t_{\rm delay}$ between the onset of MT and the explosion of the star. A simple estimate, based on the asymptotic $v_r \approx 0.2\sqrt{GM_{\rm tot}/a}$ we find (Sec. 5.3.4 and Fig. 5.12), is

$$\begin{aligned} R &\approx 0.2 \times t_{\rm delay}\sqrt{GM_{\rm tot}/a} \\ &\approx 2 \times 10^{15}{\rm cm}\left(\frac{t_{\rm delay}}{10\ {\rm yr}}\right)\left(\frac{M_{\rm tot}}{15\ M_\odot}\right)^{0.5}\left(\frac{a}{0.1\ {\rm au}}\right)^{-0.5}. \end{aligned} \tag{5.28}$$

Since the outflow speed is only ~20% that of the orbital speed, the CSM can be significantly more confined than some prior estimates which assume it is ejected near the orbital speed.

5.5.4 Future work

As also discussed in MacLeod and Loeb (2020a), there are numerous physical effects that may complicate the accretion flow around the donor star and ultimately affect the global outflow. These include radiative cooling and magnetic fields, the latter of which governs the disk's accretion onto M_2. Additionally, if the accreting secondary is a compact object, it will be a source of energetic feedback on the outer part of the disk. Because we are not including any feedback, our current simulations may be more accurate for stellar companions, as long as they are small enough for an accretion disk to form. Farther from the accretor, dust formation will occur at low temperatures and radiation pressure on the dust may become important, as modeled in Mohamed and Podsiadlowski (2007) and Mohamed and Podsiadlowski (2012)). Radiation pressure may help the gas to become more unbound from the binary.

Future work should also investigate the role of these circumbinary outflows in supernova interactions (Sec. 5.5.3) and decaying binary orbits, especially in regard to creating merging compact binaries through stable MT (Sec. 5.5.2). If the accretor is a star, one possibility is that some of its envelope is mixed into the outflow, potentially changing the outflow's composition as compared to that of the donor star. This may lead to interesting CSM compositions that can explain some classes of supernova.

5.6 Conclusion

Episodes of intense and non-conservative mass transfer occur in many binaries containing a massive star. We simulated mass transfer between a donor star and an unresolved secondary to investigate the angular momentum, velocity, and energetics of outflows. Our idealized simulations do not include cooling, and are expected to be most applicable to systems with very large mass transfer rates of $\dot{M} \gtrsim 10^{-3}\, M_\odot/\mathrm{yr}$. Our 3D simulations are performed using the PLUTO hydrodynamic code, which resolves the flow of mass from the donor, into an accretion disk around the secondary, through the outer Lagrange point (L2), and into a circumbinary outflow. For our main grid of simulations, we vary the mass ratio q, defined as the accretor mass over donor mass.

The main results of our work are:

1. Mass from the accretion disk tends to outflow in a stream originating near L2 and forming a spiral pattern (Figs. 5.2, 5.3, 5.4). The circumbinary disk outflow has a half opening angle of $\theta = 10$ to 30 degrees, increasing with

increasing q (Fig. 5.6). The simulation reaches a quasi-steady state where the mass loss rate of the donor star approximately equals the rate of mass flowing through the outer boundary (Fig. 5.7). Our main results are calculated when this quasi-steady is realized.

2. The outflowing gas has a specific angular momentum $h_{\rm loss}$ that asymptotes with radius to a value slightly less than that of the L2 point, $h_{\rm L2}$ (Fig. 5.15). This means that AM will be efficiently extracted from the binary, which will have important consequences for orbital evolution. The outflow is dominated by mass originating near L2, although a stream near L3 also contributes some mass loss, especially for higher q (Fig. 5.8).

3. $h_{\rm loss}/h_{\rm L2}$ depends moderately on q (Fig. 5.11), with values of approximately $\{0.95, 0.9, 0.8, 0.65\}$ for q of $\{0.25, 0.5, 1, 2\}$. This suggests that lower mass ratios may lead to more efficient AM loss through L2. In all cases, $h_{\rm loss}$ is much larger than the specific AM of the accretor, h_{M_2}.

4. For most q, the outflow appears to reach an asymptotic radial velocity $\overline{v}_{r,\rm inertial}$ that is between 10-20% the orbital velocity (Figs. 5.9, 5.12). Velocities may be higher for $q = 0.25$. The outflow's total specific energy remains negative but is slowly increasing, suggesting that some or all of the gas may ultimately be unbound. The density roughly follows a r^{-2} dependence (Fig. 5.9).

5. The adiabatic index of the gas, γ, and the form of the heating injected into the envelope (Fig. 5.17), do not greatly change the above results for $h_{\rm loss}$ and $\overline{v}_{r,\rm inertial}$ or change the morphology of the outflow.

Although there have been several prior works that have performed hydrodynamic simulations and seen mass outflow through L2 and/or L3, most have been focused on unstable mass transfer leading to stellar mergers. Our measurement of angular momentum carried away during stable but non-conservative mass transfer has major implications for the resulting orbital evolution. These results can be incorporated into population synthesis calculations of stable MT and resulting mergers of binary compact objects (e.g., Marchant et al., 2021; Gallegos-Garcia et al., 2021). They will also be useful for predicting the properties of circumstellar material following extreme mass loss from supernova progenitors (Wu and Fuller, 2022). Many uncertainties remain, and future work should examine cooling processes of the gas, dust

formation, MHD processes and energetic feedback from the accretor's disk, flow dynamics within the donor star, and flow dynamics farther from the binary.

Acknowledgments

We are grateful for support from the NSF through grant AST-2205974. This research benefited from interactions enabled by the Gordon and Betty Moore Foundation through Grant GBMF5076. Numerous conversations have helped lead this project to its current state. We thank Sterl Phinney for advice that initiated this project, Morgan MacLeod for help with the simulation setup, and Elias Most for advice on running the simulations on a cluster. We thank Dan Kasen and Tony Piro for useful feedback that generated more points of discussion. We are grateful to the organizers and participants of the 41ST Liége International Astrophysical Colloquium and the 2024 ZTF Theory Network Conference, at which we received advice and questions that led to new analysis. We thank the anonymous referee for their thoughtful comments which greatly improved this work. We also thank the data editor for their feedback.

This work used the Purdue Anvil supercomputer through allocation PHY240274 from the Advanced Cyberinfrastructure Coordination Ecosystem: Services & Support (ACCESS) program, which is supported by U.S. National Science Foundation grants #2138259, #2138286, #2138307, #2137603, and #2138296.

5.A Gas properties

Fig. 5.13 plots the temperature T of the gas in the equatorial plane for a typical simulation snapshot. T is calculated by assuming the total pressure is a combination of ideal gas and radiation pressure,

$$P = \frac{\rho k_b T}{\mu m_\mu} + \frac{1}{3} a_{\rm rad} T^4 \tag{5.29}$$

where k_b is the Boltzman constant, m_μ is the atomic mass unit, $a_{\rm rad}$ is the radiation constant, and μ is the mean molecular weight, assumed to be 0.61 for solar composition. In order to calculate physical values of T, ρ, and P, we adopt the fiducial case of a $M_1 = 10\ M_\odot$, $M_2 = 5\ M_\odot$ binary in a 10 day orbit (Example B in Table 5.1). However, without even assuming binary parameters, the colors of Fig. 5.13 show the relative values of T at different points in the grid. Because we do not include gas cooling, the temperatures can be quite hot ($T \gtrsim 10^5$ K).

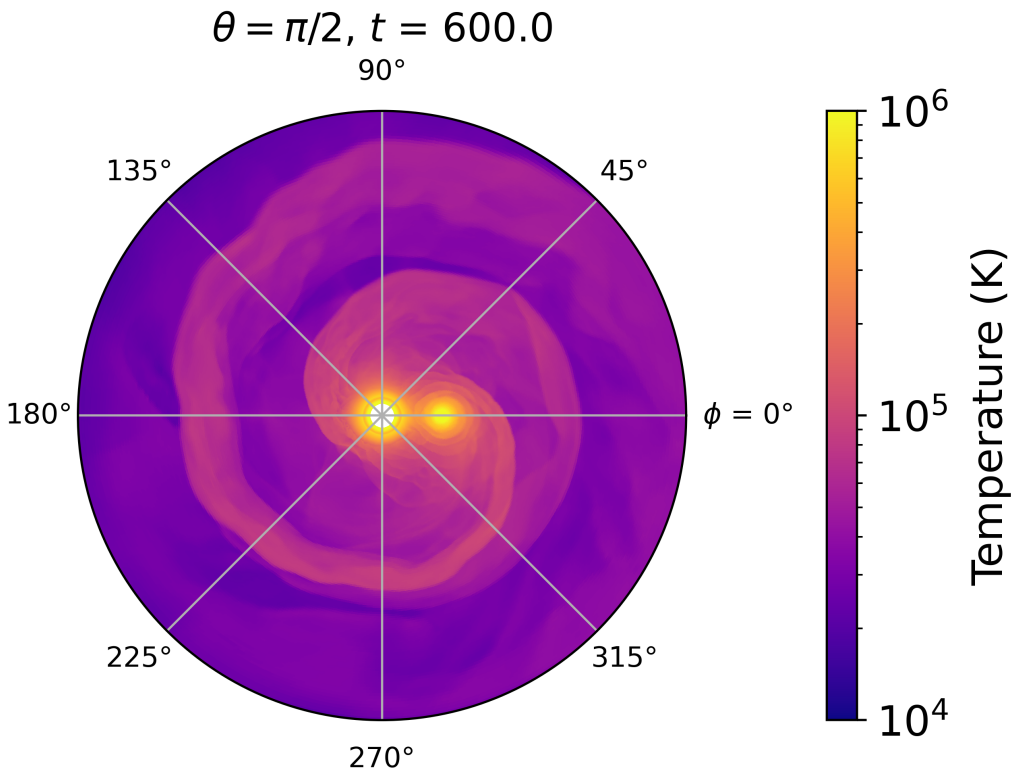


Figure 5.13: An equatorial temperature map of the gas, with the full radial extent of the domain shown, for the $q = 0.5$, intermediate heat simulation q_0.5_mid_heat. To convert from code units to physical units, we assume $M_1 = 10\ M_\odot$, $M_2 = 5\ M_\odot$, and an orbital period of 10 days.

5.A.1 Optical depth estimates

We calculate the optical depth τ and photon diffusion time $t_{\rm phot}$ for several radial lines of sight through the gas, where

$$\tau = \int_{r_0}^{r_1} \kappa \rho dr \tag{5.30}$$

and

$$t_{\rm phot} = \int_{r_0}^{r_1} \frac{\kappa \rho (r - r_0)}{c} dr \tag{5.31}$$

where r_0 and r_1 are the radial endpoints of the path integral, which is along a constant value of θ and ϕ. κ is the opacity, which we assume is the Thomson scattering opacity appropriate for solar composition, 0.34 cm^{2}g^{-1}, and c is the speed of light. The value of τ depends on which path is chosen and the amount of gas it intersects, but

we do not include the gas in the donor star's envelope in the integral. Instead, we perform integrals from outside the envelope with $r_0 \approx 0.6$, to the outer boundary, at different values of θ and ϕ.

For our $q = 0.5$ intermediate heating simulation q_0.5_mid_heat, with binary parameters of $M_1 = 10\ M_\odot$, $M_2 = 5\ M_\odot$, and an orbital period of 3 days (Example A), the approximate steady-state mass-transfer rate in physical units would be 6.9e-2 $M_\odot$/yr. Once MT in the binary has ramped up, typical values of τ at different angles are $(\theta = \pi/2, \phi = 0, \tau \gtrsim 10^7)$, $(\theta = \pi/2, \phi = \pi/2, \tau \gtrsim 10^4)$, and $(\theta \approx 0, \phi = 0, \tau \gtrsim 10^3)$. Values of $t_{\rm phot}$, in units of the orbital timescale of the binary, are $\gtrsim 10^4, \gtrsim 50, \gtrsim 1$ for the same angles. Our assumption of inefficient cooling breaks down closest to the pole, which is unsurprising given the low density in this region outside the donor star. We note that photons likely diffuse out from the disk and circumbinary outflow in the vertical direction, rather than the radial direction, so $t_{\rm phot}$ may be overestimated. See 5.A.2 for more discussion of radiative cooling.

If we instead use assume a 100 day orbital period (Example C in Table 5.1) the MT rate for the same simulation would be 2.1e-3 $M_\odot$/yr. Typical values of τ at different angles are instead $(\theta = \pi/2, \phi = 0, \tau \gtrsim 10^5)$, $(\theta = \pi/2, \phi = \pi/2, \tau \gtrsim 10^2)$, and $(\theta \approx 0, \phi = 0, \tau \gtrsim 10)$. Values of $t_{\rm phot}$, in units of the orbital timescale of the binary, are $\gtrsim 100, \gtrsim 0.1, \gtrsim 0.01$ for the same angles. Therefore, at lower MT rates, our assumptions of inefficient cooling start to break down at all angles.

These results somewhat justify our assumption of inefficient cooling of the outflow at very high MT rates. We note that the gas cooling time is longer than $t_{\rm phot}$ by a factor of $\sim (P_{\rm rad} + P_{\rm gas})/P_{\rm rad}$, which is large if the outflow is gas-pressure dominated. Additionally, the opacity could be somewhat larger than electron scattering due to free-free and bound-free absorption. However, the neglect of cooling will not be a good approximation at lower MT rates, where the photon diffusion time becomes smaller (scaling approximately with $\dot{M}$).

5.A.2 Observational appearance

This work has predicted the presence of an accretion disk as well as dense circumbinary outflows, originating mainly at L2. We characterize the observational signature of the binary system by estimating the photon trapping radius, beyond which photons can free-stream and escape the gas without scattering. Therefore, we calculate where the optical depth equals c/v, assuming that the density follows a r^{-2} dependence (Sec. 5.3.4), so that

$$\frac{c}{v_{r,\text{inertial}}} = \tau = \int_{r_{\text{trap}}}^{\infty} \kappa\rho dr = \int_{r_{\text{trap}}}^{\infty} \kappa\bar{\rho}_0 \frac{a^2}{r^2} dr \tag{5.32}$$

where $\bar{\rho}_0$ is the angle-averaged density at $r = a$, and $a = 1$ in code units. $v_{r,\text{inertial}}$ is defined in Sec. 5.3.4, and in the equation above we use a typical value of $0.15 \times v_{\text{orb}}$. Note that this integral extends to $r = \infty$ and can be evaluated analytically, whereas the estimates of τ in 5.A.1 were performed numerically out to the outer boundary of the domain.

We note that the above equation for the photon trapping radius applies even when the outflow only occupies a fraction of the solid angle (as we are using the angle-averaged density), and r_{trap} only depends on the total mass loss rate and the radial velocity of the outflow.

The value of r_{trap} can be calculated for different binary parameters. For $M_1 = 10$ $M_\odot$, $M_2 = 5$ $M_\odot$, and $a = 0.1$ au (Example A in Table 5.1), $r_{\text{trap}} \approx (5 - 6) \times a$. For $a = 0.22$ au (Example B in Table 5.1), $r_{\text{trap}} \approx a$. Note that $6a$ is outside the computational domain of our simulations, so we have assumed that typical values of $v_{r,\text{inertial}}$ are valid outside the domain as well to calculate r_{trap}. In Example A, photons would be trapped far out into the circumbinary outflow, whereas in Example B, an observer would see photons emitted from near the accretion disk.

We estimate the radiative flux F_{rad} and luminosity L_{rad} emitted at $r = r_{\text{trap}}$, as well as the color temperature T_{rad}, through the following equations:

$$F_{\text{rad}} = -\frac{4c}{3\kappa\rho} a_{\text{rad}} T^3 \frac{dT}{dr} \tag{5.33a}$$

$$L_{\text{rad}} = 4\pi r_{\text{trap}}^2 F_{\text{rad}} \tag{5.33b}$$

$$T_{\text{rad}} = \left(\frac{F_{\text{rad}}}{\sigma_{\text{SB}}}\right)^{1/4}, \tag{5.33c}$$

where σ_{SB} is the Stefan-Boltzmann constant. We find $L_{\text{rad}} \approx 10^{39}$ erg/s for both Example A and B, and $T_{\text{rad}} \approx 10,000K$ for Example A and $\approx 20,000K$ for Example B. These differences in T_{rad} and the relative location of r_{trap} suggest a range of observational signatures associated with the MT we simulate, which will be investigated further in subsequent work. The simplistic analysis above has averaged over angle and neglected any viewing angle effects (but should be accurate as

order-of-magnitude estimates), and we defer more sophisticated analysis to future work.

Future work should also perform radiation-hydrodynamic simulations of rapid MT, instead of using pure hydrodynamics as in this work. Lu et al. (2023) has predicted that ultraviolet photons from a fast disk wind, launched from the inner accretion disk, will be reprocessed into infrared radiation by the circumbinary outflow. Simulations incorporating both accretion and radiation may be able to test this picture.

5.A.3 Calculation of outflow opening angle

Here we calculate the average opening angle of outflowing gas $\theta_{\rm outflow,av}$, i.e. how closely concentrated to the equatorial plane the outflow is. For each value of ϕ, we find the angle θ' at which the density falls by a factor $f_{\rm out}$ relative to the the density in the equatorial plane

$$\rho(r > 2, \theta', \phi) < f_{\rm out} \times \ \rho(r > 2, \theta = \pi/2, \phi) \tag{5.34}$$

Only cells with $r > 2$ are included to avoid areas near the donor and accretor. We perform this calculation for $f_{\rm out} = 1/e$ and $f_{\rm out} = 1/e^2$, representing one or two e-foldings. The outflow opening angle is then $\theta_{\rm outflow} = \frac{\pi}{2} - \theta'$, because θ' is measured from the pole. Finally, we take the average of $\theta_{\rm outflow}$ over ϕ to calculate $\theta_{\rm outflow,av}$.

The outflow angle versus time for several simulations is plotted in the bottom panel of Fig. 5.6, for $f_{\rm out} = 1/e$. In general, we find that the angle for $f_{\rm out} = 1/e$ is approximately half that of $f_{\rm out} = 1/e^2$, as expected for an exponential drop-off in density.

5.A.4 Properties of disk

The accretion disk around M_2 is not the main focus of this work, and is not as well-resolved as simulations of some other works. However, Toyouchi et al. (2024) has shown that mass loss from the accretion disk is concentrated near the Lagrange points and is not from a fast wind near the accretor, so resolving the inner disk may not be necessary. This work therefore focuses on the disk outflows and their global quantities.

We find that v^2 and c_s^2, the velocity and sound speed squared, are comparable in the disk. At several M_2-centered spherical shells, i.e. $|\vec{r} - a\hat{x}|$ = constant, we calculate the density-weighted ratio of v^2 and c_s^2, i.e.

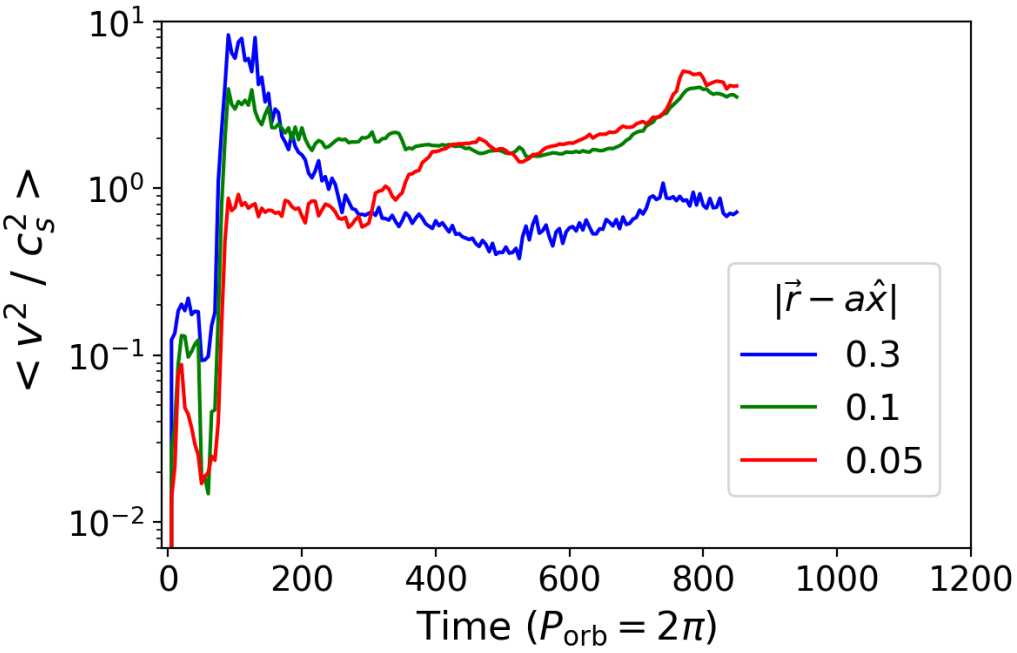


Figure 5.14: The ratio of the velocity squared to the sound speed squared (see Eq. 5.35) within the accretion disk, plotted versus simulation time. This ratio is averaged at several different spheres centered about M_2 (which is located at $\vec{r} = a\hat{x}$) . The simulation shown is the same as in Fig. 5.13 above.

$$< \frac{v^2}{c_s^2} > \equiv \frac{< \rho v^2 / c_s^2 >}{< \rho >} \tag{5.35}$$

where the $< >$ denotes averaging over a spherical shell. Note that this equation uses velocities in the co-rotating frame, because we wish to use velocities relative to M_2.

Fig. 5.14 plots $< \frac{v^2}{c_s^2} >$ at different radii around M_2, with all radii in units of a.. Once the simulation reaches a quasi-steady state, the value of $< \frac{v^2}{c_s^2} >$ is larger than unity in the inner disk, indicating it is mostly centrifugally supported but with a substantial contribution from pressure. In the outer disk, the value of $< \frac{v^2}{c_s^2} >$ is less than unity, indicating pressure support plays a major role, and the disk is very thick.

5.B Outflow at different radii

In Sec. 5.3.3, we presented our calculation of AM fluxes and $h_{\rm loss}$. To determine the spatial dependence of $h_{\rm loss}$ on distance from the binary, we calculate $h_{\rm loss}$ for several different surfaces centered about the COM and compare the value to $h_{\rm L2}$. Fig. 5.15 plots $h_{\rm loss}/h_{\rm L2}$ as a function of time at several radii for our q_0.5_mid_heat simulation. The largest area with $|\vec{r} - \vec{r}_{\rm com}| = r_{\rm max}$ is the maximum COM-centered

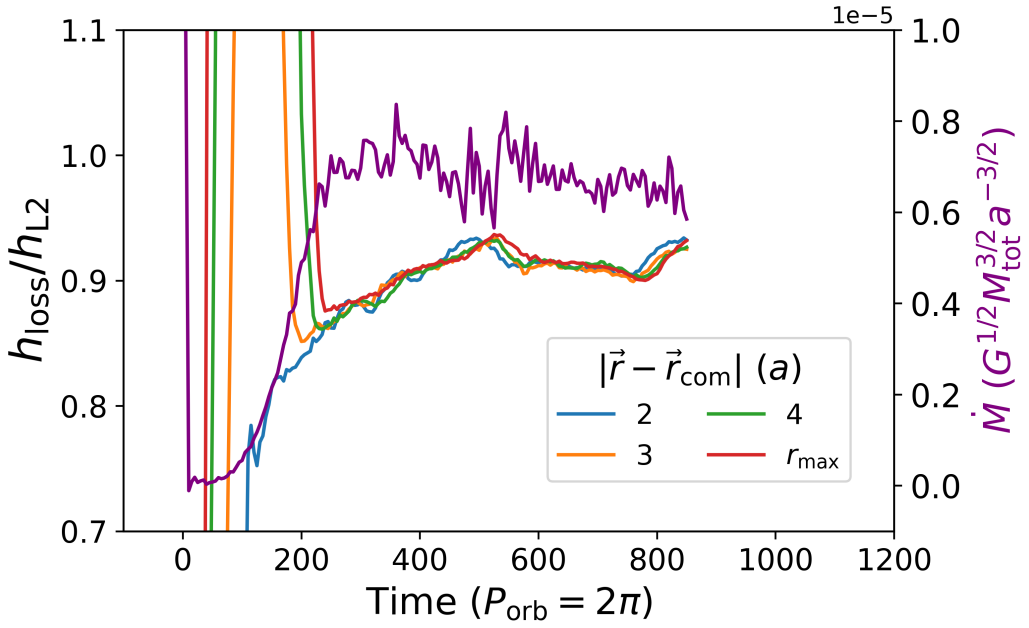


Figure 5.15: Left axis: The specific AM of outflowing material $h_{\rm loss}$, in units of the specific AM of the L2 point $h_{\rm L2}$, is plotted versus time, for the $q = 0.5$, intermediate heat simulation q_0.5_mid_heat. The value of $h_{\rm loss}$ is calculated for 4 different spherical shells centered about the binary's center of mass, and smoothed over time with a moving average. Right axis: The mass transfer rate of the donor star. For both quantities, the system reaches a steady state around $t \approx 400$.

sphere that will fit on the grid, corresponding to $r_{\rm max} \approx 4.65$ for this mass ratio. The values of $h_{\rm loss}/h_{\rm L2}$ are time-smoothed for each curve, using a rolling average of window-length $t = 50$. The values of $h_{\rm loss}$ are nearly independent of radius and converge to a value near 93% the specific AM of the L2 point. In our other plots involving $h_{\rm loss}$, we quote the value over the surface $|\vec{r} - \vec{r}_{\rm com}| = r_{\rm max}$.

Thus, for this mass ratio, escaping mass carries a specific AM similar to that of the L2 point, which is approximately three times larger than h_{M_2} for this mass ratio. This approximately supports models where the specific AM of lost material is that of L2.

5.C Convergence tests

Fig. 5.16 shows convergence testing results for the value of $h_{\rm loss}/h_{\rm L2}$. Included are two 3D simulations of low/high spatial resolution ($\delta r/r = 0.015, 0.01$), and two 2D simulations of high/very high spatial resolution ($\delta r/r = 0.01, 0.005$). Resolution in θ and ϕ is chosen to maintain roughly cubic cells in all cases. The 2D simulations

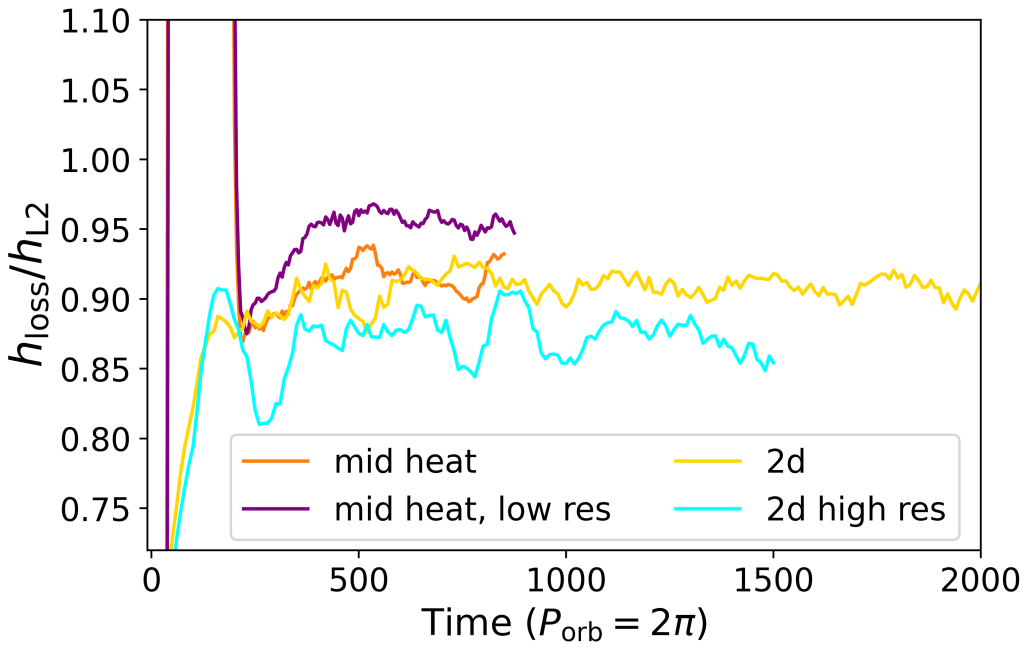


Figure 5.16: Similar to Fig. 5.11, but now showing $h_{\rm loss}/h_{\rm L2}$ for simulations of the same mass ratio $q = 0.5$ but with different spatial resolution. The two 3D simulations, q_0.5_mid_heat and q_0.5_low_res, include intermediate heating and have nearly identical setup, except one has a lower resolution. One 2D simulation has the same resolution as the higher-resolution 3D simulation, q_0.5_mid_heat, whereas the other has approximately double the spatial resolution.

are performed in polar coordinates in the equatorial plane, and reach a quasi-steady state at approximately the same time as the 3D simulations.

There appears to be a trend of slightly lower values of $h_{\rm loss}/h_{\rm L2}$ with increasing spatial resolution. Future work should investigate this issue in more detail. See also Fig. 5.17, which includes convergence testing for $h_{\rm loss}$ and also outflow velocities, but only for simulations conducted in 3D. See also discussion at end of Sec. 5.4.1, which discusses potential pitfalls involving low values of q and insufficent spatial resolution.

5.C.1 Effect of envelope heating rate

We investigate the dependence of our results on the envelope heating rate, which drives the expansion of the donor star and sets the mass transfer rate. Fig. 5.17 shows that $\overline{v}'_{r,\rm inertial}$ and $h_{\rm loss}/h_{\rm L2}$ are only weakly affected by different heating rates. See Table 5.1 for details on the varied luminosity injected and donor expansion timescales. Although the simulations reach a quasi-steady state on different

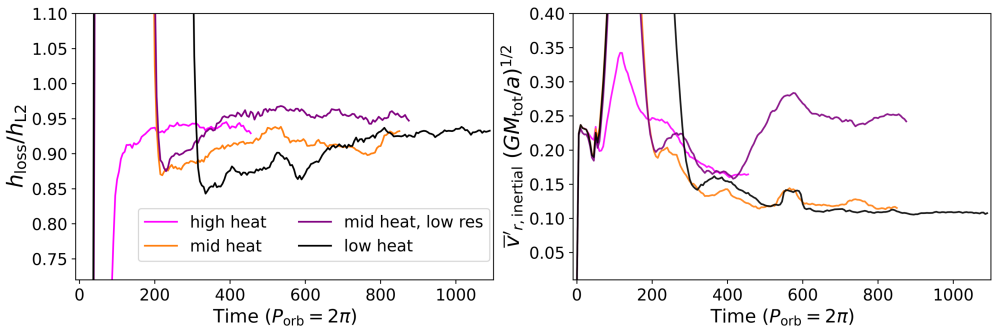


Figure 5.17: A comparison of specific AM and radial velocity of outflowing gas, for simulations of $q = 0.5$ but varying envelope heating (q_0.5_low_heat, q_0.5_mid_heat, and q_0.5_high_heat) or varying spatial resolution (q_0.5_low_res). The low resolution simulation is otherwise nearly identical in setup to the intermediate heating simulation, q_0.5_mid_heat. The left panel is constructed as in Fig. 5.11 and the right panel is constructed as in Fig. 5.12, so that the velocity is in units of $\sqrt{GM_{\rm tot}/a}$.

timescales, their steady-state values of $\overline{v}'_{r,\rm inertial}$ and $h_{\rm loss}/h_{\rm L2}$ are similar, with curves reaching similar values. We also include a simulation of lower spatial resolution, such that $\delta r/r = 0.015$, as opposed to our fiducual simulations of $\delta r/r = 0.01$. Otherwise, the lower resolution simulation is nearly identical in setup to the default intermediate heating simulation. The lower resolution simulation gives steady-state values that are moderately different from those of the corresponding higher resolution simulation.

5.C.2 Effect of softening potential

Fig. 5.18 shows the effect of changing the Plummer softening length ϵ (Eq. 5.5) on $h_{\rm loss}/h_{\rm L2}$, for 2D simulations of the equatorial plane. The value of $h_{\rm loss}/h_{\rm L2}$ is similar for 3D vs 2D simulations of similar parameters and resolution, so our results regarding ϵ can likely be extended to 3D. $h_{\rm loss}/h_{\rm L2}$ slightly decreases with decreasing ϵ, but the steady-state value is similar for $\epsilon = 0.04, 0.05$, and 0.075 and has nearly converged, whereas the value is moderately higher for $\epsilon = 0.1$ (all in units of a). Our 3D simulations use $\epsilon = 0.05$. We also tested $\epsilon = 0.025$ and experienced numerical issues such as very high values of the Mach number. Additional work will be needed to understand the effects of small ϵ, which can arise physically from compact object accretors.

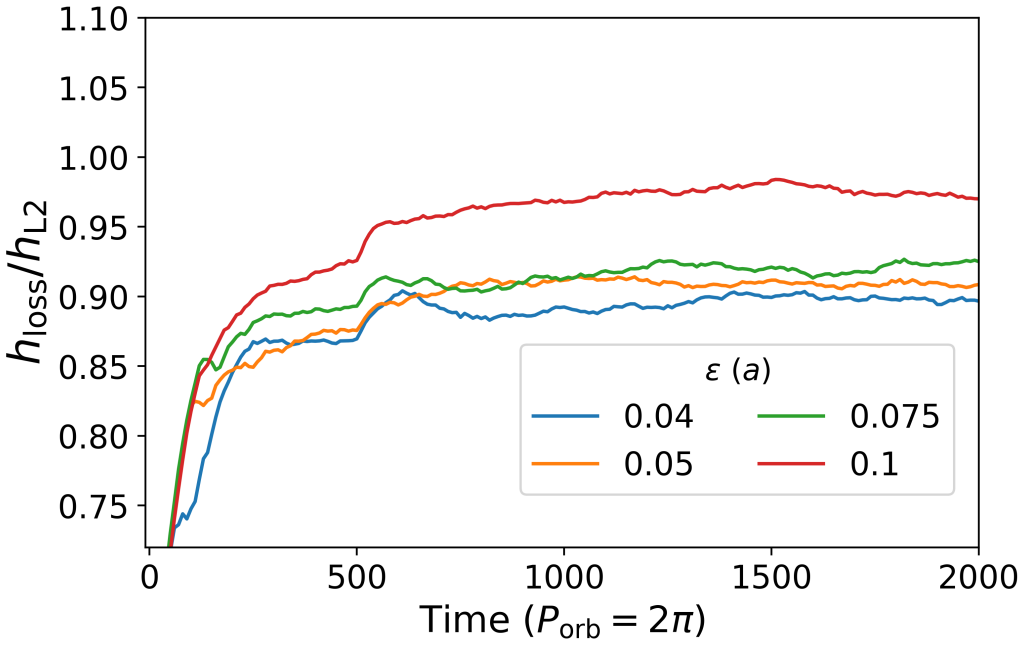


Figure 5.18: Similar to Figs. 5.11 and 5.16, but now showing $h_{\rm loss}/h_{\rm L2}$ for 2D simulations of mass ratio $q = 0.5$ but varied softening potential ϵ. Our 3D simulations use $\epsilon = 0.05$.

Chapter 6

RADIATIVELY-COOLED BINARY MASS TRANSFER: FLOW STRUCTURE, LUMINOSITIES, AND L2 OUTFLOWS ACROSS MASS TRANSFER RATES

Scherbak, Peter, Wenbin Lu, and Jim Fuller (Mar. 2026). "Radiatively Cooled Binary Mass Transfer: Flow Structure, Luminosities, and L2 Outflows Across Mass Transfer Rates". In: *Publications of the Astronomical Society of the Pacific* 138.3, p. 034206. DOI: 10.1088/1538-3873/ae453c.

High rates of stable mass transfer (MT) occur for some binary star systems, resulting in luminous transients and circumbinary outflows. We perform hydrodynamical simulations of a 10 $M_\odot$ donor star and a 5 $M_\odot$ point mass accretor, incorporating approximate effects of radiative cooling. By varying the orbital separation of the system, we probe MT rates between 10^{-5} and $10^{-1} M_\odot$/yr. Mass flows from the donor into a disk around the accretor, with significant equatorially-concentrated outflows through the outer Lagrange point L2 occurring for MT rates $\gtrsim 10^{-3} M_\odot$/yr, while the MT remains mostly conservative for lower MT rates. In all cases, any outflowing gas approximately carries the specific angular momentum of L2. The gas cooling luminosity L and temperature increases with MT rate, with $L \sim 10^5 L_\odot$ and $T \sim 10^4$ K for simulations featuring the strongest outflows, with contributions from both the circumbinary outflow and the accretor's disk . The most luminous transients associated with mass outflows will be rare due to the high MT rate requirement, but generate significant optical emission from both near the accretor and the circumbinary outflow.

6.1 Introduction

Mass transfer (MT) in binary star systems is common, especially for binaries containing massive stars (Sana et al., 2012). Episodes of MT precede the formation of gravitational wave sources (Postnov and Yungelson, 2014; Korol et al., 2022; LIGO Scientific Collaboration et al., 2023) and a large fraction of core-collapse supernova (Schneider et al., 2021). A major uncertainty related to MT is the degree to which it is conservative (Huang, 1963; Mink et al., 2007), where fully conservative MT results in the accreting star accepting all material from the donor. Non-conservative

mass transfer, which occurs in contexts including super-Eddington MT onto a compact object (e.g., Toyouchi et al., 2024), spin-up of accretors to critical rotation (e.g., Lechien et al., 2025), and thermal-timescale MT (e.g., Shao and Li, 2016; Pavlovskii et al., 2017; Klencki et al., 2022), results in material leaving the binary system, extracting angular momentum (AM). A consequent uncertainty is the amount of AM carried by the escaping mass.

If mass escapes by flowing through the outer Lagrange point, L2, which is a likely outcome in cases including an evolved massive star and stellar companion (Podsiadlowski et al., 1992), then its specific angular momentum may be comparable to that of the L2 point (e.g., Huang, 1963; MacLeod et al., 2018b). In studies of stable MT that can precede the formation of binary black holes (BBHs), Marchant et al. (2021) and Picco et al. (2024) noted that L2 mass loss may occur and that the amount of specific AM lost is a significant uncertainty that will impact the observed BBH population.

L2 mass loss has been predicted for high rates of MT ($\gtrsim 10^{-4} M_{\odot}$/yr), where gas in the accretion disk is expected to cool inefficiently and be energetic enough to escape through L2, forming a circumbinary outflow (CBO) (Lu et al., 2023). The observational appearance of the MT is unclear, with Lu et al. (2023) predicting that photons from the accretion disk will be reprocessed into the infrared.

Recently, Scherbak et al. (2025) (hereafter Paper I) performed hydrodynamical simulations of rapid, stable MT that adopted an adiabatic assumption and therefore neglected cooling. Paper I found that material indeed flowed out through L2, carrying AM similar to that of L2, and with a relatively small average radial velocity (10-20% the orbital velocity). At the outer boundary of those simulations, the material remained marginally bound to the binary, with slightly negative specific energy. This meant it was unclear if L2 mass loss in a binary could be a mechanism behind pre-supernova mass loss and extended circumstellar material (CSM) that commonly interacts with supernova ejecta (e.g., Taddia et al., 2013; Clark et al., 2020).

A major assumption in Paper I was the lack of radiative cooling, which Paper I estimated to become important at moderate MT rates $\lesssim 10^{-2} M_{\odot}/\mathrm{yr}$. While the MT in Paper I was highly non-conservative when the simulations reached a steady-state, Lu et al. (2023) has predicted that the degree of non-conservativeness should increase with the MT rate, further suggesting that behavior could differ at lower MT rates. In this paper, we extend the work of Paper I by incorporating radiative cooling into

hydrodynamical simulations, thereby expanding our simulations to cover lower and more common MT rates, where L2 mass loss may occur differently or not occur at all. In addition, the presence of cooling will result in more realistic gas temperatures, and allow for calculations of the observational appearance of the the accretor's disk and circumbinary outflows. Because we do not capture viscous accretion processes, we do not explicitly refer to an accretion disk around the accretor, but instead use terms such as "the accretor's disk", or "the disk around the accretor".

Observationally, L2 mass loss appears to be occurring in binaries SS433 (Blundell et al., 2001; Cherepashchuk et al., 2018) and W Serpentis (Shepard et al., 2024). In the case of SS433, radio/infrared images (Blundell et al., 2001; Bowler, 2010; Bowler, 2011a; Bowler, 2011b; Perez M. and Blundell, 2010) suggest the presence of outflowing circumbinary material. Infrared images of W Serpentis (Davidge, 2023) also find dust formation extending away from the central binary, suggesting the formation of a circumbinary disk that outflows through the outer Lagrange point on the side of the accretor (Shepard et al., 2024). The red transient V1309 Sco may also have undergone L2 mass loss, which would explain several peculiar features of its light curve (Pejcha, 2014).

Numerous works have investigated mass loss through the outer Lagrange point (summarized in Paper I) but only a relatively small subset have incorporated cooling and investigated various MT rates. Pejcha et al. (2016b) performed smoothed particle hydrodynamic (SPH) simulations of L2 mass-loss with radiative cooling and heating, but they initialized their material near L2 without including the donor star or accretor in their domain. Nazarenko et al. (2005) modeled MT rates between $\sim 10^{-7} - 10^{-5}$ $M_{\odot}$/yr in Algol-type binaries, noting that gas in the accretion disk can be transferred to the vicinity of L2/L3 and form an outflow, but did not discuss the fraction of material lost from the accretion disk. Mohamed and Podsiadlowski (2012) studied MT in symbiotic binaries undergoing wind Roche lobe overflow, finding that some of the wind is deflected away from the accretor and escapes through L2. Booth et al. (2016) extended this work to symbiotic binaries undergoing mass loss through a combination of winds and a Roche lobe overflow stream, incorporating a sophisticated radiative cooling model. They also found that part of the wind is channeled near L2 and escapes. Both Mohamed and Podsiadlowski (2012) and Booth et al. (2016) focused on MT rates $\sim 10^{-6}$ $M_{\odot}$/yr, whereas we focus on higher MT rates. Although they did not include cooling, Bobrick et al. (2017) investigated realistic MT rates between a WD and a neutron star through

SPH simulations, finding that mass is lost through an accretion disk wind, forming a “common envelope" around both stars. The AM carried by these winds is greater than the specific orbital AM of the neutron star, but much less than the specific AM of L2.In contrast to these works, we focus on the approximately steady-state behavior of stable MT where we track the outflow of gas, originating in the disk around the accretor, from the binary, and we vary MT rates to investigate its changing effects.

In Sec. 6.2 we discuss the numerical setup of our simulations, including the grid setup and our radiative cooling model, as well as the MT rates we probe and the astrophysical systems they may apply to. Sec. 6.3.1 characterizes the gas flow and degree of conservativeness for different MT rates, Sec. 6.3.2 the temperature, luminosity and observational appearance of the MT episodes we model, and Sec. 6.3.3 the properties of any outflows through L2, with a comparison to previous work. We conclude in Sec. 6.4.

6.2 Simulation setup

We perform Newtonian hydrodynamic simulations using the PLUTO code (Mignone et al., 2007; Mignone et al., 2012), considering MT between a donor star with core mass $M_{\rm d}$ and an accretor with mass $M_{\rm a}$, separated by a distance a in a fixed circular orbit. We solve the conservation equations of mass, momentum, and energy without any explicit viscosity, but including cooling due to radiative losses (Sec. 6.2.1). Our setup, including grid spacing, initial hydrostatic structure of the donor star, and injection of heat inside the donor star, is discussed in more detail in Paper I.

Our simulations are set in spherical coordinates r, θ, ϕ, centered at the donor star, in the co-rotating frame of the binary. The grid radius r extends from inside the donor’s envelope, not including the core, out to $5a$, with logarithmically spaced cells such that $\delta r/r = 0.01$ everywhere. The outer boundary condition is outflow, enforcing zero gradients of fluid quantities (see PLUTO documentation for more details), except for the radial velocity v_r, which is also enforced to be $v_r \geq 0$. With this “diode" boundary condition, we do not see any instabilities or reflection at the outer boundary. θ extends from 0 to $\pi/2$, with a reflective boundary condition, so that we only simulate the top hemisphere of the binary, while ϕ wraps around from 0 to 2π. θ and ϕ are spaced uniformly with size $\delta r/r$ such that cells are approximately cubic. We refer to values in code units when we non-dimensionalize using $G = M_{\rm tot} = M_{\rm d} + M_{\rm a} = a = 1$, and time t is given in units of the binary orbital period $P_{\rm orb} = 2\pi\sqrt{a^3/G(M_{\rm d} + M_{\rm a})}$.

We use the Roche_tidal_equilibrium code of Lu (2025) to help construct our donor star setup, which co-rotates with the binary. The density ρ and pressure P inside the donor star are initialized using the conditions: 1. $P = K\rho^{\gamma}$, for some entropy constant K and polytropic index γ; 2. the star is initially in hydrostatic equilibrium in the Roche potential and underfills its Roche lobe. Outside the star, ρ and P are initialized to spatially constant small values, corresponding to a low sound speed c_s. P and the internal energy $u_{\rm int}$ are related by PLUTO's "ideal" equation of state (EOS),

$$P = (\gamma - 1)\,\rho u_{\rm int}, \tag{6.1}$$

where we use the same value of γ as the polytopic index above. We inject heat inside the envelope so that it expands on a Kelvin-Helmholtz timescale $t_{\rm KH}$ much greater than the orbital dynamical timescale.

The accretor is represented by a Plummer softening potential, with softening length ϵ such that $\epsilon/a = 0.05$. The values $M_{\rm d}$ and $M_{\rm a}$ do not change over the course of the simulations, but the mass of the donor's envelope is reduced as MT occurs. We neglect the self-gravity of the donor's envelope, as well as the self-gravity of any subsequent flows, because the mass in the envelope is, by design, much less than $M_{\rm d}$ and $M_{\rm a}$.

The values controlling our setup are the same as in our fiducial simulation of Paper I, `q_0.5_mid_heat`: mass ratio $q \equiv \frac{M_{\rm a}}{M_{\rm d}} = 0.5$, $K = 0.578$ (code units), $\gamma = 1.4$ and an initial donor radius of about 75% the Roche radius. The total luminosity injected inside the donor is 4.0e-6 (code units) and $t_{\rm KH}$ is about 80 orbital periods. Although Paper I found that varying q can impact outflow properties, we leave q fixed in this work to focus on the impact of cooling, but future work should incorporate cooling and vary MT rates with different q values.

Because our goal is to incorporate cooling and investigate different MT regimes, conversions are necessary to convert from code units and give physical values of temperatures, opacities, and cooling rates. This differs from the previous simulations of Paper I which assumed adiabaticity outside the donor star, did not incorporate cooling, and were therefore, in principle, scale-free. We choose $M_{\rm tot} = 15\ M_{\odot}$, which could correspond to a massive star plus stellar or black hole accretor (although see below a discussion of which companion is most valid given our assumptions). We vary the value of a between our simulations, which effectively changes the physical MT rate between simulations via

$$\dot{M}_{\rm phys} = \left(\frac{M_{\rm tot}^{3/2} G^{1/2}}{a^{3/2}} \right) \dot{M}_{\rm code}. \tag{6.2}$$

By raising a and keeping $M_{\rm tot}$ fixed and $\dot{M}_{\rm code}$ approximately fixed, we lower $\dot{M}_{\rm phys}$. Strictly speaking, this means that we do not sample all regimes of parameter space (e.g., low $\dot{M}_{\rm phys}$ at short orbital period). However, it is reasonable to expect that $\dot{M}_{\rm phys}$ will be the main factor in determining outflow properties, and that our results can be extended to various a. Similarly, setting the scale of a determines the physical values of density, pressure, temperature, opacity, etc.

Table 6.1 summarizes the simulations that we perform, demonstrating the difference in scales used to simulate different MT rates. Note that values such as K and $L_{\rm heat}$, which are constant in code units across simulations, are different in physical units for different simulations. See Sec. 6.2.2 for a comparison to astrophysical MT rates, and Fig. 6.4 for further discussion of where our simulations fall in the parameter space of MT rate and a.

In our main suite of simulations, we do not include any heating terms due to the luminosity of either the donor star or the accretor. We do not include an explicit viscosity so we cannot capture viscous heating effects, nor can we resolve an inner accretion disk. We therefore do not model the potential launching of a fast wind that then emits X-ray and UV photons (Lu et al., 2023), or the formation of an advection dominated accretion flow (ADAF) (Yuan and Narayan, 2014; Yuan et al., 2015).

Although we are formally agnostic to the nature of $M_{\rm a}$, our setup is more appropriate when the accretor is a star smaller in radius than $M_{\rm d}$, but not a compact object. In such a case, there is no inner accretion disk, and our MT rates are not extremely super-Eddington when compared to the accretion flow power.

6.2.1 Cooling Prescription

We include energy losses due to radiative cooling, assuming that the photons primarily escape perpendicular to the orbital plane in the $\hat{z}$ direction. We estimate that the cooling power per volume, $\dot{E}_{\rm cool}$, is given by

$$\dot{E}_{\rm cool} = -\frac{4\rho\sigma_{\rm SB}T^4}{\frac{1}{\kappa} + \Sigma_z \tau_z} \tag{6.3}$$

where κ is the opacity, T the temperature of the gas, Σ_z is the gas surface density in the $\hat{z}$ direction, and τ_z is the optical depth in the $\hat{z}$ direction. This equation is inspired

Simulation	$\dot{M}_{\rm code}$	a (au)	$P_{\rm orb}$ (days)	$M_{\rm tot}^{3/2}G^{1/2}a^{-3/2}$ ($M_\odot$ yr^{-1})	$\dot{M}_{\rm phys}$ ($M_\odot$ yr^{-1})
highest_mdot	1.3e-5	0.1	3	1.1e4	1.5e-1
high_mdot	1.1e-5	0.3	15	2.2e3	2.3e-2
mid_mdot	0.7e-5	1	100	350	2.2e-3
low_mdot	0.4e-5	10	2970	5	2.0e-5

Table 6.1: Grid of 3D simulations, labeled “highest" “high" “mid" or “low" by their MT rate in physical units ($\dot{M}_{\rm phys}$). The free parameter is the orbital separation a, while $M_{\rm tot}$ is fixed at 15 $M_\odot$. The corresponding orbital period $P_{\rm orb}$ is calculated via Kepler's Third Law. The factor $M_{\rm tot}G^{1/2}a^{-3/2}$ is used to convert from $\dot{M}_{\rm code}$ to $\dot{M}_{\rm phys}$ (see Eq. 6.2), where both values are approximate steady-state values.

by several previous works that have incorporated radiative cooling (Stamatellos et al., 2007; Forgan et al., 2009; Wilkins and Clarke, 2012; Lombardi et al., 2015; Pejcha et al., 2016b), but that performed SPH simulations. Of these, Pejcha et al. (2016b) applied this cooling term to their SPH simulations of L2 mass loss, noting that their particles are not self-gravitating and the original formalism of Stamatellos et al. (2007), Forgan et al. (2009), and Lombardi et al. (2015) to develop this formula does not strictly apply.

Eq. 6.3 takes the correct forms in both the optically thick and optically thin limits. In the optically thin limit where $\frac{1}{\kappa} \gg \Sigma_z\tau_z$, the magnitude of the cooling reduces to

$$|\dot{E}_{\rm cool}| \approx \frac{4\rho\sigma_{\rm SB}T^4}{\frac{1}{\kappa}} \approx 4\rho\kappa\sigma_{\rm SB}T^4 \tag{6.4}$$

where this form represents the emitted radiation per unit volume of an optically thin gas. In the optically thick limit, where $\frac{1}{\kappa} \ll \Sigma_z\tau_z$, Eq. 6.3 reduces to

$$|\dot{E}_{\rm cool}| \approx \frac{4\rho\sigma_{\rm SB}T^4}{\Sigma_z\tau_z} \approx \rho a T^4 / \left(\frac{H_z\rho\tau_z}{c}\right) = u_{\rm rad} / \left(\frac{H_z\tau_z}{c}\right) \tag{6.5}$$

where we have estimated that $\Sigma_z = H_z\rho$ for some scale height H_z, the form of which we will discuss shortly. This represents the radiation energy density over the diffusion timescale in the $\hat{z}$ direction, $\frac{H_z\tau_z}{c}$.

We calculate T, by solving the quartic equation for the total pressure as a sum of gas and radiation pressure

$$P = \frac{\rho k_b T}{\mu m_p} + \frac{a_{\rm rad} T^4}{3}, \tag{6.6}$$

which assumes gas and radiation are in equilibrium with the same T, where k_b is the Boltzmann constant, m_p is the proton mass, and μ is the mean molecular weight. In our simulations, $\mu \approx 0.62$, appropriate for ionized Solar-composition material, but does not take into account the formation of neutral hydrogen at low temperatures, which can occur in our low-MT rate simulations. This means the temperature calculation is not quite consistent at low T, but, compared to the impact of MT rate (Sec. 6.3.2), is likely a relatively small correction that will not severely impact our T estimates. Eq. 6.6 is solved at runtime at every cell, using a Newton-Raphson root solver.

The opacity κ is estimated by interpolating tables of opacity at solar metallicity ($Z_\odot$), using tables conveniently collected in the Modules for Experiments in Stellar Astrophysics code (MESA Paxton et al., 2011; Paxton et al., 2013; Paxton et al., 2015; Paxton et al., 2018; Paxton et al., 2019; Jermyn et al., 2023). Specifically, we interpolate the table `gn93_z0.02_x0.7.data` in $\log T$ and $\log R \equiv \log \rho - 3 \log T + 18$ to estimate $\log \kappa$, using `lowT_fa05_gn93_z0.02_x0.7.data` for $\log T < 3.75$. For any values outside the tables, we use the value of κ at the outer edge of the table. The opacities we are using are Rosseland mean opacities, whereas they should technically be Planck mean opacities in the optically thin limit (see (Stamatellos et al., 2007)). We follow Pejcha et al. (2016b) in neglecting this discrepancy, given the approximations already taken in using Eq. 6.3 for our purposes. The opacity table we use, and where the points in the simulations fall on it, is visualized further in Appendix 6.C.

The final two ingredients needed in calculating Eq. 6.3 are H_z and τ_z. We estimate $\tau_z \approx \kappa \rho H_z$ at every point in the grid. This is a rough estimate of the local vertical optical depth, but doing a runtime integral over z-coordinate in spherical coordinates would be cumbersome and potentially introduce numerical artifacts. Our estimate of τ_z captures the fact that that the greatest contribution to τ_z is where the density is largest in the midplane. We estimate H_z in a local fashion as well, using an estimate appropriate to a hydrostatic disk,

$$H_z = \frac{c_s}{\Omega_{\rm eff}} \tag{6.7}$$

where the sound speed c_s is defined as $c_s^2 = \frac{\gamma P}{\rho}$ and we estimate the effective orbital frequency as

$$\Omega_{\rm eff}^2 = \frac{M_{\rm d}}{|\vec{r}|^3} + \frac{M_{\rm a}}{|\vec{r} - a\hat{x}|^3} \tag{6.8}$$

where $\vec{r}$ is the coordinate vector, as $M_{\rm d}$ is located at the origin, and $M_{\rm a}$ is located at $a\hat{x}$. This reduces to the correct limit in the disk around $M_{\rm a}$ when the second term dominates, and far out in the equatorially-concentrated circumbinary outflow surrounding both $M_{\rm d}$ and $M_{\rm a}$ when $|\vec{r} - a\hat{x}| \sim |\vec{r}|$.

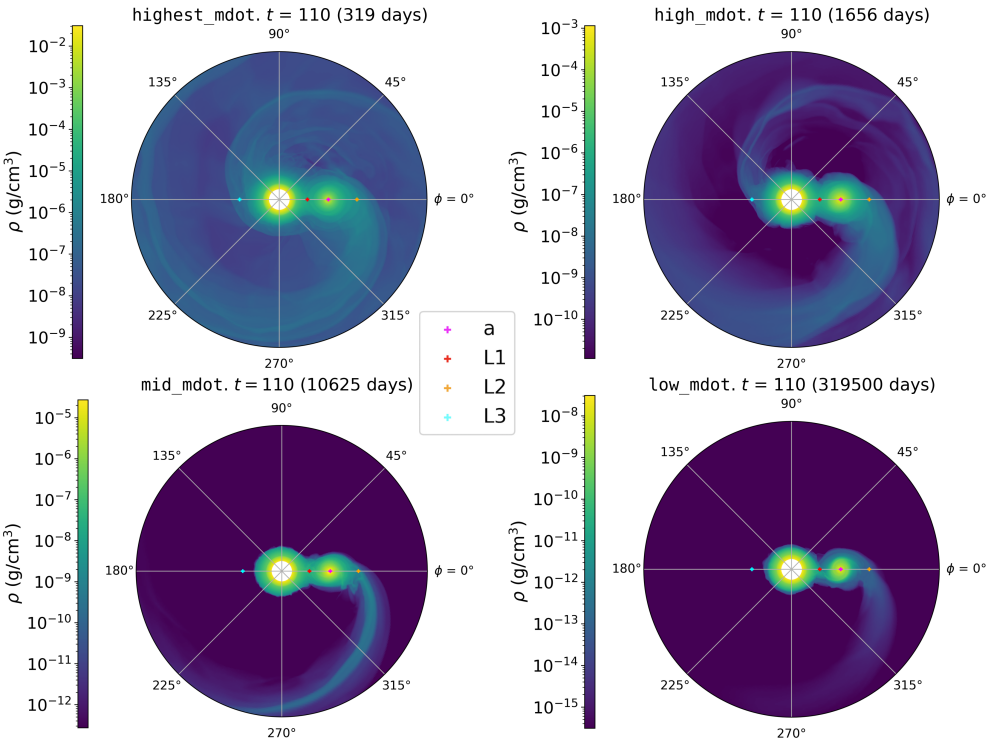


Figure 6.1: The density ρ in the equatorial plane, for simulations of varying MT rate. The orbital separation a and Lagrange points are labeled. The snapshots, representative of the simulations once they have reached a quasi-steady state, are labeled with t in units of both orbital period and days. The full domain extends to $r = 5a$, but these plots extend to $r = 3a$ to zoom in near M_a. Note the different density scale in each case.

We include cooling in PLUTO using the `radiat.c` cooling module, where we set the right hand side of the energy equation that is solved by PLUTO. We do not allow any cooling inside the Roche lobe of the donor star, as that would be likely be a

bad approximation given our cooling form is based off of a disk structure most valid surrounding $M_{\rm a}$ and both stars, not for a spherical star.

Eq. 6.3 gives the nominal form for the cooling power per volume, which acts to reduce $u_{\rm int}$. However, we also impose safeties and floors to avoid catastrophic cooling and unphysical values of T or c_s. We set that in all grid cells, $u_{\rm int}$ cannot be reduced by more than 50% in a given timestep. Test runs showed that our results are not sensitive to this value. Additionally, we set a pressure floor and a corresponding internal energy floor, which are related via the ideal EOS (Eq. 6.1). The cooling is capped such that $u_{\rm int}$ is not allowed to fall below the internal energy floor. In low density regions, where $\rho < 10^{-5}$ in code units, we set the pressure floor to be proportional to ρ, corresponding to a low sound speed floor. In higher density regions, we set a pressure floor corresponding to a temperature floor of 2000 K, with pressure and temperature related by Eq. 6.6.

We choose not to impose a temperature floor everywhere in the domain, because doing so in low density regions creates a high pressure and high sound speed. This leads to material seemingly having a large $u_{\rm int}$ and a spurious outflow of mass near the outer boundary. The downside to this approach is that T of some low-density material can become lower than covered by our opacity tables. However, these low-density regions are unimportant for the cooling luminosity and L2 outflow. If we do not impose a floor on sound speed in low density regions, the pressure and sound speed can become extremely small, leading to unphysically high Mach numbers.

Additionally, we enforce floors on ρ and P within the `UserDefBoundaries` section of PLUTO's `init.c`. This is complementary to the previous discussion of floors, as those implied a limit on the cooling power, but did not enforce floors in general during runtime. The ρ floor is set to be 10^{-10} in code units, and the P floor is the same as above. More discussion of the floors is included in Appendix 6.C.

In the `highest_mdot` simulation, numerical issues such as negative pressure occur near the pole, where the resolution is set to be low in order to avoid small timesteps. Therefore, we do not include cooling at $\theta < 0.3$ for this simulation. Because the density sharply drops near the pole and the outflow originates in the midplane, this will not affect our main results.

6.2.2 Comparison to binary MT rates

The physical MT rates we probe ($\dot{M}_{\rm phys}$ in Table 6.1) are relevant to several scenarios with massive stars in binaries. Stripped He star binaries undergoing case BB mass

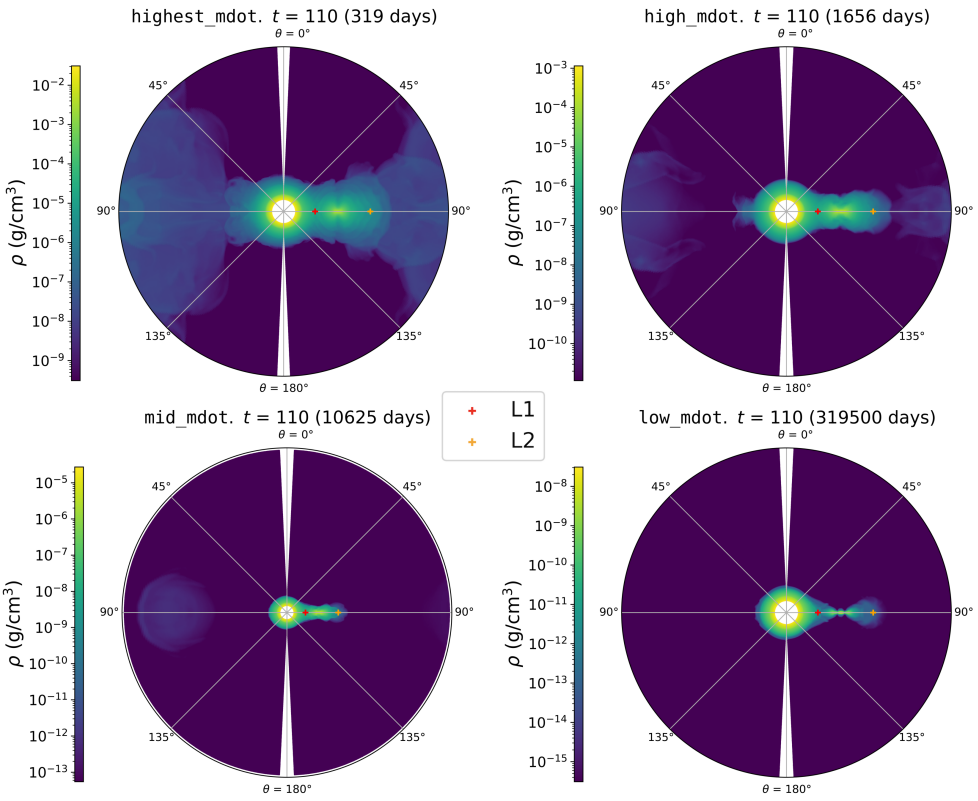


Figure 6.2: Similar to Fig. 6.1, but plotting ρ in the meridional plane lying between the donor and accretor ($\phi \approx 0$ and $\phi \approx \pi$), for simulations of varying MT rate. Plots extend to $r = 3a$, except in the case of the `mid_mdot` simulation, where we zoom out to $r = 5a$ to better show the outflow. We only simulate $\theta < \pi/2$, so the bottom half of each image is mirrored from the top. The white triangle near $\theta = 0$ is due to low grid resolution at the pole

transfer can reach MT rates of several $10^{-4} M_\odot$/yr for more than 10^4 years (Tauris et al., 2015). Massive stars expanding into the Hertzsprung gap and undergoing thermal timescale MT are expected to lose mass at rates between 10^{-3} and 10^{-2} $M_\odot$/yr (Pavlovskii et al., 2017; Marchant et al., 2021; Klencki et al., 2022). Klencki et al. (2025) probed even higher MT rates, showing that MT in such binaries can remain stable almost to 10^{-1} $M_\odot$/yr, depending on mass ratio. Finally, the rapid expansion of stripped He stars in the weeks to years before undergoing a core-collapse supernova can result in MT rates above $10^{-2} M_\odot$/yr, and the peak MT rate ($10^{-1} M_\odot$/yr) can last for hundreds of binary orbits (Wu and Fuller, 2022).

Therefore, our `high_mdot` ($10^{-2} M_\odot$/yr) simulation may apply well to massive stars expanding on the Hertzsprung gap with a binary companion, whereas the `highest_mdot` simulation ($10^{-1} M_\odot$/yr) applies only for brief evolutionary phases

mentioned above (Wu and Fuller, 2022; Klencki et al., 2025). The `mid_mdot` ($10^{-3} M_\odot$/yr) and `low_mdot` ($10^{-4} M_\odot$/yr) simulations cover the lower end of massive star thermal timescale MT rates, or potentially case BB mass transfer from He star donors.

Observationally, the systems that have likely undergone L2 mass loss have high measured MT rates. SS 433 has a MT rate of about 10^{-4} $M_\odot$/yr (Fabrika, 2004; Cherepashchuk et al., 2018), W Serpentis a rate greater than 10^{-5} $M_\odot$/yr (Gies et al., 2025) and V1309 Sco a rate that may have risen from 10^{-4} $M_\odot$/yr to almost 10^{-2} $M_\odot$/yr as the binary system approached a stellar merger (Pejcha, 2014). Unfortunately, none of these systems have measurements for the outflow rate through L2, but they do show evidence for circumbinary outflows.

6.3 Analysis

6.3.1 Morphology and mass transfer conservativeness

Fig. 6.1 shows the density in the equatorial plane for our simulations, with the colormap scale shown in physical units. We show snapshots corresponding to about 100 orbital periods after initialization. By this time, the donor star has expanded due to heating and begun Roche lobe overflow, and the MT rates have reached a quasi-steady state.

In the `highest_mdot` simulation, most of the equatorial domain is flooded with material, although the densest outflow is centered near L2, the Lagrange point on the far side of M_a. Mass easily escapes the puffy disk around M_a and flows out through L2 in a broad stream. In addition, the stream passing through L1, the inner Lagrange point, is quite puffy, and the boundary between donor, M_a's disk and the MT stream is blurred. A small amount of material also flows out in a stream originating near L3 (the outer Lagrange point on the side of the donor star), and much of it falls back onto the L2 stream, forming shocks. Note that the simulations are in the co-rotating frame, and the outflow lags behind the binary orbit in this frame.

In the `high_mdot` simulation, a thick stream still flows out near L2, but lower density voids are also visible between the spiral arms of the circumbinary outflow. The stream originating near L3 is also more diffuse.

The `mid_mdot` and `low_mdot` simulations are somewhat similar to one another, in that a relatively thin stream of material flows out of M_a's disk near L2. The outflow through L3 is extremely tenuous in these cases. The boundary of M_a's disk and the L1 stream, is more sharp in these simulations compared to `highest_mdot`. In the

`low_mdot` simulation, the L2 outflow has a very low density, as does the outer part of M_a's disk.

The same snapshots viewed edge-on, with a meriodional slice of the domain, are shown in Fig. 6.2. The gas near $M_{\rm a}$ forms a disk whose thickness increases substantially with increasing MT. Also with increasing MT rate, the opening angle θ of the circumbinary outflow (measured away from the equator) increases, although the density is always largest in the equatorial plane. For the lower MT rate simulations, the outflow is difficult to see viewed edge-on because it reaches low densities and is concentrated near the equator. In the `mid_mdot` simulation, the wrapping of the spiral arm of the outflow shows up on the left side of the donor star, on the opposite of the accretor.

We estimate the fraction β of transferred mass that is retained by the accretor by calculating $\dot{M}_{\rm donor}$, the MT rate from the donor star, and $\dot{M}_{\rm tot}$, the MT rate through the outer boundary, and using

$$\beta = 1 - \frac{\dot{M}_{\rm tot}}{\dot{M}_{\rm donor}}. \tag{6.9}$$

We note that in our simulations, material essentially either stays in the region surrounding $M_{\rm a}$ or outflows near L2. There is no sink of material onto $M_{\rm a}$, nor is there the opportunity for an ADAF flow to occur, which may instead expel material mostly *perpendicular* to the orbital plane in a jet or a wind (Yuan et al., 2015). Therefore, in the case of $M_{\rm a}$ being a compact object, there may be a competition between outflows launched from the inner disk, and equatorial L2 outflows, which should be examined in future work.

Fig. 6.3 plots the steady-state average of β for our simulations. For the `highest_mdot` simulation, $\beta \approx 0$, meaning the MT is very non-conservative, which is the same conclusion of Paper I that did not include any cooling. β monotonically increases with decreasing MT rate, meaning that the MT becomes more conservative. For the `high_mdot` simulation, $\beta \approx 0.3 - 0.5$, meaning that most of the mass still forms a circumbinary outflow, but a large fraction stays near $M_{\rm a}$. The other two simulations feature mostly conservative MT rates, although a small amount of material still flows out through L2. Therefore, between MT rates of $\sim 10^{-3}$ and $\sim 10^{-2}$ $M_\odot$, there is a significant jump in the degree of non-conservativeness (top panel of Fig. 6.3). This would constitute a threshold for highly non-conservative mass transfer in astrophysical binaries.

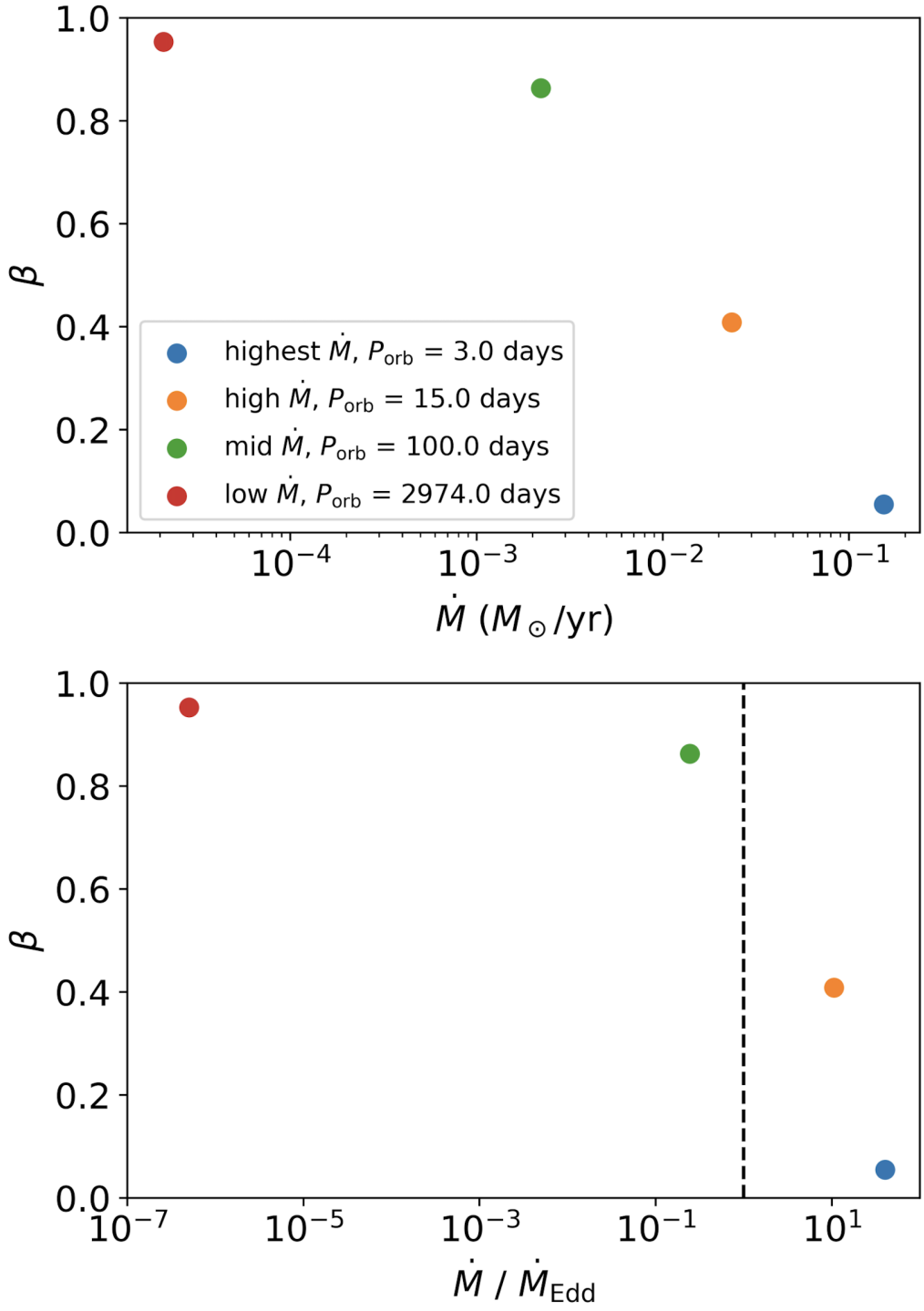


Figure 6.3: Top panel: The fraction of material retained in the disk around M_a, β, versus the MT rate $\dot{M}_{\rm donor}$ for our simulations. Bottom panel: the same quantity, plotted versus $\dot{M}_{\rm donor}$ in units of the Eddington MT rate (Eq. 6.11). The vertical dashed line shows where $\dot{M}_{\rm donor} = \dot{M}_{\rm edd}$. The values shown are time-averaged once the simulations reach a quasi-steady state, at t greater than ~ 50 (orbital periods).

In our simulations, the outflowing mass $\dot{M}_{\rm tot}$ is almost identical to the MT rate of material outward near L2, $\dot{M}_{\rm L2}$, which we calculate by integrating the mass flux over a wedge about L2, similar to the procedure in Paper I. We also estimate the MT rate near L3, $\dot{M}_{\rm L3}$, the Lagrange point on the side of the donor star. In all cases, the L2 outflow dominates, but to different degrees. For the `highest_mdot` and `high_mdot` simulations, $\dot{M}_{\rm L2} \sim 10 - 20 \times \dot{M}_{\rm L3}$, similar to our result in Paper I without any gas cooling. For the other simulations, $\dot{M}_{\rm L2} \gtrsim 10^3 \times \dot{M}_{\rm L3}$, meaning that it is extremely unfavorable for material to circle around the donor star on an equipotential that would allow it to escape near L3.

This behavior can be understood by comparing the MT rate to the Eddington-limited MT rate at the *outer* edge of the disk around $M_{\rm a}$ (Lu et al., 2023). $\dot{M}_{\rm edd}$ is defined by equating the outer disk accretion luminosity to the Eddington luminosity, such that

$$\frac{GM_{\rm a}|\dot{M}_{\rm donor}|}{r_d} = L_{\rm edd} = \frac{4\pi c G M_{\rm a}}{\kappa} \tag{6.10}$$

and solving for $|\dot{M}_{\rm donor}|$, where r_d is the radius near the outer edge of $M_{\rm a}$'s disk. Therefore,

$$\dot{M}_{\rm edd} = \frac{4\pi c r_d}{\kappa}. \tag{6.11}$$

For our simulations, we estimate $\dot{M}_{\rm edd}$ by finding the density-weighted average of $\frac{4\pi c r_d}{\kappa}$ at r_d values (in units of a) of 0.2, 0.25, and 0.3 around $M_{\rm a}$ and inside $M_{\rm a}$'s Roche lobe. Using lower values r_d mildly changes $\dot{M}_{\rm edd}$ but not enough to change the trend in Fig. 6.3. From the bottom panel of Fig. 6.3, the transition between conservative and significant non-conservative MT approximately occurs when the MT rate rises above $\dot{M}_{\rm edd}$.

Fig. 6.4 shows a comparison of our simulations to the semianalytic predictions of Lu et al. (2023), by plotting $f_{\rm L2}$, the fraction of transferred mass leaving the L2 point. Note that $f_{\rm L2}$ for our simulations is simply equal to $1 - \beta$. The colormap of Fig. 6.4 is generated using code[1] accompanying Lu et al. (2023) for the binary masses we simulate, and assuming a hydrogen rich gas of solar metallicity.

We find that $f_{\rm L2}$ is about 0.6 for the `high_mdot` simulation and about 0.1 for the `mid_mdot` simulation, but Lu et al. (2023) predicts values of > 0.9 and about 0.65,

[1] `https://github.com/wenbinlu/L2massloss`

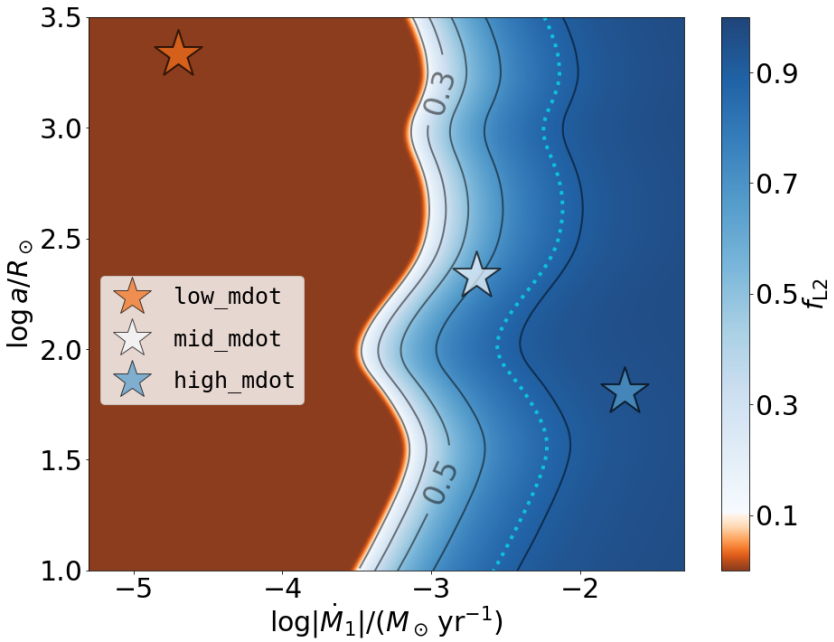


Figure 6.4: The predicted fraction of material escaping through L2, f_{L2}, for various a and MT rates. This follows the figures of Lu et al. (2023), but adapted for a 10 $M_\odot$ donor and 5 $M_\odot$ accretor. Solid lines show contours of constant f_{L2}, and the cyan dotted line shows where $\dot{M}_{\rm donor} = \dot{M}_{\rm edd}$. Stars show where our simulations lie in this parameter space, with the internal color corresponding to their f_{L2} value. The `highest_mdot` simulation is not shown for convenience, but would lie outside the right border of this plot.

respectively. For our more extreme simulations, `low_mdot` and `highest_mdot`, f_{L2} approaches 0 and 1, in general agreement with Lu et al. (2023).

In other words, our simulations imply that the MT threshold where MT becomes strongly non-conservative is higher than predicted by Lu et al. (2023), by a factor of ~2-5. More densely-sampled simulations would help determine the differences throughout the entire parameter space (e.g. if the “wriggles" of Fig. 6.4, caused by opacity variations, are robust). The reason for the difference is unclear, but may be due to geometric factors of order unity, our approximate treatment of gas cooling, or the lack of viscous accretion power in our simulations.

6.3.2 Observational appearance: Temperatures and luminosities

We calculate the cooling luminosity of the disk around $M_{\rm a}$ by integrating the power per unit volume within a sphere of radius $0.3a$, with approximates the Roche lobe of $M_{\rm a}$, i.e.

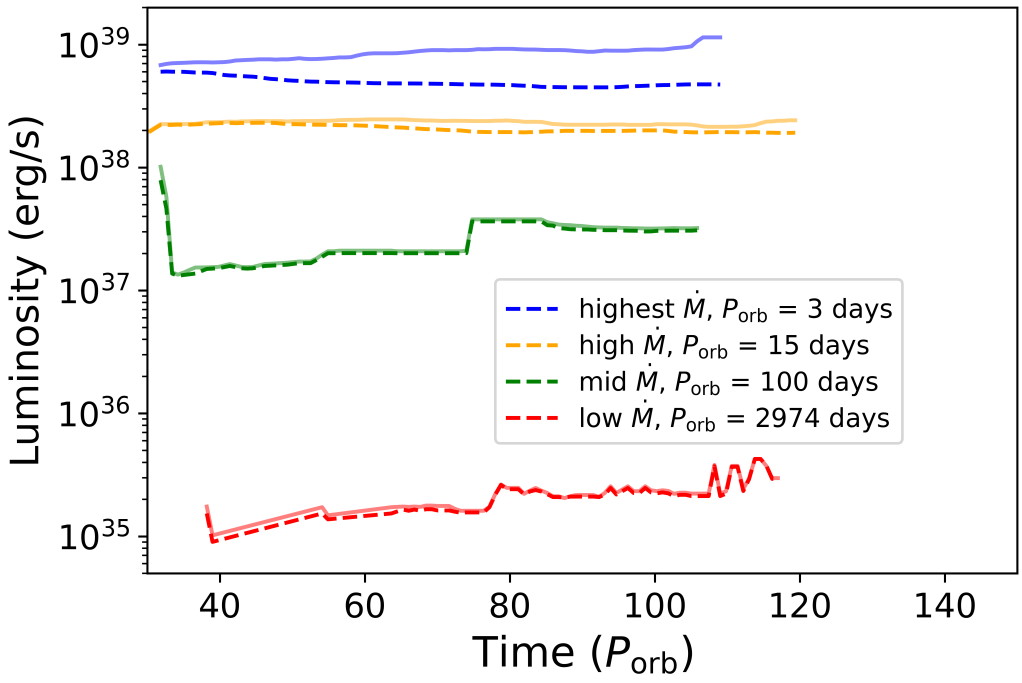


Figure 6.5: The cooling luminosity calculated within the disk around $M_{\rm a}$ (dashed lines, Eq. 6.12, and the entire computational domain (solid lines, Eq. 6.13). Curves are smoothed using a rolling average, and values are not shown at $t \lesssim 40$ because the MT rate has not ramped up to its steady-state value.

$$L_{\rm cool,\mathit{disk}} = \int_{|\vec{r}-a\hat{x}|\leq 0.3a} \dot{E}_{\rm cool} dV \tag{6.12}$$

and the cooling luminosity of all gas in the domain by integrating over the entire spherical domain

$$L_{\rm cool,\mathit{tot}} = \int_{\text{entire domain}} \dot{E}_{\rm cool} dV. \tag{6.13}$$

Note that there is no cooling inside the Roche lobe of the donor $M_{\rm d}$.

Fig. 6.5 plots the values of luminosity, in erg/s, versus time for our different simulations. Because of the vastly different orbital timescales between our simulation, time is plotted in orbital periods. Unsurprisingly, the luminosity increases with increasing MT rate, although note from Appendix 6.B that for the `highest_mdot` simulation that the gas cooling timescale is long and it is more difficult for photons to escape. For the `mid_mdot` and `low_mdot` simulations, all the cooling power comes from the disk around $M_{\rm a}$, with almost nothing from the circumbinary outflow.

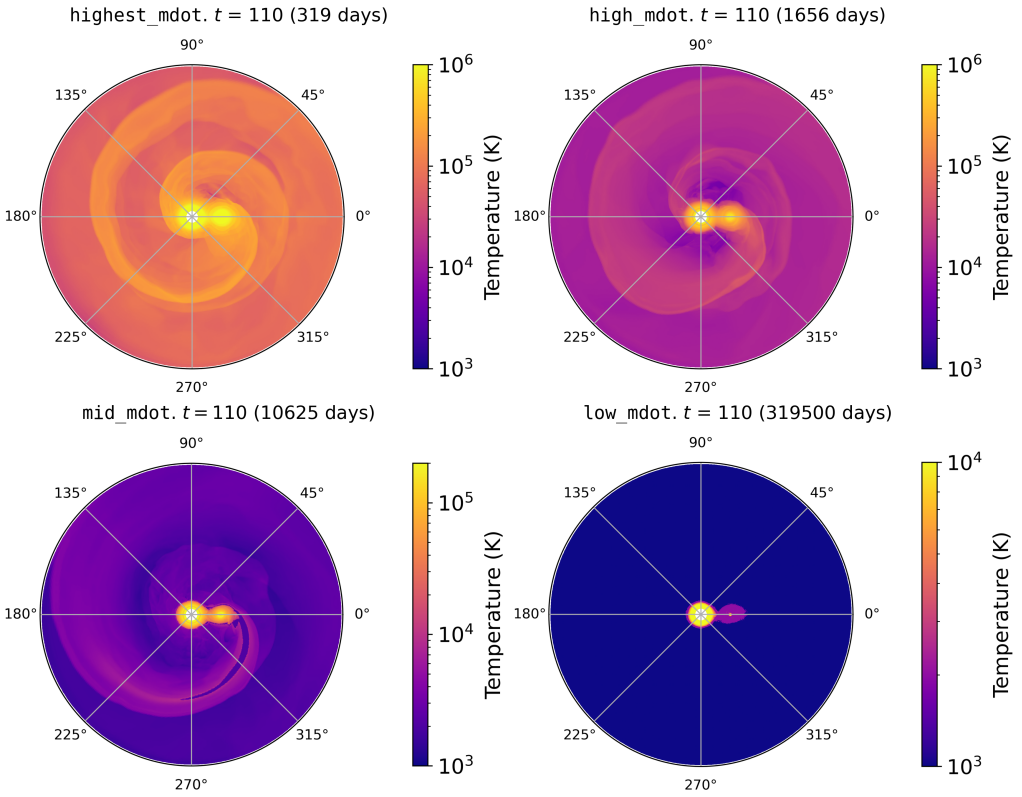


Figure 6.6: The gas temperature T in the equatorial plane for all simulations. The snapshots, representative of the simulations once they have reached a quasi-steady state, are labeled with t in both orbital periods and physical units (days). The T floor is reached in the outer regions of the `mid_mdot` simulation and almost everywhere in the `low_mdot` simulation (see text for details).

In the `highest_mdot` case, including the full domain approximately doubles the overall luminosity, so the cooling of the outflow is quite important. This is because most of the equatorial domain is flooded with material (top panel of Fig. 6.1). The `high_mdot` simulation shows intermediate behavior, where the cooling power of the outflow makes a $\sim$20% increase to the overall cooling power.

The increase of luminosity as a function of MT rate can be understood through an increase in accretion power from the disk surrounding $M_{\rm a}$. Note, however, that we do not resolve the surface of the accretor, as it is represented by a point mass with a softening potential of length $\epsilon = 0.05a$ (Sec. 6.2). When we assume that $L_{\rm cool,\mathit{disk}} \sim \frac{GM_{\rm a}\dot{M}_{\rm a}}{r_{{\rm d},\mathit{eff}}}$, we find that $r_{{\rm d},\mathit{eff}}/a \approx 0.05, 0.15, 0.2, 0.3$ for our simulations of increasing MT rate (`low_mdot`, `mid_mdot`, `high_mdot`, `highest_mdot`). For the lower MT rate simulations, $r_{{\rm d},\mathit{eff}}$ is closer to the softening radius, suggesting that the cooling power is mostly coming from the inner edge of $M_{\rm a}$'s disk. For the

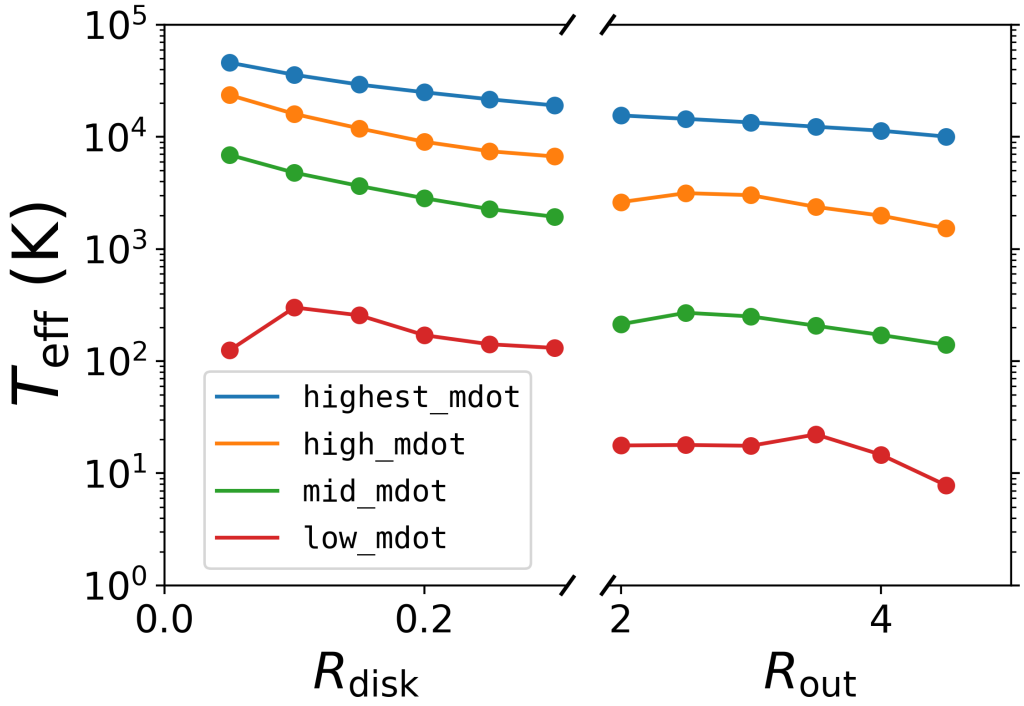


Figure 6.7: The average gas effective temperature $T_{\rm eff}$ in the disk around $M_{\rm a}$ and in the circumbinary outflow. The curves shown are calculated over cylinders of constant cylindrical radius $R_{\rm disk}$ about $M_{\rm a}$ and constant $R_{\rm out}$ about the origin (see text for details). $T_{\rm eff}$ values are averaged starting at $t = 50$ because the MT rate has not reached a steady-state value and the disks/outflow have not yet formed at early times.

higher MT rate simulations, $r_{{\rm d},eff}$ is closer to the Roche radius of $M_{\rm a}$. $\dot{M}_{\rm a}$ is much less than $\dot{M}_{\rm donor}$ in the case of the `highest_mdot` and `high_mdot` simulations, which show highly non-conservative MT.

Again, while our simulations include shock heating of the gas, they do *not* include viscous heating associated with accretion. Therefore the gas is likely to experience additional heating that, in equilibrium, also increases the cooling luminosity. Accretion onto a compact object would generate heating much larger than the shock heating occurring in the accretor's outer disk. The cooling luminosities we have calculated are therefore likely lower bounds in such cases.

The gas temperature T, defined by Eq. 6.6, also varies greatly between simulations. Fig. 6.6 plots T in the equatorial plane, at representative snapshots. For all simulations, T in $M_{\rm a}$'s disk is hotter than in the rest of the domain, due to shock heating and slower cooling. With decreasing MT rate, T is lower everywhere (note

the difference in colorbar scales between subplots). For the `low_mdot` simulation, T outside M_a's disk reaches close to a temperature floor, which can be outside our opacity tables that extend down to 1,000 K. However, because there is only a small amount of gas outflowing in this case, its cooling is not important. With the differences in T within the simulation domain, and between simulations, as well as the vastly different density scale between simulations (Fig. 6.1), we expect gas pressure and radiation pressure to respectively dominate in different regions and for different simulations (see Appendix 6.A for further discussion).

We also estimate the effective temperature $T_{\rm eff}$ of the emitted radiation by computing azimuthally averaged effective temperatures inside the disk around M_a and also in the circumbinary gas, and estimating that

$$\sigma_{\rm SB} T_{\rm eff}^4 = \int \dot{E}_{\rm cool} dz. \tag{6.14}$$

We perform this integral over z for cylinders of radius $R_{\rm disk}$ centered around M_a

$$R_{\rm disk} \equiv \left((x-1)^2 + y^2 \right)^{1/2} \tag{6.15}$$

and cylinders of radius $R_{\rm out}$ centered around the origin

$$R_{\rm out} \equiv \left(x^2 + y^2 \right)^{1/2}. \tag{6.16}$$

To generate our quoted values, we then take the average of $T_{\rm eff}$ around the cylindrical axis (an average over ϕ in the origin-centered case). Note that Eq. 6.14 approximately reduces to

$$T_{{\rm eff},est}^4 = T^4 \left(\tau_z + \frac{1}{\tau_z} \right)^{-1} \tag{6.17}$$

given our cooling form.

Fig. 6.7 plots time-averaged values of $T_{\rm eff}$ both in M_a's disk and circumbinary outflow, versus $R_{\rm disk}$ and $R_{\rm out}$ respectively. The typical values of $T_{\rm eff}$ decrease with decreasing MT rate - unsurprisingly given that higher MT rates correspond to a higher cooling luminosity (Fig. 6.5). As a function of increasing cylindrical radius $R_{\rm disk}$ around M_a or $R_{\rm out}$ around the binary, Fig 6.7 demonstrates that $T_{\rm eff}$ typically decreases monotonically, which is consistent with the equatorial plots of Fig. 6.6.

The value of $T_{\rm eff}$ reaches very low values in the circumbinary gas for the `low_mdot` simulation, which should not be trusted. In the case of such low density gas, our assumptions related to radiative cooling adopted in the simulation setup (Sec. 6.2.1), e.g. that there is an equilibrium between gas and radiation, might break down. Since the circumbinary densities and optical depths are very low, any emission would likely occur via lines (e.g., molecular lines such as CO). Dust formation may also occur and change the opacity of the gas.

As in our calculation of $L_{\rm cool}$, because our simulations do not include viscous heating, the values of T and $T_{\rm eff}$ for a more realistic accretion disk around a compact object could be significantly higher than the values calculated here.

Observable predictions

From the $T_{\rm eff}$ estimated in Sec. 6.3.2, we can estimate the observational appearance of the disk around $M_{\rm a}$ and outflows we model, although making more precise predictions will require more realistic radiative transport modeling. For $T_{\rm eff} \sim 5 \times 10^4$, 10^4, and 5×10^3 K in $M_{\rm a}$'s disk of the `highest_mdot`, `high_mdot`, and `mid_mdot` simulations respectively, this roughly corresponds to peak emission wavelengths in the ultraviolet, near-ultraviolet/optical, and optical/near-infrared. For $T_{\rm eff} \sim 10^4$, 2×10^3, and 5×10^2 K in the circumbinary outflow of the same simulations, this roughly corresponds to peak emission wavelengths in the near-ultraviolet/optical, near-infrared, and the mid-infrared, respectively.

The cooling luminosities associated with our simulations are $\sim 10^{39}$ erg/s for our `highest_mdot` simulation and $\sim 10^{38}$ erg/s for our `high_mdot` simulation. Even when just including the domain outside $M_{\rm a}$'s disk, luminosities for these two higher MT rate simulations are $\sim 5 \times 10^{38}$ erg/s and $\sim 2 \times 10^{37}$ erg/s. Our lower MT rate simulations are associated with lower luminosities, dominated by the cooling power in $M_{\rm a}$'s disk For instance, the `mid_mdot` simulation has luminosities of $\sim 10^{37}$ erg/s when including the entire domain, and $\sim 10^{36}$ erg/s outside $M_{\rm a}$'s disk.

Despite these predictions, there are multiple radiation processes that we have neglected. Although the cooling luminosity of $M_{\rm a}$'s disk tends to peak near its center (Sec. 6.3.2), we have neglected a detailed treatment of accretion power onto the surface of $M_{\rm a}$, especially if is a compact object like a neutron star. In such a case, a fast wind will likely be launched due to viscous accretion, which will emit X-ray and UV photons. These photons will be reprocessed to longer wavelengths by the circumbinary outflow — in the infrared if dust is formed (Lu et al., 2023).

However, the production of dust in the outflow is unclear. Temperatures below around 1500 K are necessary, though not sufficient, to cause dust condensation. In the `mid_mdot` simulation, such low temperatures are reached in parts of the domain above the equatorial plane, and in the `low_mdot` simulation such temperatures are reached almost everywhere outside M_a's disk, which is kept hotter by an imposed temperature floor (Fig. 6.6). However, our low temperature estimates may not be accurate and are likely may be more associated with ambient gas rather than with the outflows we primarily seek to model. A more important question is whether dust forms somewhere in the equatorial plane of our simulations, where the outflow is strongest, especially for our higher MT simulations. Although T decreases moving radially outward (Fig. 6.7), our simulation domain does not extend far enough from the binary to capture its ultimate asymptotic temperature. Pejcha et al. (2016b) shows that, for a MT rate out of L2 of $10^{-5} M_\odot$/yr, the gas temperature does not drop low enough to favor dust formation until $r = 8a$. This MT rate is intermediate to our `low_mdot` and `mid_mdot` simulations, and the gas temperatures in Pejcha et al. (2016b) are approximately similar to ours where the simulation domains overlap. However our domain does not extend far enough to reach lower temperatures (especially in the equatorial plane), preventing us from making more detailed predictions of dust formation.

6.3.3 Energetics, velocities, and angular momentum losses

We compute the specific angular momentum (AM) carried away by the outflowing gas. The specific AM (along $\hat{z}$) of the L2 point is given by $h_{\rm L2} = \Omega(r_{\rm L2} - r_{\rm com})^2$, where $r_{\rm L2}$ and $r_{\rm com}$ are the radial coordinates of L2 and the COM. In units of $\sqrt{G M_{\rm tot} a}$, $h_{\rm L2} = 1.56$ for the $q = 0.5$ binaries that we simulate.

The specific AM $\vec{h}$ of an arbitrary fluid element, with coordinate $\vec{r}$ and velocity $\vec{v}$ in the simulation frame, is given by

$$\vec{h} = (\vec{r} - \vec{r}_{\rm com}) \times \left(\vec{v} + \vec{\Omega} \times (\vec{r} - \vec{r}_{\rm com}) \right) \tag{6.18}$$

where $\vec{r}_{\rm com}$ is the coordinate of the binary's COM (in the co-rotating frame) and $\vec{\Omega}$ is the orbital frequency. We are interested predominantly in the $\hat{z}$ component of the AM, as the orbital axis of the binary is along $\hat{z}$. The rate of AM outflow $\dot{L}_z$ over a surface with area element $\vec{dA}$ is given by

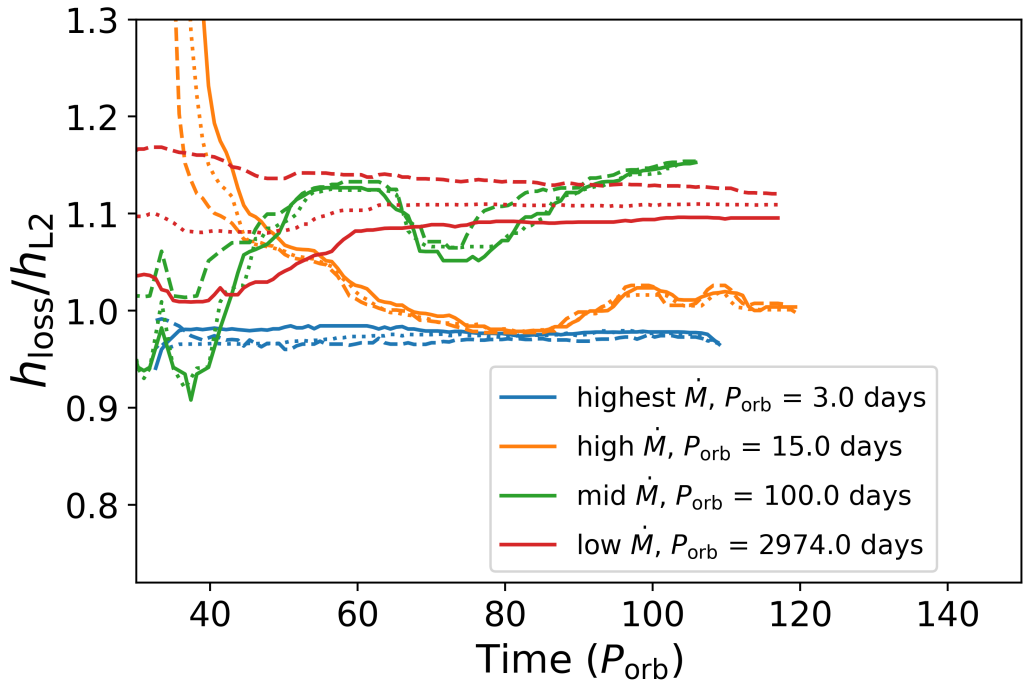


Figure 6.8: The specific AM of outflowing material $h_{\rm loss}$, in units of $h_{\rm L2}$, versus time in orbital periods. $h_{\rm loss}$ is calculated over spheres centered at the COM, of radius 3, 4, and 4.65 (dashed, dotted, solid lines) and all curves are smoothed using a rolling average.

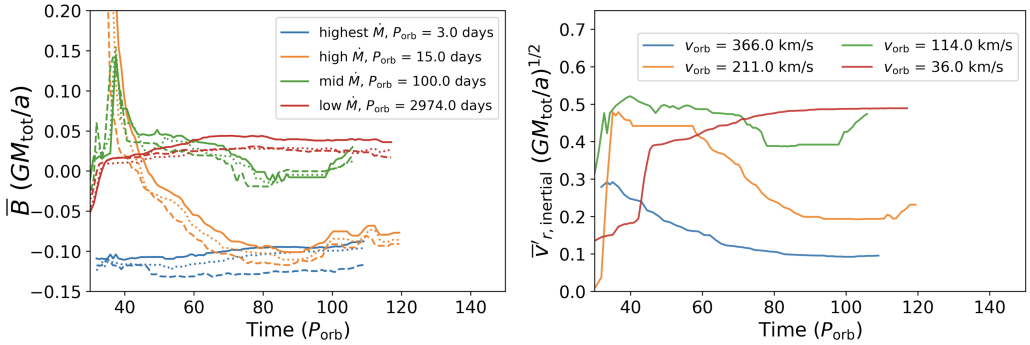


Figure 6.9: Properties related to the energy and velocity of outflowing gas. Curves are time-smoothed using a rolling average. Left: The Bernoulii parameter $\overline{B}$, in units of $GM_{\rm tot}/a$, for COM-centered spheres of $|\vec{r} - \vec{r}_{\rm com}| = 3, 4$ and $r_{\rm max} \approx 4.65$, in units of $a = 1$ (dashed, dotted, solid lines)). Right: The volume-averaged radial velocity of the outflow, $\overline{v}'_{r,\rm inertial}$ (Eq. 6.25), in units of the orbital velocity for each simulation, $\sqrt{GM_{\rm tot}/a}$, whose cgs value is shown in the legend.

$$\dot{L}_z = \int_A h_z \rho \vec{v} \cdot \vec{dA} \,. \tag{6.19}$$

Similarly, the rate of mass flow through the same surface can be written as

$$\dot{M} = \int_A \rho \vec{v} \cdot \vec{dA} \tag{6.20}$$

and the average specific AM $h_{\rm loss}$ of the outflowing material through this surface is the ratio of these two integrals, i.e.

$$h_{\rm loss} = \frac{\dot{L}_z}{\dot{M}}. \tag{6.21}$$

As in Paper I, we find that the value of $h_{\rm loss}$ asymptotes with distance from the COM to an approximately constant value. We calculate $h_{\rm loss}$ over spheres of constant $|\vec{r} - \vec{r}_{\rm com}| \approx 3, 4,$ and ≈ 4.65, where 4.65 is the largest COM-centered sphere that fits in the domain. Fig 6.8 plots the values of $h_{\rm loss}$, in units of $h_{\rm L2}$. In all cases, $h_{\rm loss} \sim h_{\rm L2}$, meaning that the outflow efficiently extracts AM from the binary - note that $h_{\rm L2}$ is much larger than the specific AM of the accretor, $h_{\rm M_a}$. For the `highest_mdot` and `high_mdot` simulations, $h_{\rm loss}/\ h_{\rm L2}$ is slightly less than unity, as in Paper I, whereas it is slightly larger than unity in the `low_mdot` and `mid_mdot` cases. However, even though AM may be mildly more efficiently extracted at these lower MT rates, far less material is actually flowing out through L2. These competing affects are discussed further in Section 6.3.4.

We also compute the velocity and energy of the outflowing gas. Velocities relative to the center of mass are given by $\vec{v}_{\rm inertial} = \vec{v} + \vec{\Omega} \times (\vec{r} - \vec{r}_{\rm com})$. The radial component $v_{r,\rm inertial}$ is calculated as

$$v_{r,\rm inertial} = \vec{v}_{\rm inertial} \cdot \frac{\vec{r} - \vec{r}_{\rm com}}{|\vec{r} - \vec{r}_{\rm com}|}. \tag{6.22}$$

The Bernoulli parameter per unit mass, B, is calculated as

$$B = \frac{|\vec{v}_{\rm inertial}|^2}{2} + u_{\rm int} + \Phi_{\rm grav} + \frac{P}{\rho}. \tag{6.23}$$

where $\Phi_{\rm grav} = -\frac{M_{\rm d}}{|\vec{r}|} - \frac{M_{\rm a}}{|\vec{r} - a\hat{x}|}$. We define the mass-weighted angle-averaged Bernoulli parameter $\overline{B}$ as

$$\overline{B} = \frac{\int \rho B dA}{\int \rho dA}, \tag{6.24}$$

where the integral is performed over spheres at constant $|\vec{r} - \vec{r}_{\rm com}|$.

The value of $\overline{B}$ asymptotes with radius, as in Paper I. Similar to the calculation above regarding $h_{\rm loss}$, we calculate $\overline{B}$ over spheres of constant $|\vec{r} - \vec{r}_{\rm com}|$. These values are plotted in the left hand panel of Fig. 6.9. The `low_mdot` and `mid_mdot` simulations have near zero or slightly positive asymptotic $\overline{B}$, meaning a large fraction of the outflow is formally unbound, whereas the `highest_mdot` and `high_mdot` simulations are bound, similar to Paper I. However, although we do include radiative cooling, we do not include any momentum deposition due to irradiation of the circumbinary gas by the stars or by $M_{\rm a}$'s disk that may help drive the gas outwards.

We also compared the energetics of the outflows to ballistic trajectories launched in corotation with L2, which tend to have positive asymptotic total energies and are described in more detail in Paper I. The outflows of the `highest_mdot` and `high_mdot` simulations feature asymptotic energies that are lower (more bound) compared to the ballistic trajectories, analogous to our Paper I results. In contrast, the outflows of the `low_mdot` and `mid_mdot` simulations have slightly positive energies, similar to the ballistic trajectories.

We calculate a characteristic radial velocity $\overline{v}'_{r,\rm inertial}$ using the radial inertial velocity $v_{r,\rm inertial}$ (Eq. 6.22),

$$\overline{v}'_{r,\rm inertial} = \frac{\int_{r=3}^{r=r_{\rm out}} \rho v_{r,\rm inertial} dV}{\int_{r=3}^{r=r_{\rm out}} \rho dV} \tag{6.25}$$

where we have performed a full volume integral for the average because, due to the spiral structure and shocks in the outflow, $v_{r,\rm inertial}$ can show a wave pattern that oscillates about an average value. The values of $\overline{v}'_{r,\rm inertial}$ are plotted in the right hand panel of Fig. 6.9. In units of the orbital velocity $v_{\rm orb}$, there is a trend that the `highest_mdot` simulation has a low $\overline{v}'_{r,\rm inertial}$ (10% $v_{\rm orb}$), the `high_mdot` simulation a somewhat higher value (20% $v_{\rm orb}$), and the lower MT simulations a substantially higher value ($40 - 50\%$ $v_{\rm orb}$). This is consistent with decreasing MT rate corresponding to a higher specific energy and Bernoulli parameter (left panel). In cgs units, the trend is different due to lower MT rate simulations having a lower $v_{\rm orb}$. The `low_mdot` simulation has the lowest outflow velocity at about 15 km/s, whereas the other 3 simulations have velocities clustered between 40-60 km/s.

Pejcha et al. (2016b) performed smoothed particle hydrodynamic (SPH) simulations, where material was initialized near L2 in co-rotation with the binary's orbit, and

Simulation	β	$h_{\rm loss}/h_{\rm L2}$	γ	$\zeta_{\rm RL}$
highest_mdot	0.05	0.95	6.7	7.9
high_mdot	0.4	1.0	7.0	6.0
mid_mdot	0.9	1.1	7.7	3.2
low_mdot	0.96	1.1	7.7	2.8

Table 6.2: For our grid of MT simulations, the fraction of mass retained in $M_{\rm a}$'s disk β (Eq. 6.9) and outgoing AM parameters $h_{\rm loss}$, in units of $h_{\rm L2}$, and γ (Eqs. 6.21 and 6.26). $\zeta_{\rm RL}$ is the mass-radius exponent of the donor's Roche radius (Eq. 6.28), with higher values generally making unstable MT more likely. The values quoted are averaged over the steady-state behavior of the simulations.

the outflow was tracked far from the binary to $r = 50a$. They found that that the asymptotic velocity of the outflow is always proportional to $v_{\rm orb}$. In contrast, we find that the average radial velocity in units of the escape speed, $\overline{v}'_{r,\rm inertial}/v_{\rm orb}$ tends to increase with decreasing MT rate. In addition, our outflows tend to be bound for highest_mdot and the high_mdot simulations, whereas the outflows in Pejcha et al. (2016b) are unbound for the same mass ratio.

These discrepancies may be understood through MacLeod et al. (2018a) and our Paper I, which found that strong outflows through L2 tend to be initialized not at co-rotation, and are therefore more bound compared to the assumptions of Pejcha et al. (2016b). Our higher MT rate simulations are in this regime. In contrast, the fact that $\overline{v}'_{r,\rm inertial}/v_{\rm orb}$ reaches a roughly constant ratio for our lower MT rate simulations seems to imply that they are in the regime consistent with Pejcha et al. (2016b), although the value is a bit higher than calculated in Pejcha et al. (2016b), where the asymptotic radial velocity is 0.2-0.35 $v_{\rm orb}$.

Overall, our results detailing the properties of the outflow - AM, velocity, and energy - are similar to that of Paper I, which included no radiative cooling, in the case of our highest_mdot and high_mdot simulations. Indeed, we found in Paper I that our adiabatic assumptions were most valid at $\gtrsim 10^{-2} M_\odot$/yr. Therefore, the results of Paper I are only valid at the very high end of MT rates, and this work delineates more accurately when the results of Paper I break down.

6.3.4 Effect on binary orbit

The parameters β and $h_{\rm loss}$, describing the fraction of the transferred mass that stays in the disk surrounding $M_{\rm a}$, and the AM carried by any escaping material, are of great consequence to the evolution of the binary's orbit. Because we are focused on snapshot of stable MT, we keep the orbital separation fixed in our simulations, but here discuss how the orbit would change over long-term MT.

It is useful to express the AM losses in terms of the dimensionless quantity γ, expressing the specific AM lost, in units of the specific AM of the binary. Therefore, if $J_{\rm orb}$ is the orbital AM,

$$\gamma = \frac{h_{\rm loss} M_{\rm tot}}{J_{\rm orb}} \tag{6.26}$$

Table 6.2 summarizes the approximate values of β and γ appropriate to the steady-state behavior of our simulations (see also Fig. 6.3). Assuming that a fraction β accretes onto $M_{\rm a}$, which can break down if $M_{\rm a}$ is a compact object and looses mass through an inner accretion disk wind, the orbital evolution of the binary then can be expressed as[2]

$$\frac{\dot{a}}{a} = -2\frac{\dot{M}_1}{M_{\rm d}}\left(1 - \beta\frac{M_{\rm d}}{M_{\rm a}} - (1-\beta)\left(\gamma + \frac{1}{2}\right)\frac{M_{\rm d}}{M_{\rm d}+M_{\rm a}}\right). \tag{6.27}$$

The last term on the right hand side of Eq. 6.27 represents orbital AM lost due to outflowing gas. Even though γ is high for the `mid_mdot` and `low_mdot` simulations, this term is close to 0 because β is close to 1. Therefore, the additional AM loss and the effect on $\dot{a}$ is minimal in these two cases. In contrast, the `high_mdot` and `highest_mdot` simulations are associated with high values of γ and low values of β, implying that this term will be large and $\dot{a}$ will be negative (as the term in parenthesis will be negative, but $\dot{M}_1$ is also negative). Although the orbit is expected to shrink in these cases, the stability of MT is determined also by the response of the donor star. This is beyond the scope of this work, as we drive MT through via heat injection and do not accurately model the donor's structural response.

However, we can estimate the value of $\zeta_{\rm RL}$, the mass-radius exponent for the Roche radius of the donor

[2]For a derivation, see Chapter 7 of O. Pols' binary evolution notes, `https://www.astro.ru.nl/~onnop/education/binaries_utrecht_notes/`

$$\zeta_{\rm RL} = \frac{\partial \ln R_L}{\partial \ln M_{\rm d}} \tag{6.28}$$

where R_L is the Roche radius of the donor star. If $\zeta_{\rm RL}$ is large compared to the exponent representing the response of the donor's radius R_* to mass loss, ζ_*

$$\zeta_* = \frac{\partial \ln R_*}{\partial \ln M_{\rm d}} \tag{6.29}$$

the overfill factor of the donor will increase and MT is likely to be unstable. We calculate $\zeta_{\rm RL}$ following the procedure in Soberman et al. (1997), and expressing $\zeta_{\rm RL}$ as

$$\zeta_{\rm RL} = \frac{\partial \ln R_L/a}{\partial \ln q'} \frac{\partial \ln q'}{\partial \ln M_{\rm d}} + \frac{\partial \ln a}{\partial \ln q'} \frac{\partial \ln q'}{\partial \ln M_{\rm d}} \tag{6.30}$$

with $q' = \frac{1}{q}$, where q' follows the mass ratio definition of Soberman et al. (1997). It is straightforward to show that

$$\frac{\partial \ln q'}{\partial \ln M_{\rm d}} = (1 + \beta q') \tag{6.31}$$

and $(\partial \ln R_L/a)/(\partial \ln q')$ can be computed using the formula of Eggleton (1983a) (see Equation 64 of (Soberman et al., 1997)). Finally, we use Eq. 6.27 to find

$$\frac{\partial \ln a}{\partial \ln q'} = \frac{-2\left(1 - \beta q' - (1-\beta)(\gamma + \frac{1}{2})\frac{q'}{1+q'}\right)}{(1 + \beta q')}. \tag{6.32}$$

This can be shown to be identical to the relevant equation in Table 5 of Soberman et al. (1997) when mass loss is through a circumbinary ring (there appears to be a typo in Equation B13 of Soberman et al. (1997), where there is a missing factor of their ϵ in order to agree with Table 5). Also note that our γ must be multiplied by a factor of $\frac{1/q}{(1+1/q)^2}$ to align with the definition of γ in Soberman et al. (1997).

The values of $\zeta_{\rm RL}$ calculated for our simulations are given in Table 6.2. We find that $\zeta_{\rm RL}$ is large, between 6-8, for the `highest_mdot` and `high_mdot` simulations, such that MT is likely to be unstable unless ζ_* is similarly large, which would correspond to a star that contracts very rapidly in response to MT. This means that a star with a radiative envelope, with $\zeta_* \gg 1$, may still undergo stable MT in these cases. For

the two lower MT rate simulations, $\zeta_{\rm RL}$ reaches a value of approximately 3. For convective-envelope stars, with $\zeta_* < 0$, MT is likely unstable for the q that we consider.

6.4 Conclusion

Episodes of rapid mass transfer (MT) ($\gtrsim 10^{-4} M_\odot$/yr) occur in many binaries containing a massive star, potentially leading to non-conservative MT and circumbinary outflows. We simulated stable MT between a 10 $M_\odot$ donor star and an 5 $M_\odot$ unresolved accretor, probing MT rates between $\sim 10^{-5}$ and $\sim 10^{-1} M_\odot$/yr by varying the orbital separation of the binary (Table 6.1). Our 3D simulations are performed using the PLUTO hydrodynamic code. They resolve the flow of mass from the donor, into a disk around the accretor, through the outer Lagrange point (L2), and into a circumbinary outflow. Radiative cooling is included at every grid cell, using tabulated opacities and an approximate treatment of photon diffusion perpendicular to the orbital plane, where the density is lowest. Our idealized simulations do not include detailed radiative transport or radiative forces.

The main results of our work are:

1. Mass from the disk around the accretor tends to outflow in a stream originating near L2, forming an equatorially-concentrated circumbinary outflow (Fig. 6.1). The fraction of gas staying in the accretor's disk, versus outflowing near L2, is expressed with the parameter β, where $\beta = 1$ implies conservative MT. We find that β decreases strongly with increasing MT rate, meaning more material outflows, and in particular rises sharply between $\sim 10^{-3}$ and $\sim 10^{-2} M_\odot$/yr (Fig. 6.3), approximately where the accretion luminosity of the outer edge of the accretor's disk becomes super-Eddington.

2. Across a wide range of MT rates, the outflowing gas has a specific angular momentum (AM) $h_{\rm loss}$ that asymptotes with radius to a value approximately equal to that of the L2 point, $h_{\rm L2}$ (Fig. 6.8) and much larger than the specific AM of the accretor. This means that, in the case of strongly non-conservative MT and significant outflows, AM will be efficiently extracted from the binary, which will have important consequences for orbital evolution.

3. The outflow reaches an asymptotic radial velocity that increases from 10% the orbital velocity to 50% the orbital velocity as the MT rate decreases from $\sim 10^{-1}$ to $\sim 10^{-3} M_\odot$/yr. In physical units, however, the radial velocity is

about 30-50 km/s for our simulations, except for the `low_mdot` simulation where it is lower (Fig. 6.9).

4. The gas cooling luminosity is dominated by the accretor's disk at low MT rates, but the outflow luminosity contributes strongly at $\sim 10^{-2} M_\odot$/yr and dominates the luminosity at $\sim 10^{-1} M_\odot$/yr (Fig. 6.5), leading to luminosities between 10^{38} and 10^{39} erg/s.

5. The gas temperature and $T_{\rm eff}$ decrease with decreasing MT rate (Figs. 6.6, 6.7), with $T_{\rm eff}$ of the circumbinary outflow $\sim 10^4, 10^3, 10^2$ K for MT rates of $\sim 10^{-1}, 10^{-2}, 10^{-3} M_\odot$/yr. The $T_{\rm eff}$ of the accretor's disk is an order of magnitude higher, peaking near the disk center, though we do not resolve the inner disk where we impose a softening potential. Dust formation may occur within the outflow, especially away from the equatorial plane and for our lower MT rate simulations.

Although there have been a few prior works that have performed hydrodynamic simulations involving outflows through L2 (and/or L3) that implemented radiative cooling losses, our work differs by systematically controlling the MT rate from the donor star and tracking its effect on the circumbinary outflow. Our measurement of the MT rates where MT transitions from conservative to non-conservative, as well as the AM carried by the outflowing gas, can be incorporated into population synthesis calculations investigating the stability of mass transfer, and orbital evolution during stable MT preceding mergers of binary compact objects (e.g., Marchant et al., 2021; Gallegos-Garcia et al., 2021). Observationally, these simulations can be used to predict the formation of material following extreme mass loss from supernova progenitors (Wu and Fuller, 2022), as well as the temperature and luminosity of outflows associated with a phase of rapid MT. However, more examination of the outflow farther away from the binary is needed to investigate the formation of dust, especially in the equatorial plane of the outflow, and the outflow's ultimate properties, which likely connect to luminous red novae (Pejcha et al., 2016b). In addition, our simulations were performed for only a single combination of donor and accretor masses, and for solar metallicity and composition, which should be extended to other massive binaries.

Acknowledgments

We are grateful for support from the NSF through grant AST-2205974. and to the Gordon and Betty Moore Foundation through Grant GBMF5076.

This work used the Purdue Anvil supercomputer through allocation PHY250215 from the Advanced Cyberinfrastructure Coordination Ecosystem: Services & Support (ACCESS) program, which is supported by U.S. National Science Foundation grants #2138259, #2138286, #2138307, #2137603, and #2138296.

We thank the anonymous referee for their thoughtful comments which greatly improved this work.

6.A Ratio of gas to radiation pressure

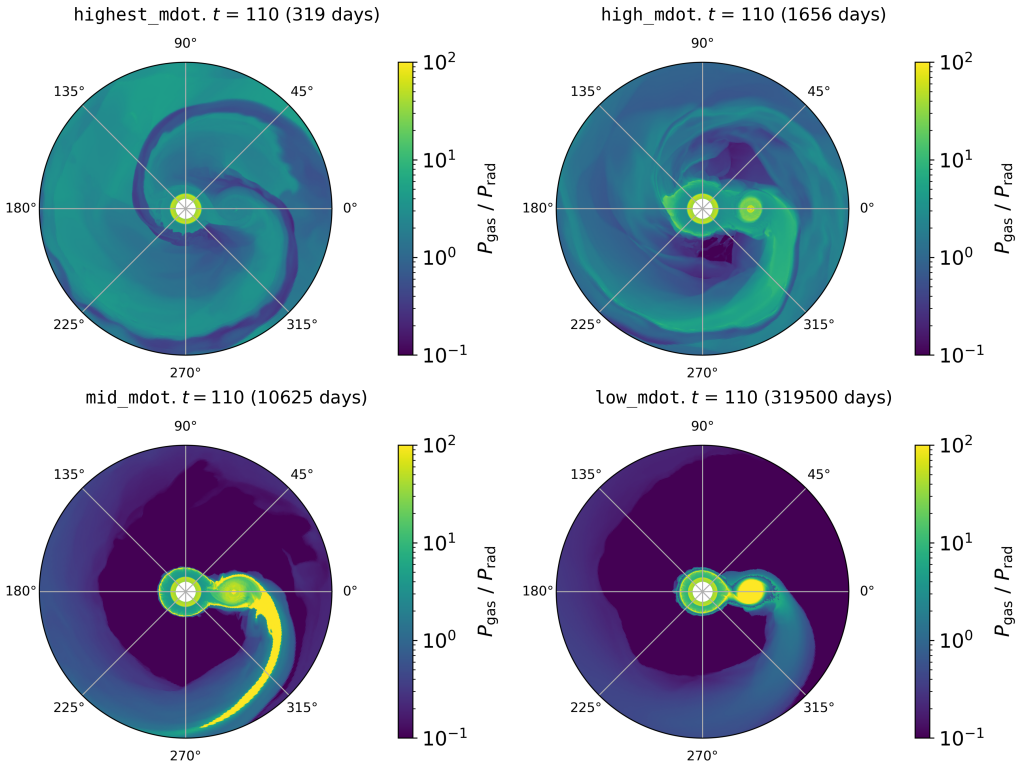


Figure 6.10: The ratio of gas pressure to radiation pressure (see Eq. 6.33) in the equatorial plane of the simulations, for snapshots representative of the quasi-steady state behavior.

Fig. 6.10 plots the ratio of gas pressure to radiation pressure in the equatorial plane, where, given ρ and P, the two terms are calculated via

$$P = \frac{\rho k_b T}{\mu m_p} + \frac{a_{\rm rad} T^4}{3}. \tag{6.33}$$

See Sec. 6.2.1 for more details related to the calculation. In general, regions with higher ρ are more gas pressure dominated. This includes $M_{\rm a}$'s disk and the circumbinary outflow originating at L2 (and L3, for the `highest_mdot` and `high_mdot` simulations. Where the density is low, radiation pressure dominates (the purple voids of Fig. 6.10). As the circumbinary gas density decreases with decreasing MT rate, likewise the simulations with decreasing MT rate are less gas pressure dominated in the circumbinary regions. However, the opposite is true in the disk around the accretor. For the `low_mdot` and `mid_mdot` simulations, the ratio of gas to radiation pressure reaches quite a high value in the center of $M_{\rm a}$'s disk, where the gas has collapsed to a cool, dense disk. Note that we are using an adiabatic index of 1.4 for our EOS (Eq. 6.1) due to limitations in the current EOS options in PLUTO. Future work should adopt a more dynamic equation of state that varies more self-consistently with T and ρ.

6.B Timescales

The ratio of the cooling timescale to mass advection timescale changes significantly between our simulations of different MT rates. The cooling timescale $t_{\rm cool}$ is given by

$$t_{\rm cool} = \frac{u_{\rm int}}{|\dot{E}_{\rm cool}|}\,. \tag{6.34}$$

The value of $t_{\rm cool}$ is estimated, with density-weighted averages, 1. within the $M_{\rm a}$'s disk at several different radii surrounding $M_{\rm a}$ and inside its Roche lobe; 2. at radii within the circumbinary outflow, at radii centered at the origin and larger than a.

The advective timescale $t_{\rm adv}$ is given by

$$t_{\rm adv} = \frac{|\vec{r} - a\hat{x}|}{v_{r,M_{\rm a}}} \tag{6.35}$$

near $M_{\rm a}$, where $v_{r,M_{\rm a}}$ is the component of velocity radially outward from $M_{\rm a}$. In the broader circumbinary outflow surrounding both stars, we estimate $t_{\rm adv}$ as simply

$$t_{\rm adv} = \frac{|\vec{r}|}{v_r} \tag{6.36}$$

where v_r is the radial component of velocity relative to the origin. We similarly perform density-weighted averages of $t_{\rm adv}$ at various radii in our domain, using the appropriate definition in $M_{\rm a}$'s disk or in the circumbinary outflow.

For the `highest_mdot` and `high_mdot` simulations, we find that $t_{\rm cool}$ is larger than $t_{\rm adv}$ in both $M_{\rm a}$'s disk and the circumbinary outflow. Because the gas is optically thick everywhere, it is difficult for radiation to escape in this case. For the `mid_mdot` simulation, $t_{\rm adv}$ is smaller than $t_{\rm cool}$ in $M_{\rm a}$'s disk, but is larger in the circumbinary outflow. This implies that the outflow cools quickly once it leaves $M_{\rm a}$'s disk. Finally, for the `low_mdot` simulation, $t_{\rm adv}$ is larger than $t_{\rm cool}$ in both $M_{\rm a}$'s disk and in the circumbinary outflow, meaning that material rapidly cools to near the internal energy floor (which is set via a temperature floor of 2000 K in the higher density regions such as the $M_{\rm a}$'s disk).

6.C Adopted opacities

Fig. 6.11 plots the tabulated value of κ used in our work as a function of ρ and T, as well as some representative points showing where the cells in the simulation domain are located in this phase-space for a representative snapshot. The opacity rises at $\log T \gtrsim 3.7$ due to H^- opacity, and is dominated by dust for $\log T \lesssim 3.1$ (Pejcha et al., 2016b).

We divide the grid domain into three representative regions: inside $M_{\rm a}$'s Roche radius (cyan points); in the equatorial plane, where ρ is the highest, but outside $M_{\rm a}$'s Roche radius (red points); everywhere else in the domain, which are therefore points above the equatorial plane and not near $M_{\rm a}$ (orange points).

The black dashed lines of Fig. 6.11 show the floors that we impose (see also Sec. 6.2.1 for the reasoning behind our floors). The vertical line at $T = 2000$ K represents our temperature floor imposed in relatively high ρ regions, whereas the curved line shows the floor on sound speed that is imposed in low density regions. The horizontal dashed line shows the density floor imposed everywhere. For the latter two lines, the floor values are the same in code units, but vary in physical units and so shift position between the two subplots.

For the `high_mdot` simulation shown in Fig. 6.11, points near $M_{\rm a}$ are safely away from the imposed floors. In this region, the dominant opacity appears to from free-free and bound-free transitions, although this is a rough estimate based on a Kramer's opacity law. Some points in the equatorial plane and many points above the equatorial plane reach the sound speed floor, which is essentially a density-

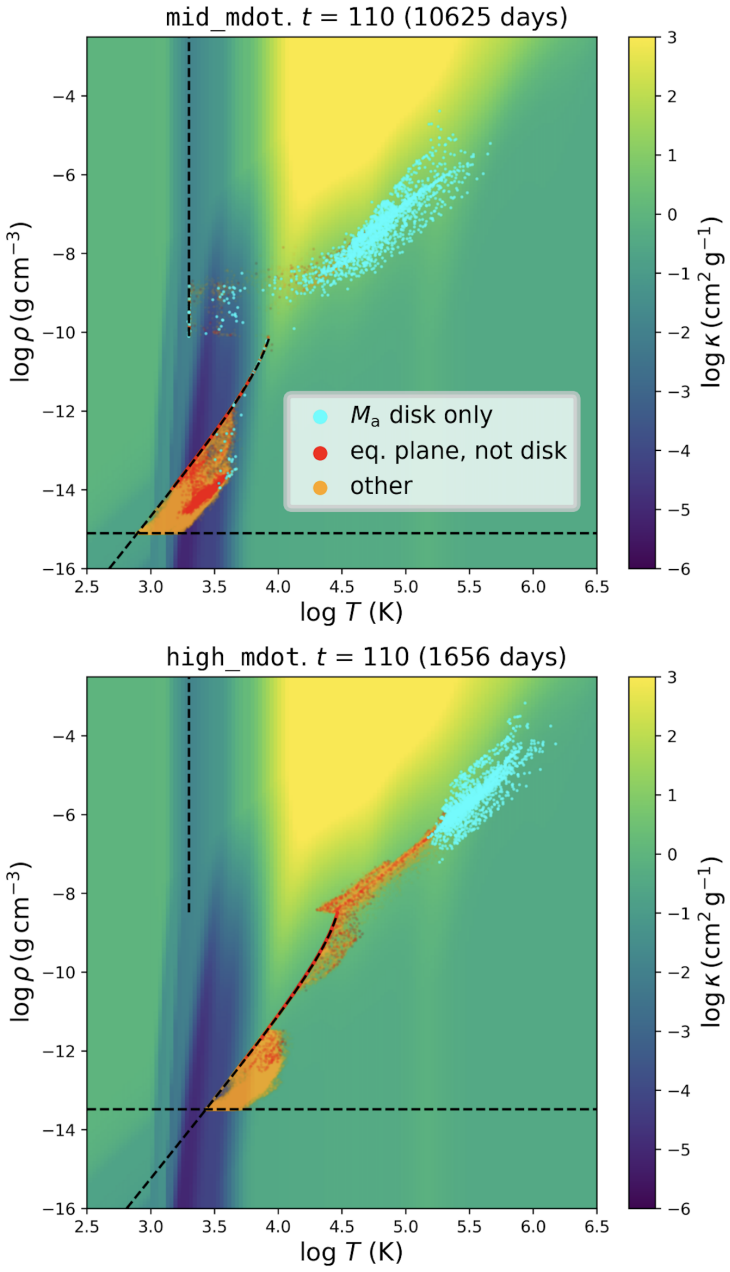


Figure 6.11: Plots of the opacity used in this work. Colored dots correspond to a sample of grid cells, corresponding to the labeled t, and where they lie in ρ, T space. Cyan points are located in the Roche lobe surrounding M_a. Red points are in the equatorial plane, excluding any points falling into M_a's Roche lobe. Orange points are sampled everywhere else in the domain, i.e. above the equatorial plane. The `highest_mdot` and `low_mdot` simulations are not shown because they are relatively similar to the subplots shown here. The black curves correspond to floors on ρ, T, and c_s (see text for details). The opacity tables used (see Sec. 6.2.1) extend down to 10^3 K, so points off the table use the value at the boundary.

dependent temperature floor. Points above the equatorial plane also tend to approach the density floor. For the `mid_mdot` simulation, most points near $M_{\rm a}$ are above the temperature floor, although some approach it. Most points elsewhere in the domain approach the density and sound speed floor. The $T = 2000$ K floor is not relevant because of the low densities in these regions - were it imposed, it would lead to an artificially high internal energy and a spurious flux of mass in the outer domain. Overall, there is a progression where the high MT rate simulations never approach the temperature floor, the `mid_mdot` simulation reaches the floor only far away from $M_{\rm a}$'s disk, and the `low_mdot` simulation reaches the floor basically everywhere.

Chapter 7

CONCLUSION AND FUTURE DIRECTIONS

This thesis has investigated the formation and evolution of close binary star systems, with mass transfer as the central thread connecting each chapter. In Chapter II and Chapter III, reverse modeling of double WD binaries established that common envelope evolution proceeds with a low and nearly constant efficiency, even when modeling strong tidal effects. Chapter IV shifted to a transient perspective, using ZTF data to show that calcium-rich gap transients prefer old, quiescent host environments, consistent with 91bg-like supernovae that likely arise from a mass-transferring WD binary. Chapters V and VI turned to the hydrodynamics of mass transfer itself, using three-dimensional simulations to characterize the circumbinary outflows that arise during rapid, stable mass transfer — first in the adiabatic limit, then with radiative cooling across a range of mass transfer rates. Together, these results form a coherent picture of how mass transfer shapes binary systems from their formation to their explosive endpoints.

7.1 Future discoveries

The coming decade will transform our understanding of the transient sky, and with it how binary mass transfer shapes stellar evolution and stellar explosions. The Vera Rubin Observatory's Legacy Survey of Space and Time (LSST) will detect approximately ten million supernovae over ten years, increasing the number of discovered transients by two orders of magnitude (Simongini et al., 2025). This statistical leap will turn currently exotic classes of supernovae — stripped-envelope Type Ib/c, interaction-powered Type Ibn and Icn, and calcium-rich gap transients like those studied in Chapter IV — from relatively small, heterogeneous samples into populations large enough to statistically constrain their progenitor systems. Weird transient classes currently known from only a handful of events will grow into real samples, potentially revealing entirely new channels and physical mechanisms, and hopefully inspiring new debates and theoretical advances. The Roman Telescope's wide infrared field of view (Rose et al., 2025) will complement this by detecting tens of thousands of Type Ia and core-collapse supernovae, along with rarer events such as superluminous supernovae and possibly pair-instability supernovae, which can be shaped substantially by mass transfer (Moriya et al., 2015; Marchant et al.,

2019; Stevance and Eldridge, 2021).

At the same time, new infrared facilities are opening a window onto dusty, optically obscured transients often associated with binary interaction. WINTER (Lourie et al., 2020; Frostig et al., 2026) and DREAMS (Soon et al., 2020) are beginning to survey the infrared transient sky systematically, with the sensitivity to detect luminous red novae (Karambelkar et al., 2023), associated with stellar mergers and common envelope events. A larger sample of luminous red novae would directly probe the rate and energetics of common envelope evolution, complementing the constraints derived in Chapter II.

Many more short-period WD binaries will likely be discovered by Roman (Digman and Hirata, 2023) and LSST (Korol et al., 2022). LISA will detect short-period WD binaries as gravitational wave sources, providing information difficult to obtain from electromagnetic observations alone (Marsh, 2011). Gravitational waves probe several aspects of tidal physics, including the tidal coupling and synchronization timescale (Biscoveanu et al., 2023; Toubiana et al., 2024), as well as dynamical tides and the internal WD structure from gravitational wave harmonics which are not found in perfectly circular and synchronized binaries (McNeill et al., 2020). These measurements would provide independent constraints on the tidal physics modeled in Chapter III, and together with the growing electromagnetic sample from ZTF (Burdge et al., 2019a; Burdge et al., 2020b), will generate a more complete picture of WD binary evolution from formation through mass transfer or merger.

7.2 Future methods and approaches

Several papers, including Chapter II, have characterized what value of $\alpha_{\rm CE}$ can reproduce observed post-CE systems, but the samples used across the literature are inhomogeneous — spanning double WDs (Nelemans et al., 2000; Nelemans and Tout, 2005), WD–main sequence (De Marco et al., 2011; Davis et al., 2012; Hernandez et al., 2021; Hernandez et al., 2022), and WD–brown dwarf binaries (Zorotovic and Schreiber, 2022), each analyzed with different methods and assumptions. A combined analysis using more advanced statistical and Bayesian methods than those employed in Chapter II could determine whether a uniform value of $\alpha_{\rm CE}$ can reproduce all of these populations simultaneously, and search for trends in efficiency with component masses, orbital periods, and other binary parameters.

Regarding tidal interactions, the modeling in Chapter III assumed the traveling wave regime, in which tidally excited waves are damped before they can reflect.

For sufficiently cool WDs, however, standing waves are likely to form instead and dissipate energy far less efficiently, changing the predicted temperatures at ultrashort orbital periods. There may therefore exist a population of relatively cool WDs in ultrashort-period binaries where tidal heating is small, which would be a natural prediction to test observationally as a follow-up to Chapter III.

Based on the results of Chapter IV, Ca-rich gap transients should be further investigated through detailed simulations of white dwarf mergers, which can generate yields and light curves. These simulations can be compared to those appropriate for 91bg-like supernova (Pakmor et al., 2010) to further test the relationship between these transient classes.

A persistent challenge in hydrodynamical simulations of mass transfer is the choice of coordinate system. Spherical coordinates are a natural fit for stellar structure, but introduce coordinate singularities at the radial origin and the poles which can restrict the timestep. Cartesian grids avoid these singularities and have been used successfully in recent simulations of binary interaction (Ryu et al., 2025), but have currently only focused on the donor star's surface, not the broad domain that was simulated in Chapters V and VI. Voronoi mesh codes such as AREPO offer a promising middle ground, adapting resolution to the local flow structure while avoiding coordinate singularities entirely (Weinberger et al., 2020; Ma et al., 2025). Improvements in the coordinate treatment would also enable tighter coupling between the simulation and the full stellar structure of the donor, allowing the star's internal response to mass loss to be followed self-consistently. With a more favorable timestep, it would become more tractable to run larger grids of simulations spanning a wider range of mass ratios and donor structures than was possible in Chapters V and VI.

The radiative cooling treatment adopted in Chapter VI, while capturing the dominant energetics, falls short of full radiation hydrodynamics. A complete treatment, as is available in codes such as Athena++ (Stone et al., 2020; Jiang, 2021; Jiang, 2022) or AREPO, would incorporate radiation pressure, radiative transfer, and the coupling between the radiation field and the gas dynamics. This becomes particularly important at higher mass transfer rates, where radiation pressure may further accelerate and unbind outflows. Dust formation in the outer regions of the outflow should also be carefully modeled, especially given the infrared appearance of luminous red novae and common envelope events, where dust reprocesses optical emission into the infrared.

The mass transfer simulations in this thesis have also neglected a full treatment of viscosity in the accretion flow around the companion star. Viscous dissipation sets the structure of the accretion disk, and determines how much of the transferred mass actually reaches the surface of the accretor. The physical origin of this viscosity is likely the magnetorotational instability (MRI) (Balbus and Hawley, 1991), which drives turbulence in disks and would require MHD simulations, though adopting the α-disk prescription (Shakura and Sunyaev, 1973) would provide an effective viscosity in the absence of full MHD. Incorporating either approach would substantially improve the fidelity of the accretion disk structure and its contribution to the transient luminosity.

Before committing to expensive three-dimensional simulations, however, it is worth revisiting the analytical foundations of mass transfer theory. One-dimensional analytic treatments remain an active area of development: recent works by Cehula and Pejcha (2023) and Marchant et al. (2021) have revisited the basic equations for calculating mass transfer rates and flows, and Cehula and Pejcha (2023) in particular have proposed a new prescription that avoids the traditional division between optically thick and optically thin regimes. Getting these analytic underpinnings right is essential for setting physically motivated initial conditions in three-dimensional simulations, and may itself resolve some of the outstanding uncertainties in binary evolution without requiring full hydrodynamical calculations at all.

7.3 Future astrophysical modeling

There are numerous places where binary interactions and mass transfer are neglected where they probably should not be, giving ripe opportunities for advances. As a first example, massive stars undergoing a pulsational pair instability supernova in a close binary, representing a potential massive binary black hole progenitor system, can easily overfill their Roche lobe, triggering enhanced mass loss not captured in 1D models (Marchant et al., 2019). As noted in Marchant et al. (2019), full hydrodynamical simulations are needed to test this and track donor mass loss, its subsequent structure, and the fate of the ejected material. In addition, such work would determine how much final BH mass is lowered compared to the single-star case, therefore revising predictions for the lower bound of the upper BH mass gap and connecting to the population of high mass BBH mergers detected by LIGO-Virgo-KAGRA.

As another example, in cataclysmic variables (CVs) undergoing hydrogen novae,

recent work has found that, surprisingly, most ejecta have a slow velocity (Shen and Quataert, 2022). Therefore, the binary potential will dominate the morphology, producing equatorially concentrated outflows rather than the commonly predicted isotropic winds. Simulations are needed to investigate further, and predict AM losses from the orbit, potentially driving more mergers, especially for low mass WDs with slow ejecta velocities and possibly explaining the observed deficit of low-mass WDs in CVs.

Finally, mass transfer does not need to occur in a narrow stream. Stars, especially asymptotic giant branch and red supergiant stars, are not perfect spheres, and extended chromospheric material (Fuller and Tsuna, 2024) can potentially be captured by the companion. Such interaction may affect the production of circumstellar material as well as stellar evolution. In addition, wind lobe overflow (WRLOF) can occur for evolved red and asymptotic giant branch stars, where winds are focused by the inner Lagrange point. While studied in some simulations of AGB stars (Mohamed and Podsiadlowski, 2007; Mohamed and Podsiadlowski, 2012), WRLOF has not been studied for red giant branch stars, which may enable improved predictions for population-synthesis models, including orbital evolution prior to later MT phases.

Each of these examples reflects a common theme: coupling what has been thought to be a single star phenomenon to the binary's potential, can offer richer and previously unpredicted behavior.

Additionally, the L2 mass loss studied in this thesis should be included in population synthesis as a mechanism of shrinking orbits without necessarily undergoing a common envelope. The effects of this, as well as better constraints on $\alpha_{\rm CE}$, can be tested with the POSYDON population synthesis code (Andrews et al., 2025), based on MESA, which offers great opportunities for improvement over previous codes.

7.4 Where will this field be in one or two decades?

Science rarely advances on a predictable schedule. It is possible that a numerical breakthrough in common envelope simulations will render Chapter II obsolete within the next few years. It is also possible that common envelope evolution remains intractable, that mass transfer never yields clean and accurate analytic prescriptions, and that the next generation of graduate students finds the whole enterprise of mass transfer stability maddening — though I suspect they will press on regardless. These things are hard to predict, and that uncertainty is part of what makes the field exciting.

Regardless of the uncertainty, there are reasons for optimism. Transient surveys are expanding across the electromagnetic spectrum, hydrodynamical simulations are becoming more sophisticated, and the stellar evolution models that underpin much of binary population synthesis still rest on assumptions that neglect mass transfer entirely - meaning there are relatively straightforward advances waiting to be made. Machine learning will continue to automate transient classification and accelerate discovery, though the most interesting science will likely come not from the well-classified events but from the strange ones that resist easy categorization.

What is certain is that we would never have learned what we know about binary stars without pointing telescopes at the sky and asking hard questions about what we find. The discovery that most massive stars live in interacting binaries was not inevitable — it required curiosity and careful observation. I am grateful to have contributed to the effort of understanding binary stars, and leave this thesis convinced that stars have been transferring mass across the cosmos long before we had the audacity to simulate it.

BIBLIOGRAPHY

Abdurro'uf et al. (Apr. 2022). "The Seventeenth Data Release of the Sloan Digital Sky Surveys: Complete Release of MaNGA, MaStar, and APOGEE-2 Data". In: *The Astrophysical Journal Supplement Series* 259, p. 35. DOI: 10.3847/1538-4365/ac4414.

Althaus, L. G. and O. G. Benvenuto (Oct. 2000). "Diffusion in helium white dwarf stars". In: *Monthly Notices of the Royal Astronomical Society* 317.4, pp. 952–964. DOI: 10.1046/j.1365-8711.2000.03825.x.

Althaus, Leandro G., Marcelo M. Miller Bertolami, and Alejandro H. Córsico (Sept. 2013). "New evolutionary sequences for extremely low-mass white dwarfs. Homogeneous mass and age determinations and asteroseismic prospects". In: *Astronomy & Astrophysics* 557, A19. DOI: 10.1051/0004-6361/201321868.

Andrews, Jeff J. et al. (Oct. 2025). "POSYDON Version 2: Population Synthesis with Detailed Binary-evolution Simulations across a Cosmological Range of Metallicities". In: *ApJS* 281.1, p. 3. DOI: 10.3847/1538-4365/adfb78.

Astropy Collaboration et al. (Oct. 2013). "Astropy: A community Python package for astronomy". In: *Astronomy & Astrophysics* 558, A33. DOI: 10.1051/0004-6361/201322068.

Astropy Collaboration et al. (Sept. 2018). "The Astropy Project: Building an Open-science Project and Status of the v2.0 Core Package". In: *The Astronomical Journal* 156.3, p. 123. DOI: 10.3847/1538-3881/aabc4f.

Astropy Collaboration et al. (Aug. 2022). "The Astropy Project: Sustaining and Growing a Community-oriented Open-source Project and the Latest Major Release (v5.0) of the Core Package". In: *The Astrophysical Journal* 935.2, p. 167. DOI: 10.3847/1538-4357/ac7c74.

Balbus, Steven A. and John F. Hawley (July 1991). "A Powerful Local Shear Instability in Weakly Magnetized Disks. I. Linear Analysis". In: *The Astrophysical Journal* 376, p. 214. DOI: 10.1086/170270.

Barkhudaryan, L. V., A. A. Hakobyan, A. G. Karapetyan, G. A. Mamon, D. Kunth, V. Adibekyan, and M. Turatto (Nov. 2019). "Supernovae and their host galaxies – VI. Normal Type Ia and 91bg-like supernovae in ellipticals". In: *Monthly Notices of the Royal Astronomical Society* 490.1, pp. 718–732. DOI: 10.1093/mnras/stz2585.

Bauer, Evan B. and Thomas Kupfer (Dec. 2021). "Phases of Mass Transfer from Hot Subdwarfs to White Dwarf Companions and Their Photometric Properties". In: *ApJ* 922.2, p. 245. DOI: 10.3847/1538-4357/ac25f0.

Bavera, Simone S., Tassos Fragos, Ying Qin, Emmanouil Zapartas, Coenraad J. Neijssel, Ilya Mandel, Aldo Batta, Sebastian M. Gaebel, Chase Kimball, and Simon Stevenson (Mar. 2020). "The origin of spin in binary black holes. Predicting the distributions of the main observables of Advanced LIGO". In: *Astronomy & Astrophysics* 635, A97. DOI: 10.1051/0004-6361/201936204.

Bavera, Simone S. et al. (Mar. 2021). "The impact of mass-transfer physics on the observable properties of field binary black hole populations". In: *Astronomy & Astrophysics* 647, A153. DOI: 10.1051/0004-6361/202039804.

Bazan, Grant and G. J. Mathews (May 1990). "Metallicity-dependent Stellar Ages and the G Dwarf Problem". In: *The Astrophysical Journal* 354, p. 644. DOI: 10.1086/168721.

Behroozi, P. (in prep.).

Behroozi, Peter, Risa H Wechsler, Andrew P Hearin, and Charlie Conroy (Sept. 2019). "UniverseMachine: The correlation between galaxy growth and dark matter halo assembly from z = 0–10". In: *Monthly Notices of the Royal Astronomical Society* 488.3, pp. 3143–3194. DOI: 10.1093/mnras/stz1182.

Bellm, Eric C. et al. (Jan. 2019a). "The Zwicky Transient Facility: System Overview, Performance, and First Results". In: *Publications of the Astronomical Society of the Pacific* 131.995, p. 018002. DOI: 10.1088/1538-3873/aaecbe.

Bellm, Eric C. et al. (Jan. 2019b). "The Zwicky Transient Facility: System Overview, Performance, and First Results". In: *Publications of the Astronomical Society of the Pacific* 131, p. 018002. DOI: 10.1088/1538-3873/aaecbe.

Bergeron, P., Rex A. Saffer, and James Liebert (July 1992). "A Spectroscopic Determination of the Mass Distribution of DA White Dwarfs". In: *The Astrophysical Journal* 394, p. 228. DOI: 10.1086/171575.

Bianchi, L., A. Conti, and B. Shiao (Oct. 2014). "VizieR Online Data Catalog: GALEX-GR6/7 data release (Bianchi+ 2014)". In: *VizieR Online Data Catalog* 2335, pp. II/335.

Bildsten, Lars, Ken J. Shen, Nevin N. Weinberg, and Gijs Nelemans (June 2007). "Faint Thermonuclear Supernovae from AM Canum Venaticorum Binaries". In: *ApJ* 662.2, p. L95. DOI: 10.1086/519489.

Biscoveanu, Sylvia, Kyle Kremer, and Eric Thrane (June 2023). "Probing the Efficiency of Tidal Synchronization in Outspiralling Double White Dwarf Binaries with LISA". In: *ApJ* 949.2, p. 95. DOI: 10.3847/1538-4357/acc585.

Blundell, Katherine M., Amy J. Mioduszewski, Tom W. B. Muxlow, Philipp Podsiadlowski, and Michael P. Rupen (Nov. 2001). "Images of an Equatorial Outflow in SS 433". In: *ApJ* 562.1, p. L79. DOI: 10.1086/324573.

Bobrick, Alexey, Melvyn B. Davies, and Ross P. Church (June 2017). "Mass transfer in white dwarf–neutron star binaries". In: *Mon Not R Astron Soc* 467.3, pp. 3556–3575. DOI: 10.1093/mnras/stx312.

Booth, R. A., S. Mohamed, and Ph. Podsiadlowski (Mar. 2016). "Modelling the circumstellar medium in RS Ophiuchi and its link to Type Ia supernovae". In: *Monthly Notices of the Royal Astronomical Society* 457.1, pp. 822–835. DOI: 10.1093/mnras/stw001.

Bours, M. C. P., T. R. Marsh, B. T. Gänsicke, and S. G. Parsons (Mar. 2015). "HST+COS spectra of the double white dwarf CSS 41177 place the secondary inside the pulsational instability strip". In: *Monthly Notices of the Royal Astronomical Society* 448.1, pp. 601–605. DOI: 10.1093/mnras/stv021.

Bours, M. C. P., T. R. Marsh, S. G. Parsons, C. M. Copperwheat, V. S. Dhillon, S. P. Littlefair, B. T. Gänsicke, A. Gianninas, and P.-E. Tremblay (Mar. 2014). "Precise parameters for both white dwarfs in the eclipsing binary CSS 41177". In: *Monthly Notices of the Royal Astronomical Society* 438.4, pp. 3399–3408. DOI: 10.1093/mnras/stt2453.

Bowler, M. G. (Oct. 2010). "Interpretation of observations of the circumbinary disk of SS 433". In: *A&A* 521, A81. DOI: 10.1051/0004-6361/201014711.

Bowler, M. G. (July 2011a). "More on the circumbinary disk of SS 433". In: *A&A* 531, A107. DOI: 10.1051/0004-6361/201016381.

Bowler, M. G. (Oct. 2011b). "SS 433: the wiggle of the wind". In: *A&A* 534, A112. DOI: 10.1051/0004-6361/201117756.

Bragaglia, Angela, Alvio Renzini, and P. Bergeron (Apr. 1995). "Temperatures, Gravities, and Masses for a Sample of Bright DA White Dwarfs and the Initial-to-Final Mass Relation". In: *The Astrophysical Journal* 443, p. 735. DOI: 10.1086/175564.

Bressan, Alessandro, Paola Marigo, Léo Girardi, Bernardo Salasnich, Claudia Dal Cero, Stefano Rubele, and Ambra Nanni (Nov. 2012). "PARSEC: stellar tracks and isochrones with the PAdova and TRieste Stellar Evolution Code". In: *Monthly Notices of the Royal Astronomical Society* 427.1, pp. 127–145. DOI: 10.1111/j.1365-2966.2012.21948.x.

Brickhill, A. J. (Sept. 1983). "The pulsations of ZZ Ceti stars". In: *Monthly Notices of the Royal Astronomical Society* 204.2, pp. 537–556. DOI: 10.1093/mnras/204.2.537.

Brown, Warren R., Mukremin Kilic, J. J. Hermes, Carlos Allende Prieto, Scott J. Kenyon, and D. E. Winget (Aug. 2011). "A 12 Minute Orbital Period Detached White Dwarf Eclipsing Binary". In: *The Astrophysical Journal* 737, p. L23. DOI: 10.1088/2041-8205/737/1/L23.

Brown, Warren R., Mukremin Kilic, Scott J. Kenyon, and A. Gianninas (June 2016). "Most Double Degenerate Low-mass White Dwarf Binaries Merge". In: *The Astrophysical Journal* 824, p. 46. DOI: 10.3847/0004-637X/824/1/46.

Brown, Warren R., Mukremin Kilic, Alekzander Kosakowski, Jeff J. Andrews, and Craig O. Heinke (Jan. 2020). "The ELM Survey. VIII. Ninety-eight Double White Dwarf Binaries". In: *The Astrophysical Journal* 889.1, p. 49. DOI: 10.3847/1538-4357/ab63cd.

Brown, Warren R., Mukremin Kilic, Alekzander Kosakowski, and A. Gianninas (Sept. 2017). "Discovery of a Detached, Eclipsing 40 Minute Period Double White Dwarf Binary and a Friend: Implications for He+CO White Dwarf Mergers*". In: *The Astrophysical Journal* 847.1, p. 10. DOI: 10.3847/1538-4357/aa8724.

Büning, A. and H. Ritter (Aug. 2004). "Long-term evolution of compact binaries with irradiation feedback". In: *A&A* 423.1, pp. 281–299. DOI: 10.1051/0004-6361:20035678.

Büning, A. and H. Ritter (Jan. 2006). "Numerical stability of mass transfer driven by Roche lobe overflow in close binaries". In: *A&A* 445.2, pp. 647–652. DOI: 10.1051/0004-6361:20053288.

Burdge, Kevin B. et al. (July 2019a). "General relativistic orbital decay in a seven-minute-orbital-period eclipsing binary system". In: *Nature* 571.7766, pp. 528–531. DOI: 10.1038/s41586-019-1403-0.

Burdge, Kevin B. et al. (Nov. 2019b). "Orbital Decay in a 20 Minute Orbital Period Detached Binary with a Hydrogen-poor Low-mass White Dwarf". In: *The Astrophysical Journal* 886.1, p. L12. DOI: 10.3847/2041-8213/ab53e5.

Burdge, Kevin B. et al. (Dec. 2020a). "A Systematic Search of Zwicky Transient Facility Data for Ultracompact Binary LISA-detectable Gravitational-wave Sources". In: *The Astrophysical Journal* 905, p. 32. DOI: 10.3847/1538-4357/abc261.

Burdge, Kevin B. et al. (Dec. 2020b). "A Systematic Search of Zwicky Transient Facility Data for Ultracompact Binary LISA-detectable Gravitational-wave Sources". In: *ApJ* 905.1, p. 32. DOI: 10.3847/1538-4357/abc261.

Burdge, Kevin B. et al. (Dec. 2020c). "An 8.8 Minute Orbital Period Eclipsing Detached Double White Dwarf Binary". In: *ApJL* 905.1, p. L7. DOI: 10.3847/2041-8213/abca91.

Burgaz, U. et al. (Feb. 2025). "ZTF SN Ia DR2: Properties of the low-mass host galaxies of Type Ia supernovae in a volume-limited sample". In: *Astronomy and Astrophysics* 694, A13. DOI: 10.1051/0004-6361/202452571.

Burkart, Joshua, Eliot Quataert, Phil Arras, and Nevin N. Weinberg (July 2013). "Tidal resonance locks in inspiraling white dwarf binaries". In: *Monthly Notices of the Royal Astronomical Society* 433.1, pp. 332–352. DOI: 10.1093/mnras/stt726.

Calzetti, Daniela, Lee Armus, Ralph C. Bohlin, Anne L. Kinney, Jan Koornneef, and Thaisa Storchi-Bergmann (Apr. 2000). "The Dust Content and Opacity of Actively Star-forming Galaxies*". In: *ApJ* 533.2, p. 682. DOI: 10.1086/308692.

Cardelli, Jason A., Geoffrey C. Clayton, and John S. Mathis (Oct. 1989). "The Relationship between Infrared, Optical, and Ultraviolet Extinction". In: *The Astrophysical Journal* 345, p. 245. DOI: 10.1086/167900.

Cehula, Jakub and Ondřej Pejcha (Sept. 2023). "A theory of mass transfer in binary stars". In: *Monthly Notices of the Royal Astronomical Society* 524.1, pp. 471–490. DOI: 10.1093/mnras/stad1862.

Cehula, Jakub and Ondřej Pejcha (Mar. 2026). "On the effects of radiation on mass transfer in binary stars". In: *Mon Not R Astron Soc* 546.3, stag014. DOI: 10.1093/mnras/stag014.

Chabrier, Gilles (July 2003). "Galactic Stellar and Substellar Initial Mass Function1". In: *PASP* 115.809, p. 763. DOI: 10.1086/376392.

Chakraborty, Sudeshna et al. (July 2024). "Type Ia Supernova Progenitor Properties and their Host Galaxies". In: *The Astrophysical Journal* 969.2, p. 80. DOI: 10.3847/1538-4357/ad4702.

Chen, Hai-Liang, Thomas M. Tauris, Xuefei Chen, and Zhanwen Han (Jan. 2022). "Formation of the Double White Dwarf Binary PTF J0533+0209 through Stable Mass Transfer?" In: *The Astrophysical Journal* 925.1, p. 89. DOI: 10.3847/1538-4357/ac3bb6.

Chen, Zhuo, Adam Frank, Eric G. Blackman, Jason Nordhaus, and Jonathan Carroll-Nellenback (July 2017). "Mass transfer and disc formation in AGB binary systems". In: *Monthly Notices of the Royal Astronomical Society* 468.4, pp. 4465–4477. DOI: 10.1093/mnras/stx680.

Cherepashchuk, A M, K A Postnov, and A A Belinski (Oct. 2018). "On masses of the components in SS433". In: *Monthly Notices of the Royal Astronomical Society* 479.4, pp. 4844–4848. DOI: 10.1093/mnras/sty1853.

Church, Ross P., Johann Dischler, Melvyn B. Davies, Christopher. A. Tout, Tim Adams, and Martin E. Beer (May 2009). "Mass transfer in eccentric binaries: the new oil-on-water smoothed particle hydrodynamics technique". In: *Monthly Notices of the Royal Astronomical Society* 395, pp. 1127–1134. DOI: 10.1111/j.1365-2966.2009.14619.x.

Clark, Peter et al. (Feb. 2020). "LSQ13ddu: a rapidly evolving stripped-envelope supernova with early circumstellar interaction signatures". In: *Monthly Notices of the Royal Astronomical Society* 492.2, pp. 2208–2228. DOI: 10.1093/mnras/stz3598.

Conroy, Charlie (2013). "Modeling the Panchromatic Spectral Energy Distributions of Galaxies". In: *Annual Review of Astronomy and Astrophysics* 51.1, pp. 393–455. DOI: 10.1146/annurev-astro-082812-141017.

Conroy, Charlie and James E. Gunn (Oct. 2010a). "FSPS: Flexible Stellar Population Synthesis". In: *Astrophysics Source Code Library*, ascl:1010.043.

Conroy, Charlie and James E. Gunn (Apr. 2010b). "The Propagation of Uncertainties in Stellar Population Synthesis Modeling. III. Model Calibration, Comparison, and Evaluation". In: *The Astrophysical Journal* 712, pp. 833–857. DOI: 10.1088/0004-637X/712/2/833.

Conroy, Charlie, James E. Gunn, and Martin White (July 2009). "The Propagation of Uncertainties in Stellar Population Synthesis Modeling. I. The Relevance of Uncertain Aspects of Stellar Evolution and the Initial Mass Function to the Derived Physical Properties of Galaxies". In: *The Astrophysical Journal* 699, pp. 486–506. DOI: 10.1088/0004-637X/699/1/486.

Cook, David O. et al. (July 2019). "Census of the Local Universe (CLU) Narrowband Survey. I. Galaxy Catalogs from Preliminary Fields". In: *ApJ* 880.1, p. 7. DOI: 10.3847/1538-4357/ab2131.

Crocker, Roland M. et al. (June 2017). "Diffuse Galactic antimatter from faint thermonuclear supernovae in old stellar populations". In: *Nature Astronomy* 1, p. 0135. DOI: 10.1038/s41550-017-0135.

Cutri, R. M. et al. (Nov. 2013). *Explanatory Supplement to the AllWISE Data Release Products*. Tech. rep., p. 1.

Dan, Marius, Stephan Rosswog, Marcus Brüggen, and Philipp Podsiadlowski (Feb. 2014). "The structure and fate of white dwarf merger remnants". In: *Monthly Notices of the Royal Astronomical Society* 438.1, pp. 14–34. DOI: 10.1093/mnras/stt1766.

Das, Kaustav K. et al. (Dec. 2023). "Probing the Low-mass End of Core-collapse Supernovae Using a Sample of Strongly-stripped Calcium-rich Type IIb Supernovae from the Zwicky Transient Facility". In: *The Astrophysical Journal* 959.1, p. 12. DOI: 10.3847/1538-4357/acfeeb.

Davidge, T. J. (May 2023). "The Environments around W Serpentis Systems: Independent Limits on System Masses and Extended Envelopes". In: *The Astronomical Journal* 165, p. 189. DOI: 10.3847/1538-3881/acc580.

Davis, P. J., U. Kolb, and C. Knigge (Jan. 2012). "Is the common envelope ejection efficiency a function of the binary parameters?" In: *Monthly Notices of the Royal Astronomical Society* 419.1, pp. 287–303. DOI: 10.1111/j.1365-2966.2011.19690.x.

Davis, Timothy A. et al. (Nov. 2014). "The ATLAS3D Project – XXVIII. Dynamically driven star formation suppression in early-type galaxies". In: *Mon Not R Astron Soc* 444.4, pp. 3427–3445. DOI: 10.1093/mnras/stu570.

De, Kishalay et al. (Oct. 2018). "iPTF 16hgs: A Double-peaked Ca-rich Gap Transient in a Metal-poor, Star-forming Dwarf Galaxy". In: *The Astrophysical Journal* 866.1, p. 72. DOI: 10.3847/1538-4357/aadf8e.

De, Kishalay et al. (Dec. 2020). "The Zwicky Transient Facility Census of the Local Universe. I. Systematic Search for Calcium-rich Gap Transients Reveals Three Related Spectroscopic Subclasses". In: *The Astrophysical Journal* 905, p. 58. DOI: 10.3847/1538-4357/abb45c.

De Marco, Orsola, Jean-Claude Passy, Maxwell Moe, Falk Herwig, Mordecai-Mark Mac Low, and Bill Paxton (Mar. 2011). "On the α formalism for the common envelope interaction". In: *Monthly Notices of the Royal Astronomical Society* 411, pp. 2277–2292. DOI: 10.1111/j.1365-2966.2010.17891.x.

Dessart, Luc and D. John Hillier (Feb. 2015). "One-dimensional non-LTE time-dependent radiative transfer of an He-detonation model and the connection to faint and fast-decaying supernovae". In: *Monthly Notices of the Royal Astronomical Society* 447.2, pp. 1370–1382. DOI: 10.1093/mnras/stu2520.

Dewi, J. D. M., O. R. Pols, G. J. Savonije, and E. P. J. van den Heuvel (Apr. 2002). "The evolution of naked helium stars with a neutron star companion in close binary systems". In: *Monthly Notices of the Royal Astronomical Society* 331.4, pp. 1027–1040. DOI: 10.1046/j.1365-8711.2002.05257.x.

Dewi, J. D. M. and T. M. Tauris (Aug. 2000). "On the energy equation and efficiency parameter of the common envelope evolution". In: *Astronomy & Astrophysics* 360, pp. 1043–1051.

Digman, Matthew C. and Christopher M. Hirata (Oct. 2023). "LISA Galactic binaries in the Roman Galactic Bulge Time-Domain Survey". In: *Monthly Notices of the Royal Astronomical Society* 525, pp. 393–401. DOI: 10.1093/mnras/stad2290.

Dimitriadis, G. et al. (Feb. 2025). "ZTF SN Ia DR2: The diversity and relative rates of the thermonuclear supernova population". In: *A&A* 694, A10. DOI: 10.1051/0004-6361/202451852.

Dong, Yuxin et al. (Mar. 2022). "Physical Properties of the Host Galaxies of Ca-rich Transients". In: *ApJ* 927.2, p. 199. DOI: 10.3847/1538-4357/ac5257.

Dorozsmai, Andris and Silvia Toonen (June 2024). "Importance of stable mass transfer and stellar winds for the formation of gravitational wave sources". In: *Monthly Notices of the Royal Astronomical Society* 530.4, pp. 3706–3739. DOI: 10.1093/mnras/stae152.

Draine, B. T. and Aigen Li (Mar. 2007). "Infrared Emission from Interstellar Dust. IV. The Silicate-Graphite-PAH Model in the Post-Spitzer Era". In: *ApJ* 657.2, p. 810. DOI: 10.1086/511055.

Eggleton, P. P. (May 1983a). "Approximations to the radii of Roche lobes". In: *The Astrophysical Journal* 268, p. 368. DOI: 10.1086/160960.

Eggleton, P. P. (May 1983b). "Aproximations to the radii of Roche lobes." In: *The Astrophysical Journal* 268, pp. 368–369. DOI: 10.1086/160960.

Ercolino, A., H. Jin, N. Langer, and L. Dessart (Apr. 2025). "Mass-transferring binary stars as progenitors of interacting hydrogen-free supernovae". In: *Astronomy & Astrophysics* 696, A103. DOI: 10.1051/0004-6361/202453426.

Ertini, K. et al. (Nov. 2023). "SN 2021gno: a calcium-rich transient with double-peaked light curves". In: *Monthly Notices of the Royal Astronomical Society* 526.1, pp. 279–298. DOI: 10.1093/mnras/stad2705.

Fabrika, S. (Jan. 2004). *The jets and supercritical accretion disk in SS433*. DOI: 10.48550/arXiv.astro-ph/0603390.

Filippenko, Alexei V. et al. (Oct. 1992). "The Subluminous, Spectroscopically Peculiar Type 1a Supernova 1991bg in the Elliptical Galaxy NGC 4374". In: *The Astronomical Journal* 104, p. 1543. DOI: 10.1086/116339.

Foley, Ryan J. (Sept. 2015). "Kinematics and host-galaxy properties suggest a nuclear origin for calcium-rich supernova progenitors". In: *Monthly Notices of the Royal Astronomical Society* 452.3, pp. 2463–2478. DOI: 10.1093/mnras/stv789.

Fontana, A. et al. (July 2009). "The fraction of quiescent massive galaxies in the early Universe". In: *A&A* 501.1, pp. 15–20. DOI: 10.1051/0004-6361/200911650.

Foreman-Mackey, Dan, Jonathan Sick, and Ben Johnson (Oct. 2014). *python-fsps: Python bindings to FSPS (v0.1.1)*. DOI: 10.5281/zenodo.12157.

Forgan, Duncan, Ken Rice, Dimitris Stamatellos, and Anthony Whitworth (Apr. 2009). "Introducing a hybrid radiative transfer method for smoothed particle hydrodynamics". In: *Monthly Notices of the Royal Astronomical Society* 394, pp. 882–891. DOI: 10.1111/j.1365-2966.2008.14373.x.

Freundlich, Jonathan and Dan Maoz (Mar. 2021). "The delay time distribution of Type-Ia supernovae in galaxy clusters: the impact of extended star-formation histories". In: *Monthly Notices of the Royal Astronomical Society* 502.4, pp. 5882–5895. DOI: 10.1093/mnras/stab493.

Frohmaier, Chris, Mark Sullivan, Kate Maguire, and Peter Nugent (May 2018). "The Volumetric Rate of Calcium-rich Transients in the Local Universe". In: *ApJ* 858.1, p. 50. DOI: 10.3847/1538-4357/aabc0b.

Frostig, Danielle et al. (Feb. 2026). *The WINTER Observatory: A One-Degree InGaAs Survey Camera to study the Transient Infrared Sky*. DOI: 10.48550/arXiv.2512.16753.

Fuller, Jim (Sept. 2017). "Pre-supernova outbursts via wave heating in massive stars – I. Red supergiants". In: *Monthly Notices of the Royal Astronomical Society* 470.2, pp. 1642–1656. DOI: 10.1093/mnras/stx1314.

Fuller, Jim and Dong Lai (Apr. 2011). "Tidal excitations of oscillation modes in compact white dwarf binaries – I. Linear theory". In: *Monthly Notices of the Royal Astronomical Society* 412.2, pp. 1331–1340. DOI: 10.1111/j.1365-2966.2010.18017.x.

Fuller, Jim and Dong Lai (Mar. 2012). "Dynamical tides in compact white dwarf binaries: tidal synchronization and dissipation". In: *Monthly Notices of the Royal Astronomical Society* 421.1, pp. 426–445. DOI: 10.1111/j.1365-2966.2011.20320.x.

Fuller, Jim and Dong Lai (Mar. 2013). "Dynamical Tides in Compact White Dwarf Binaries: Helium Core White Dwarfs, Tidal Heating, and Observational Signatures". In: *Monthly Notices of the Royal Astronomical Society* 430.1, pp. 274–287. DOI: 10.1093/mnras/sts606.

Fuller, Jim and Wenbin Lu (Apr. 2022). "The spins of compact objects born from helium stars in binary systems". In: *Monthly Notices of the Royal Astronomical Society* 511.3, pp. 3951–3964. DOI: 10.1093/mnras/stac317.

Fuller, Jim, Anthony L Piro, and Adam S Jermyn (May 2019). "Slowing the spins of stellar cores". In: *Monthly Notices of the Royal Astronomical Society* 485.3, pp. 3661–3680. DOI: 10.1093/mnras/stz514.

Fuller, Jim and Daichi Tsuna (June 2024). "Boil-off of red supergiants: mass loss and type II-P supernovae". In: *The Open Journal of Astrophysics* 7. DOI: 10.33232/001c.120130.

Gallegos-Garcia, Monica, Christopher P. L. Berry, Pablo Marchant, and Vicky Kalogera (Dec. 2021). "Binary Black Hole Formation with Detailed Modeling: Stable Mass Transfer Leads to Lower Merger Rates". In: *The Astrophysical Journal* 922, p. 110. DOI: 10.3847/1538-4357/ac2610.

Gallegos-Garcia, Monica, Jonatan Jacquemin-Ide, and Vicky Kalogera (Oct. 2024). "Angular Momentum Loss during Stable Mass Transfer onto a Compact Object: The Effect of Mass Loss via Accretion Disk Winds". In: *The Astrophysical Journal* 973.2, p. 168. DOI: 10.3847/1538-4357/ad6769.

Ge, Hongwei, Michael S. Hjellming, Ronald F. Webbink, Xuefei Chen, and Zhanwen Han (July 2010). "Adiabatic Mass Loss in Binary Stars. I. Computational Method". In: *The Astrophysical Journal* 717.2, pp. 724–738. DOI: 10.1088/0004-637X/717/2/724.

Ge, Hongwei, Christopher A. Tout, Xuefei Chen, Matthias U. Kruckow, Hailiang Chen, Dengkai Jiang, Zhenwei Li, Zhengwei Liu, and Zhanwen Han (July 2022). "The Common Envelope Evolution Outcome-A Case Study on Hot Subdwarf B Stars". In: *The Astrophysical Journal* 933.2, p. 137. DOI: 10.3847/1538-4357/ac75d3.

Gies, Douglas R., Katherine A. Shepard, Aman Kar, and Noel D. Richardson (May 2025). "TESS Light Curve of the Interacting Binary W Serpentis". In: *AJ* 169.6, p. 340. DOI: 10.3847/1538-3881/adced8.

Ginsburg, Adam et al. (Mar. 2019). "astroquery: An Astronomical Web-querying Package in Python". In: *The Astronomical Journal* 157, p. 98. DOI: 10.3847/1538-3881/aafc33.

Goldreich, Peter and Philip D. Nicholson (July 1989). "Tidal Friction in Early-Type Stars". In: *The Astrophysical Journal* 342, p. 1079. DOI: 10.1086/167665.

Goodman, Jonathan and Jonathan Weare (2010). "Ensemble samplers with affine invariance". In: *Communications in Applied Mathematics and Computational Science* 5.1, pp. 65–80. DOI: 10.2140/camcos.2010.5.65.

Gottlieb, S. and C. W. Shu (Jan. 1998). "Total variation diminishing Runge-Kutta schemes". In: *Mathematics of Computation* 67, pp. 73–85.

Graham, Matthew J. et al. (May 2019). "The Zwicky Transient Facility: Science Objectives". In: *PASP* 131.1001, p. 078001. DOI: 10.1088/1538-3873/ab006c.

Greggio, L. (Oct. 2005). "The rates of type Ia supernovae - I. Analytical formulations". In: *A&A* 441.3, pp. 1055–1078. DOI: 10.1051/0004-6361:20052926.

Haario, Heikki, Eero Saksman, and Johanna Tamminen (Apr. 2001). "An adaptive Metropolis algorithm". In: *Bernoulli* 7.2, pp. 223–242.

Hakobyan, A. A., L. V. Barkhudaryan, A. G. Karapetyan, M. H. Gevorgyan, G. A. Mamon, D. Kunth, V. Adibekyan, and M. Turatto (Nov. 2020). "Supernovae and their host galaxies - VII. The diversity of Type Ia supernova progenitors". In: *Monthly Notices of the Royal Astronomical Society* 499.1, pp. 1424–1440. DOI: 10.1093/mnras/staa2940.

Hallakoun, N. et al. (May 2016). "SDSS J1152+0248: an eclipsing double white dwarf from the KeplerK2 campaign". In: *Monthly Notices of the Royal Astronomical Society* 458.1, pp. 845–854. DOI: 10.1093/mnras/stw364.

Han, Z., Ph. Podsiadlowski, P. F. L. Maxted, and T. R. Marsh (May 2003). "The origin of subdwarf B stars - II". In: *Monthly Notices of the Royal Astronomical Society* 341.2, pp. 669–691. DOI: 10.1046/j.1365-8711.2003.06451.x.

Han, Z., Ph. Podsiadlowski, P. F. L. Maxted, T. R. Marsh, and N. Ivanova (Oct. 2002). "The origin of subdwarf B stars - I. The formation channels". In: *Monthly Notices of the Royal Astronomical Society* 336.2, pp. 449–466. DOI: 10.1046/j.1365-8711.2002.05752.x.

Han, Zhanwen, Philipp Podsiadlowski, and Peter P. Eggleton (Sept. 1994). "A possible criterion for envelope ejection in asymptotic giant branch or first giant branch stars". In: *Monthly Notices of the Royal Astronomical Society* 270.1, pp. 121–130. DOI: 10.1093/mnras/270.1.121.

Harris, Charles R. et al. (Sept. 2020). "Array programming with NumPy". In: *Nature* 585.7825, pp. 357–362. DOI: 10.1038/s41586-020-2649-2.

Heringer, E., C. Pritchet, and M. H. van Kerkwijk (Sept. 2019). "The Delay Times of Type Ia Supernova". In: *The Astrophysical Journal* 882, p. 52. DOI: 10.3847/1538-4357/ab32dd.

Hermes, J. J., Mukremin Kilic, Warren R. Brown, D. E. Winget, Carlos Allende Prieto, A. Gianninas, Anjum S. Mukadam, Antonio Cabrera-Lavers, and Scott J. Kenyon (Sept. 2012). "RAPID ORBITAL DECAY IN THE 12.75-MINUTE BINARY WHITE DWARF J0651+2844". In: *ApJL* 757.2, p. L21. DOI: 10.1088/2041-8205/757/2/L21.

Hermes, J. J. et al. (Sept. 2014). "Radius Constraints from High-speed Photometry of 20 Low-mass White Dwarf Binaries". In: *The Astrophysical Journal* 792, p. 39. DOI: 10.1088/0004-637X/792/1/39.

Hernandez, M S et al. (Feb. 2021). "The White Dwarf Binary Pathways Survey – IV. Three close white dwarf binaries with G-type secondary stars". In: *Monthly Notices of the Royal Astronomical Society* 501.2, pp. 1677–1689. DOI: 10.1093/mnras/staa3815.

Hernandez, M S et al. (May 2022). "The white dwarf binary pathways survey – VI. Two close post-common envelope binaries with TESS light curves". In: *Monthly Notices of the Royal Astronomical Society* 512.2, pp. 1843–1856. DOI: 10.1093/mnras/stac604.

Heuvel, Edward P. J. van den (Aug. 2018). "High-Mass X-ray Binaries: progenitors of double compact objects". In: *Proc. IAU* 14.S346, pp. 1–13. DOI: 10.1017/S1743921319001315.

Hjellming, Michael S. and Ronald F. Webbink (July 1987). "Thresholds for Rapid Mass Transfer in Binary System. I. Polytropic Models". In: *The Astrophysical Journal* 318, p. 794. DOI: 10.1086/165412.

Hosseinzadeh, Griffin, Curtis McCully, Ann I. Zabludoff, Iair Arcavi, K. Decker French, D. Andrew Howell, Edo Berger, and Daichi Hiramatsu (Jan. 2019). "Type Ibn Supernovae May not all Come from Massive Stars". In: *ApJL* 871.1, p. L9. DOI: 10.3847/2041-8213/aafc61.

Huang, Su-Shu (Aug. 1963). "Modes of Mass Ejection by Binary Stars and the Effect on Their Orbital Periods." In: *The Astrophysical Journal* 138, p. 471. DOI: 10.1086/147659.

Hubová, Dominika and Ondřej Pejcha (Oct. 2019). "Kinematics of mass-loss from the outer Lagrange point L2". In: *Monthly Notices of the Royal Astronomical Society* 489.1, pp. 891–899. DOI: 10.1093/mnras/stz2208.

Hunter, John D. (May 2007). "Matplotlib: A 2D Graphics Environment". In: *Computing in Science & Engineering* 9.3, pp. 90–95. DOI: 10.1109/MCSE.2007.55.

Iaconi, Roberto, Thomas Reichardt, Jan Staff, Orsola De Marco, Jean-Claude Passy, Daniel Price, James Wurster, and Falk Herwig (Feb. 2017). "The effect of a wider initial separation on common envelope binary interaction simulations". In: *Monthly Notices of the Royal Astronomical Society* 464.4, pp. 4028–4044. DOI: 10.1093/mnras/stw2377.

Iben Jr., I., M. Y. Fujimoto, D. Sugimoto, and S. Miyaji (May 1986). "Relaxation oscillations of a helium-burning star - Helium shell flashes not triggered by the accumulation of a critical mass". In: *The Astrophysical Journal* 304, p. 217. DOI: 10.1086/164155.

Iben Jr., Icko, Alexander V. Tutukov, and Alexandra V. Fedorova (Aug. 1998). "On the Luminosity of White Dwarfs in Close Binaries Merging under the Influence of Gravitational Wave Radiation". In: *The Astrophysical Journal* 503, pp. 344–349. DOI: 10.1086/305972.

Irani, I. et al. (Mar. 2022). "Less Than 1% of Core-collapse Supernovae in the Local Universe Occur in Elliptical Galaxies". In: *ApJ* 927.1, p. 10. DOI: 10.3847/1538-4357/ac4709.

Istrate, A. G., P. Marchant, T. M. Tauris, N. Langer, R. J. Stancliffe, and L. Grassitelli (Oct. 2016). "Models of low-mass helium white dwarfs including gravitational settling, thermal and chemical diffusion, and rotational mixing". In: *Astronomy & Astrophysics* 595, A35. DOI: 10.1051/0004-6361/201628874.

Ivanova, N. et al. (Feb. 2013). "Common envelope evolution: where we stand and how we can move forward". In: *The Astronomy and Astrophysics Review* 21.1, p. 59. DOI: 10.1007/s00159-013-0059-2.

Ivanova, Natalia, Surjakanta Kundu, and Ali Pourmand (Aug. 2024). "Unified Rapid Mass Transfer". In: *ApJ* 971.1, p. 64. DOI: 10.3847/1538-4357/ad583e.

Jacobson-Galán, W. V. et al. (June 2022). "The Circumstellar Environments of Double-peaked, Calcium-strong Transients 2021gno and 2021inl". In: *The Astrophysical Journal* 932.1, p. 58. DOI: 10.3847/1538-4357/ac67dc.

Jacobson-Galán, Wynn V. et al. (June 2020a). "Ca hnk: The Calcium-rich Transient Supernova 2016hnk from a Helium Shell Detonation of a Sub-Chandrasekhar White Dwarf". In: *ApJ* 896.2, p. 165. DOI: 10.3847/1538-4357/ab94b8.

Jacobson-Galán, Wynn V. et al. (Aug. 2020b). "SN 2019ehk: A Double-peaked Ca-rich Transient with Luminous X-Ray Emission and Shock-ionized Spectral Features". In: *The Astrophysical Journal* 898.2, p. 166. DOI: 10.3847/1538-4357/ab9e66.

Jacobson-Galán, Wynn V. et al. (Aug. 2020c). "SN 2019ehk: A Double-peaked Ca-rich Transient with Luminous X-Ray Emission and Shock-ionized Spectral Features". In: *The Astrophysical Journal* 898.2, p. 166. DOI: 10.3847/1538-4357/ab9e66.

Jacobson-Galán, Wynn V. et al. (Feb. 2021). "Late-time Observations of Calcium-rich Transient SN 2019ehk Reveal a Pure Radioactive Decay Power Source". In: *The Astrophysical Journal* 908.2, p. L32. DOI: 10.3847/2041-8213/abdebc.

Jermyn, Adam S. et al. (Mar. 2023). "Modules for Experiments in Stellar Astrophysics (MESA): Time-dependent Convection, Energy Conservation, Automatic Differentiation, and Infrastructure". In: *The Astrophysical Journal Supplement Series* 265.1, p. 15. DOI: 10.3847/1538-4365/acae8d.

Jiang, Yan-Fei (Apr. 2021). "An Implicit Finite Volume Scheme to Solve the Time-dependent Radiation Transport Equation Based on Discrete Ordinates". In: *The Astrophysical Journal Supplement Series* 253, p. 49. DOI: 10.3847/1538-4365/abe303.

Jiang, Yan-Fei (Oct. 2022). "Multigroup Radiation Magnetohydrodynamics Based on Discrete Ordinates including Compton Scattering". In: *The Astrophysical Journal Supplement Series* 263.1, p. 4. DOI: 10.3847/1538-4365/ac9231.

Johnson, Benjamin D. (May 2019). "SEDPY: Modules for storing and operating on astronomical source spectral energy distribution". In: *Astrophysics Source Code Library*, ascl:1905.026.

Johnson, Benjamin D., Joel Leja, Charlie Conroy, and Joshua S. Speagle (May 2021). "Stellar Population Inference with Prospector". In: *ApJS* 254.2, p. 22. DOI: 10.3847/1538-4365/abef67.

Kadam, Kundan, Patrick M Motl, Dominic C Marcello, Juhan Frank, and Geoffrey C Clayton (Dec. 2018). "Numerical simulations of mass transfer in binaries with bipolytropic components". In: *Monthly Notices of the Royal Astronomical Society* 481.3, pp. 3683–3707. DOI: 10.1093/mnras/sty2540.

Karambelkar, Viraj R. et al. (May 2023). "Volumetric Rates of Luminous Red Novae and Intermediate-luminosity Red Transients with the Zwicky Transient Facility". In: *ApJ* 948.2, p. 137. DOI: 10.3847/1538-4357/acc2b9.

Kasliwal, Mansi M. et al. (Aug. 2012). "CALCIUM-RICH GAP TRANSIENTS IN THE REMOTE OUTSKIRTS OF GALAXIES". In: *ApJ* 755.2, p. 161. DOI: 10.1088/0004-637X/755/2/161.

Kilic, Mukremin, Warren R. Brown, A. Gianninas, J. J. Hermes, Carlos Allende Prieto, and S. J. Kenyon (Oct. 2014). "A new gravitational wave verification source". In: *Monthly Notices of the Royal Astronomical Society: Letters* 444.1, pp. L1–L5. DOI: 10.1093/mnrasl/slu093.

Klencki, Jakub, Alina Istrate, Gijs Nelemans, and Onno Pols (June 2022). "Partial-envelope stripping and nuclear-timescale mass transfer from evolved supergiants at low metallicity". In: *A&A* 662, A56. DOI: 10.1051/0004-6361/202142701.

Klencki, Jakub, Gijs Nelemans, Alina G. Istrate, and Martyna Chruslinska (Jan. 2021). "It has to be cool: Supergiant progenitors of binary black hole mergers from common-envelope evolution". In: *Astronomy and Astrophysics* 645, A54. DOI: 10.1051/0004-6361/202038707.

Klencki, Jakub, Philipp Podsiadlowski, Norbert Langer, Aleksandra Olejak, Stephen Justham, Alejandro Vigna-Gómez, and Selma E. de Mink (May 2025). "A fundamental limit to how close binary systems can get via stable mass transfer shapes the properties of binary black hole mergers". In: *arXiv e-prints*, arXiv:2505.08860. DOI: 10.48550/arXiv.2505.08860.

Knigge, Christian (Sept. 2011). *The Evolution of Cataclysmic Variables*. DOI: 10.48550/arXiv.1108.4716.

Kolb, U. and H. Ritter (Sept. 1990). "A comparative study of the evolution of a close binary using a standard and an improved technique for computing mass transfer." In: *Astronomy and Astrophysics* 236, pp. 385–392.

Koposov, Sergey et al. (June 2024). *joshspeagle/dynesty: v2.1.4*. DOI: 10.5281/zenodo.12537467.

Korol, Valeriya, Na'ama Hallakoun, Silvia Toonen, and Nikolaos Karnesis (Apr. 2022). "Observationally driven Galactic double white dwarf population for LISA". In: *Monthly Notices of the Royal Astronomical Society* 511.4, pp. 5936–5947. DOI: 10.1093/mnras/stac415.

Kosakowski, Alekzander, Mukremin Kilic, and Warren Brown (Feb. 2021). "Multi-band light-curve analysis of the 40.5-min period eclipsing double-degenerate binary SDSS J082239.54+304857.19". In: *Monthly Notices of the Royal Astronomical Society* 500.4, pp. 5098–5105. DOI: 10.1093/mnras/staa3571.

Kosakowski, Alekzander, Mukremin Kilic, Warren R. Brown, and Alexandros Gianninas (May 2020). "The ELM Survey South. I. An Effective Search for Extremely Low Mass White Dwarfs". In: *The Astrophysical Journal* 894.1, p. 53. DOI: 10.3847/1538-4357/ab8300.

Kromer, M., S. A. Sim, M. Fink, F. K. Röpke, I. R. Seitenzahl, and W. Hillebrandt (Aug. 2010). "Double-detonation Sub-Chandrasekhar Supernovae: Synthetic Observables for Minimum Helium Shell Mass Models". In: *The Astrophysical Journal* 719, pp. 1067–1082. DOI: 10.1088/0004-637X/719/2/1067.

Kroupa, P. (Apr. 2001). "On the variation of the initial mass function". In: *Monthly Notices of the Royal Astronomical Society* 322.2, pp. 231–246. DOI: 10.1046/j.1365-8711.2001.04022.x.

Kupfer, Thomas et al. (Feb. 2023). *LISA Galactic binaries with astrometry from Gaia DR3*. DOI: 10.48550/arXiv.2302.12719.

Lajoie, Charles-Philippe and Alison Sills (Dec. 2010a). "MASS TRANSFER IN BINARY STARS USING SMOOTHED PARTICLE HYDRODYNAMICS. I. NUMERICAL METHOD". In: *ApJ* 726.2, p. 66. DOI: 10.1088/0004-637X/726/2/66.

Lajoie, Charles-Philippe and Alison Sills (Dec. 2010b). "MASS TRANSFER IN BINARY STARS USING SMOOTHED PARTICLE HYDRODYNAMICS. II. ECCENTRIC BINARIES". In: *ApJ* 726.2, p. 67. DOI: 10.1088/0004-637X/726/2/67.

Lau, Mike Y M, Ryosuke Hirai, Daniel J Price, and Ilya Mandel (Nov. 2022). "Common envelopes in massive stars II: The distinct roles of hydrogen and helium recombination". In: *Mon Not R Astron Soc* 516.4, pp. 4669–4678. DOI: 10.1093/mnras/stac2490.

Law-Smith, Jamie A. P. et al. (July 2022). *Successful Common Envelope Ejection and Binary Neutron Star Formation in 3D Hydrodynamics*. DOI: 10.48550/arXiv.2011.06630.

Leahy, Denis A. and Janet C. Leahy (May 2015). "A calculator for Roche lobe properties". In: *Computational Astrophysics and Cosmology* 2.1, p. 4. DOI: 10.1186/s40668-015-0008-8.

Lechien, Thibault, Selma E. de Mink, Ruggero Valli, Amanda C. Rubio, Lieke A. C. van Son, Robert Klement, Harim Jin, and Onno Pols (Sept. 2025). "Binary Stars Take What They Get: Evidence for Efficient Mass Transfer from Stripped Stars with Rapidly Rotating Companions". In: *ApJL* 990.2, p. L51. DOI: 10.3847/2041-8213/adfdd4.

Leibundgut, Bruno et al. (Jan. 1993). "SN 1991bg: A Type IA Supernova With a Difference". In: *The Astronomical Journal* 105, p. 301. DOI: 10.1086/116427.

Leja, Joel, Adam C. Carnall, Benjamin D. Johnson, Charlie Conroy, and Joshua S. Speagle (Apr. 2019). "How to Measure Galaxy Star Formation Histories. II. Nonparametric Models". In: *ApJ* 876.1, p. 3. DOI: 10.3847/1538-4357/ab133c.

Leja, Joel, Benjamin D. Johnson, Charlie Conroy, Pieter G. van Dokkum, and Nell Byler (Mar. 2017). "Deriving Physical Properties from Broadband Photometry with Prospector: Description of the Model and a Demonstration of its Accuracy Using 129 Galaxies in the Local Universe". In: *ApJ* 837.2, p. 170. DOI: 10.3847/1538-4357/aa5ffe.

Leroy, Adam K. et al. (Oct. 2019). "A z = 0 Multiwavelength Galaxy Synthesis. I. A WISE and GALEX Atlas of Local Galaxies". In: *The Astrophysical Journal Supplement Series* 244.2, p. 24. DOI: 10.3847/1538-4365/ab3925.

Li, Weidong et al. (Apr. 2011). "Nearby supernova rates from the Lick Observatory Supernova Search – II. The observed luminosity functions and fractions of supernovae in a complete sample". In: *Monthly Notices of the Royal Astronomical Society* 412.3, pp. 1441–1472. DOI: 10.1111/j.1365-2966.2011.18160.x.

Li, Zhenwei, Xuefei Chen, Hai-Liang Chen, and Zhanwen Han (Jan. 2019a). "Formation of Extremely Low-mass White Dwarfs in Double Degenerates". In: *The Astrophysical Journal* 871.2, p. 148. DOI: 10.3847/1538-4357/aaf9a1.

Li, Zhenwei, Xuefei Chen, Hai-Liang Chen, and Zhanwen Han (Feb. 2019b). "Formation of Extremely Low-mass White Dwarfs in Double Degenerates". In: *The Astrophysical Journal* 871.2, p. 148. DOI: 10.3847/1538-4357/aaf9a1.

LIGO Scientific Collaboration and KAGRA Collaboration, Virgo Collaboration et al. (Dec. 2023). "GWTC-3: Compact Binary Coalescences Observed by LIGO and Virgo during the Second Part of the Third Observing Run". In: *Phys. Rev. X* 13.4, p. 041039. DOI: 10.1103/PhysRevX.13.041039.

LIGO Scientific Collaboration and Virgo Collaboration et al. (Sept. 2019). "GWTC-1: A Gravitational-Wave Transient Catalog of Compact Binary Mergers Observed by LIGO and Virgo during the First and Second Observing Runs". In: *Physical Review X* 9.3, p. 031040. DOI: 10.1103/PhysRevX.9.031040.

Linial, Itai and Re'em Sari (Aug. 2017). "Mass-loss through the L2 Lagrange point – application to main-sequence EMRI". In: *Monthly Notices of the Royal Astronomical Society* 469.2, pp. 2441–2454. DOI: 10.1093/mnras/stx1041.

Livio, Mario and Noam Soker (June 1988). "The Common Envelope Phase in the Evolution of Binary Stars". In: *The Astrophysical Journal* 329, p. 764. DOI: 10.1086/166419.

Lombardi Jr, James C., William G. McInally, and Joshua A. Faber (Feb. 2015). "An efficient radiative cooling approximation for use in hydrodynamic simulations". In: *Monthly Notices of the Royal Astronomical Society* 447.1, pp. 25–35. DOI: 10.1093/mnras/stu2432.

Lorén-Aguilar, P., J. Isern, and E. García-Berro (June 2009). "High-resolution smoothed particle hydrodynamics simulations of the merger of binary white dwarfs". In: *A&A* 500.3, pp. 1193–1205. DOI: 10.1051/0004-6361/200811060.

Lourie, Nathan P. et al. (Dec. 2020). "The wide-field infrared transient explorer (WINTER)". In: *Ground-based and Airborne Instrumentation for Astronomy VIII*. Vol. 11447. SPIE, pp. 2064–2077. DOI: 10.1117/12.2561210.

Lu, Wenbin (May 2025). *Tidal equilibrium of a star in Roche potential*. DOI: 10.5281/zenodo.15499473.

Lu, Wenbin, Jim Fuller, Eliot Quataert, and Clément Bonnerot (Feb. 2023). "On rapid binary mass transfer – I. Physical model". In: *Monthly Notices of the Royal Astronomical Society* 519.1, pp. 1409–1424. DOI: 10.1093/mnras/stac3621.

Lubow, S. H. and F. H. Shu (June 1975). "Gas dynamics of semidetached binaries." In: *The Astrophysical Journal* 198, pp. 383–405. DOI: 10.1086/153614.

Lunnan, R. et al. (Feb. 2017). "Two New Calcium-rich Gap Transients in Group and Cluster Environments". In: *ApJ* 836.1, p. 60. DOI: 10.3847/1538-4357/836/1/60.

Lyman, J. D., A. J. Levan, R. P. Church, M. B. Davies, and N. R. Tanvir (Nov. 2014). "The progenitors of calcium-rich transients are not formed in situ*". In: *Monthly Notices of the Royal Astronomical Society* 444.3, pp. 2157–2166. DOI: 10.1093/mnras/stu1574.

Ma, Jing-Ze, Stephen Justham, Ruediger Pakmor, Andrea Chiavassa, Taeho Ryu, and Selma de Mink (Oct. 2025). *AREPO-RSG: Aspherical Circumstellar Material and Winds from Pulsating Dusty Red Supergiants in Global 3D Radiation Hydrodynamic Simulations*. DOI: 10.48550/arXiv.2510.14875.

Ma, Linhao and Jim Fuller (July 2023). "Tidal Spin-up of Black Hole Progenitor Stars". In: *The Astrophysical Journal* 952.1, p. 53. DOI: 10.3847/1538-4357/acdb74.

MacLeod, Morgan and Abraham Loeb (May 2020a). "Pre-common-envelope Mass Loss from Coalescing Binary Systems". In: *The Astrophysical Journal* 895, p. 29. DOI: 10.3847/1538-4357/ab89b6.

MacLeod, Morgan and Abraham Loeb (Apr. 2020b). "Runaway Coalescence of Pre-common-envelope Stellar Binaries". In: *The Astrophysical Journal* 893, p. 106. DOI: 10.3847/1538-4357/ab822e.

MacLeod, Morgan, Eve C. Ostriker, and James M. Stone (Dec. 2018a). "Bound Outflows, Unbound Ejecta, and the Shaping of Bipolar Remnants during Stellar Coalescence". In: *The Astrophysical Journal* 868, p. 136. DOI: 10.3847/1538-4357/aae9eb.

MacLeod, Morgan, Eve C. Ostriker, and James M. Stone (Aug. 2018b). "Runaway Coalescence at the Onset of Common Envelope Episodes". In: *The Astrophysical Journal* 863, p. 5. DOI: 10.3847/1538-4357/aacf08.

Mainzer, A. et al. (Apr. 2011). "Preliminary Results from NEOWISE: An Enhancement to the Wide-field Infrared Survey Explorer for Solar System Science". In: *The Astrophysical Journal* 731, p. 53. DOI: 10.1088/0004-637X/731/1/53.

Maoz, Dan, Filippo Mannucci, and Timothy D. Brandt (Nov. 2012). "The delay-time distribution of Type Ia supernovae from Sloan II". In: *Monthly Notices of the Royal Astronomical Society* 426.4, pp. 3282–3294. DOI: 10.1111/j.1365-2966.2012.21871.x.

Marchant, Pablo, Kaliroë M. W. Pappas, Monica Gallegos-Garcia, Christopher P. L. Berry, Ronald E. Taam, Vicky Kalogera, and Philipp Podsiadlowski (June 2021). "The role of mass transfer and common envelope evolution in the formation of merging binary black holes". In: *Astronomy and Astrophysics* 650, A107. DOI: 10.1051/0004-6361/202039992.

Marchant, Pablo, Mathieu Renzo, Robert Farmer, Kaliroe M. W. Pappas, Ronald E. Taam, Selma E. de Mink, and Vassiliki Kalogera (Sept. 2019). "Pulsational Pair-instability Supernovae in Very Close Binaries". In: *The Astrophysical Journal* 882, p. 36. DOI: 10.3847/1538-4357/ab3426.

Marsh, T R (Apr. 2011). "Double white dwarfs and LISA". In: *Class. Quantum Grav.* 28.9, p. 094019. DOI: 10.1088/0264-9381/28/9/094019.

Marsh, T. R. (July 1995). "The Discovery of a Short Period Double-Degenerate Binary Star". In: *Monthly Notices of the Royal Astronomical Society* 275.1, pp. L1–L5. DOI: 10.1093/mnras/275.1.L1.

Marsh, T. R., G. Nelemans, and D. Steeghs (May 2004). "Mass transfer between double white dwarfs". In: *Mon Not R Astron Soc* 350.1, pp. 113–128. DOI: 10.1111/j.1365-2966.2004.07564.x.

Martin, D. Christopher et al. (Jan. 2005). "The Galaxy Evolution Explorer: A Space Ultraviolet Survey Mission". In: *ApJ* 619.1, p. L1. DOI: 10.1086/426387.

Masci, Frank J. et al. (Dec. 2018). "The Zwicky Transient Facility: Data Processing, Products, and Archive". In: *PASP* 131.995, p. 018003. DOI: 10.1088/1538-3873/aae8ac.

Maxted, P. F. L., T. R. Marsh, and C. K. J. Moran (May 2002). "The mass ratio distribution of short-period double degenerate stars". In: *Monthly Notices of the Royal Astronomical Society* 332.3, pp. 745–753. DOI: 10.1046/j.1365-8711.2002.05368.x.

Mcley, Liron and Noam Soker (Dec. 2014). "Wave-driven stellar expansion and binary interaction in pre-supernova outbursts". In: *Monthly Notices of the Royal Astronomical Society* 445, pp. 2492–2499. DOI: 10.1093/mnras/stu1952.

McNeill, L O, R A Mardling, and B Müller (Jan. 2020). "Gravitational waves from dynamical tides in white-dwarf binaries". In: *Mon Not R Astron Soc* 491.2, pp. 3000–3012. DOI: 10.1093/mnras/stz3215.

Metzger, Brian D. and Ondřej Pejcha (Nov. 2017). "Shock-powered light curves of luminous red novae as signatures of pre-dynamical mass-loss in stellar mergers". In: *Monthly Notices of the Royal Astronomical Society* 471.3, pp. 3200–3211. DOI: 10.1093/mnras/stx1768.

Mignone, A. (Aug. 2014). "High-order conservative reconstruction schemes for finite volume methods in cylindrical and spherical coordinates". In: *Journal of Computational Physics* 270, pp. 784–814. DOI: 10.1016/j.jcp.2014.04.001.

Mignone, A., G. Bodo, S. Massaglia, T. Matsakos, O. Tesileanu, C. Zanni, and A. Ferrari (May 2007). "PLUTO: A Numerical Code for Computational Astrophysics". In: *The Astrophysical Journal Supplement Series* 170, pp. 228–242. DOI: 10.1086/513316.

Mignone, A., C. Zanni, P. Tzeferacos, B. van Straalen, P. Colella, and G. Bodo (Jan. 2012). "The PLUTO Code for Adaptive Mesh Computations in Astrophysical Fluid Dynamics". In: *The Astrophysical Journal Supplement Series* 198.1, p. 7. DOI: 10.1088/0067-0049/198/1/7.

Milisavljevic, Dan et al. (Sept. 2017). “iPTF15eqv: Multiwavelength Exposé of a Peculiar Calcium-rich Transient”. In: *The Astrophysical Journal* 846.1, p. 50. DOI: 10.3847/1538-4357/aa7d9f.

Mink, S. E. de, O. R. Pols, and R. W. Hilditch (June 2007). “Efficiency of mass transfer in massive close binaries - Tests from double-lined eclipsing binaries in the SMC”. In: *A&A* 467.3, pp. 1181–1196. DOI: 10.1051/0004-6361:20067007.

Moe, Maxwell and Rosanne Di Stefano (June 2017). “Mind Your Ps and Qs: The Interrelation between Period (P) and Mass-ratio (Q) Distributions of Binary Stars”. In: *ApJS* 230.2, p. 15. DOI: 10.3847/1538-4365/aa6fb6.

Mohamed, S. and Ph. Podsiadlowski (Sept. 2007). “Wind Roche-Lobe Overflow: a New Mass-Transfer Mode for Wide Binaries”. In: *Wind Roche-Lobe Overflow: a New Mass-Transfer Mode for Wide Binaries*. Vol. 372, p. 397.

Mohamed, S. and Ph. Podsiadlowski (Jan. 2012). “Mass Transfer in Mira-type Binaries”. In: *Baltic Astronomy* 21, pp. 88–96. DOI: 10.1515/astro-2017-0362.

Moran, C., T. R. Marsh, and A. Bragaglia (June 1997). “A detached double degenerate with a 1.4-h orbital period”. In: *Monthly Notices of the Royal Astronomical Society* 288.2, pp. 538–544. DOI: 10.1093/mnras/288.2.538.

Morán-Fraile, Javier, Alexander Holas, Friedrich K. Röpke, Rüdiger Pakmor, and Fabian R. N. Schneider (Mar. 2024). “Faint calcium-rich transient from a double detonation of a 0.6 M$\odot$ carbon-oxygen white dwarf star”. In: *A&A* 683, A44. DOI: 10.1051/0004-6361/202347769.

Moreno, Melvin M., Fabian R. N. Schneider, Friedrich K. Röpke, Sebastian T. Ohlmann, Rüdiger Pakmor, Philipp Podsiadlowski, and Christian Sand (Nov. 2022). “From 3D hydrodynamic simulations of common-envelope interaction to gravitational-wave mergers”. In: *A&A* 667, A72. DOI: 10.1051/0004-6361/202142731.

Moriya, Takashi J., Zheng-Wei Liu, Jonathan Mackey, Ting-Wan Chen, and Norbert Langer (Dec. 2015). “Revealing the binary origin of Type Ic superluminous supernovae through nebular hydrogen emission”. In: *A&A* 584, p. L5. DOI: 10.1051/0004-6361/201527515.

Moroni, P. G. Prada and O. Straniero (Dec. 2009). “Very low-mass white dwarfs with a C–O core”. In: *Astronomy & Astrophysics* 507.3, pp. 1575–1583. DOI: 10.1051/0004-6361/200912847.

Nandez, J. L. A., N. Ivanova, and Jr. J. C. Lombardi (Apr. 2014). “V1309 Sco—UNDERSTANDING A MERGER”. In: *ApJ* 786.1, p. 39. DOI: 10.1088/0004-637X/786/1/39.

Nandez, J. L. A., N. Ivanova, and J. C. Lombardi Jr (June 2015). "Recombination energy in double white dwarf formation". In: *Monthly Notices of the Royal Astronomical Society: Letters* 450.1, pp. L39–L43. DOI: 10.1093/mnrasl/slv043.

Nazarenko, V. V., L. V. Glazunova, and L. S. Shakun (Apr. 2005). "Two- and Three-Dimensional Hydrodynamical Simulations of Mass Transfer in Semidetached Binaries with Explicit Radiative Cooling and Self-Absorption in Their Gaseous Envelopes". In: *Astronomy Reports* 49, pp. 284–294. DOI: 10.1134/1.1898406.

Nelemans, G. and C. A. Tout (Jan. 2005). "Reconstructing the evolution of white dwarf binaries: further evidence for an alternative algorithm for the outcome of the common-envelope phase in close binaries". In: *Monthly Notices of the Royal Astronomical Society* 356.2, pp. 753–764. DOI: 10.1111/j.1365-2966.2004.08496.x.

Nelemans, G., F. Verbunt, L. R. Yungelson, and Simon F. Portegies Zwart (Aug. 2000). "Reconstructing the evolution of double helium white dwarfs: envelope loss without spiral-in". In: *Astronomy and Astrophysics* 360, pp. 1011–1018.

Nelson, L. A., W. Y. Chau, and A. Rosenblum (Dec. 1985). "Evolution of rotationally and tidally distorted low-mass, close binary systems - Implications for the minimum orbital period of cataclysmic variables". In: *The Astrophysical Journal* 299, pp. 658–667. DOI: 10.1086/163731.

Nugent, Anya E., Abigail E. Polin, and Peter E. Nugent (May 2024). *The Host Galaxies of High Velocity Type Ia Supernovae*. DOI: 10.48550/arXiv.2304.10601.

Ohlmann, Sebastian T., Friedrich K. Röpke, Rüdiger Pakmor, and Volker Springel (Dec. 2015). "HYDRODYNAMIC MOVING-MESH SIMULATIONS OF THE COMMON ENVELOPE PHASE IN BINARY STELLAR SYSTEMS". In: *ApJL* 816.1, p. L9. DOI: 10.3847/2041-8205/816/1/L9.

Olejak, Aleksandra, Jakub Klencki, Xiao-Tian Xu, Chen Wang, Krzysztof Belczynski, and Jean-Pierre Lasota (Sept. 2024). "Unequal-mass highly spinning binary black hole mergers in the stable mass transfer formation channel". In: *Astronomy & Astrophysics* 689, A305. DOI: 10.1051/0004-6361/202450480.

Pacifici, Camilla, Sree Oh, Kyuseok Oh, Jaehyun Lee, and Sukyoung K. Yi (June 2016). "TIMING THE EVOLUTION OF QUIESCENT AND STAR-FORMING LOCAL GALAXIES". In: *ApJ* 824.1, p. 45. DOI: 10.3847/0004-637X/824/1/45.

Paczynski, B. (Jan. 1976a). "Common Envelope Binaries". In: 73, p. 75.

Paczynski, B. (Jan. 1976b). "Common Envelope Binaries". In: *Structure and Evolution of Close Binary Systems*. Ed. by Peter Eggleton, Simon Mitton, and John Whelan. Vol. 73, p. 75.

Pakmor, Rüdiger, Markus Kromer, Friedrich K. Röpke, Stuart A. Sim, Ashley J. Ruiter, and Wolfgang Hillebrandt (Jan. 2010). "Sub-luminous type Ia supernovae from the mergers of equal-mass white dwarfs with mass ~0.9M⊙". In: *Nature* 463.7277, pp. 61–64. DOI: 10.1038/nature08642.

Panther, Fiona H., Ivo R. Seitenzahl, Ashley J. Ruiter, Roland M. Crocker, Chris Lidman, Ella Xi Wang, Brad E. Tucker, and Brent Groves (Aug. 2019). "SN1991bg-like supernovae are associated with old stellar populations". In: *Publications of the Astronomical Society of Australia* 36, e031. DOI: 10.1017/pasa.2019.24.

Parsons, S. G. et al. (Oct. 2017). "Two white dwarfs in ultrashort binaries with detached, eclipsing, likely substellar companions detected by K2". In: *Monthly Notices of the Royal Astronomical Society* 471.1, pp. 976–986. DOI: 10.1093/mnras/stx1610.

Parsons, Steven G. et al. (Mar. 2020). "A pulsating white dwarf in an eclipsing binary". In: *Nature Astronomy* 4, pp. 690–696. DOI: 10.1038/s41550-020-1037-z.

Pavlovskii, K., N. Ivanova, K. Belczynski, and K. X. Van (Feb. 2017). "Stability of mass transfer from massive giants: double black hole binary formation and ultraluminous X-ray sources". In: *Monthly Notices of the Royal Astronomical Society* 465.2, pp. 2092–2100. DOI: 10.1093/mnras/stw2786.

Paxton, B., L. Bildsten, A. Dotter, F. Herwig, P. Lesaffre, and F. Timmes (Jan. 2011). "Modules for Experiments in Stellar Astrophysics (MESA)". In: *ApJS* 192, p. 3. DOI: 10.1088/0067-0049/192/1/3.

Paxton, B. et al. (Sept. 2013). "Modules for Experiments in Stellar Astrophysics (MESA): Planets, Oscillations, Rotation, and Massive Stars". In: *ApJS* 208, p. 4. DOI: 10.1088/0067-0049/208/1/4.

Paxton, B. et al. (Sept. 2015). "Modules for Experiments in Stellar Astrophysics (MESA): Binaries, Pulsations, and Explosions". In: *ApJS* 220, p. 15. DOI: 10.1088/0067-0049/220/1/15.

Paxton, B. et al. (Feb. 2018). "Modules for Experiments in Stellar Astrophysics (MESA): Convective Boundaries, Element Diffusion, and Massive Star Explosions". In: *ApJS* 234, p. 34. DOI: 10.3847/1538-4365/aaa5a8.

Paxton, Bill et al. (July 2019). "Modules for Experiments in Stellar Astrophysics (MESA): Pulsating Variable Stars, Rotation, Convective Boundaries, and Energy Conservation". In: *ApJS* 243.1, p. 10. DOI: 10.3847/1538-4365/ab2241.

Pejcha, Ondřej (June 2014). "Burying a Binary: Dynamical Mass Loss and a Continuous Optically thick Outflow Explain the Candidate Stellar Merger V1309 Scorpii". In: *The Astrophysical Journal* 788, p. 22. DOI: 10.1088/0004-637X/788/1/22.

Pejcha, Ondřej, Brian D. Metzger, and Kengo Tomida (Sept. 2016a). "Binary stellar mergers with marginally bound ejecta: excretion discs, inflated envelopes, outflows, and their luminous transients". In: *Monthly Notices of the Royal Astronomical Society* 461.3, pp. 2527–2539. DOI: 10.1093/mnras/stw1481.

Pejcha, Ondřej, Brian D. Metzger, and Kengo Tomida (Feb. 2016b). "Cool and luminous transients from mass-losing binary stars". In: *Monthly Notices of the Royal Astronomical Society* 455.4, pp. 4351–4372. DOI: 10.1093/mnras/stv2592.

Pejcha, Ondřej, Brian D. Metzger, Jacob G. Tyles, and Kengo Tomida (Nov. 2017). "Pre-explosion Spiral Mass Loss of a Binary Star Merger". In: *ApJ* 850.1, p. 59. DOI: 10.3847/1538-4357/aa95b9.

Perets, H. B. et al. (May 2010). "A faint type of supernova from a white dwarf with a helium-rich companion". In: *Nature* 465.7296, pp. 322–325. DOI: 10.1038/nature09056.

Perets, Hagai B. and Paz Beniamini (June 2021). "No velocity-kicks are required to explain large-distance offsets of Ca-rich supernovae and short-GRBs". In: *Monthly Notices of the Royal Astronomical Society* 503.4, pp. 5997–6004. DOI: 10.1093/mnras/stab794.

Perez M., Sebastian and Katherine M. Blundell (Oct. 2010). "SS 433's circumbinary ring and accretion disc viewed through its attenuating disc wind". In: *Mon Not R Astron Soc* 408.1, pp. 2–8. DOI: 10.1111/j.1365-2966.2010.16638.x.

Perrefort, Daniel, Yike Zhang, Lluís Galbany, W. M. Wood-Vasey, and Santiago González-Gaitán (Dec. 2020). "A Template-based Approach to the Photometric Classification of SN 1991bg-like Supernovae in the SDSS-II Supernova Survey". In: *The Astrophysical Journal* 904.2, p. 156. DOI: 10.3847/1538-4357/abbefc.

Peters, P. C. (Nov. 1964). "Gravitational Radiation and the Motion of Two Point Masses". In: *Physical Review* 136.4B, B1224–B1232. DOI: 10.1103/PhysRev.136.B1224.

Picco, A., P. Marchant, H. Sana, and G. Nelemans (Jan. 2024). "Forming merging double compact objects with stable mass transfer". In: *Astronomy and Astrophysics* 681, A31. DOI: 10.1051/0004-6361/202347090.

Piro, Anthony L. (Nov. 2019). "Inferring the Presence of Tides in Detached White Dwarf Binaries". In: *The Astrophysical Journal* 885, p. L2. DOI: 10.3847/2041-8213/ab44c4.

Podsiadlowski, Ph., P. C. Joss, and J. J. L. Hsu (May 1992). "Presupernova Evolution in Massive Interacting Binaries". In: *The Astrophysical Journal* 391, p. 246. DOI: 10.1086/171341.

Polin, Abigail, Peter Nugent, and Daniel Kasen (Mar. 2019). "Observational Predictions for Sub-Chandrasekhar Mass Explosions: Further Evidence for Multiple Progenitor Systems for Type Ia Supernovae". In: *The Astrophysical Journal* 873, p. 84. DOI: 10.3847/1538-4357/aafb6a.

Polin, Abigail, Peter Nugent, and Daniel Kasen (Jan. 2021). "Nebular Models of Sub-Chandrasekhar Mass Type Ia Supernovae: Clues to the Origin of Ca-rich Transients". In: *ApJ* 906.1, p. 65. DOI: 10.3847/1538-4357/abcccc.

Pols, Onno (2011). *Binary Stars Lecture Notes*. Lecture notes, Utrecht University.

Postnov, Konstantin A. and Lev R. Yungelson (May 2014). "The Evolution of Compact Binary Star Systems". In: *Living Rev. Relativ.* 17.1, p. 3. DOI: 10.12942/lrr-2014-3.

Prada Moroni, P. G. and O. Straniero (Dec. 2009). "Very low-mass white dwarfs with a C-O core". In: *Astronomy and Astrophysics* 507, pp. 1575–1583. DOI: 10.1051/0004-6361/200912847.

Priedhorsky, William C. and Frank Verbunt (Oct. 1988). "Tidal Forces and Mass Transfer Instabilities in Low-Mass X-Ray Binaries". In: *The Astrophysical Journal* 333, p. 895. DOI: 10.1086/166798.

Qin, Y., T. Fragos, G. Meynet, J. Andrews, M. Sørensen, and H. F. Song (Aug. 2018). "The spin of the second-born black hole in coalescing binary black holes". In: *Astronomy & Astrophysics* 616, A28. DOI: 10.1051/0004-6361/201832839.

Quataert, E. and J. Shiode (Jan. 2012). "Wave-driven mass loss in the last year of stellar evolution: setting the stage for the most luminous core-collapse supernovae". In: *Monthly Notices of the Royal Astronomical Society: Letters* 423.1, pp. L92–L96. DOI: 10.1111/j.1745-3933.2012.01264.x.

Raghavan, Deepak, Harold A. McAlister, Todd J. Henry, David W. Latham, Geoffrey W. Marcy, Brian D. Mason, Douglas R. Gies, Russel J. White, and Theo A. ten Brummelaar (Sept. 2010). "A Survey of Stellar Families: Multiplicity of Solar-type Stars". In: *The Astrophysical Journal Supplement Series* 190, pp. 1–42. DOI: 10.1088/0067-0049/190/1/1.

Ransome, C. L. and V. A. Villar (June 2025). "Unveiling the Diversity of Type IIn Supernovae via Systematic Light-curve Modeling". In: *ApJ* 987.1, p. 13. DOI: 10.3847/1538-4357/adce03.

Raskin, Cody, Evan Scannapieco, Chris Fryer, Gabriel Rockefeller, and F. X. Timmes (Feb. 2012). "REMNANTS OF BINARY WHITE DWARF MERGERS". In: *ApJ* 746.1, p. 62. DOI: 10.1088/0004-637X/746/1/62.

Regös, Enikö, Vernon C. Bailey, and Rosemary Mardling (Apr. 2005). "Mass transfer in eccentric binary stars". In: *Monthly Notices of the Royal Astronomical Society* 358, pp. 544–550. DOI: 10.1111/j.1365-2966.2005.08813.x.

Reichardt, Thomas A, Orsola De Marco, Roberto Iaconi, Christopher A Tout, and Daniel J Price (Mar. 2019). "Extending common envelope simulations from Roche lobe overflow to the nebular phase". In: *Monthly Notices of the Royal Astronomical Society* 484.1, pp. 631–647. DOI: 10.1093/mnras/sty3485.

Ricker, Paul M. and Ronald E. Taam (Jan. 2012). "AN AMR STUDY OF THE COMMON-ENVELOPE PHASE OF BINARY EVOLUTION". In: *ApJ* 746.1, p. 74. DOI: 10.1088/0004-637X/746/1/74.

Ritter, H. (Aug. 1988). "Turning on and off mass transfer in cataclysmic binaries". In: *Astronomy & Astrophysics* 202, pp. 93–100.

Rose, B. M. et al. (July 2025). "The Hourglass Simulation: A Catalog for the Roman High-latitude Time-domain Core Community Survey". In: *ApJ* 988.1, p. 65. DOI: 10.3847/1538-4357/ade1d6.

Ruiter, Ashley J., Krzysztof Belczynski, Matthew Benacquista, Shane L. Larson, and Gabriel Williams (July 2010). "The LISA Gravitational Wave Foreground: A Study of Double White Dwarfs". In: *The Astrophysical Journal* 717.2, pp. 1006–1021. DOI: 10.1088/0004-637X/717/2/1006.

Ryu, T., R. Sari, S. E. de Mink, O. David, R. Valli, J. -Z. Ma, S. Justham, R. Pakmor, and H. Ritter (May 2025). "Binary mass transfer in 3D – Mass Transfer Rate and Morphology". In: *arXiv e-prints*, arXiv:2505.18255. DOI: 10.48550/arXiv.2505.18255.

Salmaso, I. et al. (Mar. 2025). "The diversity of strongly interacting Type IIn supernovae". In: *A&A* 695, A29. DOI: 10.1051/0004-6361/202451764.

Sana, H., S. E. de Mink, A. de Koter, N. Langer, C. J. Evans, M. Gieles, E. Gosset, R. G. Izzard, J. -B. Le Bouquin, and F. R. N. Schneider (July 2012). "Binary Interaction Dominates the Evolution of Massive Stars". In: *Science* 337, p. 444. DOI: 10.1126/science.1223344.

Sandquist, Eric L., Ronald E. Taam, and Andreas Burkert (Apr. 2000). "On the Formation of Helium Double Degenerate Stars and Pre-Cataclysmic Variables". In: *The Astrophysical Journal* 533.2, pp. 984–997. DOI: 10.1086/308687.

Scherbak, Peter and Jim Fuller (Nov. 2022). *White dwarf binaries suggest a common envelope efficiency $\alpha \sim 1/3$*. DOI: 10.5281/zenodo.7272761.

Scherbak, Peter and Jim Fuller (Jan. 2023). "White dwarf binaries suggest a common envelope efficiency $\alpha \sim 1/3$". In: *Monthly Notices of the Royal Astronomical Society* 518.3, pp. 3966–3984. DOI: 10.1093/mnras/stac3313.

Scherbak, Peter and Jim Fuller (Jan. 2024). *Ultrashort-period WD binaries are not undergoing strong tidal heating*. DOI: 10.5281/zenodo.10452487.

Scherbak, Peter, Wenbin Lu, and Jim Fuller (Sept. 2025). "Rapid Binary Mass Transfer: Circumbinary Outflows and Angular Momentum Losses". In: *The Astrophysical Journal* 990.2, p. 172. DOI: 10.3847/1538-4357/adf067.

Schlafly, Edward F. and Douglas P. Finkbeiner (Aug. 2011). "Measuring Reddening with Sloan Digital Sky Survey Stellar Spectra and Recalibrating SFD". In: *The Astrophysical Journal* 737, p. 103. DOI: 10.1088/0004-637X/737/2/103.

Schneider, F. R. N., Ph Podsiadlowski, and B. Müller (Jan. 2021). "Pre-supernova evolution, compact-object masses, and explosion properties of stripped binary stars". In: *A&A* 645, A5. DOI: 10.1051/0004-6361/202039219.

Schneider, Fabian R. N., Mike Y. M. Lau, and Friedrich K. Roepke (Jan. 2025). *Stellar mergers and common-envelope evolution*. DOI: 10.48550/arXiv.2502.00111.

Schreiber, M. R. and B. T. Gänsicke (July 2003). "The age, life expectancy, and space density of Post Common Envelope Binaries". In: *Astronomy & Astrophysics* 406, pp. 305–321. DOI: 10.1051/0004-6361:20030801.

Senzel, R. et al. (Feb. 2025). "ZTF SN Ia DR2: An environmental study of Type Ia supernovae using host galaxy image decomposition". In: *Astronomy and Astrophysics* 694, A14. DOI: 10.1051/0004-6361/202451239.

Shakura, N. I. and R. A. Sunyaev (Jan. 1973). "Black holes in binary systems. Observational appearance." In: *Astronomy and Astrophysics* 24, pp. 337–355.

Shao, Yong and Xiang-Dong Li (Dec. 2016). "NONCONSERVATIVE MASS TRANSFER IN MASSIVE BINARIES AND THE FORMATION OF WOLF–RAYET+O BINARIES". In: *ApJ* 833.1, p. 108. DOI: 10.3847/1538-4357/833/1/108.

Shen, Ken J. (May 2015). "Every Interacting Double White Dwarf Binary May Merge". In: *The Astrophysical Journal* 805, p. L6. DOI: 10.1088/2041-8205/805/1/L6.

Shen, Ken J. and Lars Bildsten (June 2009). "UNSTABLE HELIUM SHELL BURNING ON ACCRETING WHITE DWARFS". In: *ApJ* 699.2, pp. 1365–1373. DOI: 10.1088/0004-637X/699/2/1365.

Shen, Ken J. and Eliot Quataert (Oct. 2022). "Binary Interaction Dominates Mass Ejection in Classical Novae". In: *The Astrophysical Journal* 938.1, p. 31. DOI: 10.3847/1538-4357/ac9136.

Shepard, Katherine, Douglas R. Gies, Gail H. Schaefer, Narsireddy Anugu, Fabien R. Baron, Cyprien Lanthermann, John D. Monnier, Stefan Kraus, and Theo ten Brummelaar (Dec. 2024). "A Spectroscopic and Interferometric Study of W Serpentis Stars. I. Circumbinary Outflow in the Interacting Binary W Serpentis". In: *ApJ* 977.2, p. 236. DOI: 10.3847/1538-4357/ad82e7.

Shu, F. H., S. H. Lubow, and L. Anderson (Apr. 1979). "On the structure of contact binaries. III. Mass and energy flow." In: *The Astrophysical Journal* 229, pp. 223–241. DOI: 10.1086/156948.

Simongini, Andrea, Fabio Ragosta, Irene Di Palma, and Silvia Piranomonte (July 2025). "Core-collapse supernova parameter estimation with the upcoming Vera C. Rubin Observatory". In: *A&A* 699, A98. DOI: 10.1051/0004-6361/202554740.

Simonian, Gregory V and Paul Martini (Feb. 2017). "Circumstellar dust, PAHs and stellar populations in early-type galaxies: insights from GALEX and WISE". In: *Mon Not R Astron Soc* 464.4, pp. 3920–3936. DOI: 10.1093/mnras/stw2623.

Skilling, John (Nov. 2004). "Nested Sampling". In: *Bayesian Inference and Maximum Entropy Methods in Science and Engineering: 24th International Workshop on Bayesian Inference and Maximum Entropy Methods in Science and Engineering*. Vol. 735, pp. 395–405. DOI: 10.1063/1.1835238.

Skilling, John (Dec. 2006). "Nested sampling for general Bayesian computation". In: *Bayesian Analysis* 1.4, pp. 833–859. DOI: 10.1214/06-BA127.

Skrutskie, M. F. et al. (Feb. 2006). "The Two Micron All Sky Survey (2MASS)". In: *AJ* 131.2, p. 1163. DOI: 10.1086/498708.

Soberman, G. E., E. S. Phinney, and E. P. J. van den Heuvel (Nov. 1997). "Stability criteria for mass transfer in binary stellar evolution." In: *Astronomy & Astrophysics* 327, pp. 620–635.

Son, L. A. C. van, S. E. de Mink, M. Renzo, S. Justham, E. Zapartas, K. Breivik, T. Callister, W. M. Farr, and C. Conroy (Dec. 2022). "No Peaks without Valleys: The Stable Mass Transfer Channel for Gravitational-wave Sources in Light of the Neutron Star-Black Hole Mass Gap". In: *The Astrophysical Journal* 940, p. 184. DOI: 10.3847/1538-4357/ac9b0a.

Soon, Jamie et al. (Jan. 2020). "Wide-field dynamic astronomy in the near-infrared with Palomar Gattini-IR and DREAMS". In: *Advances in Optical Astronomical Instrumentation 2019*. Vol. 11203. SPIE, pp. 7–8. DOI: 10.1117/12.2539594.

Speagle, Joshua S. (Apr. 2020). "DYNESTY: a dynamic nested sampling package for estimating Bayesian posteriors and evidences". In: *Monthly Notices of the Royal Astronomical Society* 493, pp. 3132–3158. DOI: 10.1093/mnras/staa278.

Spruit, H. C. (Jan. 2002). "Dynamo action by differential rotation in a stably stratified stellar interior". In: *Astronomy and Astrophysics* 381, pp. 923–932. DOI: 10.1051/0004-6361:20011465.

Stamatellos, D., A. P. Whitworth, T. Bisbas, and S. Goodwin (Nov. 2007). "Radiative transfer and the energy equation in SPH simulations of star formation". In: *A&A* 475.1, pp. 37–49. DOI: 10.1051/0004-6361:20077373.

Stevance, H. F. and J. J. Eldridge (June 2021). "Binary pathways to SLSNe-I: SN 2017gci". In: *Monthly Notices of the Royal Astronomical Society* 504, pp. L51–L55. DOI: 10.1093/mnrasl/slab039.

Stone, James M., Kengo Tomida, Christopher J. White, and Kyle G. Felker (July 2020). "The Athena++ Adaptive Mesh Refinement Framework: Design and Magnetohydrodynamic Solvers". In: *The Astrophysical Journal Supplement Series* 249, p. 4. DOI: 10.3847/1538-4365/ab929b.

Sun, Meng, Hongbo Xia, Seth Gossage, Vicky Kalogera, Jifeng Liu, Kyle Akira Rocha, R. H. D. Townsend, and Emmanouil Zapartas (Feb. 2026). "Tides in Massive Binaries: Numerical Solutions and Semianalytical Comparisons". In: *ApJ* 998.1, p. 32. DOI: 10.3847/1538-4357/ae2dff.

Sweigart, A. V., J. C. Lattanzio, J. P. Gray, and C. A. Tout (Jan. 2000). "Gravonuclear instabilities in post-horizontal-branch stars". In: 35, p. 529.

Taddia, F. et al. (July 2013). "Carnegie Supernova Project: Observations of Type IIn supernovae". In: *A&A* 555, A10. DOI: 10.1051/0004-6361/201321180.

Tauris, T. M. and E. P. J. van den Heuvel (Apr. 2006). *Formation and evolution of compact stellar X-ray sources*. DOI: 10.48550/arXiv.astro-ph/0303456.

Tauris, T. M. et al. (Sept. 2017). "Formation of Double Neutron Star Systems". In: *ApJ* 846.2, p. 170. DOI: 10.3847/1538-4357/aa7e89.

Tauris, Thomas M., Norbert Langer, and Philipp Podsiadlowski (Aug. 2015). "Ultra-stripped supernovae: progenitors and fate". In: *Monthly Notices of the Royal Astronomical Society* 451.2, pp. 2123–2144. DOI: 10.1093/mnras/stv990.

Tayar, Jamie et al. (Apr. 2017). "The Correlation between Mixing Length and Metallicity on the Giant Branch: Implications for Ages in theGaiaEra". In: *ApJ* 840.1, p. 17. DOI: 10.3847/1538-4357/aa6a1e.

Temmink, K. D., O. R. Pols, S. Justham, A. G. Istrate, and S. Toonen (Jan. 2023). "Coping with loss - Stability of mass transfer from post-main-sequence donor stars". In: *A&A* 669, A45. DOI: 10.1051/0004-6361/202244137.

Thiele, Sarah, Katelyn Breivik, and Robyn E. Sanderson (Nov. 2021). "Applying the metallicity-dependent binary fraction to double white dwarf formation: Implications for LISA". In: *arXiv:2111.13700 [astro-ph, physics:gr-qc]*.

Toonen, Silvia, Adrian Hamers, and Simon Portegies Zwart (Dec. 2016). "The evolution of hierarchical triple star-systems". In: *Computational Astrophysics and Cosmology* 3.1, p. 6. DOI: 10.1186/s40668-016-0019-0.

Toro, E. F., M. Spruce, and W. Speares (July 1994). "Restoration of the contact surface in the HLL-Riemann solver". In: *Shock Waves* 4.1, pp. 25–34. DOI: 10.1007/BF01414629.

Toubiana, A., N. Karnesis, A. Lamberts, and M. C. Miller (Dec. 2024). "The interacting double white dwarf population with LISA: Stochastic foreground and resolved sources". In: *A&A* 692, A165. DOI: 10.1051/0004-6361/202450174.

Touchard-Paxton, C.-G., C. Frohmaier, M. Pursiainen, M. Sullivan, A. Polin, G. Dimitriadis, L. Galbany, T. L. Killestein, A. Kumar, and J. Lyman (Feb. 2025). "SN 2023xwi: forbidden line emission in the peak spectrum of a Ca-strong transient". In: *Monthly Notices of the Royal Astronomical Society* 537.2, pp. 1015–1027. DOI: 10.1093/mnras/staf069.

Toyouchi, Daisuke, Kenta Hotokezaka, Kohei Inayoshi, and Rolf Kuiper (Aug. 2024). "Radiation hydrodynamical simulations of super-Eddington mass transfer and black hole growth in close binaries". In: *Monthly Notices of the Royal Astronomical Society* 532, pp. 4826–4841. DOI: 10.1093/mnras/stae1798.

Tuna, Semih and Brian D. Metzger (Oct. 2023). "Long-term Evolution of Massive-star Post-common-envelope Circumbinary Disks and the Environments of Fast Luminous Transients". In: *The Astrophysical Journal* 955.2, p. 125. DOI: 10.3847/1538-4357/acef17.

Turatto, M., S. Benetti, E. Cappellaro, I. J. Danziger, M. Della Valle, C. Gouiffes, P. A. Mazzali, and F. Patat (Oct. 1996). "The properties of the peculiar type Ia supernova 1991bg — I. Analysis and discussion of two years of observations". In: *Monthly Notices of the Royal Astronomical Society* 283.1, pp. 1–17. DOI: 10.1093/mnras/283.1.1.

Van, K. X., N. Ivanova, and C. O. Heinke (Mar. 2019). "Low-mass X-ray binaries: the effects of the magnetic braking prescription". In: *Monthly Notices of the Royal Astronomical Society* 483, pp. 5595–5613. DOI: 10.1093/mnras/sty3489.

Verbunt, F. and C. Zwaan (July 1981). "Magnetic braking in low-mass X-ray binaries." In: *Astronomy and Astrophysics* 100, pp. L7–L9.

Waldman, Roni, Daniel Sauer, Eli Livne, Hagai Perets, Ami Glasner, Paolo Mazzali, James W. Truran, and Avishay Gal-Yam (Sept. 2011). "Helium Shell Detonations on Low-mass White Dwarfs as a Possible Explanation for SN 2005E". In: *The Astrophysical Journal* 738.1, p. 21. DOI: 10.1088/0004-637X/738/1/21.

Weinberger, Rainer, Volker Springel, and Rüdiger Pakmor (June 2020). "The AREPO Public Code Release". In: *ApJS* 248.2, p. 32. DOI: 10.3847/1538-4365/ab908c.

Wellstein, S., N. Langer, and H. Braun (Apr. 2001). "Formation of contact in massive close binaries". In: *A&A* 369.3, pp. 939–959. DOI: 10.1051/0004-6361:20010151.

Wilkins, Daniel R. and Cathie J. Clarke (Feb. 2012). "Testing the accuracy of radiative cooling approximations in smoothed particle hydrodynamical simulations". In: *Monthly Notices of the Royal Astronomical Society* 419.4, pp. 3368–3377. DOI: 10.1111/j.1365-2966.2011.19976.x.

Willcox, Reinhold, Morgan MacLeod, Ilya Mandel, and Ryosuke Hirai (Nov. 2023). "The Impact of Angular Momentum Loss on the Outcomes of Binary Mass Transfer". In: *ApJ* 958.2, p. 138. DOI: 10.3847/1538-4357/acffb1.

Woods, T. E., N. Ivanova, M. V. van der Sluys, and S. Chaichenets (Dec. 2011). "ON THE FORMATION OF DOUBLE WHITE DWARFS THROUGH STABLE MASS TRANSFER AND A COMMON ENVELOPE". In: *ApJ* 744.1, p. 12. DOI: 10.1088/0004-637X/744/1/12.

Wright, E. L. (Dec. 2006). "A Cosmology Calculator for the World Wide Web". In: *Publications of the Astronomical Society of the Pacific* 118, pp. 1711–1715. DOI: 10.1086/510102.

Wright, Edward L. et al. (Dec. 2010). "The Wide-field Infrared Survey Explorer (WISE): Mission Description and Initial On-orbit Performance". In: *The Astronomical Journal* 140, pp. 1868–1881. DOI: 10.1088/0004-6256/140/6/1868.

Wu, Samantha and Jim Fuller (Dec. 2020). "A Diversity of Wave-driven Presupernova Outbursts". In: *ApJ* 906.1, p. 3. DOI: 10.3847/1538-4357/abc87c.

Wu, Samantha C. and Jim Fuller (Nov. 2022). "Extreme Mass Loss in Low-mass Type Ib/c Supernova Progenitors". In: *ApJL* 940.1, p. L27. DOI: 10.3847/2041-8213/ac9b3d.

Xiong, H., X. Chen, Ph Podsiadlowski, Y. Li, and Z. Han (Mar. 2017). "Subdwarf B stars from the common envelope ejection channel". In: *Astronomy & Astrophysics* 599, A54. DOI: 10.1051/0004-6361/201629622.

Yoon, S.-C., Ph. Podsiadlowski, and S. Rosswog (Sept. 2007). "Remnant evolution after a carbon–oxygen white dwarf merger". In: *Monthly Notices of the Royal Astronomical Society* 380.3, pp. 933–948. DOI: 10.1111/j.1365-2966.2007.12161.x.

Yu, Hang, Jim Fuller, and Kevin B Burdge (Feb. 2021). "Tidally excited oscillations in hot white dwarfs". In: *Monthly Notices of the Royal Astronomical Society* 501.2, pp. 1836–1851. DOI: 10.1093/mnras/staa3717.

Yu, Hang, Nevin N. Weinberg, and Jim Fuller (Aug. 2020). "Non-linear dynamical tides in white dwarf binaries". In: *Monthly Notices of the Royal Astronomical Society* 496, pp. 5482–5502. DOI: 10.1093/mnras/staa1858.

Yuan, Feng, Zhaoming Gan, Ramesh Narayan, Aleksander Sadowski, Defu Bu, and Xue-Ning Bai (May 2015). "NUMERICAL SIMULATION OF HOT ACCRETION FLOWS. III. REVISITING WIND PROPERTIES USING THE TRAJECTORY APPROACH". In: *ApJ* 804.2, p. 101. DOI: 10.1088/0004-637X/804/2/101.

Yuan, Feng and Ramesh Narayan (Aug. 2014). "Hot Accretion Flows Around Black Holes". In: *Annual Review of Astronomy and Astrophysics* 52, pp. 529–588. DOI: 10.1146/annurev-astro-082812-141003.

Zahn, J. -P. (July 1975). "The dynamical tide in close binaries." In: *Astronomy and Astrophysics* 41, pp. 329–344.

Zahn, J. -P. (May 1977). "Tidal friction in close binary systems." In: *Astronomy and Astrophysics* 57, pp. 383–394.

Zahn, Jean-Paul (2008). "Tidal dissipation in binary systems". In: *EAS Publications Series* 29, pp. 67–90. DOI: 10.1051/eas:0829002.

Zapartas, E. et al. (May 2017). “Delay-time distribution of core-collapse supernovae with late events resulting from binary interaction”. In: *A&A* 601, A29. DOI: 10.1051/0004-6361/201629685.

Zenati, Yossef, Hagai B. Perets, Luc Dessart, Wynn V. Jacobson-Galán, Silvia Toonen, and Armin Rest (Feb. 2023). “The Origins of Calcium-rich Supernovae From Disruptions of CO White Dwarfs by Hybrid He-CO White Dwarfs”. In: *The Astrophysical Journal* 944.1, p. 22. DOI: 10.3847/1538-4357/acaf65.

Zenati, Yossef, Silvia Toonen, and Hagai B. Perets (Jan. 2019). “Formation and evolution of hybrid He-CO white dwarfs and their properties”. In: *Monthly Notices of the Royal Astronomical Society* 482.1, pp. 1135–1142. DOI: 10.1093/mnras/sty2723.

Zheng, Zheng and Enrico Ramirez-Ruiz (Aug. 2007). “Deducing the Lifetime of Short Gamma-Ray Burst Progenitors from Host Galaxy Demography”. In: *ApJ* 665.2, p. 1220. DOI: 10.1086/519544.

Zorotovic (2022). private communication.

Zorotovic, M., M. R. Schreiber, B. T. Gänsicke, and A. Nebot Gómez-Morán (Sept. 2010). “Post-common-envelope binaries from SDSS. IX: Constraining the common-envelope efficiency”. In: *Astronomy & Astrophysics* 520, A86. DOI: 10.1051/0004-6361/200913658.

Zorotovic, Monica and Matthias R Schreiber (Apr. 2022). “Close detached white dwarf + brown dwarf binaries: Further evidence for low values of the common envelope efficiency”. In: *Monthly Notices of the Royal Astronomical Society*, stac1137. DOI: 10.1093/mnras/stac1137.